Taylor, B., Huchon, P., Klaus, A., et al., 1999
Proceedings of the Ocean Drilling Program, Initial Reports Volume 180

8. SITE 1114[1]

Shipboard Scientific Party[2]

SITE 1114

Hole 1114A (RCB):
9°47.613′S, 151°34.504′E; 406.5 mbsl
0–352.80 mbsf cored; 43.78 m recovered (12%)

Site 1114 is just north of the crest of Moresby Seamount where seismic reflection data indicate that the basement beneath a south-southwest–dipping normal fault is shallowest. The primary objective was to determine the internal structure and composition of Moresby Seamount, particularly the nature of the basement (rock type, pressure-temperature history, structural fabric, and deformation history). A second objective was to determine the sedimentology, biostratigraphy, and vertical motion history of the ~300 m of local sedimentary cover, which may correspond to the uplifted and partly eroded synrift sequence.

In Hole 1114A, we drilled ~286 m of Pliocene–Pleistocene sediments separated by a 6-m-thick tectonic breccia from a metadolerite that forms the basement. The dolerite was metamorphosed under low-grade greenschist facies conditions before its upper part, which contained a chilled margin, was reactivated by normal faulting, leading to its unroofing.

The sediments consist of rift-related, mostly volcaniclastic, turbidites deposited in middle bathyal water depths (500–2000 m). The benthic foraminiferal assemblage is characteristic of a suboxic environment of deposition, which may correspond either to a basinal situation with restricted circulation or to the oceanographic oxygen minimum situated at middle to upper bathyal water depths. From bottom to top, the deposition changed from mostly coarse-grained sandstones, ~100 m thick, to a finer grained intercalation of sandstones, siltstones, and claystones. The mineralogy of the sandstones suggests that most of the turbidites were derived from calc-alkaline extrusive rocks, but minerals

[1]Examples of how to reference the whole or part of this volume.
[2]Shipboard Scientific Party addresses.

Ms 180IR-108

and clasts from ultramafics and metamorphics (serpentinite and calc-schists) are also present, as well as ubiquitous bioclasts.

Only the uppermost sediments are Pleistocene in age. The indurated sediments below 35 cm in Core 180-1114A-2R are all late and middle Pliocene (from >1.67 Ma to 3.09–3.25 Ma) and were deposited at rates of at least 176 m/m.y. The offset of the porosity vs. depth curve suggests that from 220 to >400 m of the Pleistocene section has been removed, which we tentatively relate to the uplift of Moresby Seamount in the footwall of bounding normal fault systems.

The deformation in the recovered sedimentary rocks preferentially occurs in the fine-grained strata, where it is expressed as a scaly fabric with numerous striated surfaces. It increases in intensity approaching the tectonic breccia. The bedding dips in the upper ~110 m range from 0° to 30°, then increase to 25°–60° below that. The FMS data reveal that (1) bedding dip directions are dominantly northwest but range from north to west; (2) the basement/sediment faulted contact outlined by the breccia dips ~60° toward the southwest, slightly oblique to the main normal fault that offsets basement by >2 km; and (3) in contrast, faults within the overlying sedimentary rocks mostly dip to the north, but a few dip to the south just above the breccia. The sense of motion on faults within the sedimentary rocks is dominantly normal, but reverse and oblique slip faults also exist. These observations suggest that a component of left-lateral motion exists on the bounding, south-southwest-dipping normal fault, in agreement with regional evidence for north-south extension.

The brecciated fault contact is also marked by an abrupt increase in the degree of hydrothermal alteration. The alteration in the breccia and metadolerite is characterized by massive clay and calcite veins that crosscut numerous quartz and epidote veins. In the breccia, the latter veins are restricted to the clasts. The hydrothermal alteration tends to decrease downward in the metadolerite, suggesting that fluids were channeled into the tectonic breccia.

OPERATIONS

Transit to Site 1114

During the ~3.6-nmi transit (in dynamic positioning mode) to Site 1114, a rotary core barrel (RCB) bottom-hole assembly (BHA) was prepared with a new bit and a mechanical bit release. The ship arrived on location at 2015 hr on 12 July 1998, and a positioning beacon was deployed. However, this beacon could not be used for positioning because it had shifted into half-repetition-rate mode, possibly because of interference from one of the precision depth recorders (PDR) (12 or 3.5 kHz). The ship returned to the Global Positioning System (GPS) coordinates, and a second beacon was deployed at 2130 hr.

Hole 1114A

While we lowered the pipe to determine seafloor depth, the strong current caused the knobby drilling joints to drag in the guide horn. This allowed the heave compensator to close, leading the driller to incorrectly assume the seafloor had been tagged. As a result, several water cores were recovered before Hole 1114A was eventually spudded

at 406.5 meters below sea level (mbsl) at 0130 hr on 13 July 1998 (Tables T1, T2).

The RCB Cores 1R through 31R were taken from 0 to 295.4 meters below seafloor (mbsf). The intervals l42–180 and 257–276 mbsf were characterized by a rapid rate of penetration (ROP) and extremely poor recovery (0%–4%). The small amount of recovery indicated the presence of sand in these intervals. Metamorphic rocks were first recovered at ~300.0 mbsf (in Core 32R), and coring continued to 352.8 mbsf (Core 37R). While coring there were several episodes when we lost acoustic contact with the positioning beacons. A third positioning beacon was deployed at 1340 hr on 14 July, but contact with this beacon was lost almost immediately. At 1642 hr, a fourth beacon was deployed using the Zodiac ~150 m up current from Hole 1114A. The intent was to have the beacon drift with the >1.5-nmi/hr current while sinking to the bottom and to end up closer to the actual spud location. No further positioning problems were encountered.

While we prepared to retrieve Core 37R, the hole collapsed, packing off the annulus and preventing circulation. The pipe was raised 80 m above the bottom of the hole on two separate occasions before circulation could be established. We spent 6.25 hr trying to get back to the bottom to resume coring without success; therefore, we decided to run wireline logs in the portion of the hole that remained open. The bit release sleeve was shifted at 316.0 mbsf; however, the bit did not release. The pipe was picked up to 304.0 mbsf while the pipe was rotated by the top drive. The bit released between 304 and 316 mbsf, and the hole was displaced with 90 bbl of sepiolite mud. The pipe was raised to 80.0 mbsf, and we rigged up for logging.

The first logging run with the triple combo was logged from 304.0 to ~60 mbsf. The second logging run with the Formation MicroScanner-(FMS) sonic tool was able to log up from 299.0 mbsf. Once logging was completed (0545 hr on 16 July) we ran the open-ended drill pipe back in the hole as far as possible (107.0 mbsf) and displaced the hole with 35 bbl of 10.5-ppg bentonite gel mud. The drill string was pulled clear of the seafloor at 0625 hr and the four positioning beacons were recovered in 1.25 hr. At 0800 hr on 16 July 1998, the drilling assembly cleared the rig floor and we began the transit to Site 1115 (proposed site ACE-l5A). Core recovery from Hole 1114A was 43.78 m (12%).

T1. Site 1114 coring summary, p. 120.

T2. Site 1114 coring summary by section, p. 121.

F1. Lithologic log of succession at Site 1114, p. 45.

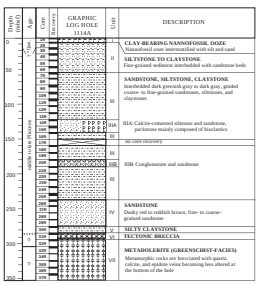

F2. Bed-by-bed log of succession in Hole 1114A, p. 46.

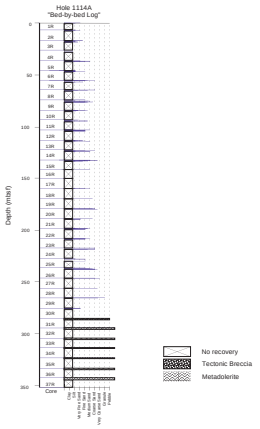

LITHOSTRATIGRAPHY

Introduction

Nearly 286 m of sediments and sedimentary rocks above a contact with a basement of metamorphic rocks was cored in Hole 1114A. Seven lithostratigraphic units are recognized on the basis of sediment or rock type, grain size, sedimentary structure, color, compositions determined in smear slides and thin sections, bulk mineralogy (X-ray diffraction [XRD]), and carbonate determinations. The recovery was poor, and geophysical logs (especially FMS) were useful to help reconstruct the succession.

The lithostratigraphic units recognized are shown in Figure F1, and a bed-by-bed log is shown in Figure F2. Unit I is a surficial, soft pelagic and hemipelagic ooze and clay. By contrast, all the underlying units are at least partly lithified. Unit II consists mainly of siltstone to claystone. Unit III, by far the thickest, is composed of intercalated sandstone, silt-

stone, and claystone. Two subunits are recognized within Unit III: (1) Subunit IIIA is a thin interval of calcite-cemented siltstone and sandstone and very minor limestone (packstone) and (2) Subunit IIIB is distinguished by the presence of minor granule conglomerates. In Unit IV, the sandstones change to an unusual dusky red color. Below this is a thin interval of finer grained silty claystone forming Unit V underlain by a tectonic breccia (Unit VI) that overlies metadolerite (see "Igneous and Metamorphic Petrology," p. 16).

Lithostratigraphic Unit I

Description: clay-bearing nannofossil ooze
Interval: 180-1114A-1R-1, 0–37 cm
Depth: 0.0–0.37 mbsf
Age: Pleistocene

Lithostratigraphic Unit I is represented by only 37 cm in Section 1R-1 in which the following sediment types are present.

Foraminifer-Bearing Nannofossil Ooze and Clay

This is pale, homogeneous, fine-grained ooze and clay, with scattered foraminifers and rare laminations rich in planktonic foraminifers (e.g., interval 180-1114A-1R-1, 7–32 cm). A calcium carbonate analysis of Sample 180-1114A-1R, 15–16 cm, indicates a value of 65 wt%. In smear slides, the calcareous clay contains rare quartz, volcanic glass (colorless and brown), opaque minerals, planktonic foraminifers, calcareous nannofossils, radiolarians, and sponge spicules (see "Site 1114 Smear Slides," p. 42). The XRD analyses reveal the presence of only calcite and minor plagioclase within one sample of foraminifer-bearing nannofossil ooze (Table T3).

T3. XRD analysis of sediments, p. 125.

Silt

Silts observed in smear slides are made up of quartz, plagioclase, volcanic rock fragments, volcanic glass (partly devitrified), and carbonate grains together with rare accessory minerals (pyroxene and amphibole), pyrite, and sponge spicules (see "Site 1114 Smear Slides," p. 42). Common planktonic foraminifers, nannofossils, and rare sponge spicules are also present. An impregnated thin section contains quartz, plagioclase, basaltic lithoclasts, altered acidic grains, devitrified glass, hornblende, pyroxene, organic-rich (plant?) material, and rare planktonic foraminifers set in a clay-rich matrix (see "Site 1114 Thin Sections"). In addition, occasional thin interbeds of silt contain small angular intraclasts (several millimeters) of indurated quartz-rich siltstone (e.g., interval 180-1114A-1R-1, 32–37 cm).

Sand

There are occasional thin beds of foraminifer sand with rare detrital material. In smear slides, this sediment contains, in addition to planktonic foraminifers and calcareous nannofossils, rare quartz, volcanic glass, opaque grains, calcite grains (undifferentiated), radiolarians, and sponge spicules (see "Site 1114 Smear Slides," p. 42).

Pebbles

Small (several centimeters), angular pebbles of quartz-rich siltstone are found just above the contact with the underlying lithified sediment (Unit II; e.g., interval 180-1114A-1R-1, 32–37 cm).

Interpretation

Lithostratigraphic Unit I is interpreted as calcareous pelagic and hemipelagic sediment that accumulated during the Pleistocene at a middle bathyal water depth (500–2000 m) (see "Biostratigraphy," p. 27). There is an abrupt change from soft pelagic and hemipelagic ooze and clay of Unit I to well-lithified sedimentary rocks of Unit II, which is interpreted as an unconformity (see "Lithostratigraphic Unit II," p. 5). Nannofossil Subzones NN19E and NN19F are missing (see "Biostratigraphy," p. 27); possible reasons are discussed in the concluding depositional history discussion. The planktonic foraminifer-rich sands may record episodes of relatively high productivity or be caused by winnowing of the clay fraction. The silts contain fine-grained volcaniclastic sediment, including altered volcanic lithoclasts and glass. Similar volcaniclastic material is strewn through the background pelagic and hemipelagic sediments. Recovery was inadequate to more fully document depositional processes.

Lithostratigraphic Unit II

Description: siltstone to claystone
Interval: Cores 180-1114A-2R through 6R
Depth 6.6–55.0 mbsf
Age: late Pliocene–Pleistocene

Lithostratigraphic Unit II is marked by an abrupt change from soft sediment to much less calcareous lithified claystone to siltstone.

Claystone

The claystone is dark green and structureless with *Chondrites* burrows imparting a slight color mottling. The claystone is locally silty or sandy and both silt- and sand-filled burrows are present. Determinations of calcium carbonate content indicate values ranging from 3.1 to 4.4 wt% (see "Organic Geochemistry," p. 31). Smear slides show that the claystone is rich in nannofossils with rare quartz, feldspar, biotite, clay, colorless volcanic glass, accessory minerals, calcite, and planktonic foraminifers (see "Site 1114 Smear Slides," p. 42). Silty claystones contain rare foraminifer tests and detrital sand grains. The XRD analysis of a silty claystone (Sample 180-1114A-5R-1, 17–18 cm; see Table T3), indicates the presence of major plagioclase and quartz, and minor pyroxene, chlorite, amphibole, and illite. The XRD analysis of a claystone (Sample 180-1114A-6R-2, 4–4.5 cm; see Table T3) indicates the presence of major plagioclase and minor quartz, pyroxene, and illite.

Siltstone

Siltstones occur either as homogenous intervals (several tens of centimeters thick) or as thin beds or partings. The siltstone is slightly calcareous, based upon reaction with dilute HCl. The unit is characterized by

repetitive intercalations of siltstone and claystone. For example, nine such transitions were noted in Section 3R-2. Several of the silts grade into silty clay, but the base of the beds can rarely be observed owing to drilling disturbance. Where preserved, the bases of the beds are sharp. Partings exhibit diffuse tops and bases (e.g., interval 180-1114A-3R-1, 49–52 cm). These partings are mainly structureless and poorly sorted with angular fine-sand grains, including quartz, feldspar, rock fragments, and accessory minerals (pyroxene and amphibole). The rock is locally tectonically deformed (see **"Structural Geology,"** p. 20).

In smear slides, the clayey silts were observed to contain common quartz, clay, and nannofossils, and rare feldspar, biotite, volcanic rock fragments, volcanic glass (mainly colorless), accessory minerals, calcite, planktonic foraminifers, and sponge spicules (see **"Site 1114 Smear Slides,"** p. 42).

Sandstone

Very thin beds of fine-grained sandstone exhibit sharp, scoured bases and gradational tops (e.g., interval 180-1114-3R-1, 57–58 cm). Several medium beds (<20 cm) of fine-grained sandstone grade up into siltstone, then silty claystone (e.g., interval 180-1114A-2R-2, 42–60 cm). Sharp bases are rarely preserved (e.g., Section 6R-1). A possible reason is that these intervals were more sand rich and were commonly not recovered by drilling. In one instance, fine-planar lamination was noted (i.e., interval 180-1114A-5R-1, 68–93 cm; see Fig. **F3**). The relative abundance of fine- to medium-grained sandstone increases toward the base of the unit (i.e., Section 5R-1).

In smear slides, the sandstones contain feldspar, quartz, and reddish altered rock fragments (see **"Site 1114 Smear Slides,"** p. 42). In addition, two thin sections contain unaltered plagioclase, quartz, planktonic foraminifers, muscovite, basaltic and acidic rock fragments, and phosphatic grains (Fig. **F4**). A small number of grains of polycrystalline quartz were observed (see **"Site 1114 Thin Sections"**). XRD analysis additionally reveals the presence of plagioclase, quartz, hornblende, pyroxene, calcite, rare chloritic grains, vesicular glass, and opaque grains set in a carbonate cement (Table **T3**).

Interpretation

Lithostratigraphic Unit II records argillaceous hemipelagic sediment interspersed with siltstone and fine to rare medium-grained sandstone, interpreted as turbidites. The benthic foraminifer assemblage indicates middle bathyal water depths (see **"Biostratigraphy,"** p. 27). The silty claystone, siltstone, and sandstone all contain similar volcaniclastic sediment assumed to have been derived from a calc-alkaline source area, in view of the nature of the mineral grains (mainly quartz, plagioclase, biotite, and amphibole). Compared to Unit I, there were marked increased detrital constituents, as opposed to calcareous pelagic sediment, including plankton, either because of a decrease in primary productivity or because of dilution by increased volcaniclastic input. Also, the calcium carbonate content is greatly diminished (see **"Organic Geochemistry,"** p. 31), reflecting the decreased abundance of nannofossils in Unit II compared to Unit I. However, bottom conditions remained oxidizing in view of the presence of *Chondrites* burrows.

F3. Parallel-laminated sand overlying clay; bioturbated siltstone, **p. 47.**

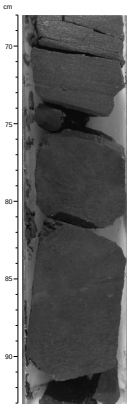

F4. Volcaniclastic sandstone, **p. 48.**

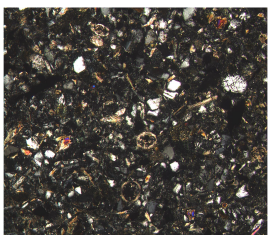

Lithostratigraphic Unit III

Description: sandstone, siltstone and claystone
Interval: Cores 180-1114A-7R through 25R, except for Subunit IIIA (14R-1, 80 cm, through 15R-CC) and Subunit IIIB (20R-1, 0–60 cm)
Depths: 55.0–237.6 mbsf, except for 123.2–141.6 mbsf (Subunit IIIA) and 180.1–180.7 mbsf (Subunit IIIB)
Age: late Pliocene to middle Pliocene

Lithostratigraphic Unit III makes up the greater part of the succession in Hole 1114A, although the recovery was very poor (Fig. F1). However, the missing intervals were reconstructed by using geophysical log and FMS data. In addition, two thin distinctive intervals were recovered. Subunit IIIA is composed of calcite-cemented siltstone and sandstone and minor limestone (packstone), mainly composed of bioclasts. Subunit IIIB, lower in the section, is composed of conglomerate and sandstone.

The following lithologies are present in decreasing order of abundance: sandstone, siltstone, and claystone.

Sandstone

Abundant sandstone varies from weakly to strongly calcareous. The sandstones are mainly fine to medium grained, but locally coarse grained (e.g., interval 180-1114A-24R-1, 7–11 cm). Colors are predominantly dark gray to locally dark greenish gray in the upper part, but then change to brown to reddish brown in the lower part of the succession (i.e., below Core 15R).

Many of the sandstones are thin to medium bedded and exhibit normal grading, although inverse to normal grading is seen rarely (Fig. F5). For example, in interval 180-1114A-7R-2, 0–53 cm, four beds of sandstone 10–25 cm thick grade upward from medium- to fine-grained sandstone, then to siltstone, and then to claystone at the top. Where visible, the bases of individual beds are sharp (e.g., 180-1114A-12R-1, 54 cm).

Most of the sandstones are structureless, but planar lamination is occasionally present, especially in the lower part of individual graded sandstones (e.g., intervals 180-1114A-9R-2, 20–76 cm; 12R-1, 0–5.5 cm; and 12R-1, 56–75.5 cm; see Fig. F6). Exceptionally, convolute lamination was noted, followed abruptly by low-angle planar lamination (intervals 180-1114A-11R-CC, 15–24 cm, and 23R-1, 49–69 cm; see Fig. F7). The base of this particular bed is sharp. In addition, small (3 cm × 1 cm) shale rip-up clasts were locally noted in the upper part of the succession (interval 180-1114A-13R-1, 61–102 cm).

The sandstone is weakly (e.g., interval 180-1114A-7R-1, 8–11 cm) to strongly (e.g., interval 180-1114A-8R-1, 15–34 cm) bioturbated in places. Individual burrows are commonly sand filled. Fragments or laminae rich in woody organic matter are locally abundant within sand beds in the upper part of the unit (intervals 180-1114A-7R-2, 0–33 cm; 8R-1, 0–11 cm; 9R-1, 53.5 cm; and 11R-1, 26.5–27.5 cm). Lower in the unit organic-rich matter was rarely observed (e.g., intervals 180-1114A-15R, 100–110 cm, and 21R-1, 33–49 cm).

Scattered benthic foraminifers were rarely observed (intervals 180-1114A-12R-1, 65–75.5 cm, and 15R-2, 0–35 cm). Within a few intervals, relatively coarse grained volcaniclastic material, especially red altered

F5. Inverse-to-normal graded sandstone, p. 49.

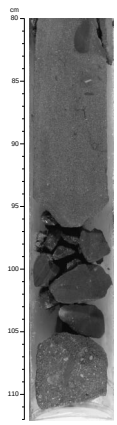

F6. Sandstone with sharp lower bedding planes and parallel laminations, p. 50.

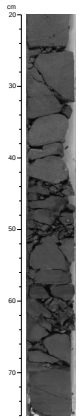

F7. Truncated convolute laminations in sandstone, p. 51.

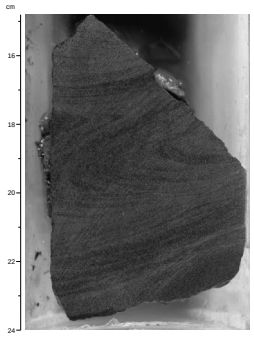

grains (e.g., intervals 180-1114A-9R-2, 0–34 cm and 71–76.5 cm), was evident in the sandstone when viewed with a hand lens.

Smear slides of the sandstone allowed us to identify quartz, plagioclase, biotite, clay, subrounded chloritic basic volcanic rock fragments, volcanic glass, rare accessory minerals (i.e., hornblende and biotite), inorganic calcite, and foraminifers (see "Site 1114 Smear Slides," p. 42). Within single samples the volcanic glass ranges from nondevitrified glass (green and colorless; e.g., Sample 180-1114A-15R-1, 20 cm), to both fresh and devitrified glass (colorless; e.g., Sample 180-1114A-23R-1, 84 cm) to mainly devitrified glass (colorless; e.g., Sample 180-1114A-24R-3, 1 cm).

XRD analysis of the sandstone (see Table T3) reveals major amounts of plagioclase and quartz, and minor amounts of calcite, pyroxene, amphibole, chlorite, and possibly smectite. However, most of the available information on sandstone composition was provided by the study of eight thin sections from throughout Unit III (see "Site 1114 Thin Sections").

The typical sandstones are poorly sorted and contain mainly angular to subangular grains (see "Site 1114 Thin Sections"). Most of the sandstones contain a silty matrix but a few are cemented by calcite spar (e.g., interval 180-1114A-11R-CC, 18–20 cm). Sandstones in the upper part of the succession (above Core 13R) contain plagioclase, quartz, basalt, biotite, pyroxene, hornblende, rare planktonic foraminifers, calcite, opaque grains, pyrite framboids, intraclasts of micrite, plant debris, shell fragments, phosphatic grains (collophane), rare limestone lithoclasts, and rare spherulitic zeolite.

The basalt-derived material in different samples ranges from crystalline basalt with microphenocrysts of olivine (commonly flow banded) to pyroxene-phyric basalt to black glassy basalt to basalt with variolitic texture to red partly devitrified basic glass (hyaloclastite) to green chloritized basic extrusive rock and to very rare blue chlorite.

In addition, there are rare occurrences of large laths of muscovite, locally abundant polycrystalline quartz (of probable metamorphic origin), calc-schist, muscovite schist, and rare green chloritic schist (Figs. F8, F9). The white mica is commonly pleochroic (colorless to bluish). In addition, several grains of serpentinite were noted in Sample 180-1114A-12R-1, 3–4 cm, and rare grains of chromite are also present.

Based on the study of six thin sections, there is a change in the composition of the sandstones below ~110 mbsf, marked by an increased input of texturally immature sandstones with fresh basaltic lithoclasts and related phenocrysts (pyroxene and olivine). However, metamorphic-derived lithoclasts (e.g., calc-schist and serpentinite) were not observed in the underlying sandstones. Otherwise, the composition is generally similar to the sandstone described above (e.g., interval 180-1114A-26R-1, 96–97 cm). Also, unlike the upper part of the succession, bioclasts are locally abundant and include coral, shell fragments, calcareous algae, bryozoans, and benthic foraminifers (e.g., Sample 180-1114A-22R-1, 74–76 cm). Small rounded lithoclasts of partly recrystallized limestone are also present (in the last-mentioned sample). Several sandstones from low in the succession are very poorly sorted with angular, broken mineral grains. Also, relatively rare acidic grains (Figs. F8, F9) are present in addition to mainly basaltic ones.

F8. Digital photomicrograph of polycrystalline quartz grain in detrital grains, p. 52.

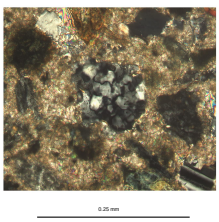

F9. Elongate grain of detrital calc-schist, p. 53.

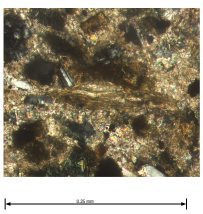

Siltstone

Siltstone is present as interbeds between sandstone and claystone and forms the upper part of graded sand beds. Siltstone is structureless or rarely planar laminated (e.g., interval 180-1114A-11R-2, 44–49 cm). In a few intervals, the siltstone is present as very thin (<3 cm) normal-graded couplets of thickly to thinly laminated siltstone passing into claystone (Fig. F10). Each of the graded couplets exhibits a sharp base with traces of scouring. Rare bioturbation is present in the overlying claystone.

F10. Sharp-based (scoured) siltstone beds, p. 54.

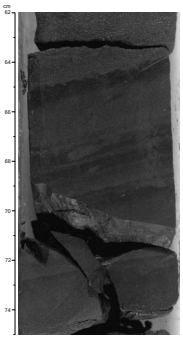

In smear slides, the following constituents are seen: quartz, plagioclase, biotite, clay, volcanic rock fragments (basic and acidic), volcanic glass, opaque mineral grains, pyrite, and common inorganic carbonate grains, together with rare foraminifers and nannofossils (see "Site 1114 Smear Slides," p. 42), and occasional sponge spicules. Quartz grains are rarely observed to be undulose. Foraminifer tests from lower in the succession are pyrite filled. Several samples are sufficiently rich in plagioclase to be termed (fine grained) arkose. A thin section of a relatively well sorted siltstone (Sample 180-1114A-22R-1, 74–76 cm) contains subangular grains of quartz, plagioclase, common small muscovite laths, biotite (kinked), green chlorite, polycrystalline quartz, pyroxene, green chloritic grains, rare fragments of calcareous algae, and minute volcanic-derived grains (see "Site 1114 Thin Sections").

XRD analysis of siltstone reveals the presence of plagioclase, quartz, calcite, chlorite, and possibly smectite (see Table T3). In addition, one thin section of cross-bedded siltstone was studied (Sample 180-1104A-22R-1, 74–76 cm). This is quite well sorted and includes mainly angular grains of quartz, plagioclase, and muscovite (as minute laths), as well as rare grains of volcanic rock, biotite (as kinked laths), chloritic material, pyroxene, polycrystalline quartz, and rare calcareous algae.

Claystone

Subordinate dark gray claystone is found between the sandstones and siltstones. The claystone is mainly weakly burrowed to well burrowed (intervals 180-1114A-23R-1, 26–45 cm; and 9R-CC, 0–4.5 cm). The clay is only weakly lithified, especially where present between graded sandstones (e.g., interval 180-1114A-11R-1, 36.5–52.5 cm). Relative to sandstone, clay is very subordinate, especially in the lower part of the succession and was commonly recovered only as angular fragments (i.e., drilling breccia; e.g., Section 21R-CC).

Smear slides of the claystone ("Site 1114 Smear Slides," p. 42) reveal quartz, plagioclase, biotite, clay, rare minute volcanic rock fragments, volcanic glass, pyrite, inorganic calcite, accessory minerals, poorly preserved nannofossils, and rare planktonic foraminifers. XRD analysis indicates the presence of major amounts of quartz and plagioclase and variable, mainly minor, amounts of calcite, amphibole, pyroxene, and illite (Table T3).

Subunit IIIA

Description: calcite-cemented siltstone and sandstone, packstone mainly composed of bioclasts
Interval: Sections 180-1114A-14R-1, 80 cm, through 15R-CC
Depth: 123.2–141.6 mbsf

Subunit IIIA is restricted to minor recovery in only Cores 14R and 15R. It is distinguished by the occurrence of texturally mature relatively coarse grained, calcite-cemented sandstone, siltstone, and rare bioclastic limestone.

Calcite-Cemented Sandstone

This sandstone is poorly sorted with scattered bioclasts and intraclasts of dark siltstone. In the middle part of Subunit IIIA inverse to normal grading was occasionally observed (e.g., interval 180-1114A-15R-1, 39–48 cm). The sediments are fine to medium grained at the base and then change to coarse and very coarse grained, and then back to medium grain size at the top of the bed. The sand is rich in shell fragments, quartz, feldspar, and rock fragments (Fig. **F11**). The composition is one of mixed carbonate and volcaniclastic grains, including coral, calcareous algae, and shell fragments together with detrital grains. Subangular lithoclasts (<2 mm) of altered volcanic rocks are also present. The intraclasts and bedding are nearly vertical as a result of tectonic deformation (see **"Structural Geology,"** p. 20).

Two thin sections revealed a composition that is very similar to that of the adjacent sandstones of Unit III above and below (see Fig. **F12**), but the texture of the sandstones in Subunit IIIA differs markedly. It is characterized by well-rounded clasts and abundant carbonate bioclasts derived from a shallow-water setting. Sample 180-1114A-14R-1, 106–108 cm, is dominated by well-rounded grains of basalt together with quartz, zoned plagioclase, amphibole, acidic extrusive grains, and rare brown glass (see **"Site 1114 Thin Sections"**). The bioclasts are calcareous algae, echinoderm plates, shell fragments, coral, and benthic foraminifers. The sediment is well cemented by calcite spar.

Sandy Limestone (Packstone)

Two small pieces of well-cemented bioclastic sandy limestone were recovered in the core catcher of Section 14R-CC. The bioclasts are very poorly sorted and comprise calcareous algae, coral fragments, echinoderm plates and spines, and foraminifers. Numerous grains (<2 mm in size) of very altered volcanic rock and several (similar sized) elongate siltstone rip-up clasts are present.

F11. Calcite-cemented sandstone rich in bioclasts, **p. 55.**

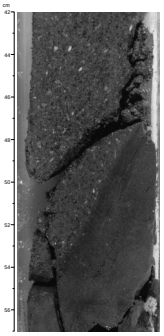

F12. Volcaniclastic sandstone, **p. 56.**

Subunit IIIB

Description: conglomerate and sandstone
Interval: 180-1114R-20R-1, 0–60 cm
Depth: 180.1–180.7 mbsf

Subunit IIIB consists of minor granule conglomerate and sandstone that are present only in the interval 180-1114A-20R-1, 0–60 cm.

Granule Conglomerate

The conglomerate consists of angular clasts up to 0.9 cm long set in a matrix of coarse-grained sandstone. Texturally, the sediment is poorly sorted. The clasts show a very vague subhorizontal alignment. Clasts are mainly volcanic (dark basalt) with a few white carbonate bioclasts. The sandstones in the cores above and below interval 180-1114A-20R-1, 0–60 cm, are of similar composition to those of the present subunit. This subunit is thus recognized only on the basis of the presence of gravel-sized clasts.

Interpretation

Unit III, as well as Subunit IIIA, records variable deposition from turbidity currents in a middle bathyal setting during middle–late Pliocene time (see "Biostratigraphy," p. 27). The normal grading is suggestive of deposition from decelerating currents. Burrowing is present but rarely well developed, suggesting that bottom conditions were possibly suboxic but not reducing. However, beneath the seafloor fully anoxic conditions were probably developed during deposition of the whole of Unit III, as suggested by the subdued colors and common abundance of organic matter of mainly terrestrial origin (i.e., woody material), locally elevated contents of organic carbon (up to 1.4%; see "Organic Geochemistry," p. 31), and common pyrite. Subunit IIIA records deposition of sediment ultimately derived from a shallow-water depositional setting (see "Depositional History," p. 15, for further discussion). In addition, the granule conglomerates are interpreted as deposits from high-density turbidity currents (Pickering et al., 1989).

The provenance of Unit III was from a volcanic arc-type terrane, including a range of basic, andesitic, and vitric volcanics. It is notable that the provenance of the detrital component of the fine-, medium-, and coarse-grained sediments is very similar. This suggests that the sediment was derived relatively locally from within a single basin and was not derived from different source areas. The presence of variolitic textured basalt suggests that some of the basalts were extruded subaqueously. On the other hand, volcanic glass is relatively minor and typically altered, suggesting that explosive subaerial (or near subaerial) volcanism is not greatly represented. Many of the volcaniclastic-rich sandstones are texturally immature. Samples from near the base include unaltered glassy basalt and olivine, suggesting that the volcanic material was eroded rapidly and redeposited without significant subaerial weathering.

In addition, the rare muscovite laths, strongly recrystallized (polycrystalline) quartz, rare calc-schist, and very fine grains of mica schist are inferred to have been derived from a low-grade metamorphosed volcanic terrane.

The geophysical and FMS logs support the above interpretation (see "Downhole Measurements," p. 38). Only features interpreted as being of primary stratigraphic significance are mentioned here; details of the structural features including the evidence for the dip of bedding, location, and orientation of fractures are presented in "Structural Geology," p. 20. From the top of the logged interval (~96 mbsf) to 125 mbsf (near the top of Subunit IIIA), the response on most logs is similar and is interpreted to reflect relatively uniform deposition of claystone, siltstone, and sandstone. The FMS images indicate well-developed layering with thin sandstones ~10 cm thick standing out as resistive layers. Around 120–140 mbsf, the gamma-ray and resistivity logs peak, suggesting that more sandy beds may be present, possibly correlating with Subunit IIIA. From 113 to 118 mbsf, possible cross bedding is present. At 125 mbsf, the hole conditions deteriorated and the FMS images are more difficult to interpret.

The photoelectric effect and the corrected limestone porosity log show a highly variable response between 142.5 and 200 mbsf (with 11 major peaks ~2 m thick and 12 smaller peaks ~1 m thick). This overall interval includes Subunit IIIA composed of calcite-cemented siltstone, sandstone, and packstone in which calcium carbonate content is elevated (up to 4.6 wt% and locally higher, based on other smear-slide

observations). However, the amplitude of these peaks is considered to be too great to be explicable by increased calcium carbonate content alone, even if limestone was present but not recovered (see "Downhole Measurements," p. 38). Instead, the variable photoelectric effect could correlate with the presence of reduced iron minerals (e.g., pyrite, marcasite, or siderite). XRD analysis indicated a single occurrence of marcasite but at a greater depth (~240 mbsf; see Table T3). In addition, pyrite was commonly observed in the cores and smear slides.

A small peak in resistivity at 177.5 mbsf, equivalent to a position near the top of Subunit IIIA, may indicate the presence of a thin sandstone interval. Variably sandy intervals appear to be present from 128 to 177 mbsf. From 179 to 181.5 mbsf, there is a distinctly resistive interval that may correlate with relatively coarse grained sandstone making up Subunit IIIB. The Th/U ratio reaches a maximum at this depth and may indicate high input of relatively radiogenic volcaniclastic sandstone. This interval could also contain U-rich organic matter derived from a shallow-water setting by mass flow processes. There is then an interval of low resistivity from 223 to 228 mbsf that correlates with an enlarged caliper located within the lower part of Unit III (beneath Subunit IIIB). One other feature is the presence of a tight-limbed fold observed in the cores from ~208 mbsf that could possibly represent a slump fold, although a tectonic origin (i.e., deformation of sediment while still soft) cannot be ruled out (see "Structural Geology," p. 20).

Lithostratigraphic Unit IV

Description: fine- to coarse-grained sandstone
Interval: Cores 180-1114A-26R through 29R
Depth: 237.6–276.1 mbsf
Age: middle to late Pliocene

The unit is predominantly sandstone that is distinguished from Unit III mainly by a change from a grayish to a dusky red brown color. Individual sandstone intervals vary from well lithified to less well lithified.

Sandstone

The sandstone is fine to coarse grained and ranges from weakly lithified to well lithified. It is mainly fine to medium grained, but is rarely coarse grained with scattered granules up to 4 mm in size (e.g. interval 180-1114A-29R-CC, 0–7.5 cm). Unfortunately, the recovery of these sandstones was minimal, and it is not possible to specify information including bed thickness and the nature of contacts.

Smear slides of the less lithified material (see "Site 1114 Smear Slides," p. 42) revealed quartz and plagioclase, together with rare biotite, clay, volcanic rock fragments (see Fig. F13), devitrified volcanic glass, accessory minerals, calcite rhombs, and foraminifers (see "Site 1114 Smear Slides," p. 42). XRD analysis confirmed the presence of major amounts of plagioclase and minor quartz, pyroxene, and amphibole. In addition, very minor claystone was seen in XRD to contain quartz, plagioclase, calcite, and minor pyrite, marcasite, chlorite, possible smectite, illite, and amphibole (see Table T3).

Two thin sections of sandstone from Unit IV were studied (see Fig. F13). One was present only a few centimeters above the tectonic breccia forming Unit VI (see "Lithostratigraphic Unit VI," p. 14). This is similar to the sandstones higher in the succession and includes plagioclase,

F13. Digital photomicrograph of basalt clast with flow-banded microphenocrysts, p. 57.

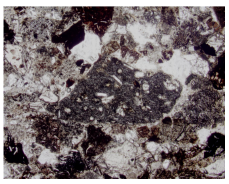

clinopyroxene, lithoclasts of clinopyroxene–phyric basalt, variolitic basalt, devitrified basic glass (hyaloclastite), minor acidic volcanics, and rare polycrystalline quartz (altered acidic volcanic rock?), chloritic grains, and organic material.

Interpretation

Unfortunately, there is inadequate information on sedimentary characteristics and paleobathymetry to specify the mode of deposition. It is assumed, however, that the sandstones record very similar deposition by turbidity currents as in Unit III, and a similar provenance from a calc-alkaline type volcanic arc terrane is inferred, including unaltered volcanic rocks.

Below 233 mbsf, the hole conditions were generally poor and FMS images are difficult to interpret (see **"Downhole Measurements,"** p. 38). Unit IV includes a zone of faulting (see **"Structural Geology,"** p. 20). Locally, at ~249 mbsf, an interval of low resistivity may correlate with the presence of strongly altered dusky red sandstones in the cores.

Lithostratigraphic Unit V

Description: silty claystone
Interval: Core 180-1114A-30R through Section 31R-1, 25 cm
Depths: 276.1–286.05 mbsf
Age: middle to late Pliocene

This unit is restricted to silty claystone with minor siltstone and sandstone. The fine grain size contrasts strongly with the overlying coarse-grained sandstone of Unit IV. This unit is only weakly lithified in places. It is also strongly deformed (see **"Structural Geology,"** p. 20), which inhibits sedimentological analysis.

F14. Highly deformed siltstone, **p. 58.**

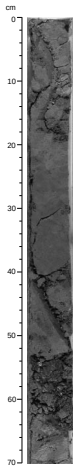

Silty Claystone, Calcareous Silt, and Clay

The silty claystone and fine-grained sandstone are highly deformed, and few primary sedimentary structures can be discerned other than several thin, sharp-based interbeds of fine-grained sandstone (<10 cm thick; see Fig. **F14**).

In smear slide, the calcareous silt contains quartz, plagioclase, biotite, clay, accessory minerals (hornblende), inorganic calcite, rare nannofossils, and sponge spicules (see **"Site 1114 Smear Slides,"** p. 42). A sample of calcareous clay is similar in composition and includes numerous inorganic calcite crystals. Associated clay contains major amounts of plagioclase, quartz, and minor smectite?, chlorite, and pyroxene.

One sandstone bed (interval 180-1114A-30R-CC, 0–22 cm) is composed of angular and rounded fragments of claystone and siltstone (2–3 mm); these are very strongly deformed and brecciated, and are set in a fine- to medium-grained, poorly sorted matrix. A smear slide of the sandstone revealed an arkosic composition marked by common plagioclase, altered volcanic rock fragments (including basalt; Fig. **F15**), accessory minerals (pyroxene, hornblende), rare quartz, and inorganic calcite. A thin section of the sandstone indicates it contains grains of quartz, feldspar, pyroxene, epidote, biotite, hornblende, variolitic basalt, acidic volcanics, dolerite, and carbonaceous material (see **"Site 1114 Thin Sections"**). XRD analysis of the sandstone revealed major

F15. Digital photomicrograph of basaltic and andesitic lithoclasts, **p. 59.**

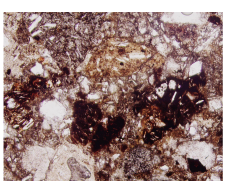

amounts of plagioclase and quartz, and minor chlorite, smectite?, and pyroxene (Table T3).

The base of Unit V is composed of only weakly indurated brown clay (interval 180-1114A-31R-1, 0–15 cm) within thin (several millimeters), weakly indurated silt laminae and secondary color mottling.

Interpretation

Unit V records a period of mainly fine-grained deposition with only very subordinate siltstones and sandstones deposited by turbidity currents. The composition of rare sandstones remains similar to that of the sandstones of Unit IV without a trace of lithologies derived from the local metamorphic basement (see "Igneous and Metamorphic Petrology," p. 16).

Lithostratigraphic Unit VI

Description: tectonic breccia
Interval: Sections 180-1114A-31R-1, 25 cm, through 31R-CC
Depth: 286.05–287.35 mbsf
Age: middle to late Pliocene

Unit VI is a thin but distinctive interval of tectonic breccia that separates the sediments of Unit V above from metamorphic rocks beneath (Unit VII). The unit is subdivided into two parts.

The upper part of the unit is a breccia (interval 180-1114A-31R-1, 25–74 cm) composed of angular to subangular clasts of greenschist, <0.6 cm in size, set in a greenish matrix that also includes scattered, well-rounded grains (red, brown, and colorless). A crude layering is present but without any recognizable sedimentary structures or bedding planes.

A smear slide of the matrix contains quartz, plagioclase, clay, accessory minerals, opaque grains, and inorganic calcite. A thin section revealed an unusual texture and composition. The greenish silty matrix contains subrounded grains of chlorite/actinolite schist and altered dolerite.

The lower part of the unit is a contrasting type of breccia (intervals 180-1114A-31R-1, 74–130 cm, and 31R-CC, 0–18 cm) that is composed of weakly indurated angular clasts (<1 cm in size) of finely crystalline, very altered greenschist set in a greenish silty matrix. Careful inspection did not reveal the presence of any sedimentary grains. In places, relict altered veins are present that can be traced through the body of the rock. Patchy yellow/brown alteration is also present (on a scale of several centimeters).

A smear slide was found to contain quartz, plagioclase, biotite, clay, accessory minerals, and inorganic calcite. A thin section exhibits brecciated actinolite schist, with angular clasts and evidence of veining and partial silicification. This material is similar in lithology to the underlying "basement" (see "Igneous and Metamorphic Petrology," p. 16). In addition, a vein infill contains major amounts of plagioclase, calcite, kaolinite, smectite?, and minor quartz (Table T3).

Interpretation

The breccia is tectonic in origin, and no sedimentary constituents associated with the overlying succession were identified. The upper unit (interval 180-1114A-31R-1, 25–74 cm) contains numerous angular, to

subangular, to subrounded clasts of altered metamorphic rock. The more rounded grains are not interpreted as sedimentary grains. More probably they are fragments of tectonic breccia that were subrounded by shearing associated with faulting. On the other hand, the lower unit (intervals 180-1114A-31R-1, 74–130 cm, and 31R-CC, 0–18 cm) includes a vein fabric that although altered and deformed, is seen as being inherited from the underlying metamorphic basement. In addition, an unusual occurrence of kaolinite within the veins of the tectonic breccia may relate to low-temperature hydrothermal alteration of the intrusive basement rocks. The presence of chloritized vein fills also suggests that hydrothermal alteration played an important role.

An interval of ~287.7–292 mbsf corresponding to the tectonic breccia is imaged on the FMS as a dark, conductive interval (see **"Downhole Measurements,"** p. 38). The image is similar to the shear zones located at the Unit IV/Unit V boundary and suggests that only part of this fault breccia was recovered. Little textural or other structural information could be gained because of the insufficient quality of the data, most likely owing to enlarged hole diameters. However, there is a big increase in resistivity at 292 mbsf, which corresponds to the contact between Unit VI and the metamorphic basement beneath. This contact is sharp and dips at ~40° to the southwest subparallel to the inferred orientation of the fault zone on seismic profiles (see **"Downhole Measurements,"** p. 38).

Lithostratigraphic Unit VII

Description: metadolerite (greenschist facies)
Interval: Cores 180-1114A-32R through 37R
Depth: 295.4–352.8 mbsf

Lithostratigraphic Unit VII is composed of metadolerite that is brecciated and contains quartz, calcite, and epidote veins. This unit is described in detail in **"Igneous and Metamorphic Petrology,"** p. 16.

Depositional History

The geophysical and FMS log data help to fill major gaps in the recovery and are interpreted to suggest that the succession as a whole consists of alternating sandy and silty/clayey sediments with a maximum of sand ~180 mbsf corresponding to Subunit IIIB, then becoming generally more silty downward.

Sedimentation at Site 1114 records rapid rift-related volcaniclastic deposition that can only be dated as middle–late Pliocene in age. Almost the entire succession was deposited by redepositional processes including turbidity currents of variable concentrations in an upper bathyal setting (150–500 m; see **"Biostratigraphy,"** p. 27). The recorded succession began with an interval of relatively fine grain size (Unit V). The origin of the overlying dusky red sandstones of Unit V is unclear, but could relate to (oxidative) diagenesis (i.e., related to fluid flow within the sediment), and may thus not reflect primary depositional characteristics. Unit III preserves relatively monotonous turbidity current deposits that rarely reached conglomerate size (i.e., granule conglomerate of Subunit IIIB).

In addition, there was a single interval of sandstone and rare packstone, Subunit IIIA, that was deposited by turbidity currents. These include abundant shallow-water derived fossils and well-rounded clasts

of basalt and other volcanic rocks. These sediments record an unusual supply of sand from a high-energy littoral source (i.e., coastal or shoal).

The accumulation of coarse-grained sediments is probably related to turbidity currents that changed to deposition of fine-grained sediments. There was then a dramatic change from the well-lithified clastic sedimentary rocks of Units II through IV to superficial Quaternary clay-bearing nannofossil ooze. The probable explanation of the strong difference in lithification state is that at least several hundred meters of the sediments was deposited and then removed, presumably by current activity (i.e., winnowing), slumping, or tectonic processes resulting from the uplift of the seamount. The hiatus in the sedimentary record is reflected by the absence of micropaleontologic Subzones NN19E–F (see "Biostratigraphy," p. 27). Removal of at least 165 m is inferred from the porosity vs. depth relationship of the sediment of Site 1114 (see "Physical Properties," p. 32). This was followed by pelagic and hemipelagic deposition in a setting removed from clastic sediment input, which probably occurred after uplift of the Moresby Seamount to near its present position.

Throughout the deposition of sand and sandstone at Site 1114 derivation was from a calc-alkaline-type volcanic terrane. Volcaniclastic sediments were probably eroded from the Miocene Trobriand Arc (including Amphetts Island and Egum Atoll) (Lock et al., 1987; Davies et al., 1987). This arc was uplifted during rifting of the Woodlark Basin in the Pliocene or earlier (Goodliffe et al., 1993). The volcanic arc was not deeply eroded at this stage because plutonic rock detritus is rare or absent. On the other hand, the unusual grains of muscovite, calc-schist, locally abundant polycrystalline quartz and rare serpentinite, and zircon are inferred to have been derived from an ultramafic ophiolitic terrane and metamorphic basement, as exposed in the D'Entrecasteaux Islands and southeastern Papua New Guinea (Davies, 1980; Davies and Warren, 1988). The metamorphic debris and ophiolite-derived grains are present mainly above 125 mbsf and may thus be related to rift faulting and uplift of metamorphic basement in the vicinity of the Moresby Seamount.

After deposition, the entire sedimentary succession, except the thin, surficial sediments of Quaternary age, experienced faulting concentrated within discrete zones (see "Structural Geology" p. 20). It is assumed that this deformation relates to uplift of the Moresby Seamount. If this is correct, then the uplift probably took place between late Pliocene and Pleistocene deposition of Unit II and Pleistocene accumulation of Unit I. In detail, the absence of nannofossil Subzones NN19E and NN19F (see "Biostratigraphy," p. 27), in contrast to a continuous stratigraphic record from Subzone NN19B downward within the talus derived from the Moresby Seamount (see "Biostratigraphy," p. 27, in the "Sites 1110–1113" chapter), suggests that uplift of the seamount took place between 0.46 Ma (top of Subzone NN19F) and ~1.67 Ma (base of Subzone NN19E).

IGNEOUS AND METAMORPHIC PETROLOGY

Introduction

In Hole 1114A, 67 m of metamorphosed and brecciated igneous basic rocks was encountered below 286 m of Pliocene–Pleistocene claystone, siltstone, and sandstone (see "Lithostratigraphy," p. 3). Core recovery

below the sediments averaged 13%. Pebbles of igneous material were first encountered in a tectonic breccia in Core 180-1114A-31R. Massive metamorphosed dolerite was recovered from 295.4 mbsf (Core 180-1114A-32R) downward to the base of the hole at 352.8 mbsf. This metadolerite has been subjected to intense brittle deformation and hydrothermal alteration. In general, the extent of both decreases in the dolerite toward the base of the hole. See "Structural Geology," p. 20, for more details regarding the deformational history of these rocks.

Lithologic Description

Dolerite in the Tectonic Breccia

Dolerite clasts were recovered in the tectonic breccia (Section 180-1114A-31R-1) overlying the massive dolerite. The clasts in the upper part of the breccia (e.g., interval 180-1114A-31R-1, 25–74 cm) exhibit quartz and epidote veins crosscutting the rocks and late-stage, massive clay alteration. The matrix itself is free of this generation of veins. A weakly developed layering is defined by the clasts elongated into the matrix. Secondary veins filled with calcite occur at the boundary between the clasts and the matrix. This tectonic breccia evolves downward in intervals 180-1114A-31R-1, 74–130 cm, and 31R-CC, 0–18 cm, into a very fine grained zone in which the structural relationship between the different generations of veins and the nature of the clasts (massive replacement with clay) are difficult to observe.

Massive Dolerite

The rocks recovered at Site 1114 can be classified as one lithologic unit referred to as a brecciated metadolerite. Classification as metadolerite is based upon the patchy presence of fresh to slightly altered dolerite within the same lithologic unit and the presence of relict plagioclase and clinopyroxene in thin section, occurring as typical intergrowths of clinopyroxene and plagioclase, reflecting the original ophitic or granular texture. The intergrowths and texture, in addition to the chemistry (see "Chemistry," p. 18), are reminiscent of the fresh dolerite from Site 1109 (Figs. F16A, F16B, F17). These rocks are fine to medium grained. They originally contained 20%–40% plagioclase and 40%–60% clinopyroxene and had an ophitic to granular texture, similar to fresh dolerite from Site 1109 and throughout the metadolerite from the talus at Sites 1108 and 1110–1113. A similar chilled margin to that described in Hole 1109D (Section 180-1109D-51R-4) is observed in Section 180-1114A-36R-1. The actual contact between the glassy margin and the dolerite is brecciated, which indicates that the original contact (veins of glassy material intruding upward into the dolerite) was reactivated during the deformation (Fig. F18). The glass had a variolitic texture but is now completely replaced by very fine grained material, which could not be fully identified optically, but consists largely of an intergrowth of sericite, zoisite, and albite (saussurite) replacing plagioclase, and a minor amount of epidote replacing clinopyroxene. This penetrative hydrothermal alteration is associated with the brecciation of the dolerite. Indeed, epidote, chlorite, and quartz (related to the hydrothermal alteration) fill veins up to 10 mm wide, which crosscut the dolerite, developed contemporaneously to the brecciation because they crosscut the breccia or are fragmented into the breccia (Fig. F19). Subsequently, chlorite, clay, and trace amounts of pyrite, natrolite, and celadonite

F16. Brecciated and unaltered metadolerite with intergrowths, p. 60.

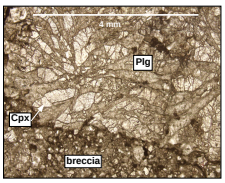

F17. Dolerite with thin quartz veins, p. 62.

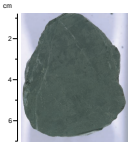

F18. Glassy margin within brecciated metadolerite, p. 63.

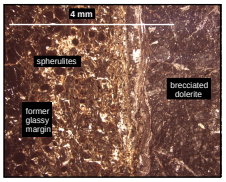

F19. Metadolerite with quartz vein crosscut by fractures, p. 64.

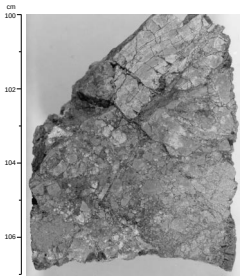

occurred in veins and in the vesicles. The clinopyroxene remained relatively stable during this stage; we observed this phase to be well preserved in the brecciated dolerite. In the most highly altered examples all minerals in the dolerite are replaced by patches exhibiting a plumose or spherulitic texture, consisting of a very fine intergrowth of fibrous tremolite, chlorite, and clay that radiate from a common center.

The rocks also show a series of subsequent crosscutting relationships between a series of intersecting fractures, which give the rocks an intense cataclastic texture (Fig. F19). Specific crystallization is not observed along these fractures, but the fracturing is intensified, the grain sizes decrease, and a matrix of very fine grained, dark brown clay occurs. In some areas the fractures reactivate previous veins (see "Structural Geology," p. 20, for more details). In this case, quartz grains that fill the inner part of the veins are ductilely deformed (Fig. F20), which indicates the presence of fluids until the very latest stages of the metamorphic and structural evolution.

F20. Metadolerite with offset quartz grains, p. 66.

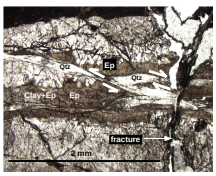

Chemistry

Only a minimal amount of analytical work was undertaken on board for Site 1114 because of the highly veined nature of the rocks. We restricted our analyses to two samples, and results are reported in Tables T4 and T5, along with the analytical results of a metadolerite pebble from Site 1108, an epidote-rich schist from Site 1111 (presumed to be an extremely altered dolerite), and the average of results for the dolerite cored at Site 1109 (the less altered material). These analyses have been arranged in descending order of volatile content to allow a clearer view of the effects of alteration. The dolerite from Site 1108 is moderately altered; it contains fresh clinopyroxene but the plagioclase is totally replaced by sericitic material. One of the samples from Site 1114 (Sample 180-1114A-36R-2, 40–44 cm) is massive and relatively unaltered with only restricted plagioclase sericitization visible in thin section. The other (Sample 180-1114A-36R-1, 70–72 cm) is highly sheared with a clear foliation visible in hand specimen and, again, the original feldspar has been entirely replaced.

T4. Major element composition of dolerite and metadolerite, p. 126.

T5. Trace element composition of dolerite and metadolerite, p. 127.

Tables T4 and T5 do show some variability between the analyses, although not spectacular, and how much to ascribe to hydrothermal alteration and how much to ascribe to normal variations in the dolerite composition is not immediately apparent. There is, however, no consistent trend, and we conclude that chemical alteration is minimal.

The data in Tables T4 and T5 show the following consistent changes (i.e., the altered rocks are all changed in the same sense relative to the unaltered dolerite): Al_2O_3 and CaO loss; Fe_2O_3, MgO, Na_2O, K_2O, LOI, Ba, and Rb gain. However, we need to be critical of these results because they do not always correspond to previous results (e.g., those of Humphris et al., 1998), and they do not often follow the LOI values, which are thought to be the best index of alteration. Of the added components, only Fe_2O_3 and MgO correspond at all or closely with this criterion, and none of the lost components does. We also note that Humphris et al. (1998) did not find significant variations in Al_2O_3, alkali metals, or Ba in their samples. Ni appears to show a significant increase with alteration, as found by Humphris et al. (1998), but Sr increases, the reverse of findings by Humphris et al. (1998). We conclude from this discussion that the rocks may have gained some components and lost others through alteration, but the evidence is highly

equivocal and, in general, the chemical changes have not been overwhelming in spite of the considerable alteration of mineral assemblages and mechanical deformation.

In conclusion, we emphasize that this study has not included the most altered rocks, which we have termed epidosite and is well represented in the talus at Sites 1110–1113 (see **"Igneous and Metamorphic Petrology,"** p. 11, in the "Sites 1110–1113" chapter) and only occasionally at Site 1114.

The differentiation state of these rocks is very similar (i.e., the FeO*/MgO ratio, where FeO* = total iron as FeO; see Table **T4**), making the above comparisons relatively simple. In fact, only one rock is significantly different from the others (i.e., Sample 180-1111A-16R-CC, 8–15 cm; Table **T4**). This rock is more evolved and also has a lower silica content, which suggests that it may follow the Skaergaard type differentiation of falling silica with increasing Fe/Mg ratio (Wager and Brown, 1968). Unfortunately, this is the most altered sample, and the lower silica content may be because of the alteration, as found by previous workers, but the data are insufficient to allow a distinction between these alternatives.

If an account is taken of the possible hydrothermal addition of K, it is likely that the Site 1114 rocks, just as at Site 1109, fall in the field of mid-ocean ridge basalts, although this overlaps with neighboring fields: island arc tholeiites and other low-K tholeiites; therefore, we can only conclude that they belong to the low-K tholeiites and may well be the same as other rocks of this type in the area, which have previously been interpreted as primitive island arc crust (Rogerson et al., 1993).

Interpretation

This unit was formerly dolerite, which was metamorphosed under low-grade greenschist facies conditions before the unroofing of the Moresby Seamount and was subjected to considerable deformation, fracturing, and permeation by fluids. It is likely that this material is the source of the dolerite recovered in the talus. Fluid circulation is inferred from the numerous veins filled with quartz, epidote, and pyrite. This fluid is responsible for the brecciation (fluid-assisted fracturing) of the rocks, although there is no evidence from the existing analyses for pervasive chemical alteration. However, such alteration might be found in the most altered rocks, which were not sampled because of the intensity of brecciation and veining.

The decreasing alteration with depth in the dolerite suggests that it is caused by the proximity of the upper levels to a fault zone along which fluids were channeled. Although it seems likely that these rocks were originally dolerites similar to those at Site 1109, it is not easy to visualize the precise geological nature of the terrain we have sampled. Dolerites generally occur in isolated bodies as sills or dikes, although they can also be found in sheeted dike complexes such as those of ophiolites like Troodos, Cyprus (Robertson and Xenophontos, 1993). Massive sill complexes are also known, although the grain size of these dolerites does not suggest very large intrusions because sills (and dikes) more than a few tens of meters thick tend to develop a gabbroic texture. These are, therefore, minor intrusions that collectively seem to make up a substantial areal extent. It is possible that at Site 1114 we have encountered a sheeted dike complex, perhaps related to the Papuan ophiolite (e.g., Davies and Jaques, 1984). In other areas the ophiolite is represented by the Lokanu Volcanics and equivalents (such as the

Loluai Volcanics of Woodlark Island, referred to in the "Site 1109" chapter) that were encountered at the bottom of the Nubiam well in the Cape Vogel Basin at about 2300 mbsf. These rocks generally have the character of oceanic basalts and related rocks. It is not impossible that these are the rocks at the top of Moresby Seamount, which have been uplifted and unroofed by movement along the detachment fault to the north of Site 1114 from a depth where greenschist facies conditions prevailed.

STRUCTURAL GEOLOGY

Introduction

The 352-m-thick section drilled in Hole 1114A penetrated 286 m of Pliocene–Pleistocene claystones, siltstones, and sandstones (see "Lithostratigraphy," p. 3) that overlie a tectonic breccia and 67 m of metamorphosed basic igneous rocks (Fig. F21). The petrology of this metadolerite is described in "Igneous and Metamorphic Petrology," p. 16.

This section describes the deformation of the sedimentary column, the nature of the breccia that occurs between 286 and 292 mbsf, and the structure of the underlying metamorphic basement.

Sedimentary Rocks

Structural observations and measurements indicate that the recovered sedimentary section can be subdivided into three distinct structural domains. Domain I corresponds to undeformed sediments of lithostratigraphic Unit I (Section 180-1114A-1R-1 [0–6.6 mbsf]). Because they are exempt of tectonic deformation, they are not described in this section. Domain II represents slightly fractured and inclined siltstones and claystones of lithostratigraphic Unit II and the upper part of Unit III (Cores 180-1114A-2R to 7R [6.6–64.6 mbsf]).

Domain III extends from Cores 180-1114A-8R (64.6 mbsf) through 30R (285.8 mbsf). It includes moderately to strongly deformed sandstones, siltstones, and claystones of lithostratigraphic Units III and IV, and part of Unit V. Deformation is characterized by highly inclined bedding, faults, and scaly fabrics. The lowermost part of Domain III is obviously more deformed but poor recovery (~10%), especially from 141 to 180 mbsf, precludes a comprehensive description of the deformation in this domain. In this latter interval the structural description is based on FMS data only and can be found in "Downhole Measurements," p. 38. Underlying Domain III is Domain IV (Section 180-1114A-31R-1 [285.8–287.1 mbsf]), which consists of a 1.30-m-thick (recovered thickness) tectonic breccia that separates the deformed sediments from the massive metamorphic basement rocks (Domain V).

Domain II (6.6–64.6 mbsf)

Evidence of deformation is only occasionally observed in Domain II. It mainly exists in the inclined bedding that usually dips between 10° and 20° with a mode of 15° (Fig. F22). Because no evidence of soft-sediment deformation is observed along this section, the bedding dip is attributed to fault-induced tilting. Brittle deformation is weakly expressed by rare shallow-dipping faults that are locally coated by

F21. Summary of structural features at Site 1114, p. 67.

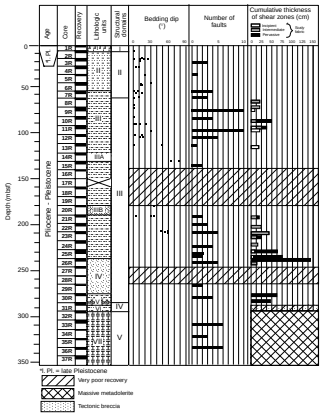

F22. Bedding dips in Domain II, p. 68.

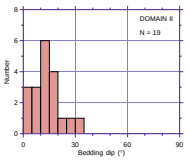

pyrite (e.g., interval 180-1114A-7R-2, 30–35 cm) and exhibit striations. The observed slickensides indicate dip-slip movements (e.g., interval 180-1114A-3R-2, 0–40 cm). The frequency of faults increases significantly downward from 55.24 to 56.87 mbsf (Sections 180-1114A-7R-2 and 3), and the lower limit of Domain II is defined at the bottom of Section 7R-3.

Domain III (64.6–285.8 mbsf)

The boundary between Domains II and III is placed at the first occurrence of scaly fabrics at 64.6 mbsf (Section 180-1114A-8R-1). This limit is also marked by an increase in the frequency of the fracture network and the changes might reflect an increasing gradient of deformation downward.

Bedding measurements show a wide range of dip from horizontal to 80°, but average ~15° (Fig. F23). The higher bedding inclinations are found in the middle part of Domain III from 113 to 199.4 mbsf with values of 35° in Section 180-1114A-21R-1 (189.8–190.4 mbsf); 50° in Section 13R-1 (112.8–114.0 mbsf); and 65°–80° in Section 15R-1 (132.0–133.3 mbsf; Fig. F24). In Section 180-1114A-23R-1 (208.8–209.9 mbsf), steeply inclined strata dipping at 60° in the flank of a tight core-scale fold of probable gravitational origin indicate that part of the bedding dip may have been caused locally by early soft-sediment deformation. However, the consistent development of inclined beds throughout most of the recovered section of Domain III favors their tectonic origin, which is consistent with seismic reflection data. Very poor recovery (0.8%–3.6%) from 141.6 to 180.1 mbsf (Cores 180-1114A-16R to 19R) and from 247.3 to 266.5 mbsf (Cores 27R to 28R) makes it difficult to state whether steeply dipping beds are present along this entire section. However, FMS images confirm that within Domain III strata are inclined between 10° and 55°, as at 131 mbsf (40°) and in the interval 177–180 mbsf (25°; see "Downhole Measurements," p. 38). Faults occur throughout Domain III and their frequency is nearly constant, as shown in Figure F21. The fault population of Domain III is characterized by a large range of dips from 0° to 90°, but with an average ~30°–40° (Fig. F25). As observed between 74.2 and 95 mbsf (Sections 180-1114A-9R-1 to 11R-1) most of the shallow-dipping (0°–30°) structures occur in close association with the scaly-fabric bands described below (Fig. F26A, F26B), but are not seen in the FMS images. On the other hand, steeper faults are commonly observed in more sandy intervals, and the nature of the crosscutting relationships between shallow and steeply dipping fault sets is not clearly established from core observations.

Although the majority of the slickensided fault surfaces measured in Domain III are dip slip (66%), oblique (19%) and pure strike-slip faults (15%) also are present (Fig. F27). Oblique extensional faults are well documented in Section 180-1114A-21R-1 (189.8–190.4 mbsf) where finely laminated siltstones and claystones of lithostratigraphic Unit IIIA are offset with an apparent normal displacement of a few millimeters by an array of microfaults dipping at 65° and showing a shallow plunging slickenside lineation indicative of a lateral movement. Evidence for reverse microfaults is also documented in Section 180-1114A-15R-1 (132.0–133.3 mbsf; Fig. F28); therefore, Domain III appears to be a composite fault zone, including dip-slip (normal and reverse), oblique, and strike-slip faults.

On FMS images, most fractures dip toward the north and the north-northwest, but a few dip to the south-southeast (conjugates?) and to

F23. Bedding dips in Domain III, p. 69.

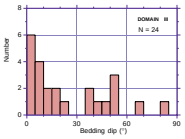

F24. Inclined strata in sandstones of lithostratigraphic Unit III, p. 70.

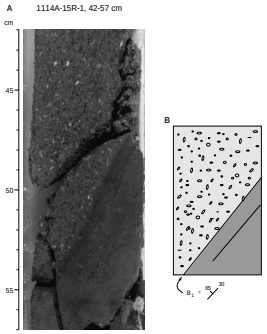

F25. Dip of faults in sediments in Hole 1114A, p. 71.

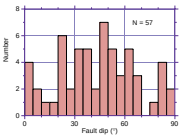

F26. Examples of scaly fabric and related faults in Domain III, p. 72.

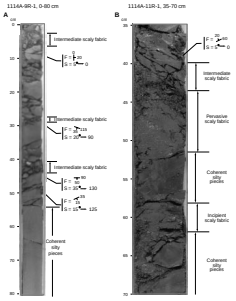

F27. Fault dip vs. plunge of slickensides in Domain III, p. 73.

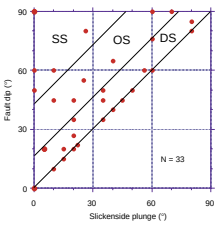

the northeast (see **"Downhole Measurements,"** p. 38). The west-southwest–dipping fractures present from 280 to 295 mbsf mark the master fault (see below) that separates the sedimentary sequence from its basement. The histogram of fracture dip vs. depth deduced from FMS data also indicates that the mean inclination of the fractures steepens markedly with depth from 40° to 60° in the interval 40–120 mbsf and from 50°to 80° in the interval 180–210 mbsf. The lower dips observed below in the interval 280–295 mbsf are related to the master fault discussed later.

Scaly fabrics are the most characteristic tectonic features of Domain III. They occur in bands of various thicknesses involving fine-grained, clay-rich material. The origin of scaly fabrics as either tectonic or core-induced features has been debated during previous ODP legs (e.g., see Shipley, Ogawa, Blum, et al., 1995). The scaly fabrics recognized in Hole 1114A are interpreted to result primarily from tectonic deformation. However, this fabric might have been later emphasized during coring and the relative contribution of the two processes is difficult to estimate. Nevertheless, the vertical distribution and variations displayed by the scaly fabrics are confidently assigned to changes in the deformation, and they are, therefore, used as qualitative strain markers. Three main types of scaly fabrics have been distinguished, and their distribution is shown in Figure **F21:**

1. Incipient scaly fabrics are expressed by an incipient fissility of the clay material that splits into parallel-spaced joint and fracture networks bounding centimeter- to millimeter-thick intervals of intact claystones (Fig. **F26**). Where measured, the fissility planes are roughly parallel to bedding. Because no evidence of displacement is observed along the individual surfaces, the original sedimentary structures are still visible.
2. Intermediate scaly fabrics correspond to centimeter- to millimeter-sized angular and elongate fragments of indurated and more silty material embedded into finely spaced and polished surfaces (Fig. **F26**). No preferred arrangement of the fragments is noticed.
3. Pervasive scaly fabrics are characterized by anastomosing and finely interpenetrative systems of shiny and polished surfaces forming millimeter-scale phacoids (Fig. **F26**). Because of this peculiar three-dimensional fabric, no planar orientation has been identified within the more pervasively deformed intervals. As a consequence, the angular relationships (parallel or oblique) between the scaly fabric and the lithologic boundaries of the deformed bands could not be defined.

At several levels, intervals up to 5–10 cm long of intact siltstones and claystones pass progressively upward and downward into zones of closely spaced joint/fracture networks in the incipient scaly fabric. Furthermore, the different types of scaly fabrics commonly show vertical gradational boundaries, for example, in Sections 180-1114A-9R-1 (74.2–75.6 mbsf) and 11R-1 (93.5–94.5 mbsf; Fig. **F26**). These observations allow us to assign the development of scaly fabrics to tectonic processes, probably involving local increase in strain (under the same stress conditions) throughout particular fine-grained intervals. Within each individual scaly-fabric zone no reliable marker of strain is observed. However, most of them contain discrete striated fault planes lying roughly parallel to the lithologic boundaries, as clearly evidenced in Sections 180-1114A-9R-1 and 11R-1 (Fig. **F26**). Assuming that both scaly fabric and sliding

F28. Reverse microfaults in Unit III sandstones in Domain III, **p. 74.**

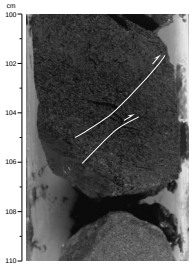

planes have been formed synchronously as a response to the same ambient stress, it can be argued that a significant component of layer-parallel shearing has taken place during deformation, which in turn excludes a strict relation of the initiation of scaly fabrics to flattening under vertical stress.

Evidence for the development of scaly fabrics is provided by observations from 113.4 to 114 mbsf (interval 180-1114A-13R-1, 60–120 cm), where highly fractured sandstones pass downward into silty and clayey material displaying incipient scaly fabric (Fig. F29). The sandstones form decimeter-long coherent pieces cut by steep conjugate fractures dipping between 60° and 70°. Further down, the density of fractures increases, resulting in the fragmentation of the siltstones and sandstones into decimeter- to centimeter-sized elongate angular fragments. The size of the fragments decreases downward toward the silty and clayey scaly-fabric band, which in turn is disrupted by parallel shallow-dipping fault planes.

These sliding surfaces are likely to be coeval with the above-mentioned steeper conjugate fault network present in the more competent sandy levels and their synchronous development may result from an almost vertical principal maximum stress oblique to the lithologic boundary, thereby inducing a shear component (Fig. F29). Substantial decoupling must have also occurred between the contrasting grain-sized layers involved in the deformation. Each scaly-fabric band is, therefore, likely to form a discrete shear zone and the bands' distribution determines the vertical structural zonation of Domain III.

The cumulative thickness of scaly-fabric bands measured in each core reveals that the frequency of occurrence and thickness of individual shear zones increase downward from Cores 180-1114A-8R through 30R (Fig. F21). The prominent scaly-fabric band identified in Cores 180-1114A-25R to 26R (228.0–247.3 mbsf) roughly coincides with a zone where logging caliper data show that the diameter of the hole was enlarged (see "Downhole Measurements," p. 38). The upper part of the cored section from 64.6 to 151.3 mbsf (Cores 180-1114A-8R to the top of 16R) is typically dominated by incipient and intermediate scaly fabrics, whereas intermediate and pervasive scaly fabrics are prevalent in the middle and lower parts of the section from 189.8 to 295.4 mbsf (Cores 21R to 31R). A quite similar vertical polarity is observed in the proportion of deformed and undeformed clay intervals within each core (Table T6). It clearly shows that the ratio of total clay thickness vs. scaly-fabric thickness increases from ~40% from 64.6 to 151.3 mbsf (Cores 8R to 16R, or possibly 21R, because of the recovery problem) to almost 100% in the deepest part of the section, where all of the clay-rich material is deformed.

The lowermost part of the deformed sedimentary section is very poorly recovered from 247.3 to 276.1 mbsf (Cores 180-1114A-27R to 29R), and it then passes at 276.1 mbsf (top of Core 30R) into a weakly indurated and fine-grained pale reddish clay-rich matrix containing pieces of silty claystones and subordinate sandstones. This interval is extensively deformed and exhibits pervasive scaly fabric; it is further crosscut by steeply dipping faults (60°–90°). No indication for sense of displacement is observed.

In contrast with basement rocks described below, the sedimentary section cored in Hole 1114A lacks extensive hydrothermal mineralization. Only two examples of fault surfaces coated with pyrite are present in intervals 180-1114A-7R-2, 30–35 cm (55.54 mbsf), and 11R-CC, 10–14 cm (95.17 mbsf), and very few millimeter-thick calcite-filled veinlets

F29. Association of steep conjugate faults and scaly-fabric bands, p. 75.

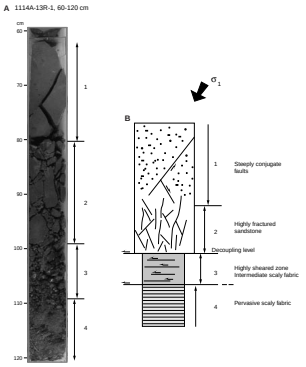

T6. Thickness of clay-rich material vs. clay thickness, p. 128.

were observed in Section 24R-2 (218.8–219.6 mbsf), whereas quartz-filled veins are present in one sandstone pebble in Section 26R-1 (237.6–238.8 mbsf).

Domain IV: Tectonic Breccia (286.05–287.35 mbsf)

Sections 180-1114A-31R-1 and 31R-CC consist of a greenish tectonic breccia extending from 286.05 to 287.35 mbsf that is subdivided into two parts. The upper part (interval 180-1114A-31R-1, 25–74 cm) is composed of angular to subangular clasts of greenschist in a matrix containing quartz, plagioclase, clay, accessory minerals, opaque grains, and inorganic calcite. It also includes scattered well-rounded red, brown, and colorless grains (see "Lithostratigraphy," p. 3).

The lower part (intervals 180-1114A-31R-1, 74–130 cm, and 31R-CC, 0–18 cm) is composed of a fine-grained matrix enclosing scattered angular millimeter- to centimeter-sized fragments that are similar to the underlying dolerite. The clasts inherited from the dolerite are crosscut by numerous quartz- and epidote-filled veins that do not extend through the matrix (Fig. F30). The preferred orientation of the clasts within the matrix outlines a weakly developed layering in the breccia. A second generation of calcite-filled veins crosscut the breccia; they are very often at the boundary between the clasts and the matrix (Fig. F31). These veins are sheared in a plane parallel to the layering defined by the oriented clasts (Fig. F32). Late fractures crosscut the breccia at high angles with respect to the layering (Fig. F31).

The lowermost part of the breccia is characterized by a reduction of grain size associated with massive alteration of both the matrix and the clasts. The layering defined in the upper part of breccia is still well expressed.

From these observations we infer that the formation of the tectonic breccia postdates the emplacement of quartz + epidote veins in the dolerite and is contemporaneous with the formation of calcite veins. The breccia was later disrupted by steep fractures.

F30. Thin section of breccia with veins crosscut by fracture, p. 76.

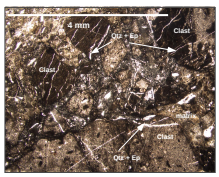

F31. Thin section of dolerite with quartz and epidote veins, p. 77.

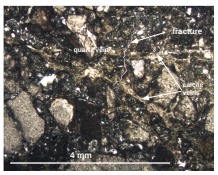

F32. Thin section of calcite vein affected by shearing deformation, p. 78.

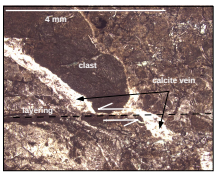

Domain V: Metadolerite (292.0–352.8 mbsf)

The massive metadolerite was first recovered at 295 mbsf in Core 180-1114A-32R through Core 37R (bottom at 352.8 mbsf). However, FMS data indicate a sharp change of resistivity compared to the overlying sediments at 292 mbsf. The increase of resistivity related to the presence of the dolerite shows the upper limit of the dolerite, which constitutes Domain V. Although the poor and fragmented recovery does not allow a complete description of its tectonic evolution, two types of tectonic breccia are observed.

The first one (B1) consists of a penetrative breccia resulting from brittle to ductile fragmentation of the dolerite throughout the entire section with an intensity that decreases downward. This breccia consists of a centimeter-sized cataclastic zone composed of a fine-grained dark brown clay matrix containing fragments of pyroxene and plagioclase ("Lithostratigraphic Unit VI," p. 14).

The second type of breccia (B2) consists of a fine-grained blue-green matrix containing fragments of the underlying dolerite. This 8.4-m-thick breccia is localized in the upper part of the section at the boundary between the overlying sediments and the dolerite; it corresponds to tectonic Domain IV described in "Domain IV," p. 24, and to lithostratigraphic Unit V (see "Lithostratigraphic Unit V," p. 13).

The deformation history of the dolerite can be summarized as follows:

Stage 1: At the base of the sequence, from interval 180-1114A-36R-1, 80–150 cm, to Section 37R-CC (334.7–352.8 mbsf) the deformation mainly comprises the development of subvertical and subhorizontal veins up to 2 cm wide filled with quartz and epidote (Fig. **F17;** also see **"Igneous and Metamorphic Petrology,"** p. 16). These veins are thought to be the first generation of veins and fractures that occurred during the deformation of the dolerite. Thin sections confirm the occurrence of the first generation of veins contemporaneous with the breccia; it is present either crosscut by the penetrative breccia B1 or scattered as clasts into the breccia (Fig. **F33**). The observation of thin sections from the lower part of the dolerite confirms that breccia B1 is more diffuse than in the upper part and locally contains preserved relics of the ophitic texture (Fig. **F16;** also see **"Igneous and Metamorphic Petrology,"** p. 16).

Stage 2: From the bottom to the top (Sections 180-1114A-36R-1 to 34R-1 [335.4–314.7 mbsf]), the intensity of the brecciation increases in the middle of the section with the presence of a centimeter-sized cataclastic zone dipping 45°–65° (Fig. **F34**). In the breccia B2 we observe veins filled with calcite (vein 2) affected by shearing deformation (see Figs. **F32, F36**), which indicates a continuing shearing evolution responsible for the brecciation of the dolerite. In this interval the penetrative breccia is overprinted by the development of conjugate north-south faults dipping 65° toward the east or the west (with respect to core orientation defined in **"Structural Geology,"** p. 14, in the "Explanatory Notes" chapter). These faults are in some cases an intensification of the brecciation and occurred as shear zone in the dolerite (see Fig. **F34;** and **"Igneous and Metamorphic Petrology,"** p. 16). In other samples, these structures occurred as fractures crosscutting the dolerite. The shear zones are dominant at the bottom of the sequence, whereas the fractures are dominant on top of the sequence. Slickenside lineations are present on the fault planes and indicate complex relative motion that is either normal, reverse, or strike slip. As the geometry of the shear zones and the fractures are equivalent (orientation, dip, and chronological occurrence), we interpret it as the same structural event observed at different depths in the sequence and associated with fluid circulation. The interval between the faults ranges from 5 to 8 cm, and the angle between the faults is at ~120°.

Stage 3: In the upper part of the sequence (Sections 180-1114A-32R-1 to 34R-2), the dolerite is massively fractured. The interval between the fractures is 2–4 cm, and the angle between the fractures is at ~90°, visible in both the hand specimens (Fig. **F35**) and thin sections (Fig. **F31**). This brittle event is also observed in the sediments overlying the dolerite.

In summary, the following chronological evolution can be deduced from the observations described above (Fig. **F36**):

F33. Thin section of brecciated dolerite with quartz and epidote veins, **p. 79.**

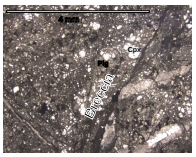

F34. Brecciated dolerite dipping 45°, with quartz-epidote–rich vein, **p. 80.**

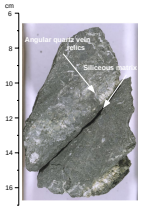

F35. Brecciated dolerite with conjugate horizontal and vertical fractures, **p. 81.**

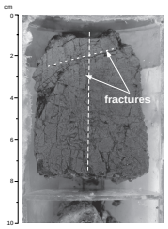

F36. Sketch of tectonic evolution of the dolerite breccia at Site 1114, **p. 82.**

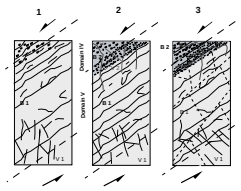

Stage 1: Development of the penetrative breccia B1 and of the first generation of veins filled with quartz and epidote;
Stage 2: Development of the veins filled with calcite mainly in the upper part of the section and development of breccia B2 and the conjugate faults; and
Stage 3: Continuing evolution of the fault zone, shearing of the calcite veins in the tectonic breccia, and fracturing of the whole sequence from the bottom to the top of the dolerite, including the breccia B2 and the overlying sediments.

As this tectonic evolution is associated with a retrograde metamorphic evolution under greenschist facies conditions (see **"Igneous and Metamorphic Petrology,"** p. 16), the three tectonic stages described above are related to the unroofing of the dolerite along a 60°–65° dipping normal fault expressed by the development of the breccia.

Synthesis

In Hole 1114A, Pliocene–Pleistocene synrift sediments overlie metamorphic basement rocks along a major extensional fault zone dipping at 60°–65° to the south-southwest. In the metadolerite forming the footwall of the fault, extensional faulting is expressed by fracturing that increases in intensity upward close to the fault contact and, thus, results in the brecciation of the metadolerite. The brittle deformation recorded by the sedimentary sequence in the hanging wall of the fault is typical of a large-scale shear zone comprising discrete shear bands parallel to the bedding, which consistently dips 0°–40° to the north-northwest. The intensity of the shear strain decreases gradually upward throughout the sedimentary succession.

The layer-parallel shear fabrics are disrupted by a composite fault system including dip-slip normal faults as well as oblique and reverse faults. Most of the faults dip to north, north-northwest, and northwest, and their dip shallows significantly upward (Fig. **F37**). Two northeast-dipping faults are also imaged by FMS in the upper part of the logged section between 100 and 120 mbsf where we also note that both bedding and fault strikes are anticlockwise rotated by ~20°–30° with respect to their deeper counterparts (Fig. **F37B**).

The wide range of bedding dips observed from 65 to 286 mbsf, in association with the more intense network of steep faults downhole, may indicate that differential rotations of strata have occurred at depth within fault-bounded compartments. In map view and in vertical section, this steep fault network lies at relatively high angles (30°–40°) to the master fault mentioned above (Fig. **F37**).

Likewise, the layer-parallel shear zones present in the lower part of the sedimentary sequence are sharply cut at depth by the master fault. Such angular relationships between the most prominent structures forming the Moresby Seamount suggest a multistaged extensional fault history involving notably late oblique faulting in agreement with recent regional kinematics.

F37. Geometry of structures at Site 1114, **p. 83.**

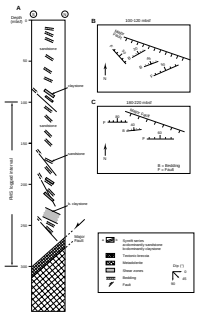

BIOSTRATIGRAPHY

Calcareous Nannofossils

Abundance and Preservation

Samples 180-1114A-1R-CC to 2R-1, 30–32 cm, contain abundant, well-preserved nannofossils. Samples 180-1114A-2R-1, 35–37 cm, to 7R-CC contain mostly few to common nannofossils with some almost barren intervals. Preservation ranges from poor to good (mostly moderate). From Core 180-1114A-8R to 32R (in which the last sediment was recovered) nannofossils are mostly rare with some barren or almost barren intervals. Preservation is poor to moderate (mostly poor).

Zonation

Sediment contained in Sample 180-1114A-1R-CC is in Zone NN20 through Subzone NN21A, based on the presence of *Gephyrocapsa omega* and *Emiliania huxleyi* (very rare) and the absence of *Pseudoemiliania lacunosa* (Fig. **F38;** Table **T7**). A lithified pebble under the sediment in the bottom of Sample 180-1114A-1R-CC contains *Helicosphaera sellii* and is, therefore, assigned to Subzones NN19C–D or older. Sample 180-1114A-2R-1, 30–32 cm (light green mud) contains the same assemblage and is also Subzones NN19C–D or older. This sample rests unconformably on Sample 180-1114A-2R-1, 35–37 cm (grayish black mudstone), which is Subzone NN19B or older based on the first downhole occurrence of *C. macintyrei*. The abundance and preservation of nannofossils decline markedly below this level, and specific zonal markers are absent. We found only rare, poorly preserved discoasters (including *Discoaster* cf. *D. brouweri*) in Samples 180-1114A-12R-CC and 31R-1, 22–24 cm, indicating Subzone NN18 or older.

F38. Biostratigraphic units and ages for Hole 1114A, **p. 84.**

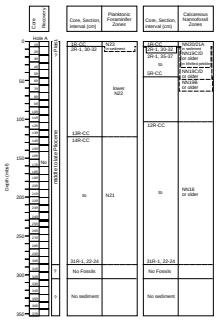

Planktonic Foraminifers

Abundance and Preservation

In the low-oxygen benthic environments of this hole, planktonic foraminifers are thought to have been partly dissolved, and the residues represent incomplete assemblages. Because some of the key species are fairly resistant to dissolution, a stratigraphy could be determined for this hole.

Planktonic foraminifers were abundant and their preservation was good in Samples 180-1114A-1R-CC and 2R-1, 30–32 cm; common to abundant and with moderate to poor preservation in Samples 180-1114A-3R-2, 47–49 cm, 8R-CC, 19R-CC, 25R-CC, 29R-CC, 12–14 cm, and 31R-1, 22–24 cm; and few to rare with moderate to poor preservation in 2R-CC through 6R-CC, 9R-CC through 11R-CC, 13R-CC, 16R-CC, 18R-CC, 20R-CC, 22R-CC, 23R-CC, 26R-CC, and 30R-CC. The core-catcher samples of the following cores were barren of planktonic foraminifers: Cores 180-1114A-4R, 7R, 12R, 14R, 15R, 21R, 24R, 27R, and 29R through 32R. No core-catcher samples were obtained for Cores 180-1114A-17R and 28R.

T7. Calcareous nannofossils, Hole 1114A, **p. 129.**

Zonation

Planktonic foraminiferal zonation for Site 1114 is summarized in Figure F38, and Table T8 shows the stratigraphic distribution of species.

T8. Planktonic foraminifers, Hole 1114A, p. 130.

Sample 180-1114A-1R-CC is placed in late Pleistocene–Holocene planktonic Zone N23, based on the presence of *Bolliella calida* and pink *Globigerinoides ruber,* whose presence indicates an age no younger than 120 ka.

Samples 180-1114A-2R-1, 30–32 cm, through 13R-CC, are placed in the lower part of Zone N22, based on the presence of *Globorotalia truncatulinoides, G. tosaensis,* and *Globigerinoides fistulosus*. Sample 180-1114A-2R-1, 30–32 cm, contains the last-appearance datum (LAD) of *G. fistulosus* (1.6 Ma), and Sample 180-1114A-13R-CC, 9–12 cm, contains the first-appearance datum (FAD) of *G. truncatulinoides* (2.58 Ma), which marks the base of the zone.

Sections between Samples 180-1114A-14R-CC and 31R-1, 22–24 cm, are assigned to Zone N21, based on the presence of *G. tosaensis* and *G. crassaformis* and the absence of *G. truncatulinoides*.

Dentoglobigerina altispira (LAD 3.09 Ma) and *Sphaeroidinella dehiscens* s.s. (FAD = 3.25 Ma) are present in Sample 180-1114A-31R-1, 22–24 cm. This is the lowest fossiliferous sample overlying the metamorphic basement and is no older than middle Pliocene (~3.25 Ma), based on the presence of *S. dehiscens* s.s.

Benthic Foraminifers

The foraminiferal assemblage at the sediment/water interface was not retained in this hole, which was drilled in a water depth of 407 m. A middle bathyal water depth (500–2000 m) is indicated by the benthic foraminifers of Pleistocene age in Cores 180-1114A-1R and 2R, although the species represented in the samples varied as specified below.

Sample 180-1114A-1R-CC (Zone N23) contained *Globocassidulina subglobosa, Ceratobulimina pacifica, Cibicidoides rugosus, Eggerella bradyi, Gyroidina altiformis, Laticarinina pauperata, Martinottiella* sp., *Oridorsalis umbonatus, Parrelloides bradyi, Sphaeroidina bulloides,* and *Uvigerina asperula*. Sample 180-1114A-2R-2, 30–32 cm (Zone N21), contained *Bolivinita quadrilatera, Bulimina aculeata, B. striata, Cassidulina neocarinata, Uvigerina bradyana,* and *Valvulineria* sp.

From Sample 180-1114A-2R-CC through 25R-CC (Zone N21), the benthic assemblages are dominated by *Globobulimina* spp. These foraminifers are known to inhabit sediments with relatively high organic content deposited under low-oxygen conditions. In some cases, as in Samples 180-1114A-3R-2, 47–49 cm, 8R-CC, and 25R-CC, the globobuliminids are accompanied by *Ceratobulimina pacifica* and other typical middle bathyal species, whereas, in other instances only a species of *Valvulineria,* a crushed multilocular agglutinated species, and *Bathysiphon* accompany the globobuliminids. The environment of deposition is interpreted as one of fluctuating low oxygen possibly associated with the boundaries of the oceanographic oxygen minimum at upper bathyal to upper middle bathyal depths, or of a basinal situation with restricted circulation.

Detrital sands of volcanogenic origin in Samples 180-1114A-18R-CC, 26R-CC, and 27R-CC contain only rare specimens of the inner neritic (<50 m) transported species *Asterorotalia gaimardii* and *Elphidium craticulatum*.

Sample 180-1114A-31R-1, 22–24 cm (Zone N21), the lowest fossiliferous sample overlying the metamorphic basement, contains diverse benthic foraminifers, among them *Gyroidina* sp., *Martinottiella* sp., and *Uvigerina hispida,* which are indicative of middle bathyal depths. *Rotalia* sp. may have been introduced into this sample through downslope transport.

Sediment Accumulation Rate

We estimated an average sedimentation rate based on nannofossil and foraminifer datum events at Site 1114 (Fig. F39). The average sedimentation rate for the horizon from 6.95 to 266.62 mbsf is calculated to be at least 176 m/m.y.

PALEOMAGNETISM

The investigation of magnetic properties at Site 1114 included (1) the measurement of bulk susceptibility of whole core sections, (2) point susceptibility and remanent magnetization of archive-half core sections, and (3) magnetic susceptibility and its anisotropy and remanent magnetization of discrete samples.

Magnetic Susceptibility

Magnetic susceptibility measurements were made on whole-core sections as part of the multisensor track (MST) analysis (see **"Physical Properties,"** p. 32), and on half-core sections as part of the archive multisensor track (AMST) analysis. The MST and AMST susceptibilities values (uncorrected for volume) ranged between values on the order of 10^{-5} and 10^{-2} SI (Fig. F40).

The mean susceptibility, the degree of anisotropy (P_j) and the shape parameter (T) for the susceptibility ellipsoid (Jelinek, 1981), and the inclinations of the maximum (K_{max}) and minimum (K_{min}) susceptibility axes of the ellipsoid for discrete samples are shown in Figure F41. Mean susceptibilities were on the order of 10^{-3} to 10^{-2} SI; these values were notably higher than those at previous sites. The high susceptibility values suggest that ferrimagnetic minerals dominate the susceptibility. The P_j values averaged ~1.1 above ~120 mbsf. All samples except three showed T values above 0.5, indicating the predominance of oblate magnetic fabrics. Above 150 mbsf where data were corrected for tilted beds, K_{min} axes were steep (ranging between ~60° and 90°) and K_{max} axes were shallow (ranging between 0° and 25°). Data below ~150 mbsf were not interpreted because of the paucity of tilt-corrected data.

The oblate magnetic fabrics coupled with the subvertical orientations of K_{min} axes and the subhorizontal orientations of K_{max} axes probably reflect the compaction of sediments.

Remanent Magnetization

Measurements of remanent magnetization were made on relatively undisturbed sections from archive-half cores and on discrete samples taken from working-half core sections. Results are shown in Figures F42 and F43.

F39. Age-depth relationship at Site 1114, p. 85.

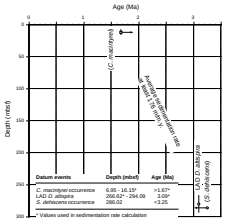

F40. Susceptibility data from MST and AMST measurements, Site 1114, p. 86.

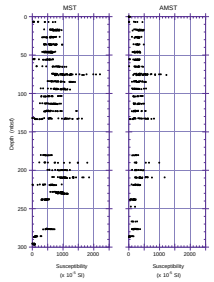

F41. AMS data from discrete sample measurements, p. 87.

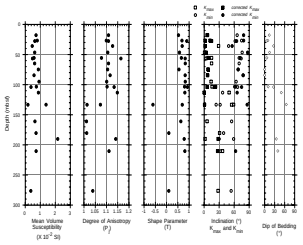

F42. Demagnetization behavior of discrete samples from core sections, p. 88.

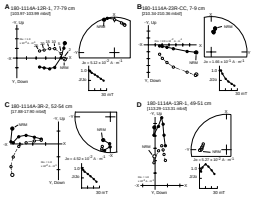

A total of 21 discrete samples were measured. Initial natural remanent magnetization (NRM) intensities were on the order of 10^{-2} to 10^{-1} A·m^{-1}. About 30% or more of the initial intensity remained after AF demagnetization at 25 mT. Demagnetization behavior of discrete samples showed the presence of two or more magnetic components. A soft component was removed between 2 and 10 mT after the removal of a viscous component between 0 and 2 mT. The soft component generally showed a steep to moderately steep downward direction. After removal of the soft component, 9 of 21 samples showed a stable component that decayed approximately linearly toward the origin of the vector demagnetization plot between 15 and 25 mT (Fig. **F42A, F42B**); this component is referred to as the characteristic remanent magnetization (ChRM). The other samples yielded either curved demagnetization trajectories indicating significant overlap in the coercivity spectra of two components or linear trajectories not decaying toward the origin of the vector plot (Fig. **F42C, F42D**). The demagnetization behavior shown by these samples suggests the presence of another component with higher coercivities.

Intensity of remanent magnetization of long cores after AF demagnetization at 25 mT was dominantly on the order of 10^{-2} A·m^{-1}. Low intensities on the order of 10^{-4} A·m^{-1} occurred near the top of the recovered section (Fig. **F43**).

Inclinations showed dominantly normal polarities throughout most of the measured cores. Declinations were highly scattered as a result of the RCB drilling process. Discrete sample results did not consistently support the long-core data.

Because of poor recovery and discontinuous data sets, no attempt was made to interpret the data in terms of the magnetic polarity time scale.

F43. Downhole plots of declination, inclination, and intensity, **p. 89.**

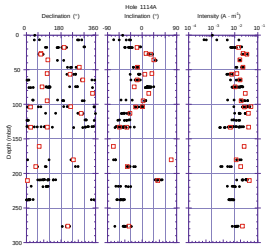

INORGANIC GEOCHEMISTRY

The interstitial water (IW) sampling program at Site 1114 was limited because of difficult coring conditions and low core recovery. Five IW samples were obtained: three from the upper 76 mbsf and one each from 210 and 229 mbsf.

Results and Discussion

The IW was analyzed for salinity, pH, alkalinity, major cations (Na^+, K^+, Ca^{2+}, and Mg^{2+}) and anions (Cl^- and SO_4^{2-}), Li^+, Sr^{2+}, and SiO_2. Results of shipboard inorganic chemical analyses are presented in Table **T9.** The salinity, alkalinity, and dissolved Na^+, Cl^-, SO_4^{2-}, and Mg^{2+} concentrations all remain in a narrow range. Only dissolved K^+, Ca^{2+}, Li^+, Sr^{2+}, and SiO_2 exhibit significant variations. Because of the limited data obtained, observed IW compositional variations can only be interpreted with caution.

T9. Interstitial water geochemistry, Hole 1114A, **p. 131.**

The low alkalinity and near-seawater SO_4^{2-} concentration in all IW samples indicate that either no significant microbially mediated oxidation of organic matter takes place in the sediment column, or that evidence of previous organic matter diagenesis has been erased either by diffusion or by fluid flow through the fractures observed in the sediments (see **"Structural Geology,"** p. 20). Because of the existence of concentration gradients of certain nonconservative IW constituents

downhole (e.g., K^+), extensive present-day fluid flow through the sediment column seems unlikely.

Increasing dissolved Li^+ and Ca^{2+} concentrations downhole suggest an input of these elements at depth, possibly through the alteration of volcanic minerals in the sediments or by upward diffusion of remnant hydrothermally altered fluids. It should be noted, however, that dissolved Li^+ is depleted relative to seawater (27M/kg) in all IW samples from this site, albeit less so in the two deeper samples. Dissolved Li^+ in IW from Sites 1110 and 1111 was also found to be depleted relative to seawater (see **"Inorganic Geochemistry,"** p. 21, in the "Sites 1110–1113" chapter).

The variations in dissolved Sr^{2+} are unusual. A depletion relative to seawater (84 µM) occurs in the four shallower samples, whereas a return to a near-seawater value is observed in the deepest sample. Concentrations of dissolved Sr^{2+} are decoupled from those of dissolved Ca^{2+}. Thus, dissolution of biogenic calcite seems unlikely to be responsible for the Sr^{2+} increase deeper downhole, and the source of Sr^{2+}, as that of Ca^{2+}, may be the alteration of basement rocks.

A depletion of K^+ downhole is inconsistent with upward diffusion from basement of a remnant hydrothermal fluid as proposed above. Such a fluid should also be enriched in K^+. However, it is possible that formation of kaolinite, observed by X-ray diffraction (see **"Lithostratigraphy,"** p. 3, and Table **T3**), may deplete any upward diffusing fluid of its dissolved K^+.

Dissolved SiO_2 concentrations are generally low except in Sample 180-1114A-9R-1, 142–152 cm. The low dissolved SiO_2 concentration may reflect typical sedimentary diagenetic reactions that occur deep within sedimentary sequences such as observed at Site 1109 (see **"Inorganic Geochemistry,"** p. 54, in the "Site 1109" chapter). Low concentrations of this constituent, however, may also be consistent with alteration of basement rocks by hydrothermal fluids, which could promote silicate mineral precipitation in the overlying sediment column.

Although IW is slightly depleted in dissolved Mg^{2+} relative to seawater, the lack of any gradient suggests either erasure of any evidence of sedimentary reactions through an input of seawater, or a lack of reactions that can remove this element from pore fluids. This contrasts sharply with what is observed at Sites 1109 and 1115 (see **"Inorganic Geochemistry,"** p. 54, in the "Site 1109" chapter and **"Inorganic Geochemistry,"** p. 38, in the "Site 1115" chapter), where the alteration of volcanic minerals and subsequent formation of clay minerals such as smectites generally leads to depletion of this constituent downhole.

The composition of IW at this site contrasts substantially with what has been observed at other sites drilled during Leg 180, suggesting that tectonic activity and possibly hydrothermal fluid circulation have influenced sediments and affected the fluid chemistry. However, insufficient data are available to identify unequivocally individual processes.

ORGANIC GEOCHEMISTRY

At Site 1114, the shipboard organic geochemistry consisted of determination of TOC, inorganic carbon, total carbon, total nitrogen, and total sulfur in sediments, in addition to the routine hydrocarbon gas safety monitoring procedure. The analytical techniques used are out-

lined in "Organic Geochemistry," p. 25, in the "Explanatory Notes" chapter.

Volatile Hydrocarbons

Headspace methane concentrations were found to be low and remained <5 ppmv throughout Hole 1114A (Table T10). Only one other hydrocarbon, ethylene, was detected at a very low concentration (0.1 ppmv).

T10. Headspace gas in sediments, Hole 1114A, p. 132.

$CaCO_3$, Sulfur, Organic Carbon, and Nitrogen

The $CaCO_3$ concentration was below 5–10 wt% for most of the sediments (Table T11; Fig. F44), except for a surficial ooze (65 wt%) and two samples from 219 and 231 mbsf (17 and 24 wt%). Organic carbon content (Table T11) was low (<1%) throughout Hole 1114A (Fig. F44) with the exception of a peak of 1.4% at 231 mbsf, which corresponds to a thin ash layer containing small fragments of woody material. The C/N ratios showed a mixture of predominantly marine (C/N = <8) and mixed marine/terrigenous (C/N = 8–20) organic material throughout the hole. Total sulfur contents were low, averaging 0.33% (Table T11). The single-point maximum at 238 mbsf (1.64%) corresponded to a section containing significant pyritization.

T11. Carbon, calcium carbonate, nitrogen, and sulfur, Hole 1114A, p. 133.

F44. $CaCO_3$, organic carbon, and C/N ratio profiles, p. 90.

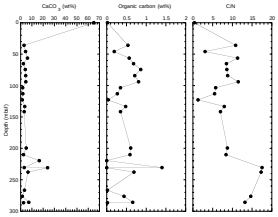

MICROBIOLOGY

Only two samples were obtained at Site 1114 for microbiological analysis. Bacteria were present in both samples examined. At 17.25 mbsf there were 6.9×10^6 cells/cm^3, of which 3.3×10^5 cells/cm^3 were dividing or recently divided; at 45.97 mbsf there were 2.4×10^6 cells/cm^3, including 6.7×10^4 cells/cm^3 dividing and divided cells. These data are consistent with the model of Parkes et al. (1994).

PHYSICAL PROPERTIES

Introduction

At Site 1114 one borehole was advanced to a total depth of 352.8 mbsf, with a cumulative recovery of 12.4%. Physical properties evaluation at the site included nondestructive measurements of bulk density, bulk magnetic susceptibility, natural gamma ray, and *P*-wave velocity on unsplit core using the MST. Discrete measurements of longitudinal and transverse *P*-wave velocities and index properties were collected on split cores. Depending on the level of sediment induration, thermal conductivity was measured from either unconsolidated whole cores or discrete rock slices. Poor recovery and fragmented cores at the top (Core 180-1114A-1R), middle (Cores 16R through 19R), and at the base of the borehole (Cores 33R through 37R) precluded use of the MST for continuous measurements at these locations. Measurements of compressive strength and undrained shear strength were also restricted because of a high level of lithification from Core 180-1114A-2R to the bottom of the succession.

Density and Porosity

Bulk densities at Site 1114 were derived from both GRAPE measurements conducted on unsplit cores and discrete density measurements on sediment and rock samples (Table T12 and in ASCII format in the TABLES directory). A full compilation of gamma-ray attenuation porosity evaluator (GRAPE) data (in ASCII format) is presented with the MST measurement data set on the accompanying Lamont-Doherty Earth Observatory (LDEO) CD-ROM. Composite profiles of these independently derived bulk densities indicate a fair agreement between the two, with the discrete measurements correlating to the upper boundary of the GRAPE densities (Fig. F45). However, because of the high magnitude of scatter in the GRAPE data, our discussion will focus primarily on the discrete bulk density profile.

Bulk densities change abruptly from ~1.60 g·cm^{-3} at ~7 mbsf to >2.00 g·cm^{-3} at ~17 mbsf (Fig. F46A). This discontinuity in the density profile likely reflects an erosional unconformity that resulted in high sediment bulk densities at shallow depths (see "Biostratigraphy," p. 27, and "Lithostratigraphy," p. 3). Below the discontinuity bulk densities remain fairly constant to a depth of 55 mbsf, ranging only between 1.95 and 2.05 g·cm^{-3}. This depth range corresponds to the siltstones and claystones of lithostratigraphic Unit II. Between 60 and 90 mbsf, the bulk densities are also characterized by little scatter and average ~2.05 g·cm^{-3}. This interval corresponds to litho-stratigraphic Unit III, which comprises sandstones, siltstones, and claystones. At 90 mbsf, the bulk densities abruptly increase from 2.00 to greater than 2.20 g·cm^{-3} and remain between 2.10 and 2.20 g·cm^{-3} to 120 mbsf. The increase does not correspond to a change in lithology or a unit boundary, and, unfortunately, poor core recovery hinders an interpretation of the density change. From 120 to 140 mbsf, the bulk densities show another increase with values ranging between 2.20 and 2.40 g·cm^{-3}. These measurements may reflect the carbonate–rich intervals within lithostratigraphic Subunit IIIA.

Below a region of no recovery (140–180 mbsf), the bulk densities average ~2.30 g·cm^{-3} from 180 to 190 mbsf, reflecting the thin conglomerate and coarse sandstone of lithostratigraphic Subunit IIIB. Below 190 mbsf, the bulk densities average ~2.10 g·cm^{-3} before increasing to nearly 2.40 g·cm^{-3} at 240 mbsf. This trend in density corresponds to a lithostratigraphic change from siltstones, sandstones, and claystones to a sandstone containing sulfides and smectite (Core 180-1114A-26R; see "Lithostratigraphy," p. 3). The presence of these minerals may be conducive to the observed higher bulk density. Below 275 mbsf to the base of the borehole, bulk densities increase from <2.10 to >2.60 g·cm^{-3}. The abrupt increase correlates with the change in lithology from silty claystone (lithostratigraphic Unit V) to tectonic breccia (lithostratigraphic Unit VI) and metadolerite (lithostratigraphic Unit VII).

Grain density data were derived from the same discrete samples from which bulk densities were measured. Grain densities average ~2.70 g·cm^{-3} from the seafloor to 240 mbsf (Fig. F46B). However, slightly higher densities at 75 and 135 mbsf may be representative of noted carbonate input (see "Organic Geochemistry," p. 31, and "Lithostratigraphy," p. 3) and the high at 180 mbsf corresponds to the presence of carbonate–cemented conglomerates. Deviation in the grain density begins ~270–280 mbsf, where low grain densities reflect the presence of

T12. Index properties measurements, p. 134.

F45. Site 1114 bulk density, p. 91.

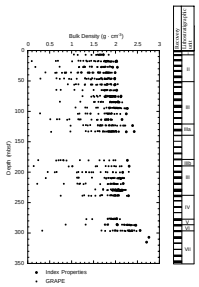

F46. Site 1114 profiles of discrete bulk density, grain density, and porosity, p. 92.

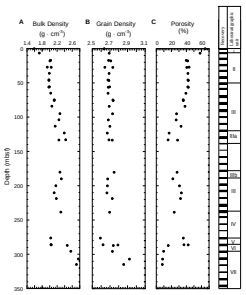

silty claystone. Below 290 mbsf, grain densities of the tectonic breccia (lithostratigraphic Unit VI) and metadolerite (lithostratigraphic Unit VII) increase to nearly 3.0 g·cm^{-3}.

The porosity profile strongly reflects bulk density variations, as expected from the measurement method (see **"Physical Properties,"** p. 28, in the "Explanatory Notes" chapter). At Site 1114, porosities average ~41% from 18 to 56 mbsf and then generally decrease to an average of 22% from 56 to 133 mbsf. Below 180 mbsf, porosity averages 26%. Deeper than 260 mbsf, porosities increase to an average of 42% before abruptly decreasing to ~9% (Fig. **F46C**). The porosity minima correlate to distinct lithostratigraphic units, with the lows from 120 to 130 mbsf and 275 to 353 mbsf corresponding to the carbonate–cemented sandstones and siltstones of lithostratigraphic Subunit IIIA and the tectonic breccia and dolerite at the base of the succession, respectively.

Surprisingly, the values throughout the entire porosity profile are low, as illustrated by seafloor and near-seafloor values of 65% and 58%, respectively, and an average porosity of 41% even in the shallow depth range of 17–56 mbsf. Low porosities toward the base of the profile are understandable and are likely the result of extended compaction and burial. The anomalous seafloor porosities may reflect an environment in which sediment deposited on the top of Moresby Seamount has been removed. More difficult to interpret, however, is the abrupt decrease in porosity from near-seafloor values of 58%–40% at 17 mbsf. As discussed in the bulk density section, this discontinuity is likely representative of an unconformity within the upper 10 m of the succession. To investigate this hypothesis further, it must first be noted that even though the porosity profile is comprised of values lower than those seen in earlier Leg 180 boreholes, the structure of the profile below 17 mbsf is generally consistent with a negative exponential variation often seen in normally compacting sediments (Athy, 1930). Fitting a least-squares curve to the porosity profile supports the presence of an unconformity because the relationship between depth and porosity in the deeper sediments of the succession is not consistent with the surface porosity (Fig. **F47A**). Moreover, sediment erosion is consistent with (1) the absence of the upper part of micropaleontologic Zone N21 and Subzones NN19E–F within the upper 10 m of the borehole, which indicates a hiatus in the sedimentary record between at least 0.46 and 1.25 Ma (see **"Biostratigraphy,"** p. 27) and (2) the interpretation of reflection seismic data suggesting the truncation of reflectors (see **"Miocene–Quaternary Arc and Forearc,"** p. 4, in the "Background and Regional Setting" chapter). To estimate the thickness of sediment that may have been eroded, a least-squares exponential curve was fit to a porosity profile that included only the data between 17 mbsf and the transition into metamorphic rock (Fig. **F47B**). The curve fitting predicts an initial porosity of 42.4% and a compaction decay constant of 0.0026 m^{-1}. Extrapolating this porosity-depth relationship to the surface, assuming initial porosities between 65% (i.e., seafloor porosity values from Site 1114) and 75% (i.e., seafloor porosities from other Leg 180 sites), implies that as much as 220 m of sediment has been removed from the upper stratigraphic units at the site. As this estimate is derived from a sparse data set, further analysis was conducted with the density-porosity logging data set (see **"Downhole Measurements,"** p. 38). Superposing index properties porosities onto the logging data, removing washout zones, and extrapolating the porosity depth relationship to the surface indicates that more than 400 m of sediment may have been eroded from Site 1114 (Fig. **F47C**).

F47. Regression least-squares exponential curves of porosity for Site 1114, **p. 93.**

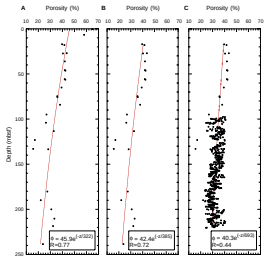

Compressional Wave Velocity

Compressional wave, or *P*-wave, velocity was measured on whole cores using the MST *P*-wave logger (PWL). On split cores, the PWS3 contact probe system was used to measure velocities. In Cores 180-1114A-1R and 2R, only transverse velocities were measured with the split core remaining in the core liner. From Core 180-1114A-3R to the bottom of the borehole, the level of induration was sufficient for ~10-cm^3 cubes to be cut from the cores, thereby allowing for velocity measurement in the transverse (x and y) and longitudinal (z) directions. Discontinuous and fractured cores yielded poor-quality PWL results, and thus this discussion will be limited to PWS velocity data.The PWS data can be found in Table **T13** and in ASCII format in the **TABLES** directory.

Velocities obtained in the upper 100 m of the borehole range from ~1700 to ~2600 m·s^{-1}, which are slightly higher values than expected for shallow-marine sediments. However, higher velocities correspond to the low porosity values observed in shallow sediments at this site and may also reflect the influence of recent erosion, as discussed in **"Density and Porosity,"** p. 33, and **"Depositional History,"** p. 15. The x, y, and z velocities from below the seafloor to 100 mbsf all show a fairly linear increase with depth (Fig. **F48**). Between 120 and 130 mbsf, the linear trend is disrupted by a point spike to nearly 4000 m·s^{-1}, after which the velocities return to values less than 3000 m·s^{-1}. This abrupt increase coincides with lithostratigraphic Subunit IIIA, which is comprised of carbonate–cemented siltstones and sandstones as well as packstones. Below 180 mbsf within lithostratigraphic Units III, IV, and V, the triaxial velocities remained relatively constant, ~2500 m·s^{-1}. In the lower 60 m of the borehole, the velocities increase to between 4300 and 6600 m·s^{-1} within the tectonic breccia and metadolerite of lithostratigraphic Units VI and VII, respectively.

Further evaluation of the triaxial velocity measurements indicates that transverse velocities are faster than longitudinal velocities when velocities remain below 2600 m·s^{-1} (Fig. **F49A**). On the contrary, longitudinal velocities are faster than transverse velocities in a velocity range of 3200 to 6600 m·s^{-1}. Such a trend suggests that transverse velocities generally dominate in the sandstones, siltstones, and claystones, whereas the longitudinal velocities dominate in the calcite-cemented unit and the low-porosity metamorphic units. Maximum velocity anisotropies range from 5% to 8% (Fig. **F49B**). A reversal in the anisotropy occurs at 90 mbsf, where the anisotropy changes abruptly from 4.6% to –1.3%, thereby indicating faster transverse velocities compared with longitudinal velocities. The depth of the reversal is slightly below the first documentation of shear deformation in the sediment section (56 mbsf) and corresponds to an interval characterized by high bedding dip (see **"Structural Geology,"** p. 20).

Thermal Conductivity

Thermal conductivity measurements were conducted primarily on split cores from Site 1114. The needle method was used only on the first core and the half-space method was used thereafter. The thermal conductivity values presented in Figure **F50** are averages of repeat measurements in the same interval. A full compilation of the data is presented in Table **T14** and in ASCII format in the **TABLES** directory.

Thermal conductivity values are governed primarily by pore space, and thus the thermal conductivity profile (Fig. **F50**) parallels that of the

T13. Longitudinal and transverse velocities for cores, **p. 135.**

F48. Site 1114 *P*-wave transverse (x, y) and longitudinal (z) velocities, **p. 94.**

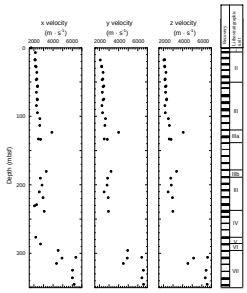

F49. Site 1114 longitudinal velocity vs. transverse velocity, and anisotropy, **p. 95.**

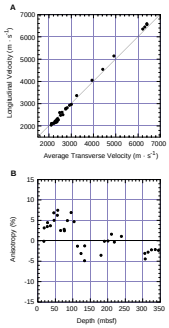

F50. Site 1114 thermal conductivity, **p. 96.**

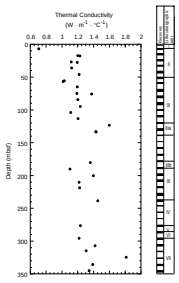

T14. Thermal conductivity values, Site 1114, **p. 136.**

porosity (Fig. F46C). The abrupt change in thermal conductivity from the seafloor value of 0.7–1.2 $W \cdot m^{-1} \cdot °C^{-1}$ at 17 mbsf reflects a stratigraphic hiatus occurring within the upper 10 m of the borehole. Below the unconformity, the thermal conductivity values remain >1.0 $W \cdot m^{-1} \cdot °C^{-1}$, probably being a function of the unusually low porosities noted in the porosity-depth profile. On average, the thermal conductivity values increase slightly with depth, with values ranging from <1.2 $W \cdot m^{-1} \cdot °C^{-1}$ to an average of 1.4 $W \cdot m^{-1} \cdot °C^{-1}$. Two isolated thermal conductivity highs, 1.6 $W \cdot m^{-1} \cdot °C^{-1}$ at 123 mbsf and 1.8 $W \cdot m^{-1} \cdot °C^{-1}$ at 324 mbsf, correspond to calcareous siltstone (lithostratigraphic Subunit IIIA) and metadolerite (lithostratigraphic Unit VII), respectively.

Magnetic Susceptibility

At Site 1114 estimates of magnetic susceptibility readings were routinely obtained as part of the MST measurement. The quality of magnetic susceptibility data is often poor in RCB-cored boreholes such as Site 1114, commonly because of a reduced core diameter and a propensity for fracturing that usually accompanies RCB-coring methods. The low recovery throughout the succession at Site 1114 also limits the degree of interpretation that can be placed on the magnetic susceptibility data. The full data set can be found as part of the MST compilation (in ASCII format) on the accompanying LDEO CD-ROM.

The magnetic susceptibility data comprise three segmented profiles separated by zones of poor recovery: 18 to 135 mbsf, 180 to 240 mbsf, and 275 to 300 mbsf (Fig. F51A). Within the first section the average magnetic susceptibility decreases slightly from 5 to 4 × 10^{-3} SI before increasing to a maximum of 10 × 10^{-3} SI between 70 and 80 mbsf. Below the susceptibility maximum, the average returns to less than 5 × 10^{-3} SI before increasing to a final peak average ~6 × 10^{-3} SI between 120 and 135 mbsf (Fig. F51A). The minimal fluctuation in magnetic susceptibility from 20 to 55 mbsf corresponds to the siltstones and claystones of lithostratigraphic Unit II, whereas the remainder of the profile parallels a unit of interbedded sandstone, siltstone, and claystone. Correlating documented grain size (see the "Core Descriptions" contents list for core images) with the magnetic susceptibility profile indicates that even though the fine to medium sands correspond to the two peaks, both sands and clays can exhibit apparent susceptibility highs and susceptibility lows. This observation agrees with the findings from Sites 1108 and 1109.

From 180 to 240 mbsf, magnetic susceptibility values increase from an average of 2.5 to >6 × 10^{-3} SI at a depth of 210 mbsf. The susceptibility then generally decreases with depth to <4 × 10^{-3} SI. This depth interval corresponds to the interbedded siltstones, sandstones, and claystones of Unit III. Correlating grain size to magnetic susceptibility in this interval indicates that, like the 0–140 mbsf interval, both sands and clays exhibit apparent highs, although the susceptibility peaks here correspond to predominantly clay units. Magnetic susceptibility values in the lower section of the borehole decrease from an average of 4 × 10^{-3} SI to nearly 0, paralleling the transition from silty claystone to tectonic breccia and ultimately to metadolerite.

F51. Site 1114 magnetic susceptibility and NGR data, p. 97.

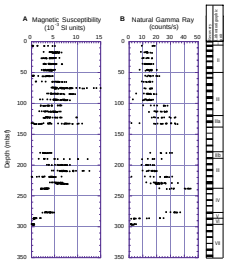

Natural Gamma Ray

Natural gamma ray (NGR) emissions were recorded on cores from Site 1114 as part of continuous MST measurements. A full compilation of NGR values is presented with the MST measurement data set (in ASCII format) on the accompanying LDEO CD-ROM.

The NGR data indicate a fairly constant NGR count between 10 and 20 counts/s from the seafloor to 100 mbsf (Fig. F51B). Below this depth interval from 100 to 142 mbsf, the counts abruptly increase to ~30 counts/s. From the typical relationship between radioactive elements and lithology type (i.e., an increasing NGR count with increasing clay content), one might expect this trend to indicate a transition from sandy units to clay-dominated units. Instead, the increase in NGR count corresponds to the transition from the sandstones in lithostratigraphic Unit III to the carbonate–rich sandstones of lithostratigraphic Subunit IIIA. The interpreted interval of lithostratigraphic Unit III and Subunit IIIA was based on low recovery (see "Lithostratigraphy," p. 3), and thus it may be argued that the units do not represent data sufficient for a comparison with physical properties NGR values. However, conventional logging data and FMS interpretation effectively supplement the lithostratigraphic interpretation and strongly suggest a continuous succession of alternating sand and silty clays over the entire length of the lithostratigraphic Unit III and Subunit IIIA interval. Further evaluation of grain-size distribution for Unit III and Subunit IIIA (see the "Core Descriptions" contents list) indicates that the increase in NGR count is a function of increasing sand content. This trend suggests the presence of radioactive sands, which is confirmed by increasing uranium, thorium, and potassium observed from 122 to 140 mbsf in the logging data (see "Downhole Measurements," p. 38).

Below 180 mbsf, NGR values decrease from ~25 counts/s at 180 mbsf to ~12 counts/s between 200 and 220 mbsf. From 220 to 240 mbsf, the gamma-ray count increases to nearly 30 counts/s. The 180 to 240 mbsf depth interval corresponds primarily to lithostratigraphic Unit III, with the sandstone Unit IV spanning the lower 5 m of the interval. Once again, the apparent NGR trend cannot be related to lithostratigraphic changes or unit boundaries, although comparison to grain-size distribution and logging data indicates the presence of radioactive sands at 180 and 240 mbsf. Toward the base of the borehole, the NGR count drops to nearly zero within the metadolerite.

Comparison of Core Data with Results of Downhole Measurements

Data from downhole logging fill gaps in physical properties measurements and allow us to assess whether index properties data are representative of the cored section. This is particularly important at Site 1114 where core recovery was only 12.4%. In general, index properties determinations of bulk density are in good agreement with the logging data (Fig. F52). Two exceptions are observed between 120 and 140 mbsf, where index properties bulk density exceeds that from the logging. A feasible explanation is that these samples were from layers that were too thin to be represented by the 40-cm resolution of the density logging tool (RHOM). Logging data below 220 mbsf indicate very low bulk densities, but data quality in this zone may be degraded by washouts located from 223 to 235 mbsf, 241 to 247 mbsf, 277 to 280 mbsf, and 288 to 292 mbsf (see "Downhole Measurements," p. 38; shaded zones,

F52. Site 1114 bulk density and velocity data, p. 98.

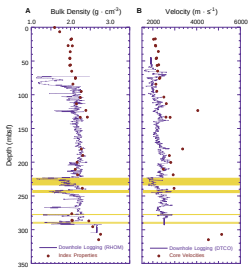

Fig. F52). Physical properties measurements of longitudinal (z-direction) velocity are generally high relative to data from downhole sonic velocity logs (Fig. F52). The reason for this discrepancy is unclear. One possible explanation relates to the 1-m resolution of the sonic logging tool (DTCO), which could have aliased the response from thin, high-velocity layers. Alternately, the bias may be caused by preferential index properties sampling of higher velocity material, a procedure necessary for supplementing the acoustic impedance contrast calculations.

DOWNHOLE MEASUREMENTS

Operations

One triple combo and two FMS-sonic (see Table T7, p. 74; Fig. F15, p. 66; both in the "Explanatory Notes" chapter) logging runs were recorded in Hole 1114A (see Table T15). A composite plot of the logs is presented in Figure F53. Natural gamma-ray (HNGS) data were logged downward from 26 m above seafloor in the pipe to locate the mudline, where the string was stopped for 3 min to provide a depth reference for the temperature-logging tool (TLT) temperature log. Upon reaching open hole at 80.5 mbsf, all data except those from the accelerated porosity sonde (APS) were logged during the descent to a total depth of 305 mbsf (about 10 m above where the bit had been released), below which the tool string could not pass. The APS data were not collected because this tool requires activating the formation with the minitron source that would degrade subsequent HNGS runs. An upward log was then recorded at 300 m/hr. The pipe was raised to 74.5 mbsf, and the log was recorded up to mudline, where it was held for ~10 min to run calibrations and to give the TLT log another depth reference.

For the second run, the pipe was lowered again to 80 mbsf and the FMS-sonic string (see Table T7, p. 74; Fig. F15, p. 66; both in the "Explanatory Notes" chapter) was lowered. The string reached a depth of 298 mbsf and an upward log was recorded to 96 mbsf (Table T15), although FMS logging was ended at 122 mbsf. The tool string was lowered again, and a second pass was made from 298 to 39 mbsf. The bottom of the pipe was raised to 74.5 mbsf, and FMS logging ended at 107 mbsf. The logging speed for both FMS-sonic runs was 300 m/hr.

Depth Shifts

The drill-pipe measurement of the mudline was 418.0 meters below rig floor (mbrf). Based on the HNGS log from the triple combo run, the mudline wireline depth was identified at 417.5 mbrf (Fig. F54). This value is used to present data in terms of meters below seafloor. The depth shift for the first and second FMS-sonic runs was 418.25 m and was derived by correlating the natural-gamma spectrometry tool (NGT) from the FMS-sonic tool strings with that of the triple combo run within the intervals between 110 and 120 mbsf (Fig. F55A) and between 215 and 224 mbsf (Fig. F55B). These intervals were chosen for their characteristic large variations.

T15. Logging operations, p. 139.

F53. Hole 1114A composite log, p. 99.

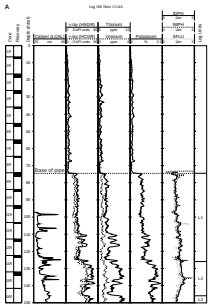

F54. Hole 1114A depth-shifted total gamma ray at mudline, p. 103.

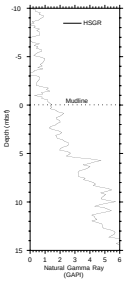

F55. Hole 1114A depth-shifted total gamma ray from triple combo and FMS-sonic string, p. 104.

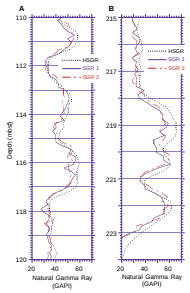

Log Quality

Log quality is degraded in areas of enlarged diameter and rapidly changing hole diameter (see "Downhole Measurements," p. 34, in the "Explanatory Notes" chapter). In Hole 1114A the caliper from the triple combo run reached maximum extension in the following intervals: 223–235 mbsf, 241–247 mbsf, 277–280 mbsf, and 288–292 mbsf (Fig. F53A). In addition, the caliper nears full extension between 156 and 166 mbsf.

Log Analysis

The relationship between the neutron porosity (APLC) and density porosity (DPHI) measurements was used to distinguish between high clay content and low clay content (clean) lithologies. Relative to Site 1109, the discrepancy between the neutron and density porosities is small, indicating overall lower clay content. Porosity values from both tools are significantly lower than at Hole 1109D. The low porosities (~40%) near the top of the logged interval suggest that these sediments have experienced greater burial than their present depth. With some exceptions, porosity decreases from the top of the logged interval to ~200 mbsf. The porosity data below 200 mbsf are difficult to interpret because of washouts but appear uniform where not washed out. Sonic velocities generally increase from the top of the logged interval (70 mbsf) to 200 mbsf and become more variable from 200 mbsf to the total logged depth of 284 mbsf (Fig. F53B).

In addition to considering the separation between the neutron and density porosities, the definition of log units also considered values from the natural gamma ray and photoelectric effect (PEFL). As was observed in Hole 1109D, uranium content varies little and the total gamma ray seems controlled mainly by the thorium and potassium contents. At previous sites of Leg 180, it has been noted that gamma-ray counts increase within sand layers. This correlation was used in log analysis of Hole 1114A.

A PEFL value greater than 5 barns/e^- generally indicates carbonate. However, data from Hole 1114A are surprising in that PEFL values are extremely high, reaching 12 barns/e^-. Log analysis defined five logging units (Fig. F56). Distinctive characteristics of each unit are described below.

F56. Hole 1114A log units and correlations, p. 105.

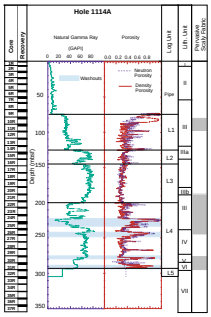

Log Unit L1 (80–126 mbsf)

In this interval, the neutron porosity is larger than the density porosity by ~0.15–0.20, indicating some clay content. This difference decreases downhole, suggesting an upward-fining trend. The PEFL values also increase downhole over this interval, with values reaching 5 barns/e^- at 126 mbsf. Gamma-ray values generally range from 26 to 41 GAPI units with the exception of the interval between 113 and 117 mbsf where several peaks range between 50 and 60 GAPI units. Velocities increase from ~1.9 to 2.5 km·s^{-1} at 116 mbsf, then decrease to ~2.0 km·s^{-1} at the base of log Unit L1.

Log Unit L1 is correlative with the upper part of lithostratigraphic Unit III, which is interbedded sandstone, siltstone, and claystone (see "Lithostratigraphic Unit III," p. 7).

Log Unit L2 (126–146 mbsf)

In most of the logs, this unit is similar in character to log Unit L1. The primary difference is that gamma-ray values step up to between 44 and 79 GAPI units. Generally, neutron porosity is greater than density porosity, but this difference rarely exceeds 0.10, suggesting a cleaner (lower clay content) formation than log Unit L1. The PEFL values range between 4 and 5 barns/e$^-$, which would typically be considered consistent with a carbonate–bearing lithology. However, carbonate content in this interval is <6 wt% (see **"Organic Geochemistry,"** p. 31); therefore, other minerals may be responsible for the PEFL values here (see discussion in **"Log Unit L3,"** p. 40). Log Unit L2 coincides with lithostratigraphic Subunit IIIA, which consists of calcite-cemented siltstone, sandstone, and bioclastic packstone (see **"Lithostratigraphic Subunit IIIA,"** p. 9).

Log Unit L3 (146–198 mbsf)

This unit is defined by its PEFL values, which are consistently greater than 5 barns/e$^-$ and reach peak values of 10–12 barns/e$^-$. These high values suggest the presence of iron-bearing minerals. The density and neutron porosities are very similar in this unit, indicating low clay content. Gamma-ray values range between 59 and 82 GAPI units. Below 178 mbsf, resistivity values step up, but this change is not accompanied by significant variations in any other logs.

Log Unit L3 lies within lithostratigraphic Unit III, including Subunit IIIB (see **"Lithostratigraphic Unit III,"** p. 7). Low recovery within this interval makes it difficult to assess the source of the elevated PEFL values. Pyrite is commonly noted within the core descriptions and may contribute to the elevated PEFL values that characterize this unit. The top boundary of lithostratigraphic Unit IIIB containing conglomerate and coarse sandstone may correlate with the step increase in resistivity noted at 178 mbsf. However, the increased resistivity persists to a depth of ~220 mbsf, whereas lithostratigraphic Subunit IIIB was determined to extend only to ~190 mbsf.

Log Unit L4 (198–292 mbsf)

In log Unit L4 the hole is frequently enlarged, thereby affecting log quality (Fig. **F53A**). Two of the washout intervals (at 223–235 mbsf and 288–292 mbsf) coincide with increased incidence of pervasive scaly fabrics noted in core description (see **"Structural Geology,"** p. 20). In much of log Unit L4 the neutron porosities are larger than the density porosities by ~0.05, suggesting some clay content. The difference reaches as high as 0.20 in thin (several meter) intervals, suggesting increased clay content, and meter-scale zones exist where neutron porosity falls below density porosity, suggesting clean units. Between 198 and 250 mbsf, the PEFL values decrease downhole from 5 to 3 barns/e$^-$. From 250 mbsf to the bottom of log Unit L4, PEFL values remain ~4 barns/e$^-$, with two distinct drops to ~3 barns/e$^-$ at 278 and 290 mbsf. Gamma-ray values show large variation between 198 and 235 mbsf. A peak in gamma-ray values occurs at 210 mbsf and coincides with a peak in resistivity. Below 235 mbsf, gamma-ray data show less variation, generally ranging from 60 to 70 GAPI units.

Log Unit L4 overlaps lithostratigraphic Units IV, V, and VI, which consist of sandstone, silty claystone, and a tectonic breccia, respectively

(see "Lithostratigraphic Unit IV," p. 12, "Lithostratigraphic Unit V," p. 13, and "Lithostratigraphic Unit VI," p. 14). These units are not distinguishable on the logs because of both washouts and lack of coverage by the upper tools of the triple combo tool string.

Log Unit L5 (292–302 mbsf)

This unit and its contact with overlying log Unit L4 are shown most clearly on the FMS images, which are described in "Borehole Geometry, Magnetic Field, and FMS Dynamics," p. 41. The upper boundary of log Unit L5 was selected as the bottom of the washouts. It is highly resistive and corresponds to the metadolerite (see "Igneous and Metamorphic Petrology," p. 16).

Borehole Geometry, Magnetic Field, and FMS Dynamics

The accelerometer data of the FMS-sonic run show that the hole deviation increases from 0.5° near the top of the borehole to more than 2° near the bottom of the logged interval (Fig. F57). Acceleration magnitudes indicate scatter in tool movement, which represents some tool sticking during the passes. The azimuth data of Pad 1 from the two FMS passes indicates a 90° difference for most of the passes (Fig. F58). Consequently, the second pass directly underlies the first for most of the logged interval. The FMS caliper data indicate loss of pad contact for both calipers at depths of 223–235 mbsf, 240–247 mbsf, and 288–292 mbsf (Fig. F59). Between 156 and 167 mbsf, one reading is near the maximum while the other caliper indicates a hole size of 28–30 cm. In general, the hole is very elliptical between 135 and 200 mbsf, with the larger diameter trending 50°. This direction is consistent with the strike of bedding noted in the FMS images. It is important to note that FMS-based data are oriented relative to geographic north.

The magnetometer measurement yields both inclination and magnitude of the total field. These measurements are strongly influenced by the pipe when approaching it. Although magnitudes of magnetic intensity show a consistent offset between Pass 1 and Pass 2, the character of the logs is very similar. The magnetic intensities increase downhole until 210 mbsf and then remain relatively constant (Fig. F60). Magnetic inclination decreases from –29.7° at the top of the logged section to –30.3° at the bottom (Fig. F60).

FMS Images

Two passes of the FMS tool were run in Hole 1114A in an effort to provide greater coverage of the borehole wall (Table T15). However, the two images overlie each other over much of the logged interval despite rotation of the tool between passes. Good quality FMS images were acquired between ~105 and 298 mbsf with the exception of large, frequent washouts as shown in the caliper log (Fig. F59). The FMS processing steps included speed correction, depth shifting, and static and dynamic normalization using a 1-m window. The first-pass FMS images were depth shifted an additional 0.1 m to correct a constant vertical offset observed between the two images. Remaining vertical offsets (<0.05 m) between the two images vary throughout the logged interval and appear to be caused by differential accelerations caused by sticking, which will be corrected by further processing postcruise.

F57. Hole 1114A geometry from FMS inclinometry data, p. 106.

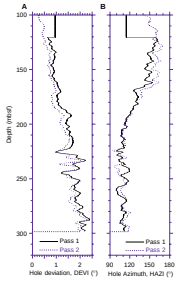

F58. FMS Pad 1 azimuth with respect to geographic north in Hole 1114A, p. 107.

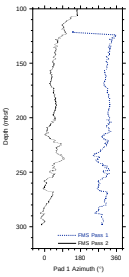

F59. Hole 1114A FMS caliper data, p. 108.

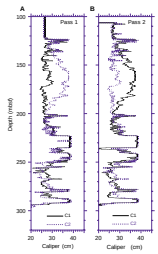

F60. Hole 1114A magnetic field from FMS magnetometer, p. 109.

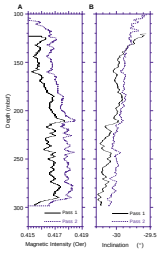

The FMS interpretation is organized according to log units defined in this section (Fig. F56). Hole 1114A is generally characterized by thin (~10 cm), moderately resistive beds that are heavily fractured. Bed dips throughout Hole 1114A average 38° with a mean northwestward dip direction of 320° (Figs. F61, F62, F63). Fractures show two prominent dip distributions in Hole 1114A. Above ~260 mbsf, fractures dip 68° with a northward dip direction of 355° (Figs. F61, F62, F63). Below 280 mbsf (i.e., within the fault zone), fractures dip 65° with a southwestward dip direction of 230°, which is consistent with the south-southwest–dipping normal fault orientation determined from the seismic reflection data.

Log Unit L1 (80–126 mbsf)

Log Unit L1 is characterized by moderately resistive beds interpreted as clayey layers occasionally interlayered with 10- to 15-cm-thick, highly resistive beds, which are inferred to be sand and possibly calcium-carbonate–rich layers (Fig. F64). Beds are cut by numerous thin conductive fractures that are occasionally observed to be filled with resistive material, which is consistent with calcite cement. Bed dips increase with depth within this short unit from ~20° to 45°, whereas dip directions are consistently to the northwest (Fig. F63). Fractures dip 40°–60° to the northwest; however, minor fractures dipping 60° to the east-northeast are also observed to crosscut the northwest-dipping beds.

Log Unit L2 (126–146 mbsf)

Calcium carbonate–rich sediments of lithostratigraphic Subunit IIIA correlate with the more highly resistive layers of log Unit L2 (see "Subunit IIIA," p. 9). Beds show a slight change in dip direction to the west-northwest with dips between 35° and 55° (Fig. F63). Fractures are poorly defined within this unit. Image quality is degraded throughout much of this interval because of poor pad contact with the borehole wall.

Log Unit L3 (146–198 mbsf)

The upper portion of log Unit L3 displays overall low resistivity above 178 mbsf, which is likely related to clays as well as heavy (i.e., conductive) mineral content indicated by the PEFL (Figs. F53B, F65). Pyrite recognized in the core samples is suggested to be the dominant conductive mineral in this unit (see "Lithostratigraphy," p. 3). A distinct increase in large-scale resistivity begins at 179 mbsf with the top of a 1.5-m-thick highly resistive layer (Fig. F66). Below 170 mbsf, both bed and fracture dip directions verge northward with depth and steadily increase in dip from 30° to 50° and 35° to 80°, respectively (Fig. F63).

Log Unit L4 (198–292 mbsf)

Large washouts and borehole irregularities commonly degrade FMS image quality within this unit. Between 208 and 216 mbsf, however, image quality is very good and the two FMS images do not overlap (Fig. F67). Log Unit L4 displays overall low resistivity, which suggests increased conductive mineral content. The trend of increasing bed and fracture dips and northward verging dip direction observed in Unit L3 (see "Log Unit L3," p. 40) continues within Unit L4 as far as 215 mbsf (Fig. F63), below which large washouts preclude image interpretation.

F61. Wulff stereographic projection of beds and fractures in Hole 1114A, p. 110.

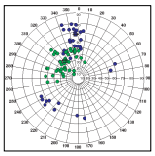

F62. Hole 1114A bed and fracture dip orientations, p. 111.

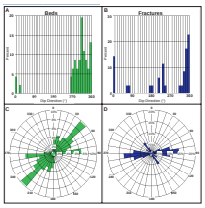

F63. Hole 1114A variation of bed and fracture orientation with depth, p. 112.

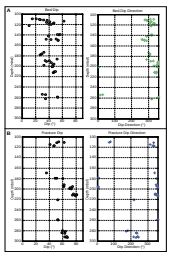

F64. Hole 1114A statically normalized FMS image and tadpole plot, log Unit L1, p. 113.

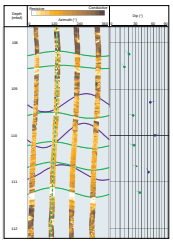

F65. Hole 1114A statically normalized FMS image and tadpole plot, upper log Unit L3, p. 114.

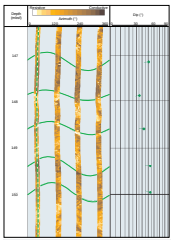

As shown in Figure F67, steep 80°-dipping fractures cut more shallow 40°-dipping beds, and both beds and fractures display north-northwestward dip directions.

Log Unit L5 (~292–302 mbsf)

Below ~292 mbsf, highly resistive material continues to the base of the FMS log. The top of log Unit L5 is defined by steep (65°) southwestward–dipping, fracture-bounded beds, whereas below 293 mbsf it appears relatively structureless with few well-defined, continuous fractures. The tectonic breccia-metadolerite contact described in cores correlates in depth approximately with the top of log Unit L5 (see "Lithostratigraphic Unit VI," p. 14, and "Lithostratigraphic Unit VII," p. 15, and "Igneous and Metamorphic Petrology," p. 16).

It is difficult to select the boundary between the tectonically brecciated metadolerite and the metadolerite basement. Although FMS images above 292 mbsf are partially obscured by poor pad contact, a coarse-textured, highly resistive 1-m-thick bed appears at 290.5 mbsf. Based on the strong resemblance in both structure and microresistivity response to the material below 292 mbsf, this bed is interpreted to be similar material to that of log Unit L5 (Fig. F68). Below this 1-m-thick layer a relatively thin (≤1-m-thick) layer is washed out with the exception of a small portion of the borehole between 240° and 360°, which suggests continuity between the beds above and below. It is reasonable to infer that the partially washed-out interval above ~292 mbsf consists of metadolerite that has been brecciated to various extents.

Temperature Data

The TLT data reveal the temperature profile within the pipe (Fig. F69) and in open hole (Fig. F70) where 23.4°C is reached at 304 mbsf. The tool string was held on bottom for a few minutes, and warming of the bottom hole is evident. However, the data record was not long enough to extrapolate in situ temperatures. Although the tool was held at mudline for ~10 min, the temperature continued to decrease and a stable temperature was not reached. The lowest recorded value was 15.0°C. No in situ temperature measurements were possible at Site 1114. Based on the TLT data, we estimate that a lower limit for the thermal gradient is 0.03°C·m^{-1}. The actual gradient is probably significantly higher.

F66. Hole 1114A statically normalized FMS image and tadpole plot, lower log Unit L3, p. 115.

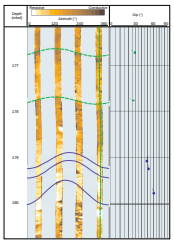

F67. Hole 1114A dynamically normalized FMS image and tadpole plot, log Unit L4, p. 116.

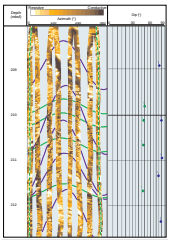

F68. Hole 1114A dynamically normalized FMS image and tadpole plot, log Unit L5, p. 117.

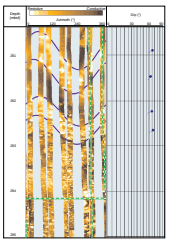

F69. Temperature data from TLT in and above Hole 1114A, p. 118.

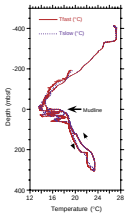

F70. Hole 1114A temperature data, p. 119.

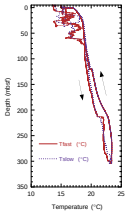

REFERENCES

Athy, L.F., 1930. Density, porosity, and compaction of sedimentary rocks. *AAPG Bull.,* 14:1–24.

Davies, H.L., 1980. Folded thrust fault and associated metamorphics in the Suckling-Dayman Massif, Papua New Guinea. *Am. J. Sci.*, 280-A, 171–191.

Davies, H.L., Honza, E., Tiffin, D.L., Lock, J., Okuda, Y., Keene, J.B., Murakami, F., and Kisimoto, K., 1987. Regional setting and structure of the western Solomon Sea. *Geo-Mar. Lett.,* 7:153–160.

Davies, H.L., and Jaques, A.L., 1984. *Emplacement of ophiolite in Papua New Guinea*. Spec. Publ.—Geol. Soc. London, 13:341–350.

Davies, H.L., and Warren, R.G., 1988. Origin of eclogite-bearing, domed, layered complexes ("core complexes") in the D'Entrecasteaux Islands, Papua New Guinea. *Tectonics*, 7:1–21.

Goodliffe, A., Taylor, B., Hey, R., and Martinez, F., 1993. Seismic images of continental breakup in the Woodlark Basin, Papua New Guinea. *Eos,* 74:606.

Humphris, S.E., Alt, J.C., Teagle, D.A.H., and Honnorez, J.J., 1998. Geochemical changes during hydrothermal alteration of basement in the stockwork beneath the active TAG hydrothermal mound. *In* Herzig, P.M., Humphris, S.E., Miller, D.J., and Zierenberg, R.A. (Eds.), *Proc. ODP, Sci. Results,* 158: College Station, TX (Ocean Drilling Program), 255–276.

Jelinek, V., 1981. Characterization of the magnetic fabric of rocks. *Tectonophysics,* 79:63–67.

Lock, J., Davies, H.L., Tiffin, D.L., Murakami, F., and Kisomoto, K., 1987. The Trobriand subduction system in the western Solomon Sea. *Geo-Mar. Lett.,* 7:129–134.

Parkes, R.J., Cragg, B.A., Bale, S.J., Getliff, J.M., Goodman, K., Rochelle, P.A., Fry, J.C., Weightman, A.J., and Harvey, S.M., 1994. A deep bacterial biosphere in Pacific Ocean sediments. *Nature,* 371:410–413.

Pickering, K.T., Hiscott, R., and Hein, F.J., 1989. *Deep-marine Environments: Clastic Sedimentation and Tectonics:* London (Unwin Hyman).

Robertson, A.H.F., and Xenophontos, C., 1993. Development of concepts concerning the Troodos Ophiolite and adjacent units in Cyprus. *In* Prichard, H.M., Alabaster, T., Harris, N.B.W, and Neary, C.R. (Eds), *Magmatic Processes and Plate Tectonics*. Geol. Soc. Spec. Publ. London, 76:85–119.

Rogerson, R., Queen, L., and Francis, G., 1993. The Papuan ultramafic belt arc complex. *In* Wheller, G.E. (Ed.), *Islands and basins: correlation and comparison of onshore and offshore geology*. CCOP/SOPAC Misc. Rept. 159:28–29.

Shipley, T.H., Ogawa, Y., Blum, P., et al., 1995. *Proc. ODP, Init. Repts.,* 156: College Station, TX (Ocean Drilling Program).

Wager, L.R., and Brown, G.M., 1968. *Layered Igneous Rocks:* London (Oliver and Boyd).

Figure F1. Lithologic log of the succession recovered at Site 1114.

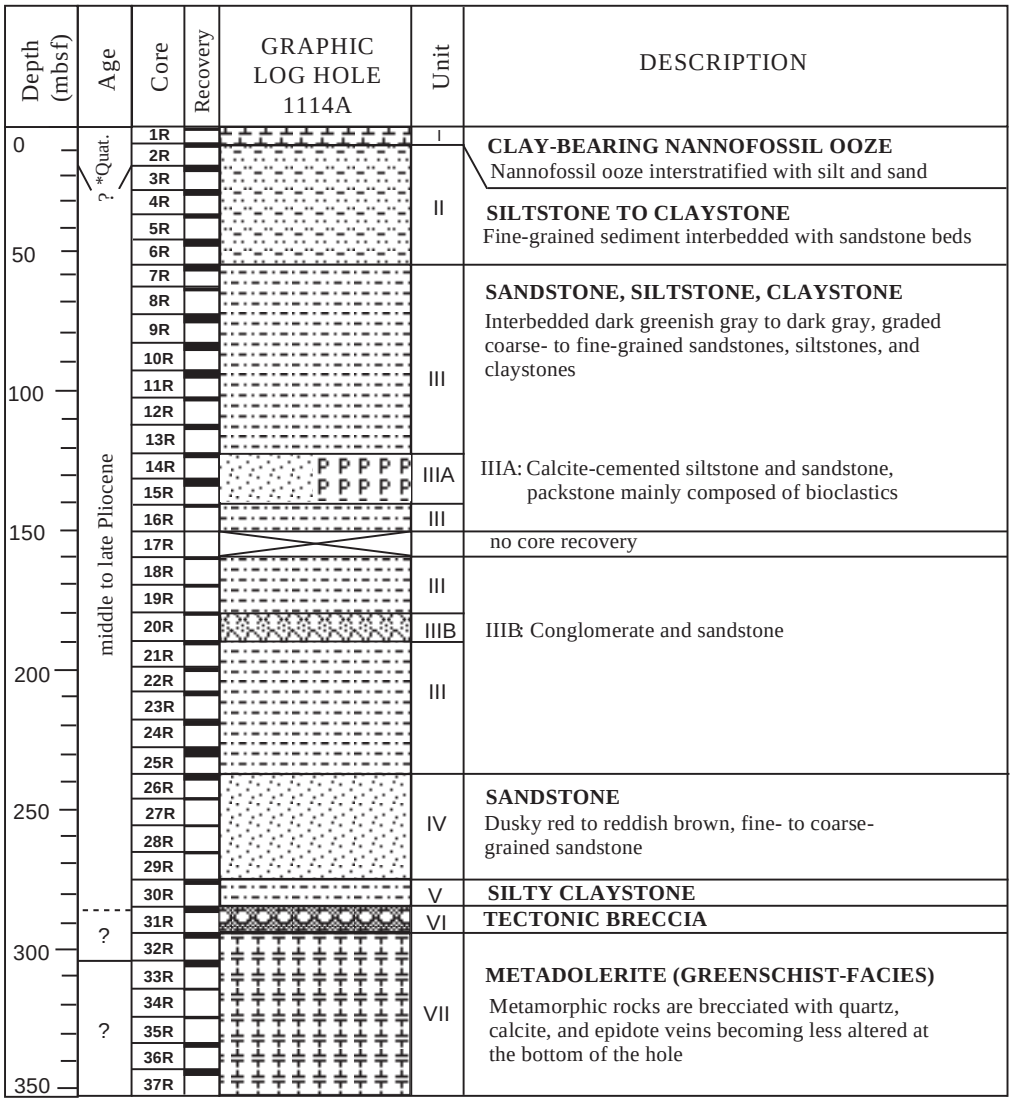

*Quat. = Quaternary

Figure F2. Bed-by-bed log of the succession in Hole 1114A.

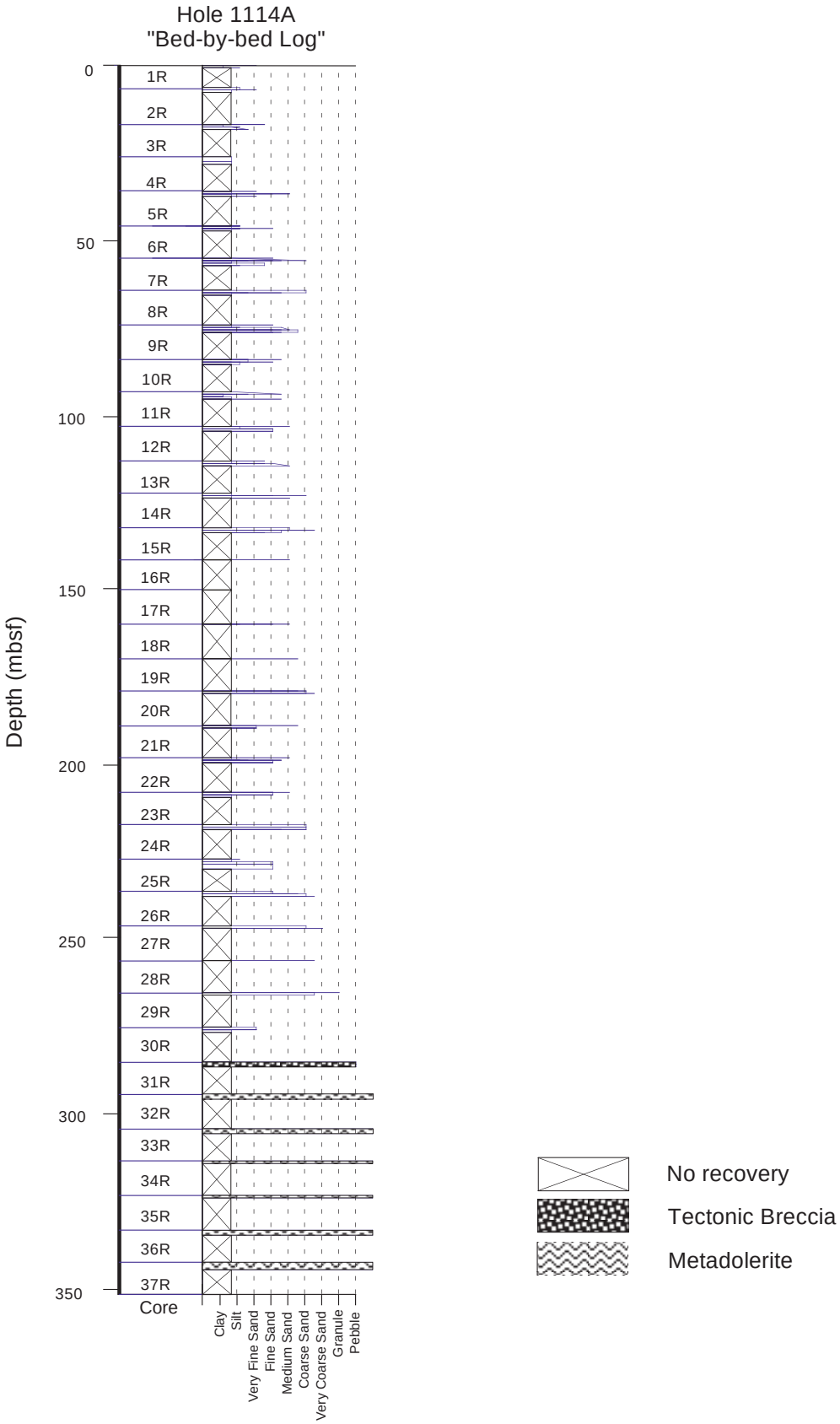

Figure F3. Parallel-laminated sand (68–73 cm) sharply overlying clay. Highly bioturbated siltstone (*Chondrites).* Bioturbation is so pervasive that original bedding is rarely preserved (86 cm) (interval 180-1114A-5R-1, 68–93 cm).

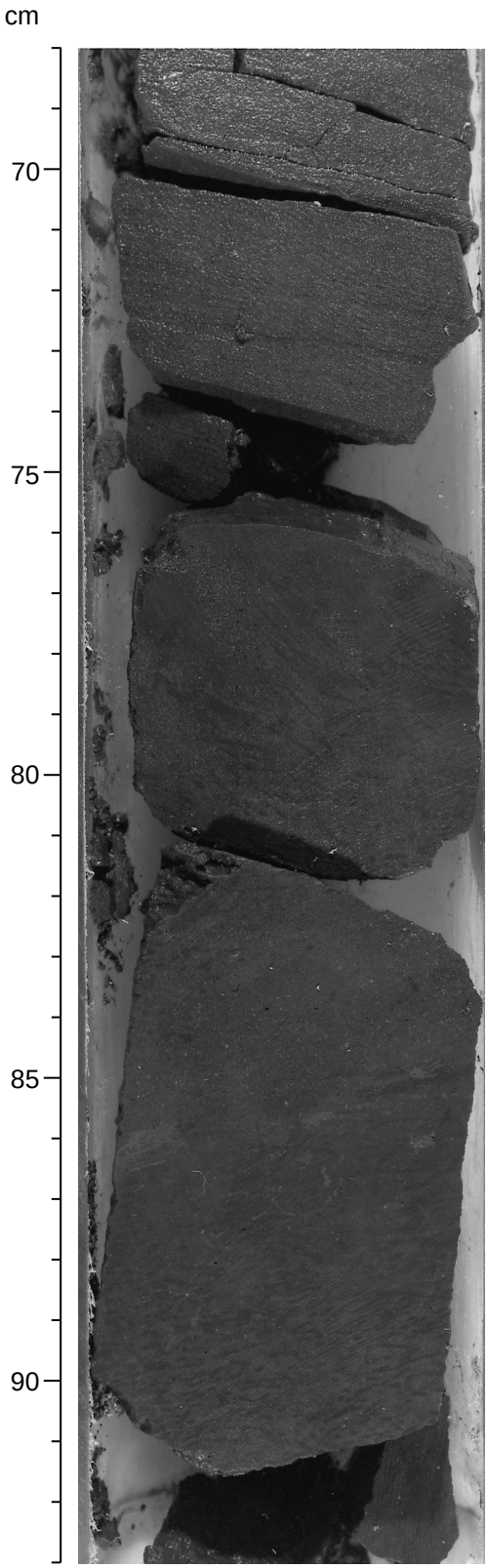

Figure F4. Digital photomicrograph (crossed nicols) of a fine-grained volcaniclastic sandstone with unaltered plagioclase, quartz, mica (muscovite and biotite), planktonic foraminifers, and other bioclasts. Numerous dark basaltic fragments are nearly invisible (interval 180-1114A-3R-1, 50–52 cm).

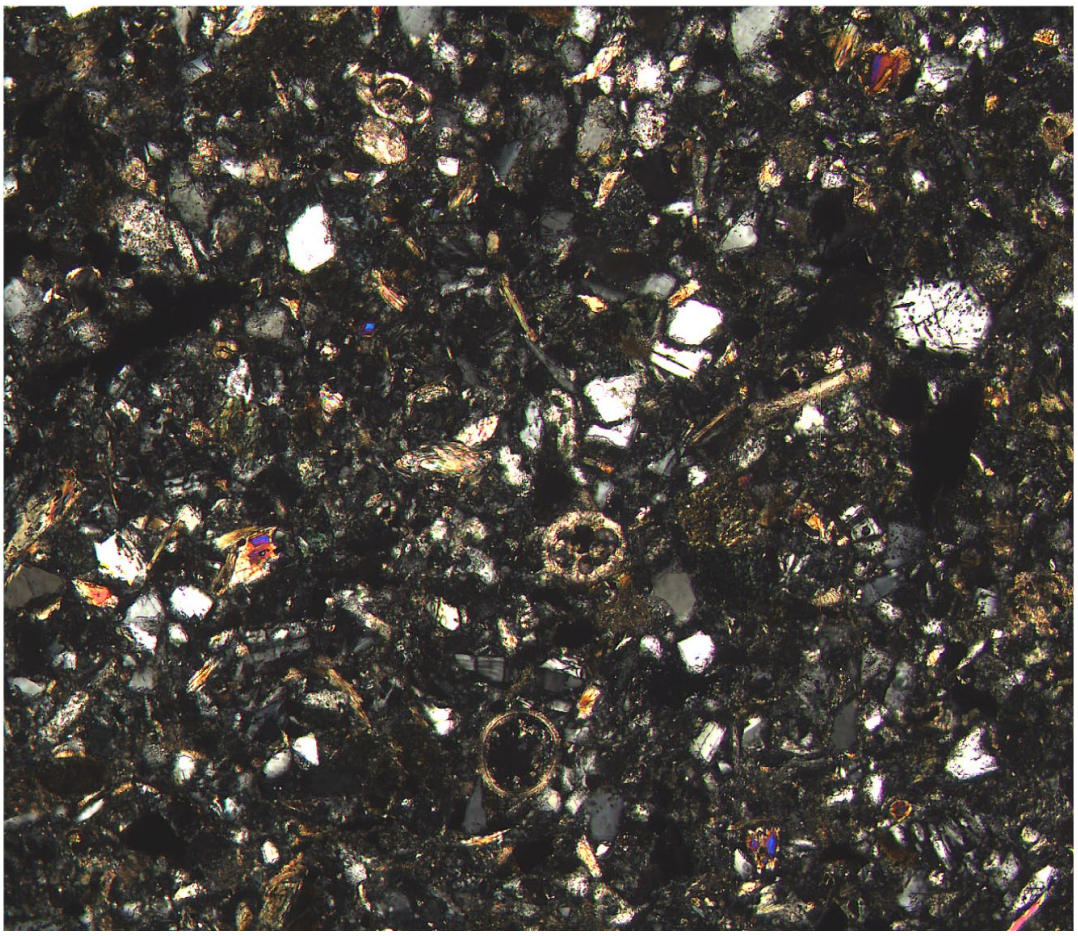

Figure F5. Inverse-to-normal graded sandstone bed. The upper part of the bed has scattered mudstone clasts oriented at different angles (interval 180-1114A-14R-1, 80–112 cm).

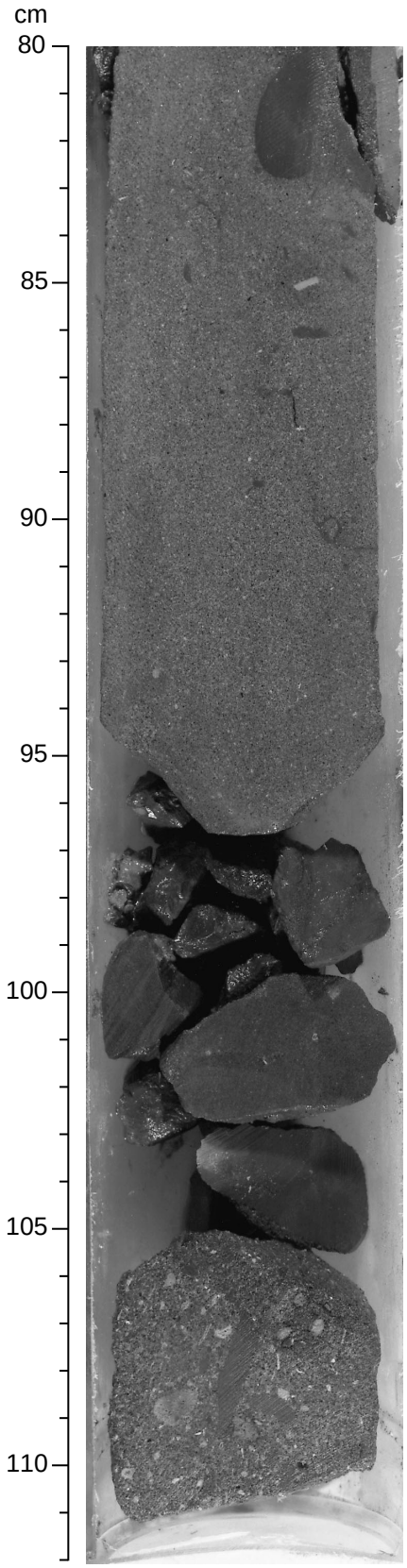

Figure F6. Medium-grained sandstone showing sharp lower bedding planes and parallel laminations in the lower part of the beds (interval 180-1114A-9R-2, 20–76 cm).

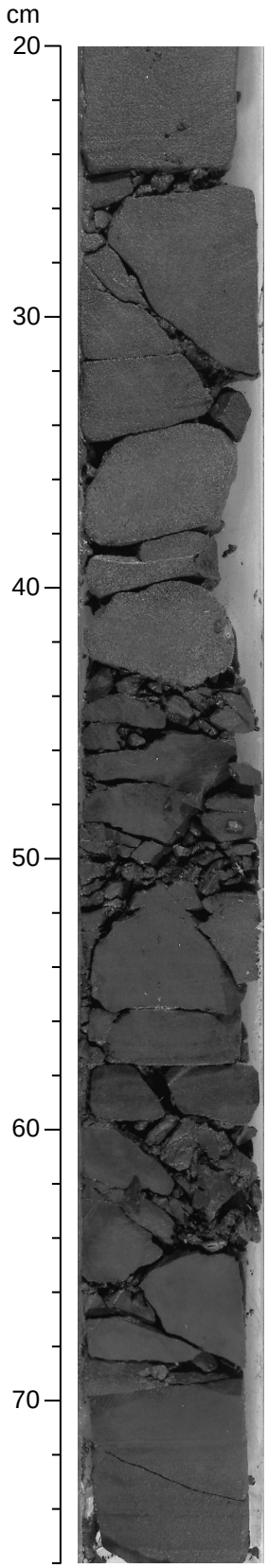

Figure F7. Convolute laminations in fine-grained sandstones that overlie a parallel-laminated interval and are truncated by an overlying parallel-laminated interval (interval 180-1114A-11R-CC, 15–24 cm).

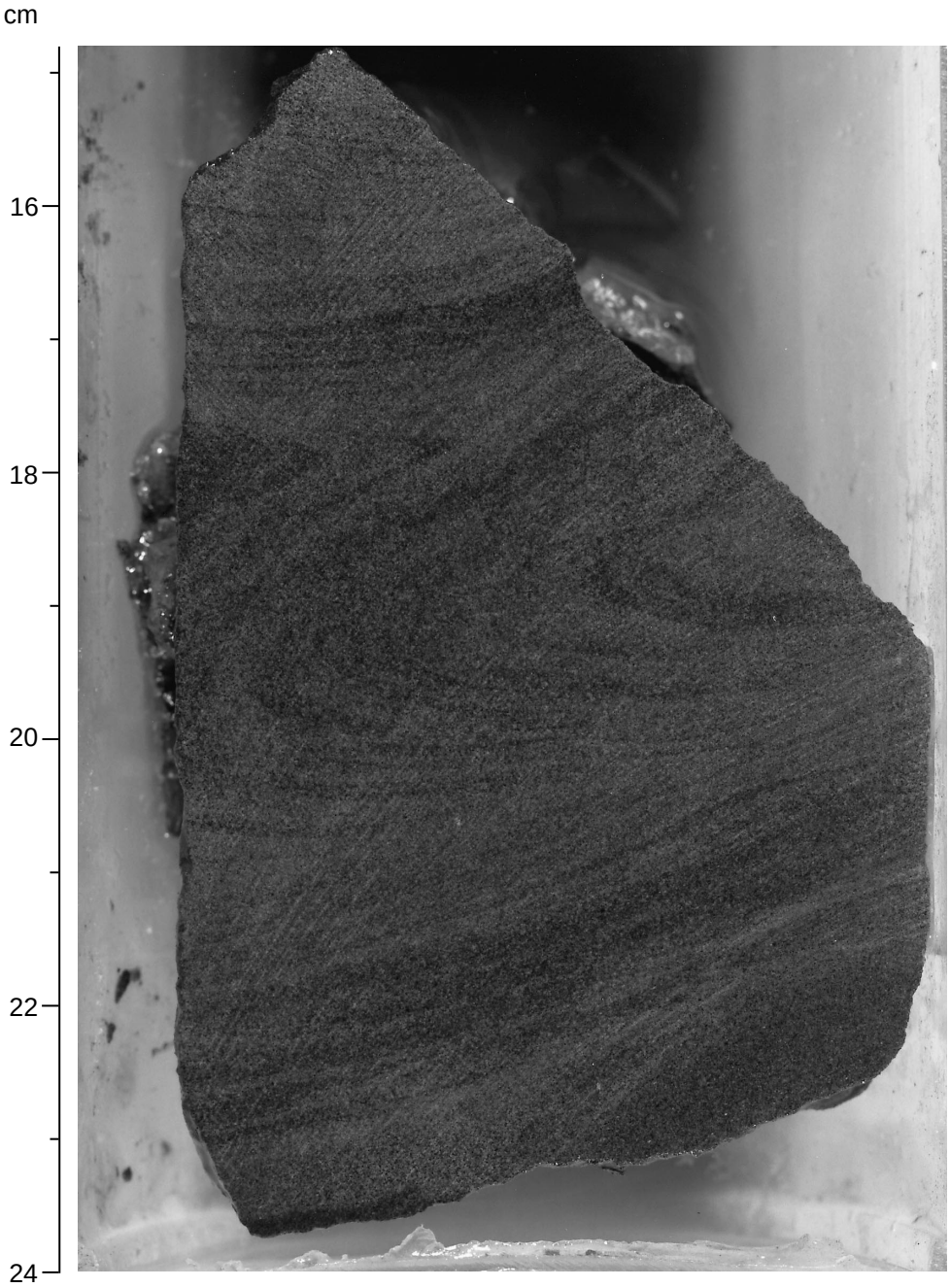

Figure F8. Digital photomicrograph (crossed nicols) of a polycrystalline quartz grain set within other detrital grains and calcite spar cement. The polycrystalline quartz is inferred to be of metamorphosed volcanic origin (interval 180-1114A-11R-CC, 18–20 cm).

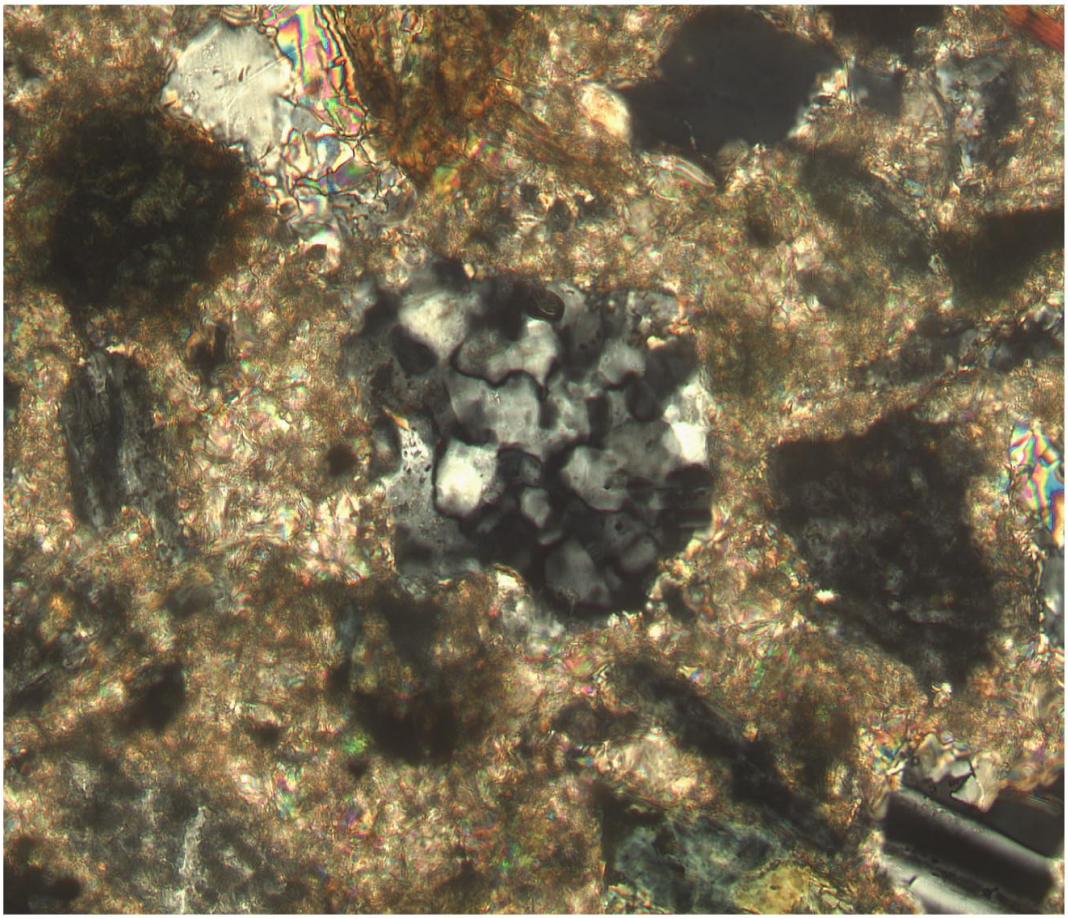

Figure F9. Digital photomicrograph (crossed nicols) of an elongate grain of detrital calc-schist composed of calcite and anastomosing biotite laths. Other detrital grains are plagioclase and quartz cemented by calcite spar (interval 180-1114A-11R-CC,18–20 cm).

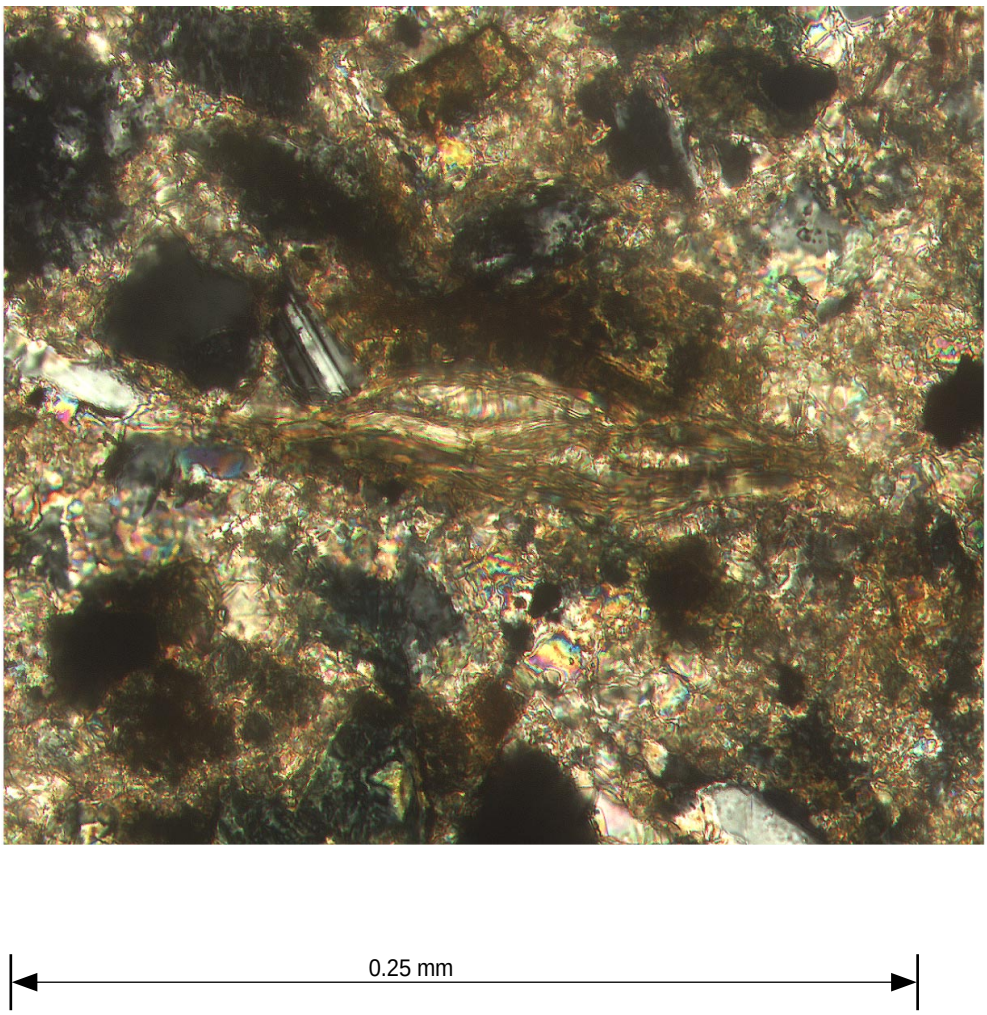

Figure F10. Several sharp-based (scoured) siltstone beds, some of which grade into claystone. Loads and pseudonodules are present below the bases of some beds (interval 180-1114A-12R-1, 62–75 cm).

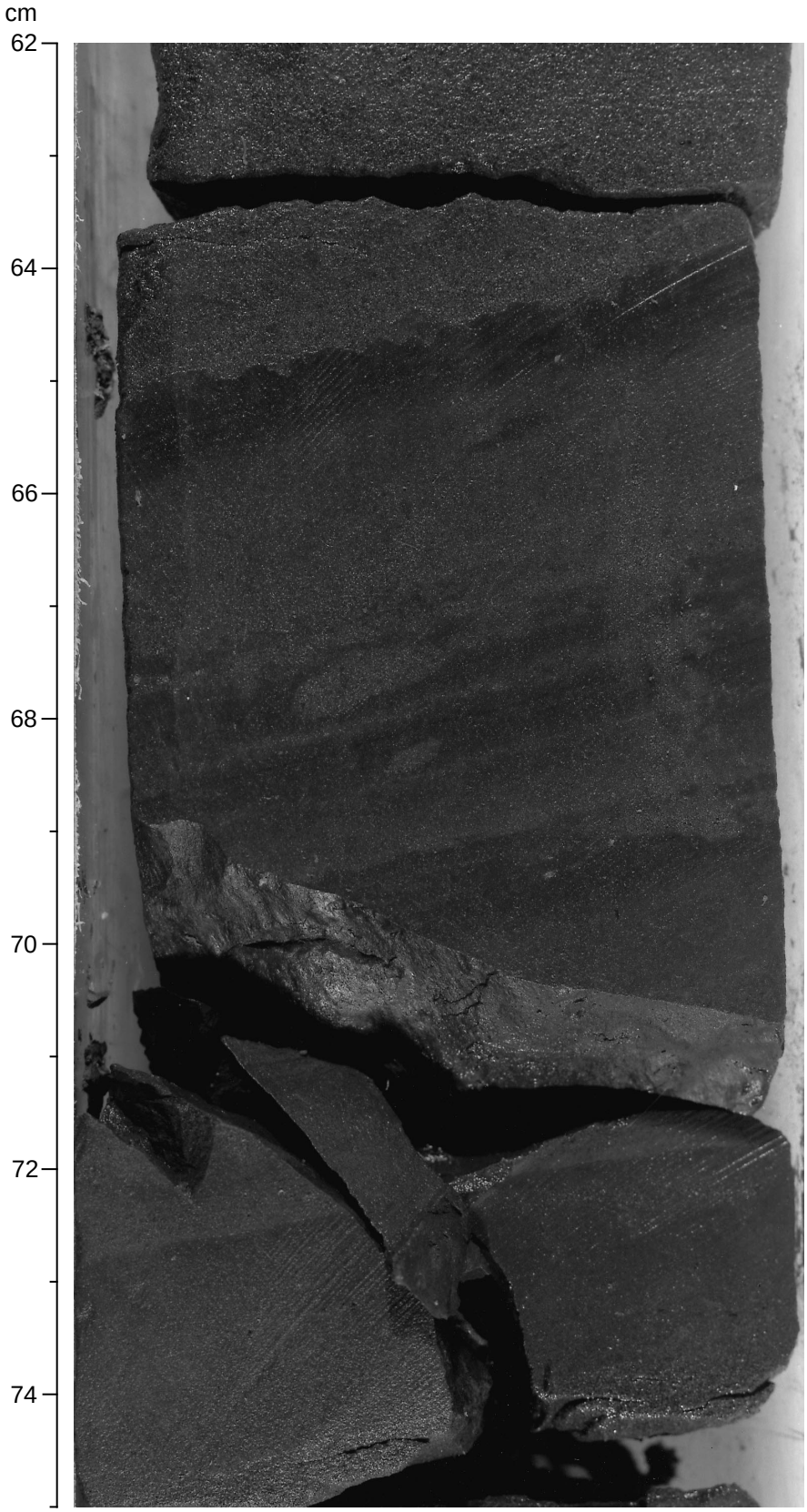

Figure F11. Calcite-cemented sandstone rich in bioclasts (42–54 cm). This sandstone has very coarse to granule-sized particles. Note the steep dip (interval 180-1114A-15R-1, 42–57 cm).

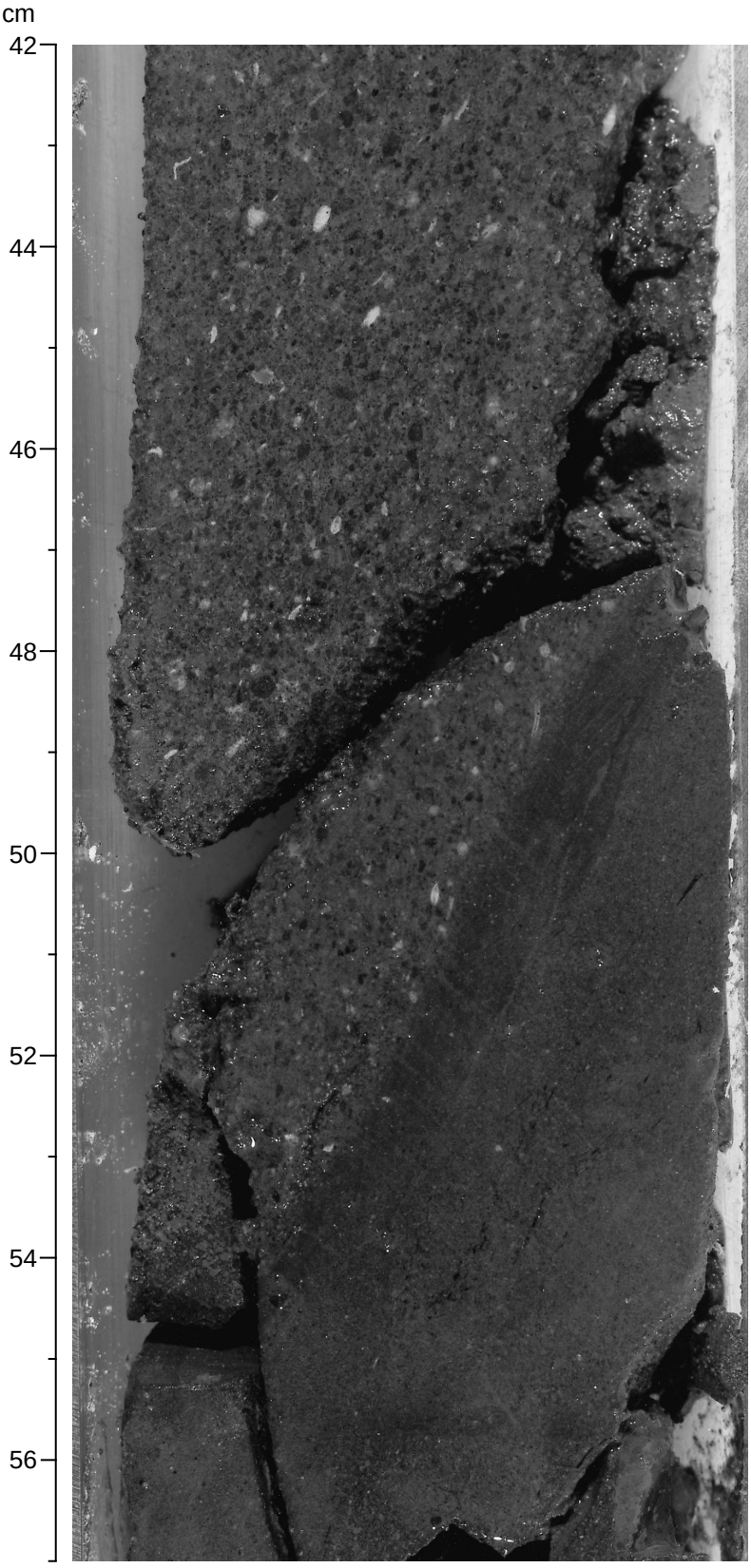

Figure F12. Digital photomicrograph (crossed nicols) of a coarse-grained volcaniclastic sandstone. A subrounded lithoclast of basalt with microphenocrysts of feldspar and clinopyroxene is present in the center. In addition, surrounding acidic clasts (dark, speckly) are present. Other grains are pyroxene, biotite, quartz, feldspar, and bioclastic grains set with a calcite spar cement (interval 180-1114A-15R-1, 46–48 cm).

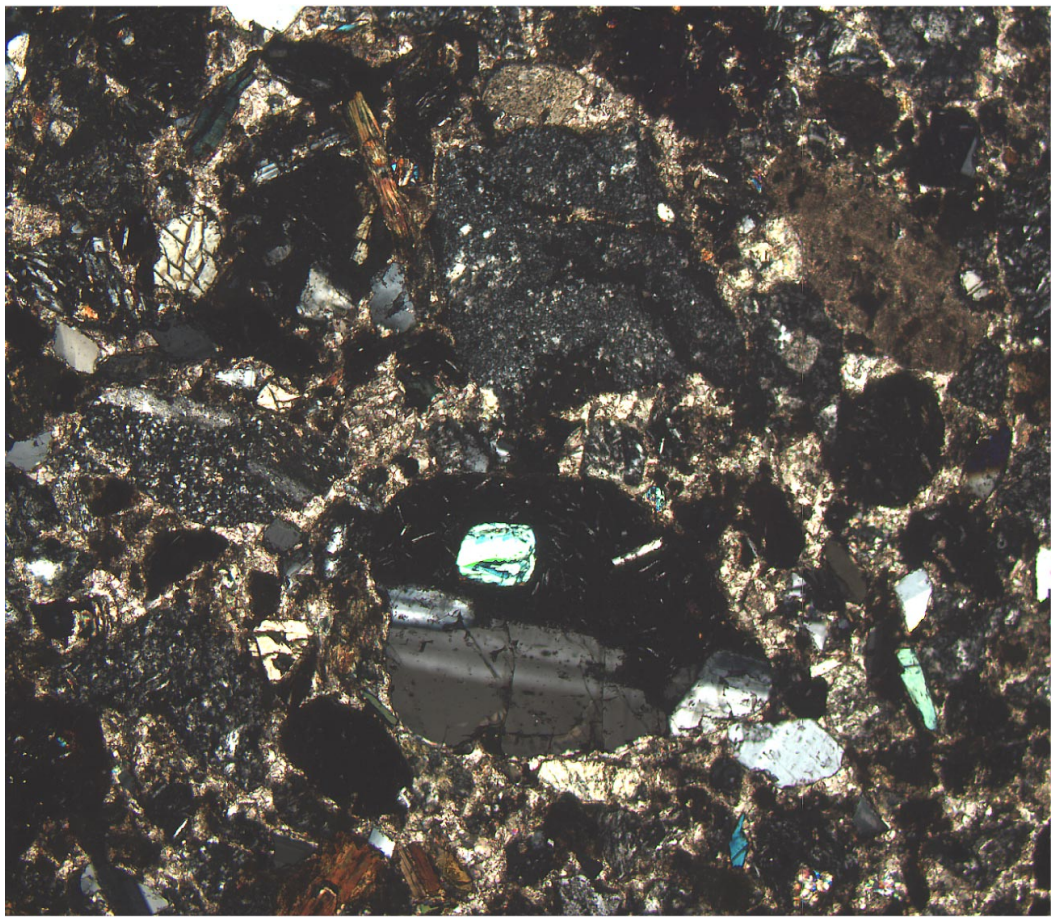

Figure F13. Digital photomicrograph (plane-polarized light) of a basalt clast with flow-banded microphenocrysts of feldspar and clinopyroxene set in a detrital volcaniclastic matrix. Dark grains are glassy basalt (interval 180-1114A-28R-CC, 3-7 cm).

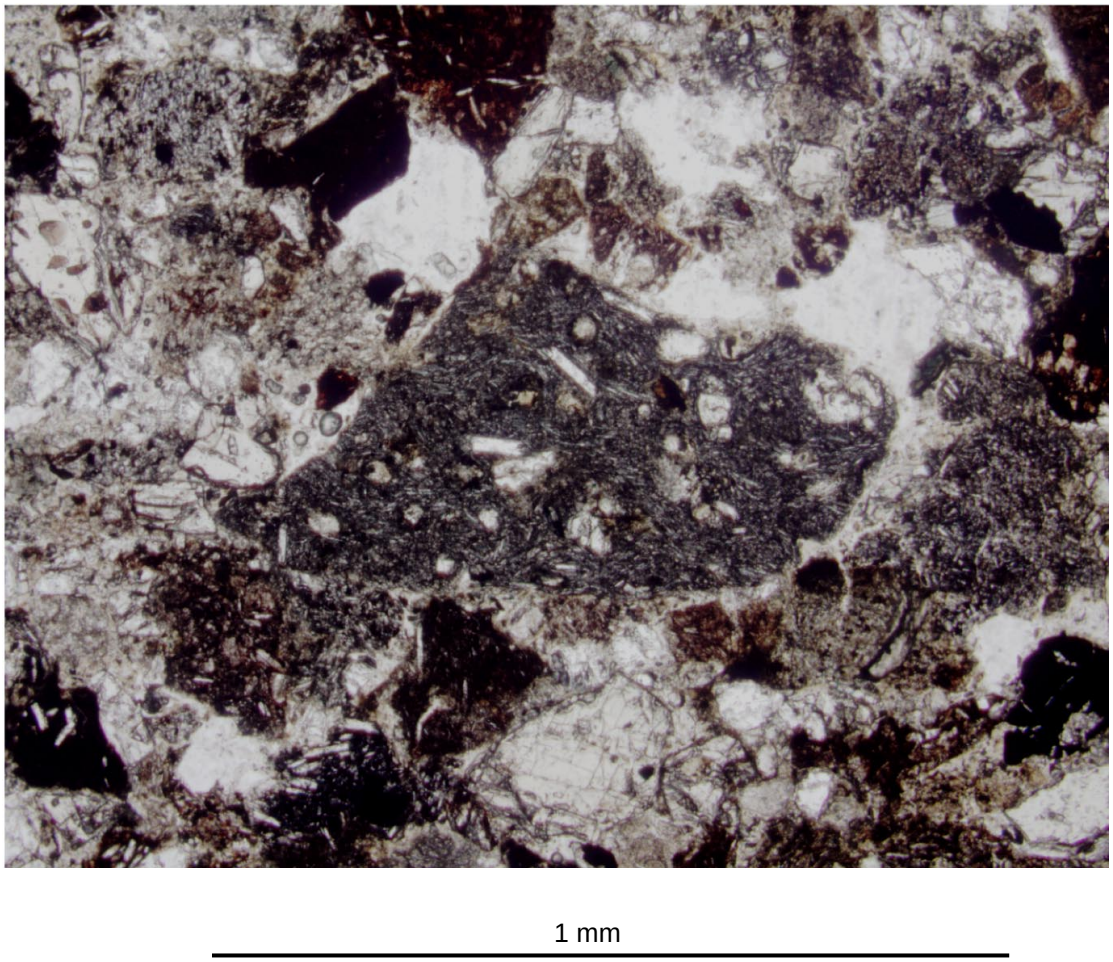

Figure F14. Highly deformed siltstone (0–53 cm). Many of the sediments in this unit have suffered such intense deformation that most of the original sedimentary structures are not preserved. Fractures are instead visible (interval 180-1114A-30R-1, 0–70 cm).

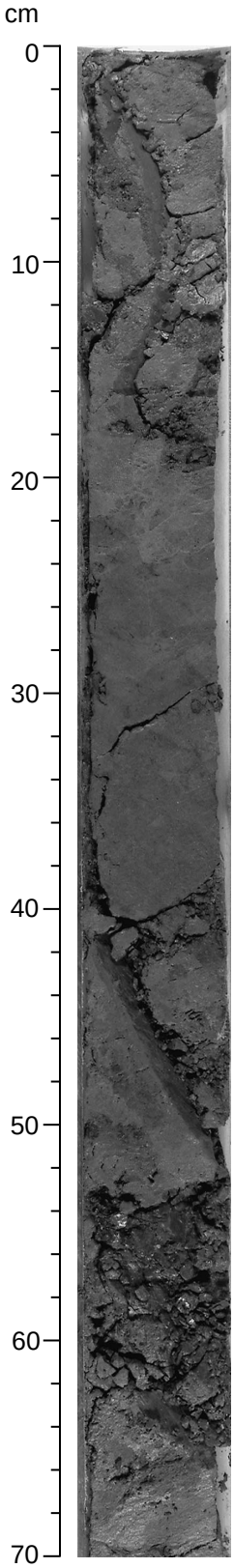

Figure F15. Digital photomicrograph (plane-polarized light) of a basaltic (dark, glassy) and andesitic (translucent, upper) lithoclasts, with microphenocrysts of plagioclase and clinopyroxene. Cement is minimal (interval 180-1114A-30R-CC,1–4 cm).

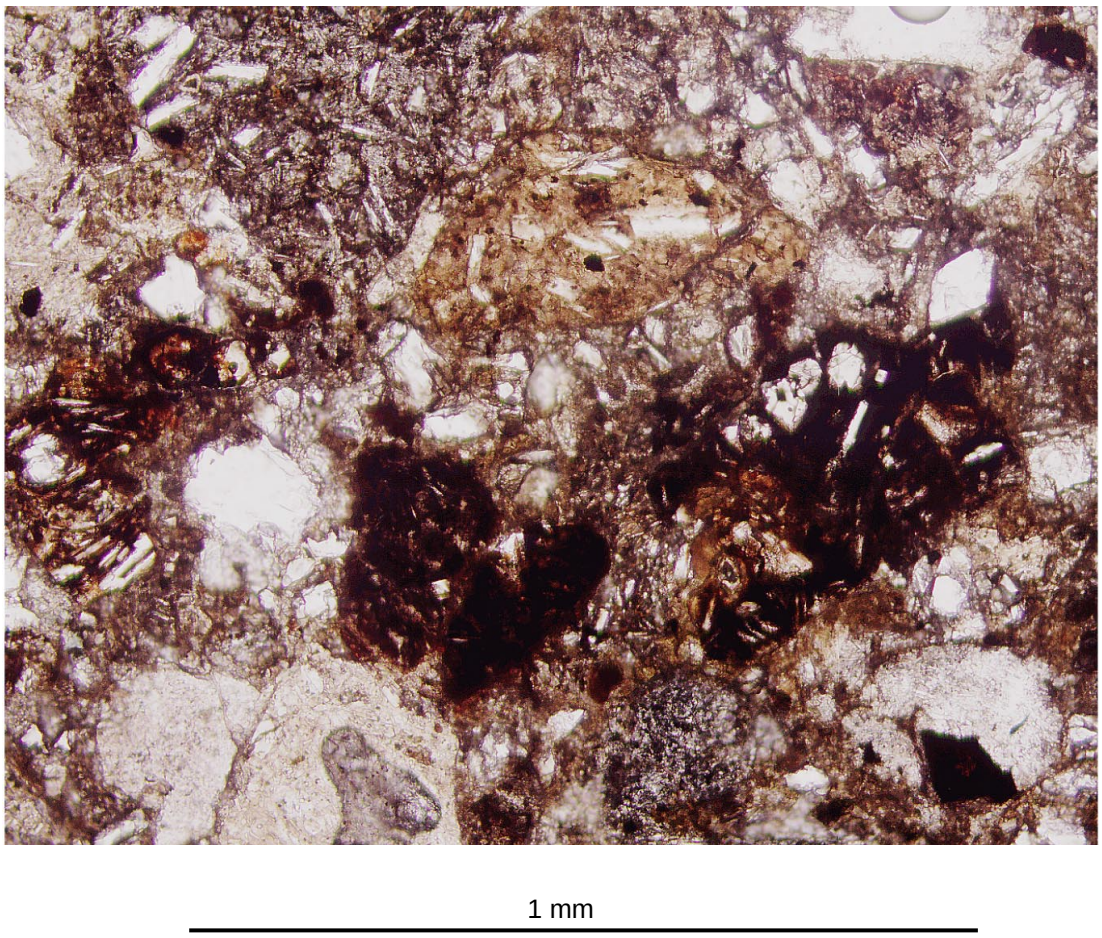

Figure F16. A. Digital photomicrograph (plane-polarized light) of a brecciated metadolerite showing a relic intergrowth of plagioclase (Plg) and clinopyroxene (Cpx) (Sample 180-1114A-35R-1, 24–27 cm). (Continued on next page.)

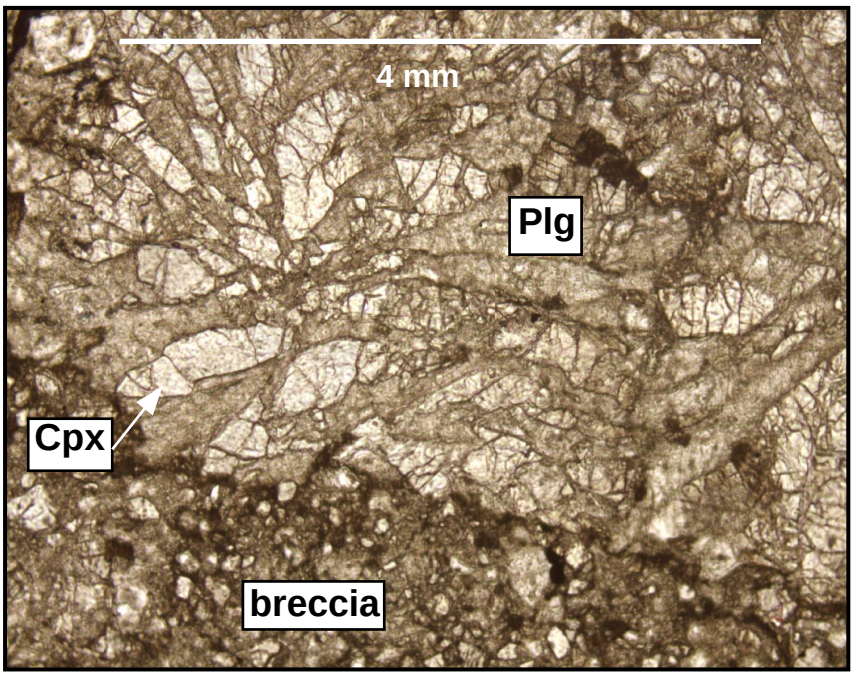

Figure F16 (continued). B. Digital photomicrograph (crossed nicols) of a relatively unaltered dolerite showing granular texture (altered plagioclase, fresh clinopyroxene, and Fe oxide are noted) (Sample 180-1114B-35R-1, 126–128 cm).

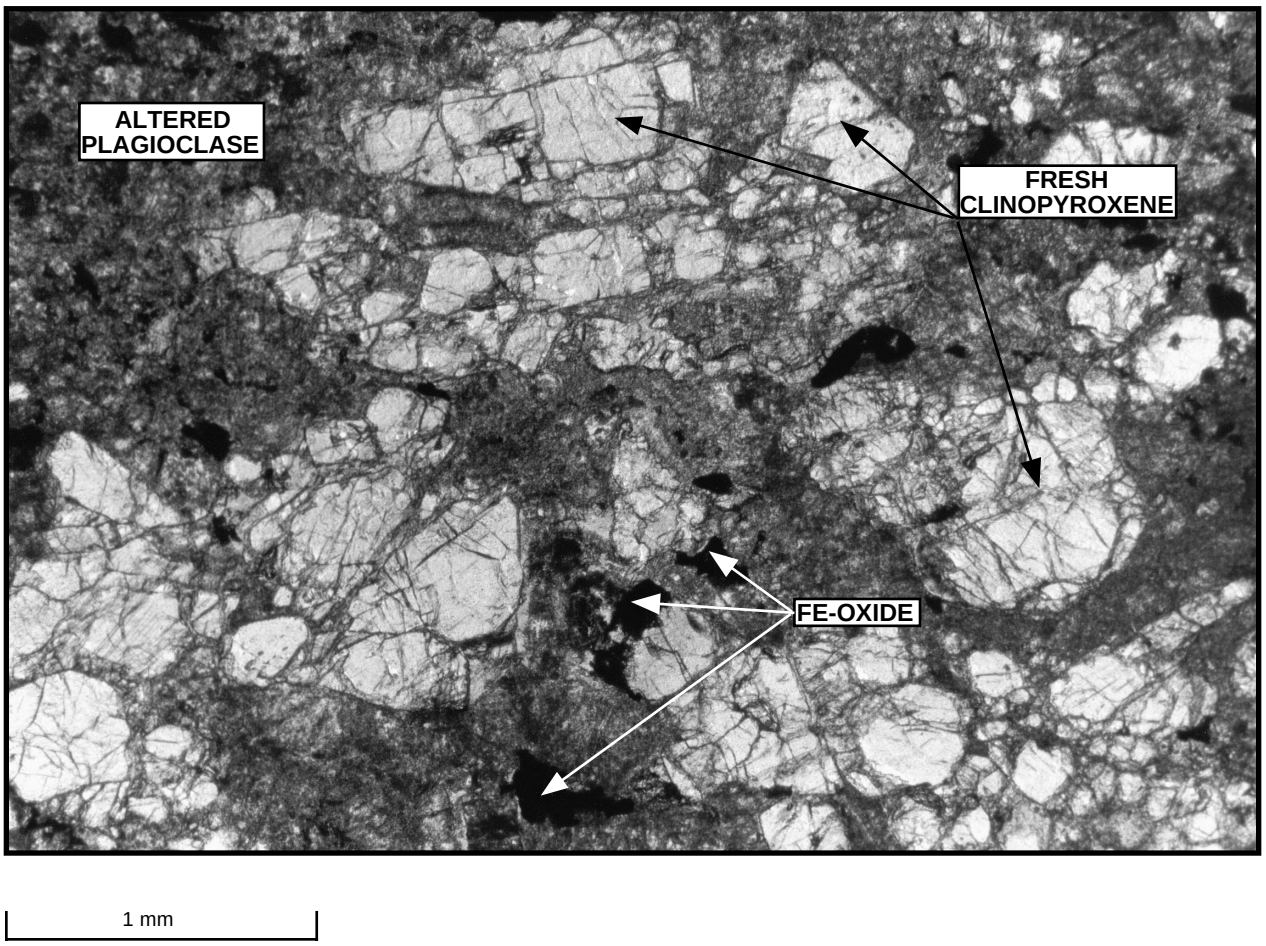

Figure F17. Hand specimen of a relatively fresh dolerite with a few thin quartz veins. This approaches the unaltered protolith of the metadolerite unit at Site 1114 (interval 180-1114A-36R-2, 1–7 cm).

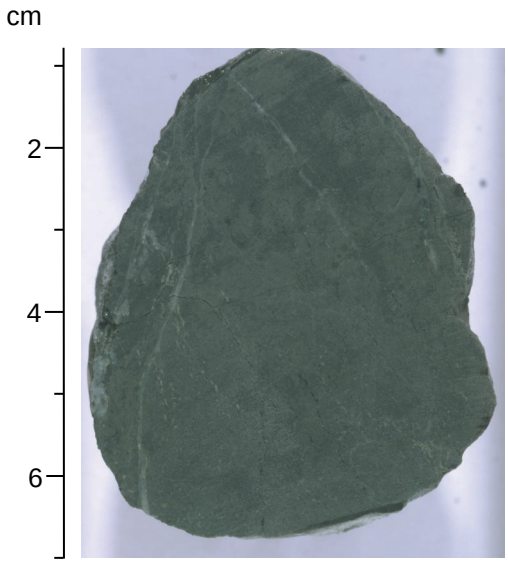

Figure F18. Digital photomicrograph (crossed nicols) of a former glassy margin within a brecciated metadolerite exhibiting a spherulitic texture (Sample 180-1114A-36R-1, 127–134 cm).

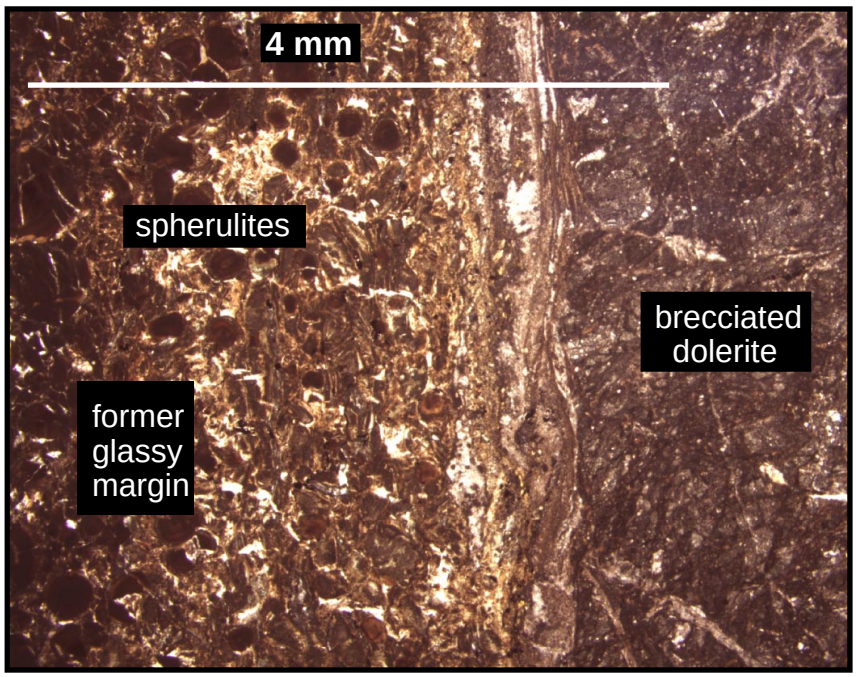

Figure F19. A. Hand specimen of metadolerite with a 1–2 cm thick quartz vein crosscut by fractures (interval 180-1114A-33R-1, 100–107 cm). (Continued on next page.)

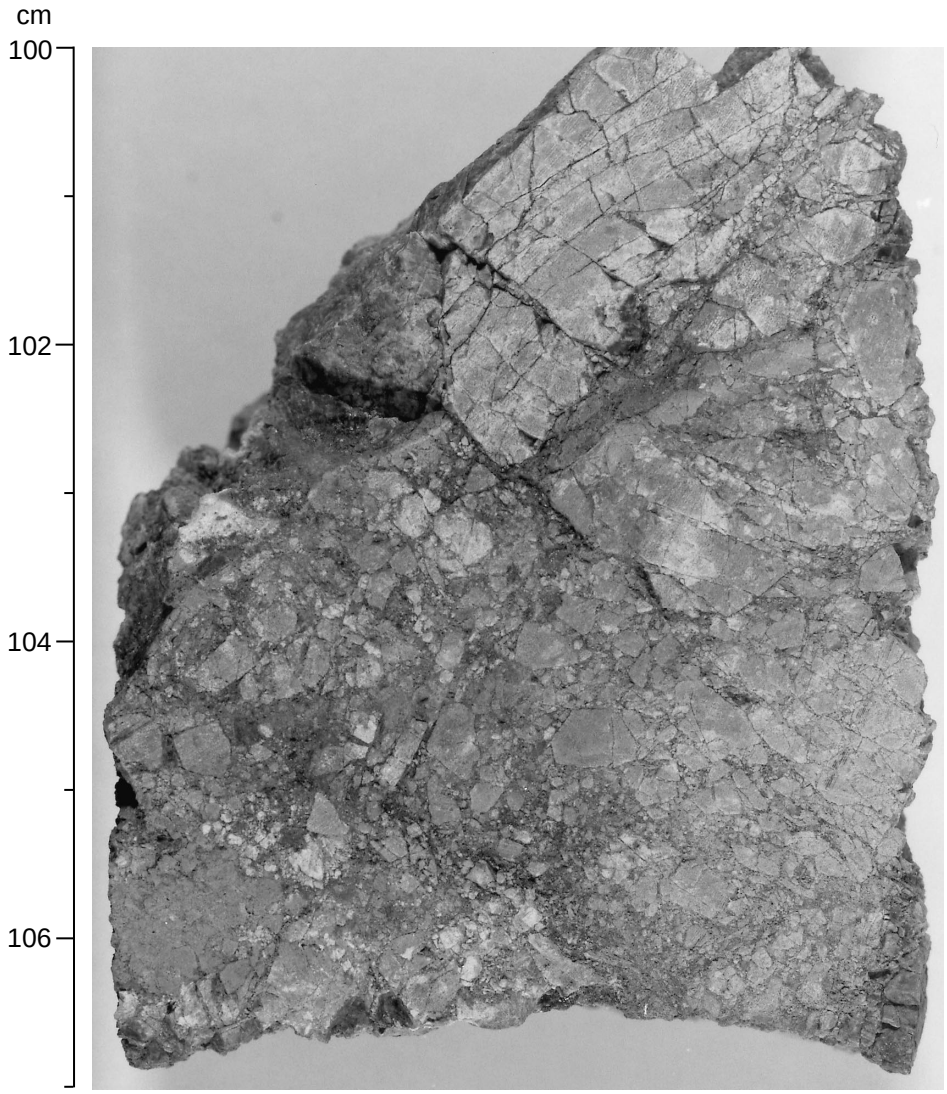

Figure F19 (continued). B. Digital photomicrograph (plane-polarized light) of brecciated metadolerite (Sample 180-1114A-33R-1, 67–69 cm) showing a subhorizontal fault crosscut by a subvertical fault. These faults (arrows) crosscut the original brecciated fabric of the rock and previous vein (vein) contemporaneous to the brecciation. Note the decreased grain size and clay matrix within the crosscutting faults. Refer to "Structural Geology," p. 20, for more details.

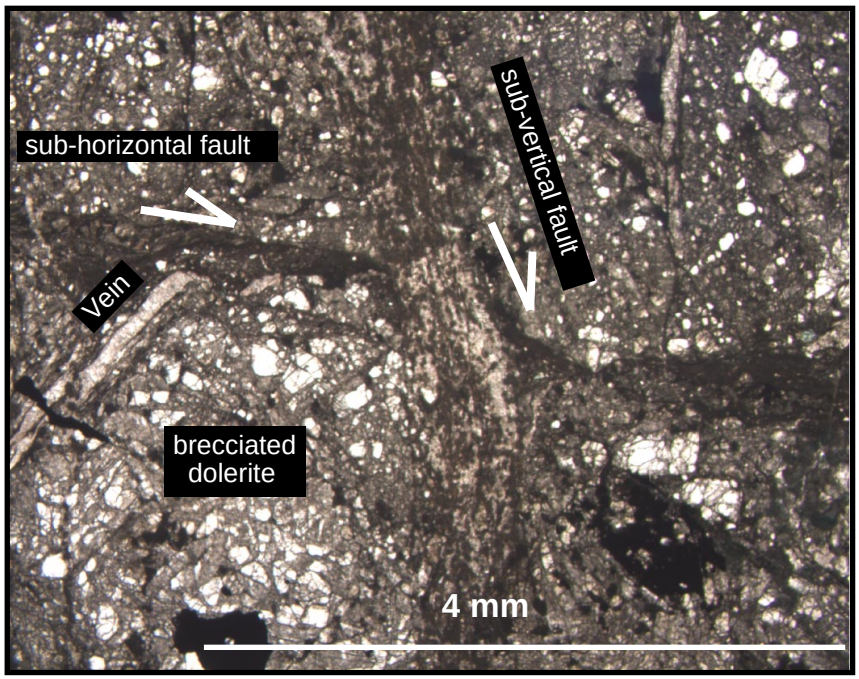

Figure F20. Digital photomicrograph (plane-polarized light) of a metadolerite showing elongated quartz grains offset by both normal and reverse faulting (arrows) crosscut by late fracture (Sample 180-1114A-33R-2, 24–26 cm). Qtz = quartz; Ep = epidote; Clay + Ep = clay and epidote.

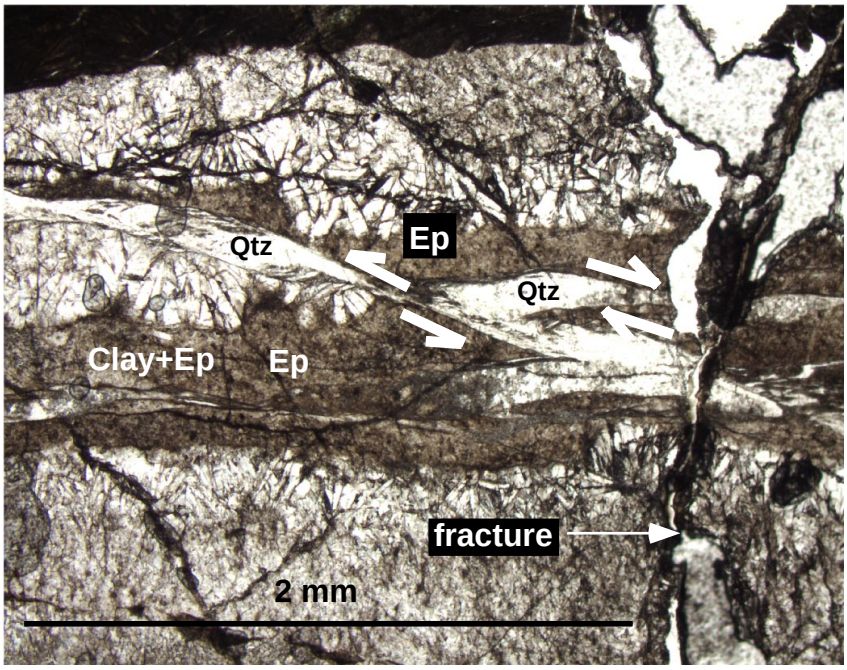

Figure F21. Summary of the main structural features observed at Site 1114.

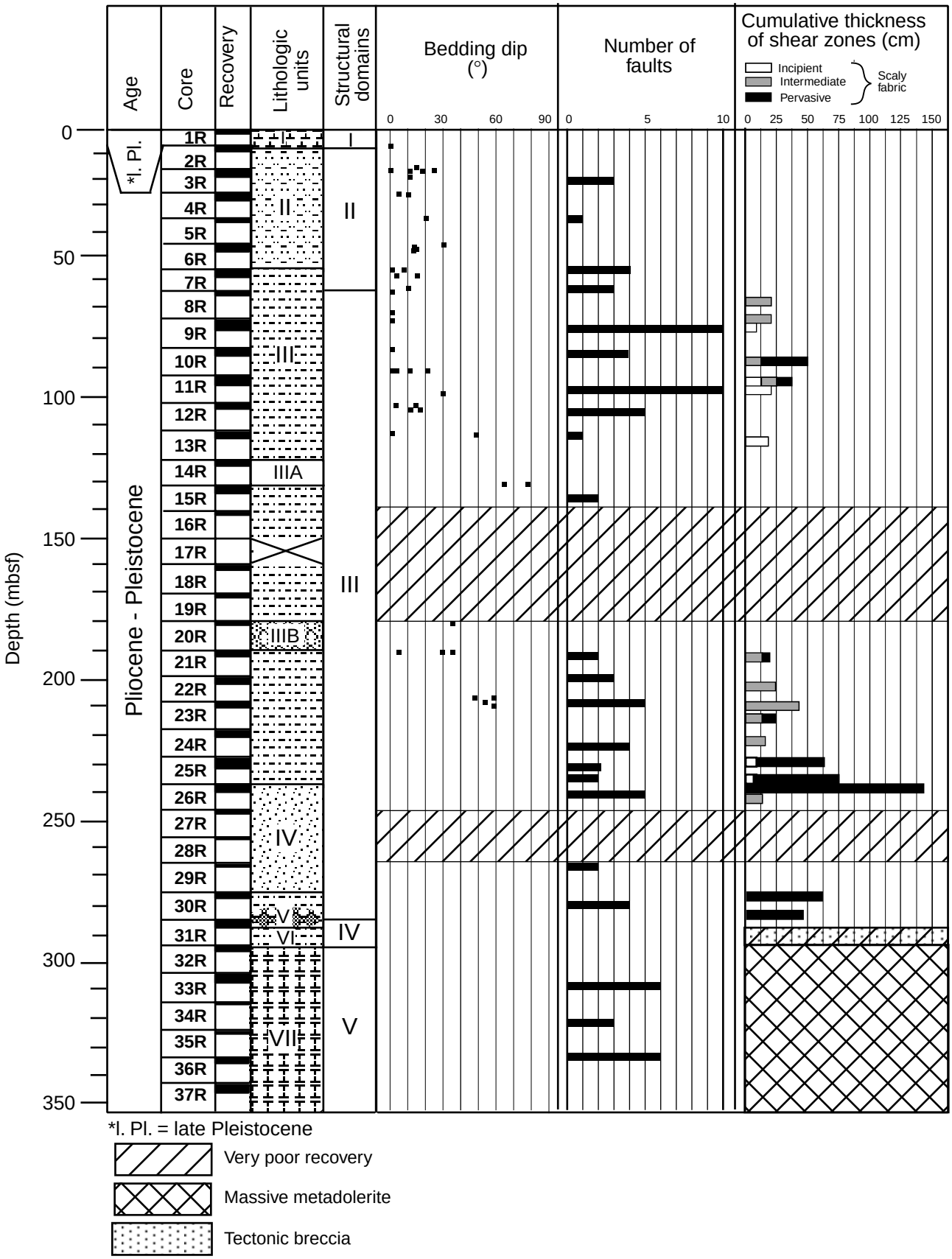

Figure F22. Bedding dips measured on cores in Domain II. N = number of measurements.

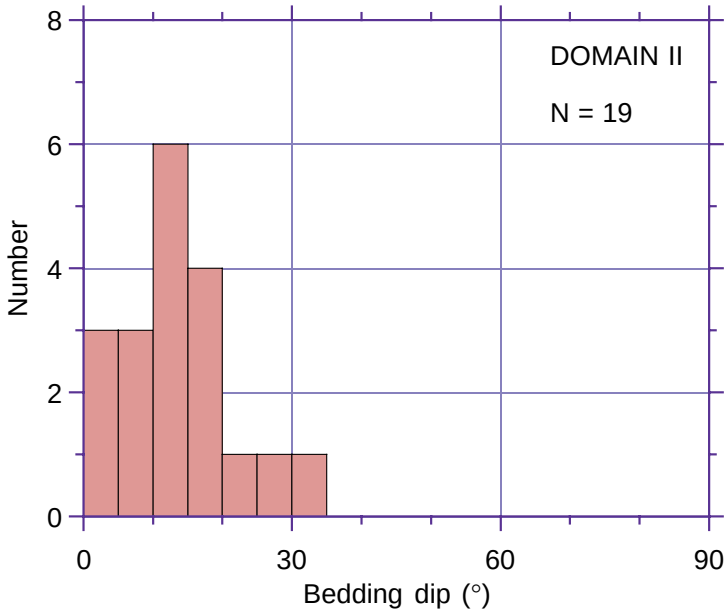

Figure F23. Bedding dips measured on cores in Domain III. N = number of measurements.

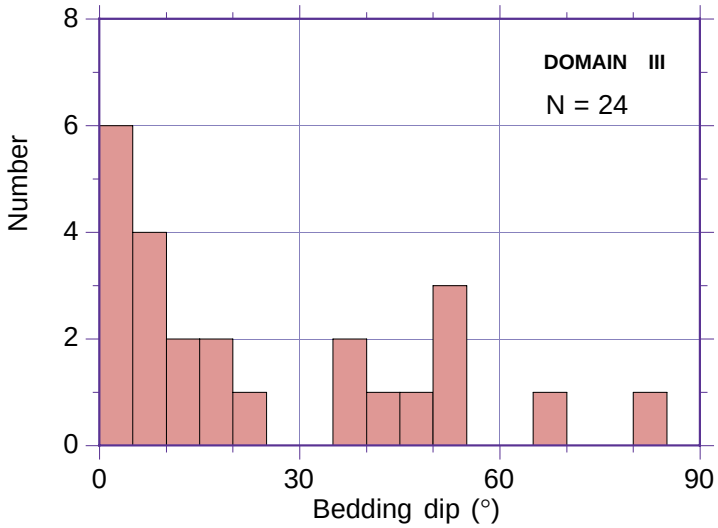

Figure F24. A. Example of steeply inclined strata in sandstones of lithostratigraphic Unit III (see **"Lithostratigraphy,"** p. 3) (interval 180-1114A-15R-1, 42–57 cm). **B.** Sketch of the interval. B_1 = bedding (strike and dip in core reference frame).

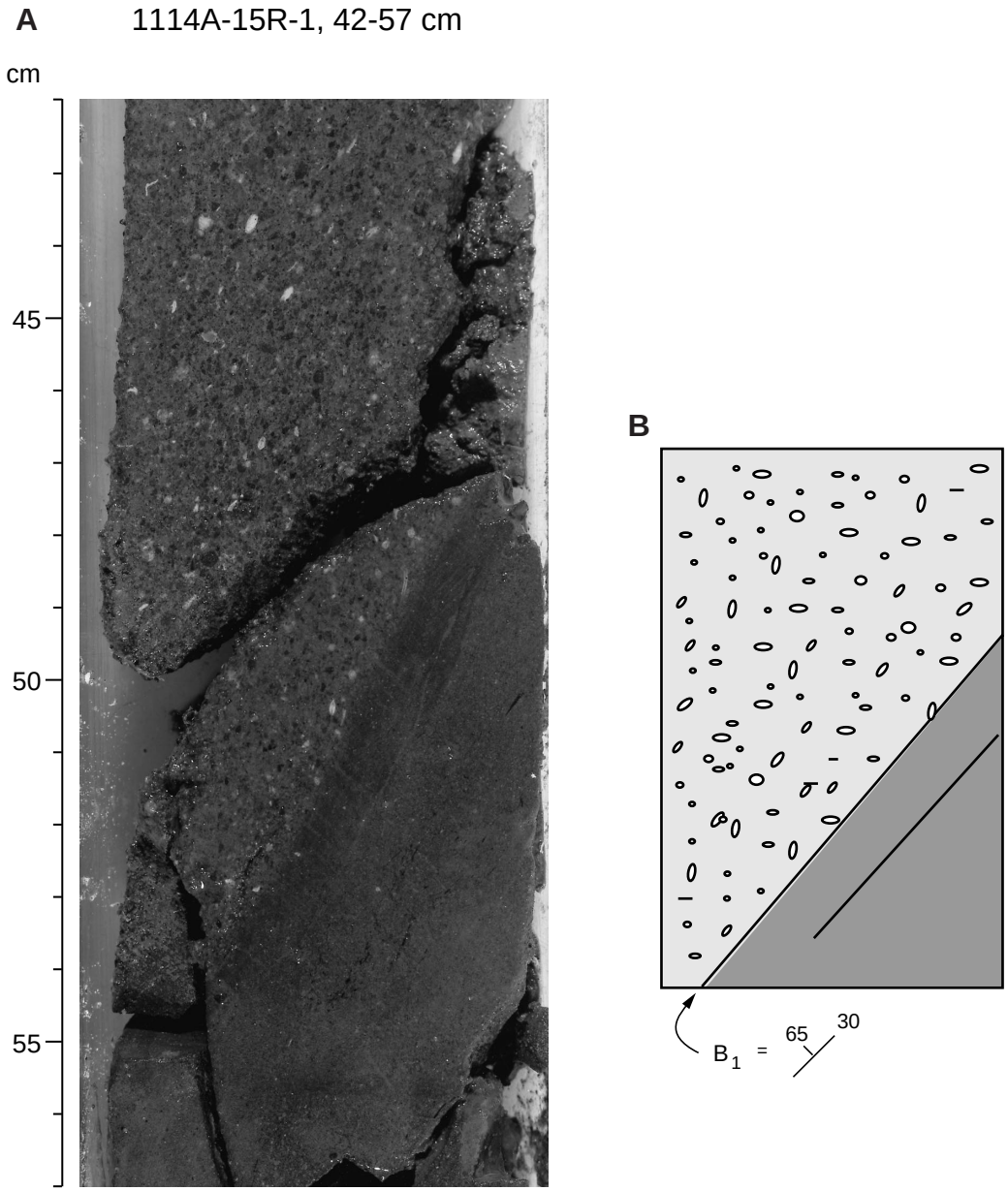

Figure F25. Dip of faults measured in the sedimentary succession of Hole 1114A. N = number of measurements.

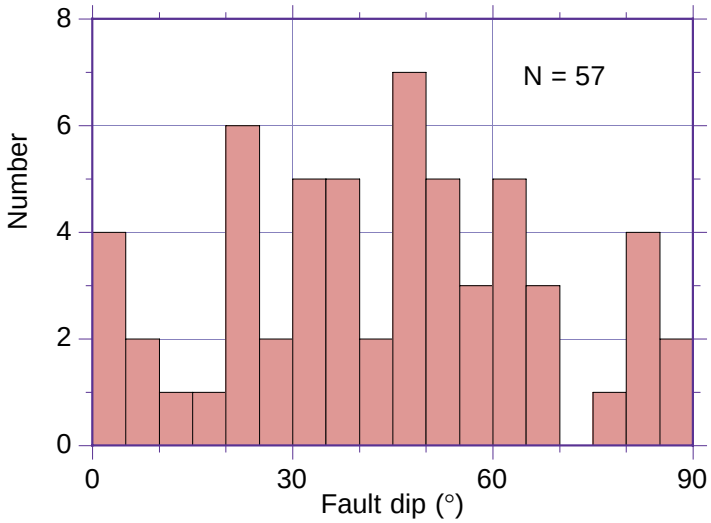

Figure F26. Examples of scaly fabric and related shallow to moderately dipping faults in clay-rich material of structural Domain III. **A.** Interval 180-1114A-9R-1, 0–80 cm (74.2 mbsf). **B.** Interval 180-1114A-11R-1, 35–70 cm, (93.5 mbsf). Orientations in core reference frame: F = fault plane; S = slickenside lineation.

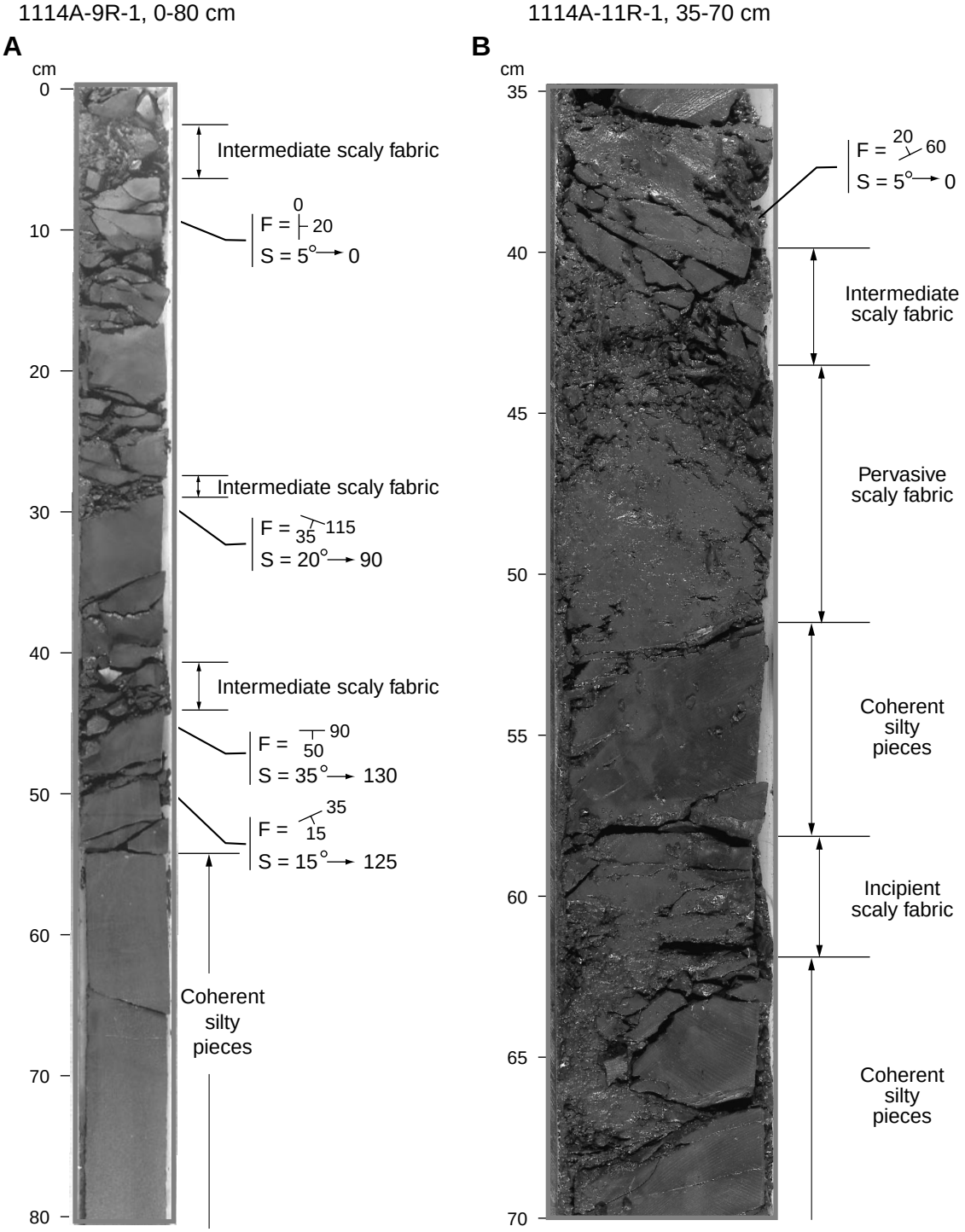

Figure F27. Fault dip vs. plunge of the corresponding slickensides in Domain III. DS = dip slip; OS = oblique slip; SS = strike slip; N = number of measurements.

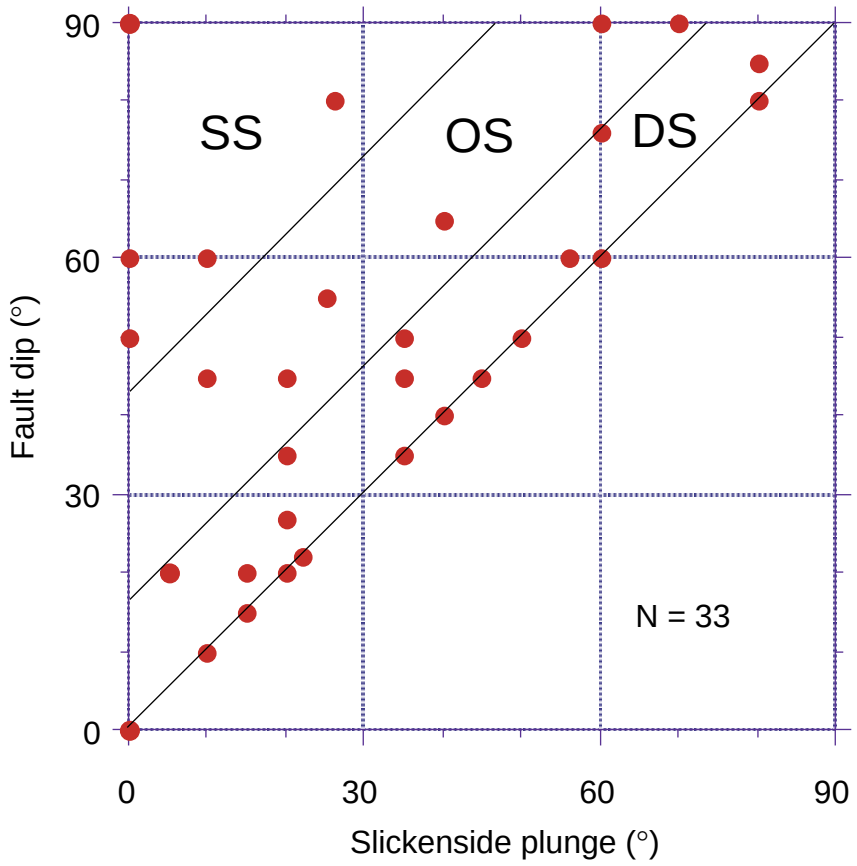

Figure F28. Array of moderately inclined reverse microfaults in litihostratigraphic Unit III sandstones in structural Domain III (interval 180-1114A-15R-1, 100–110 cm [132 mbsf]). The apparent reverse offset of an initially elongate organic-rich fragment is a few millimeters.

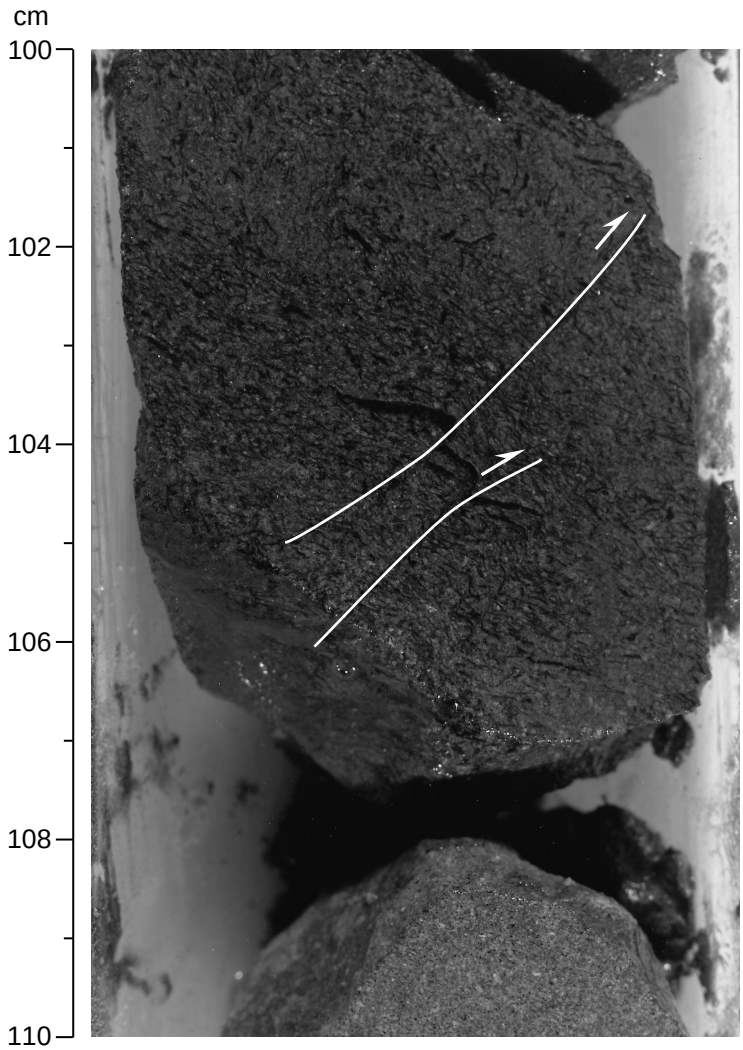

Figure F29. Association of steep conjugate faults (in sandy material) and shallow scaly-fabric bands (in clay-rich levels) consistent with an almost vertical maximum stress, oblique to the lithologic boundary. **A.** Split core (interval 180-1114A-13R-1, 60–120 cm). **B.** Sketch showing the types of deformation within this interval. σ_1 = maximum stress direction.

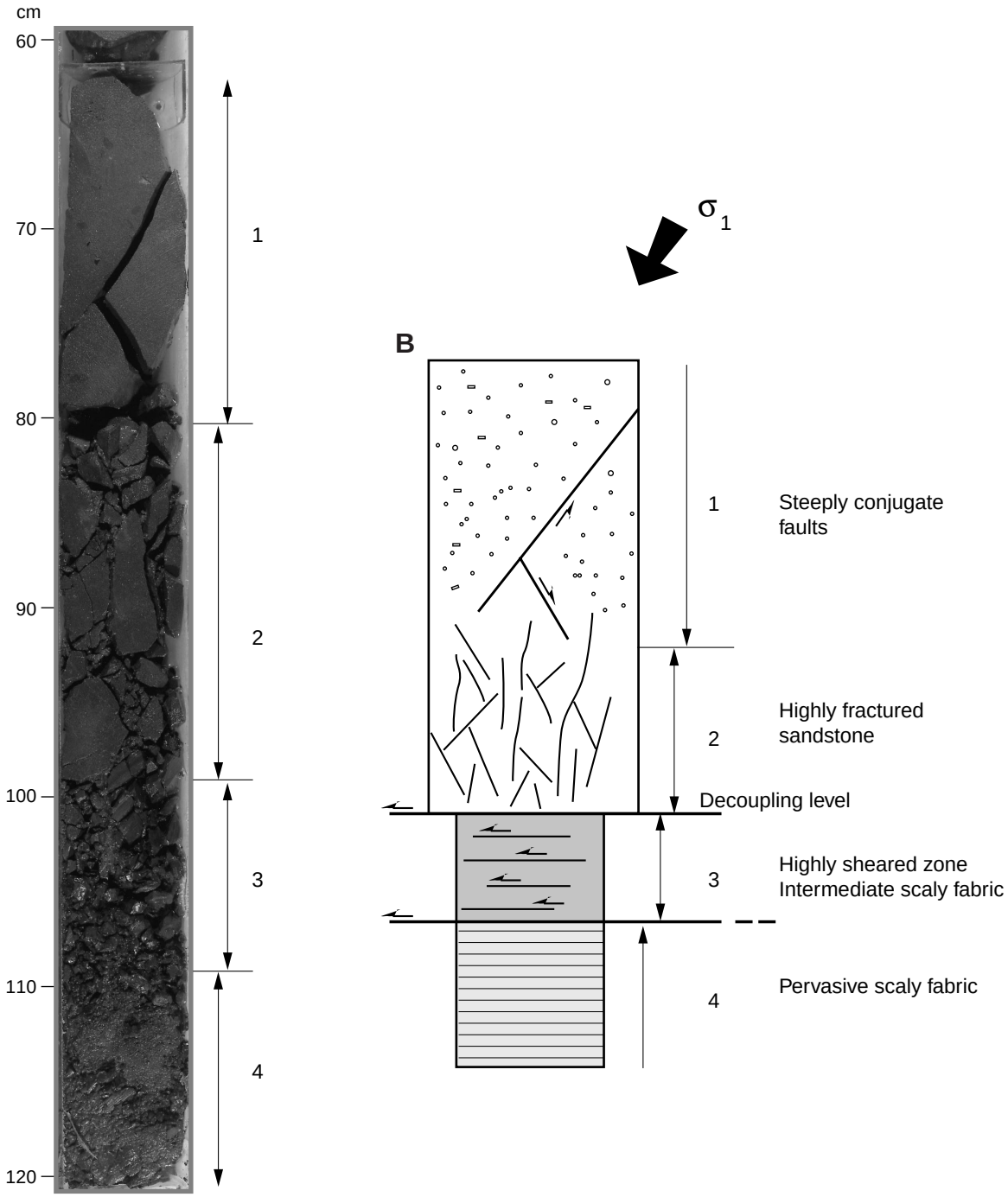

Figure F30. Digital photomicrograph (plane-polarized light; Sample 180-1114A-32R-1, 27–28 cm) of the breccia B2 (see **"Domain V: Metadolerite,"** p. 24, for definition) on top of the dolerite, showing a vein filled with quartz (Qtz) and epidote (Ep), crosscut by the breccia. Clast = altered metadolerite.

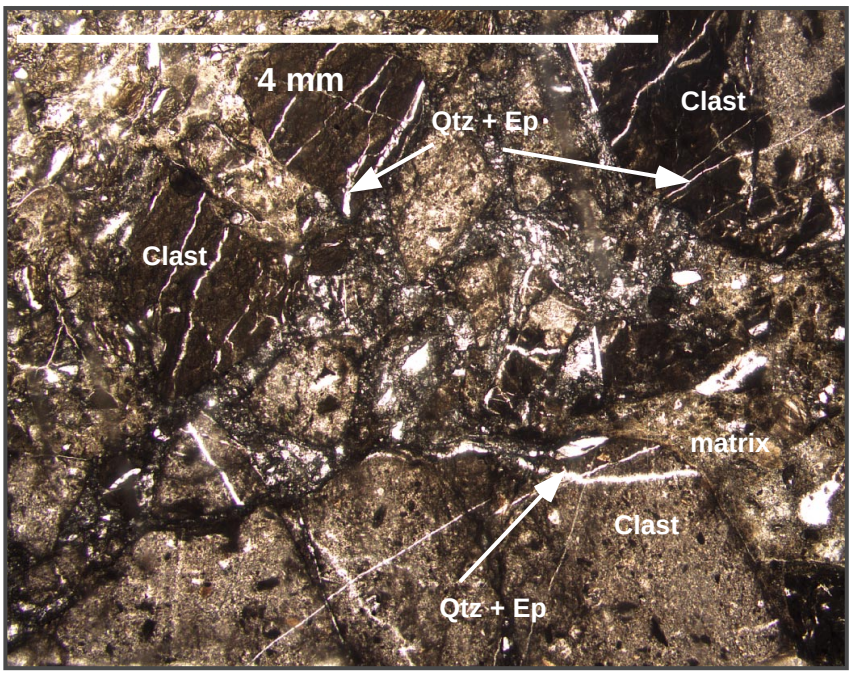

Figure F31. Digital photomicrograph (plane-polarized light) of breccia B2 (see **"Domain V: Metadolerite,"** p. 24, for definition), showing the calcite veins crosscut by a vertical fracture. Arrows show the veins filled with quartz or calcite.

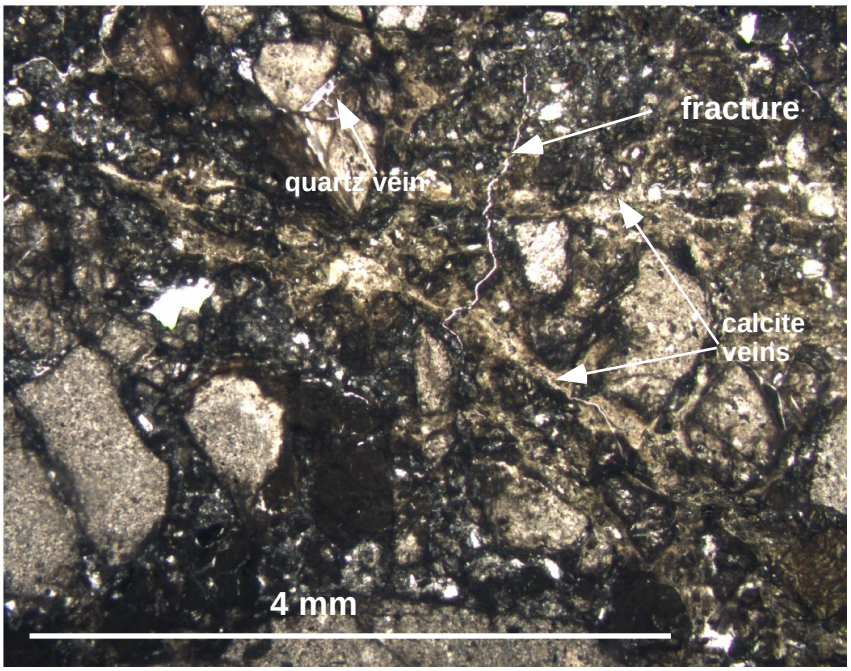

Figure F32. Digital photomicrograph (plane-polarized light) from the breccia B2 (see "Domain V: Metadolerite," p. 24, for definition) showing the calcite vein affected by shearing deformation.

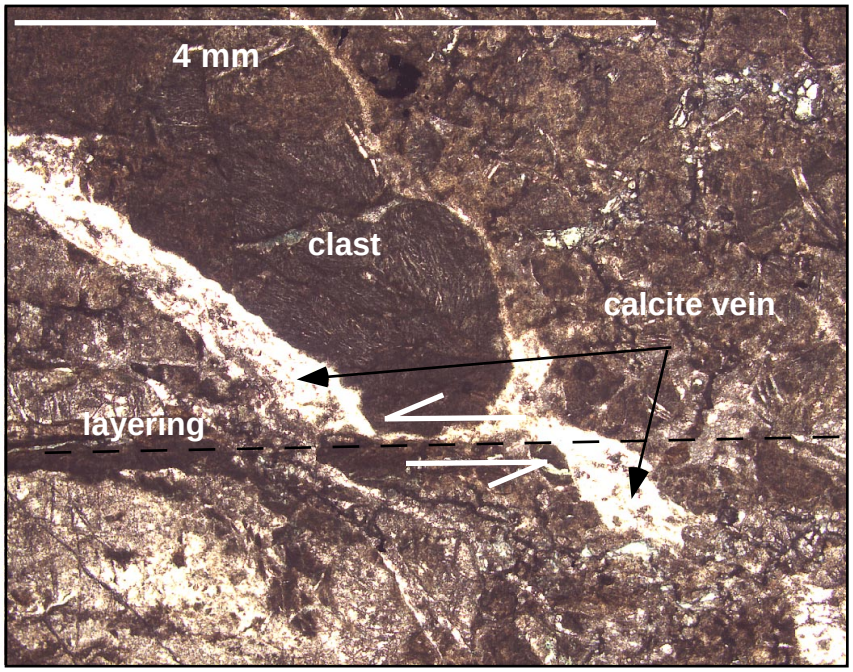

Figure F33. Digital photomicrograph (plane-polarized light; Sample 180-1114A-33R-1, 67–69 cm) of the brecciated dolerite at the bottom of the sequence, showing veins filled with quartz and epidote fragmented into the dolerite. Plg = plagioclase; Cpx = clinopyroxene.

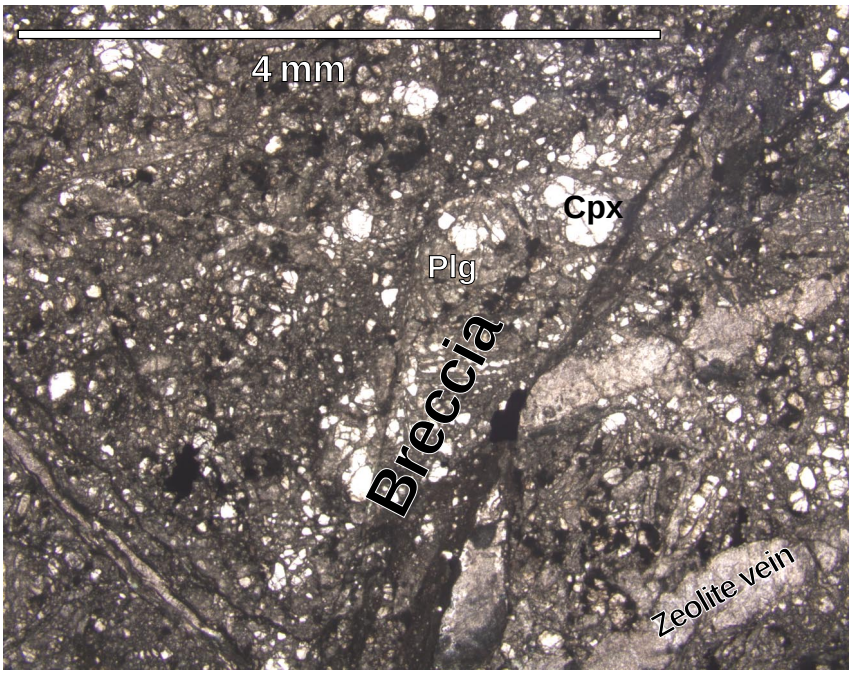

Figure F34. Hand specimen of the brecciated dolerite showing the dipping of the breccia (45°) and the quartz-epidote–rich vein fractured into the breccia (Section 180-1114A-34R-1).

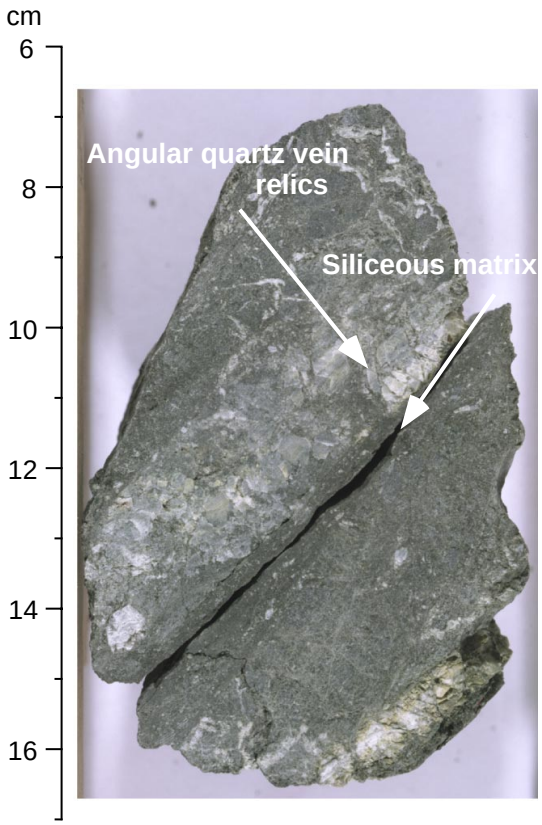

Figure F35. Hand specimen of the brecciated dolerite showing conjugate horizontal and vertical fractures (Section 180-1114A-32R-2).

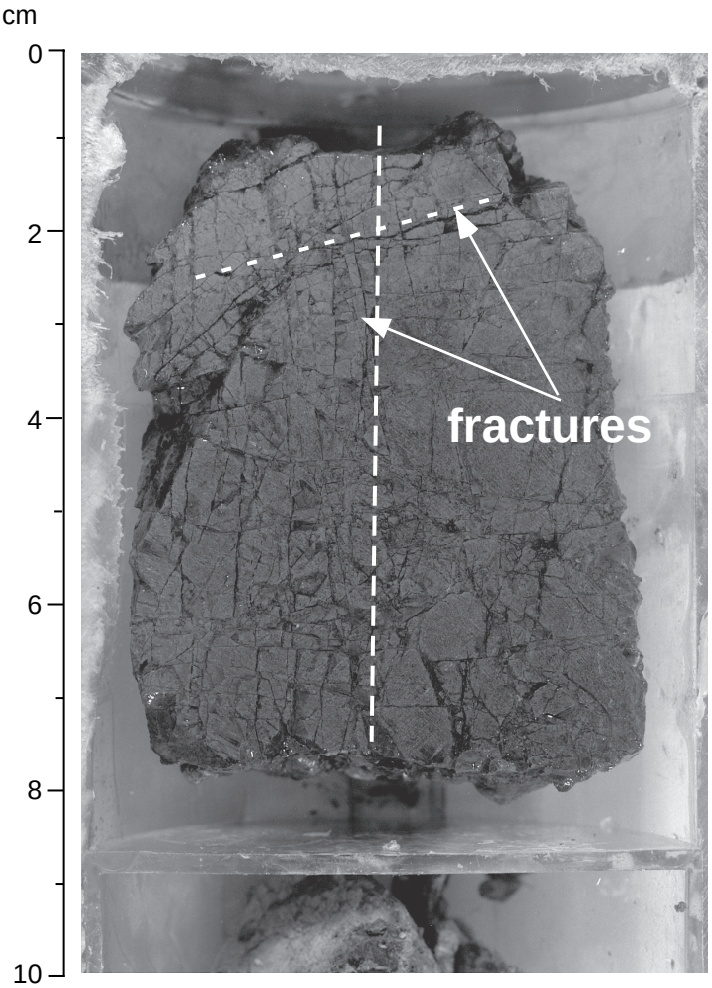

Figure F36. Schematic representation of the tectonic evolution of the dolerite breccia (stage 1, stage 2, and stage 3). B1 = breccia 1; B2 = breccia 2 (shaded area) on top of the brecciated metadolerite; V1 = vein 1; V2 = vein 2.

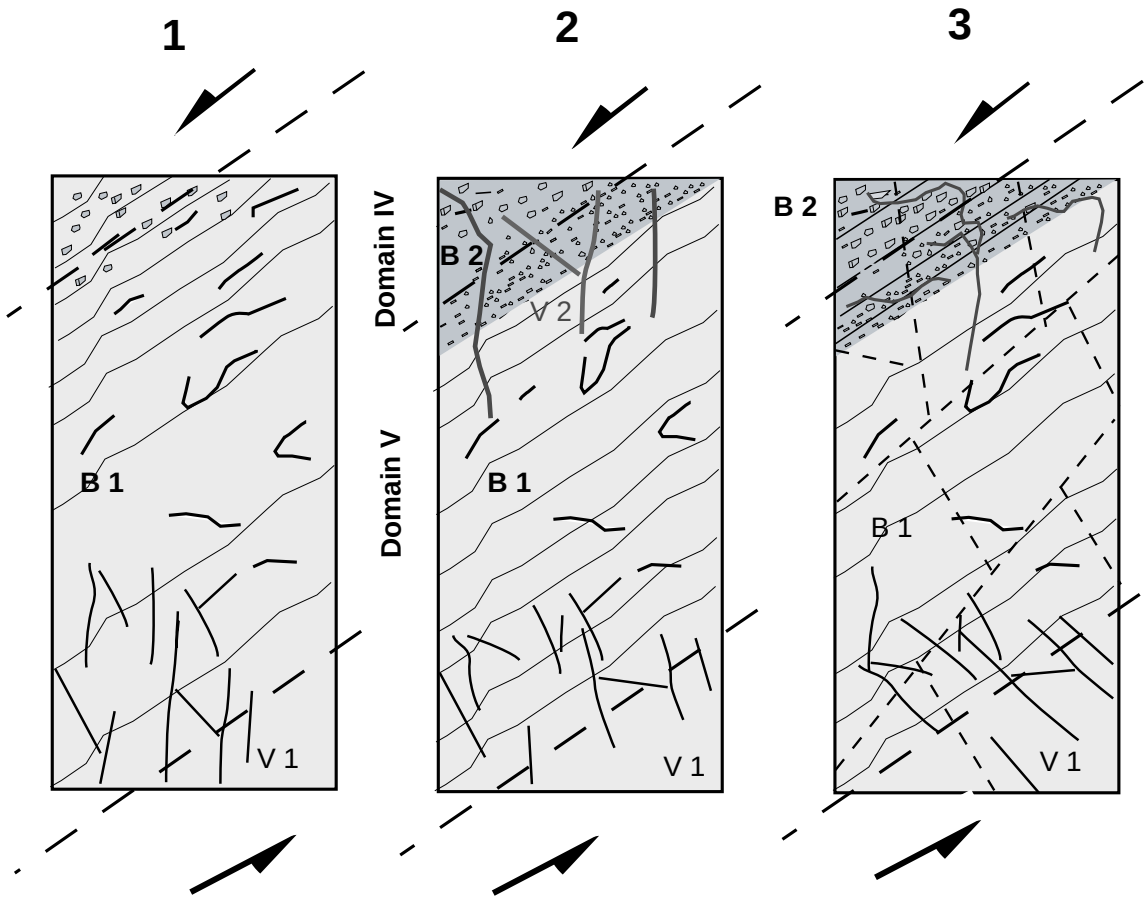

Figure F37. Geometry of structures identified at Site 1114 from core observations and FMS images. **A.** Schematic structural log of Hole 1114A. Bedding dip attitudes along the uppermost part of the log (between 0 and 100 mbsf) are deduced from core measurements and seismic reflection. S = south; N = north. **B.** Map view of the bedding and fault patterns at shallow level (~100–120 mbsf). Only two examples of northeast-dipping faults are documented. **C.** Map view of the bedding and fault patterns at greater depth (~180–220 mbsf). F = trace of faults; B = strike of bedding. The mutual angular relationships between the different types of structures are correct, but their location is only indicative. Note that at shallow level the dip of the fault decreases, whereas both faults and beds have suffered an anticlockwise rotation of ~20°–30° with respect to the deeper structures.

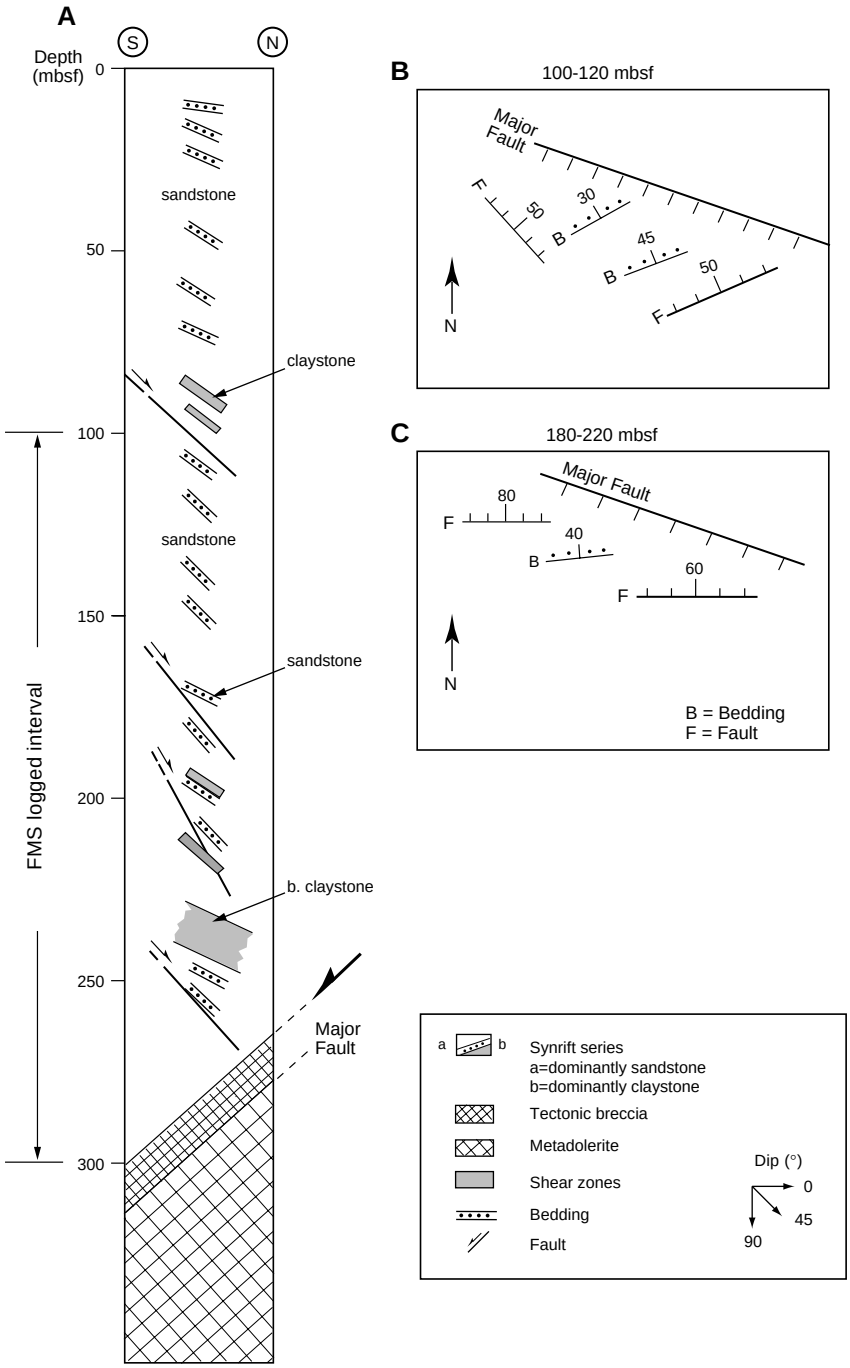

Figure F38. Biostratigraphic units and ages for Hole 1114A. Dashed lines indicate that the true zonal boundary may lie above or below the indicated level.

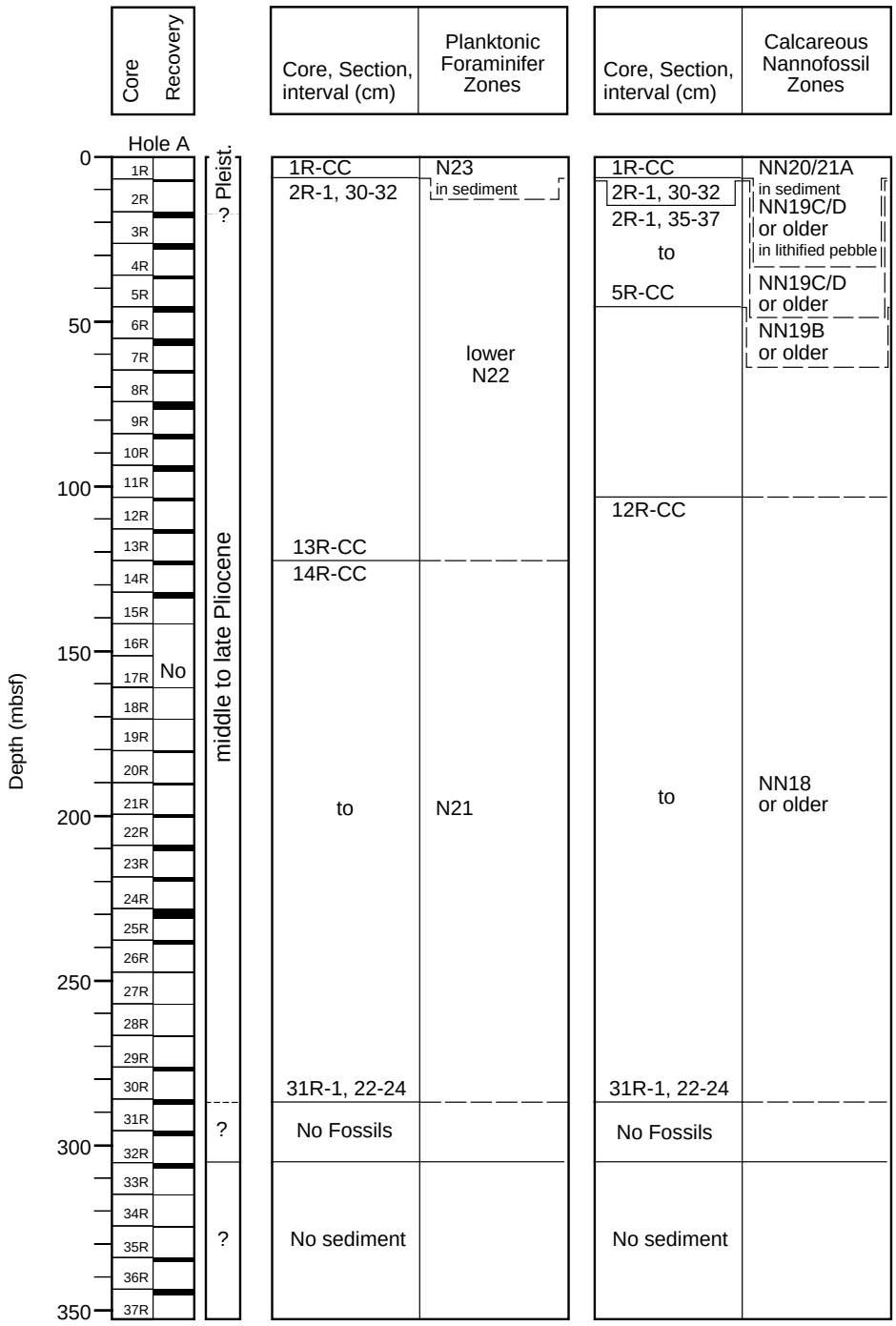

Figure F39. Age-depth relationship at Site 1114, based on nannofossil (square) and planktonic foraminifer (circle) datum events.

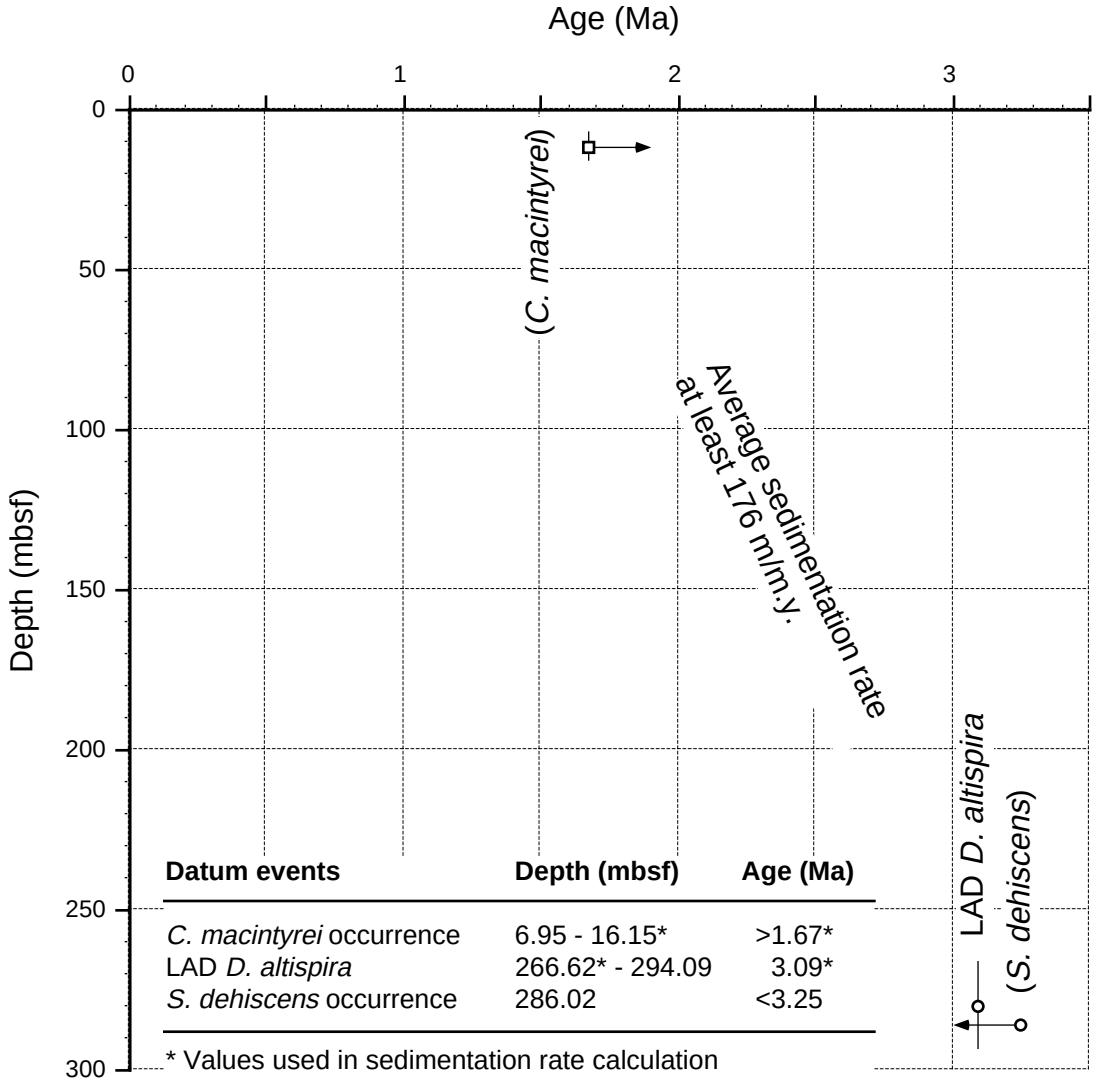

Datum events	Depth (mbsf)	Age (Ma)
C. macintyrei occurrence	6.95 - 16.15*	>1.67*
LAD *D. altispira*	266.62* - 294.09	3.09*
S. dehiscens occurrence	286.02	<3.25

* Values used in sedimentation rate calculation

Figure F40. Susceptibility data (uncorrected for volume) from MST and AMST measurements, Site 1114.

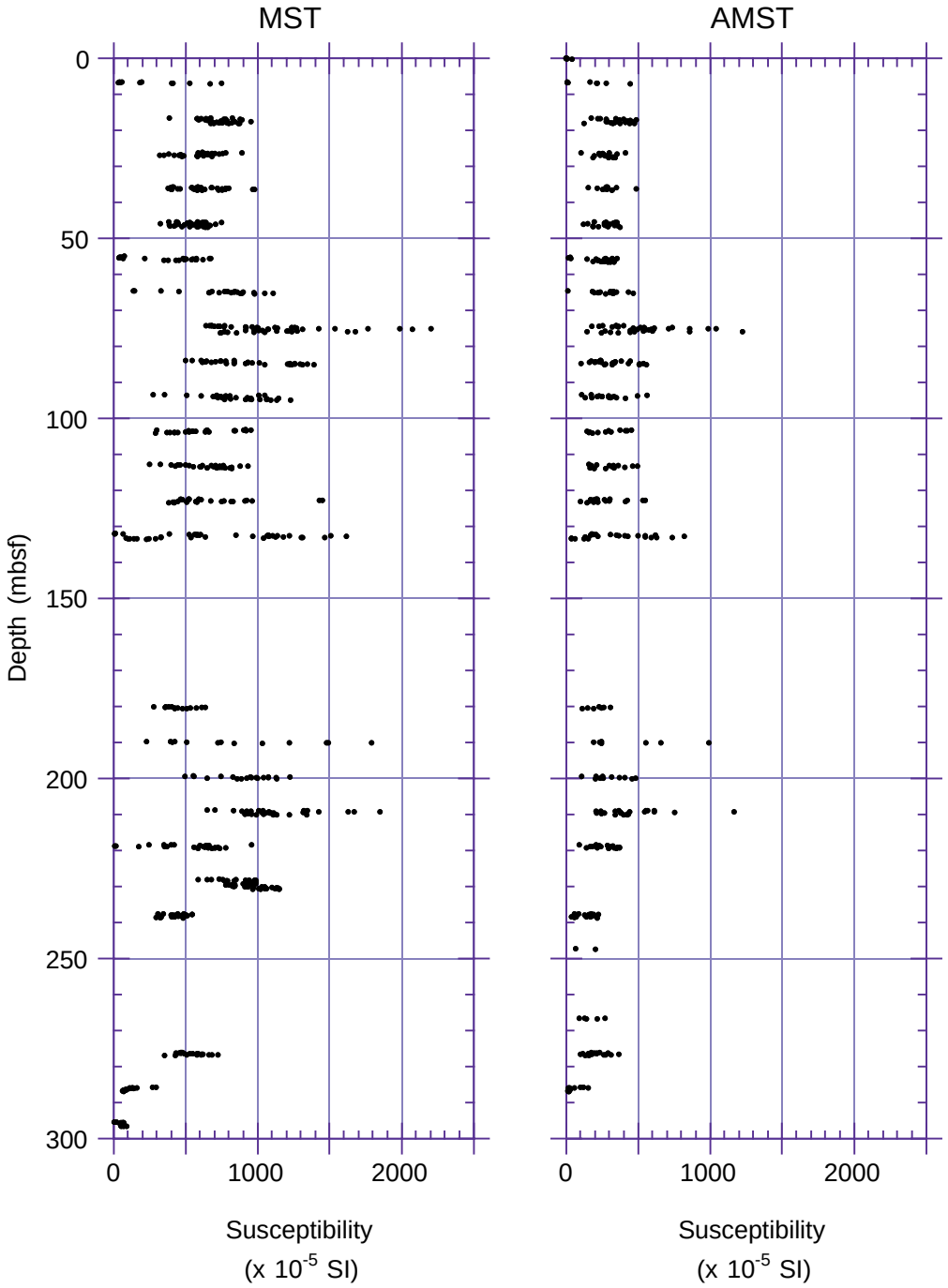

Figure F41. Susceptibility and its anisotropy (AMS) data from discrete sample measurements, Site 1114. Degree of anisotropy (P_j) and shape parameter (T) calculated according to Jelinek (1981). K_{max} and K_{min} are the maximum and minimum axes, respectively, of the susceptibility ellipsoid and are shown corrected for bedding tilt as filled circles and squares; uncorrected data are shown as open circles and squares.

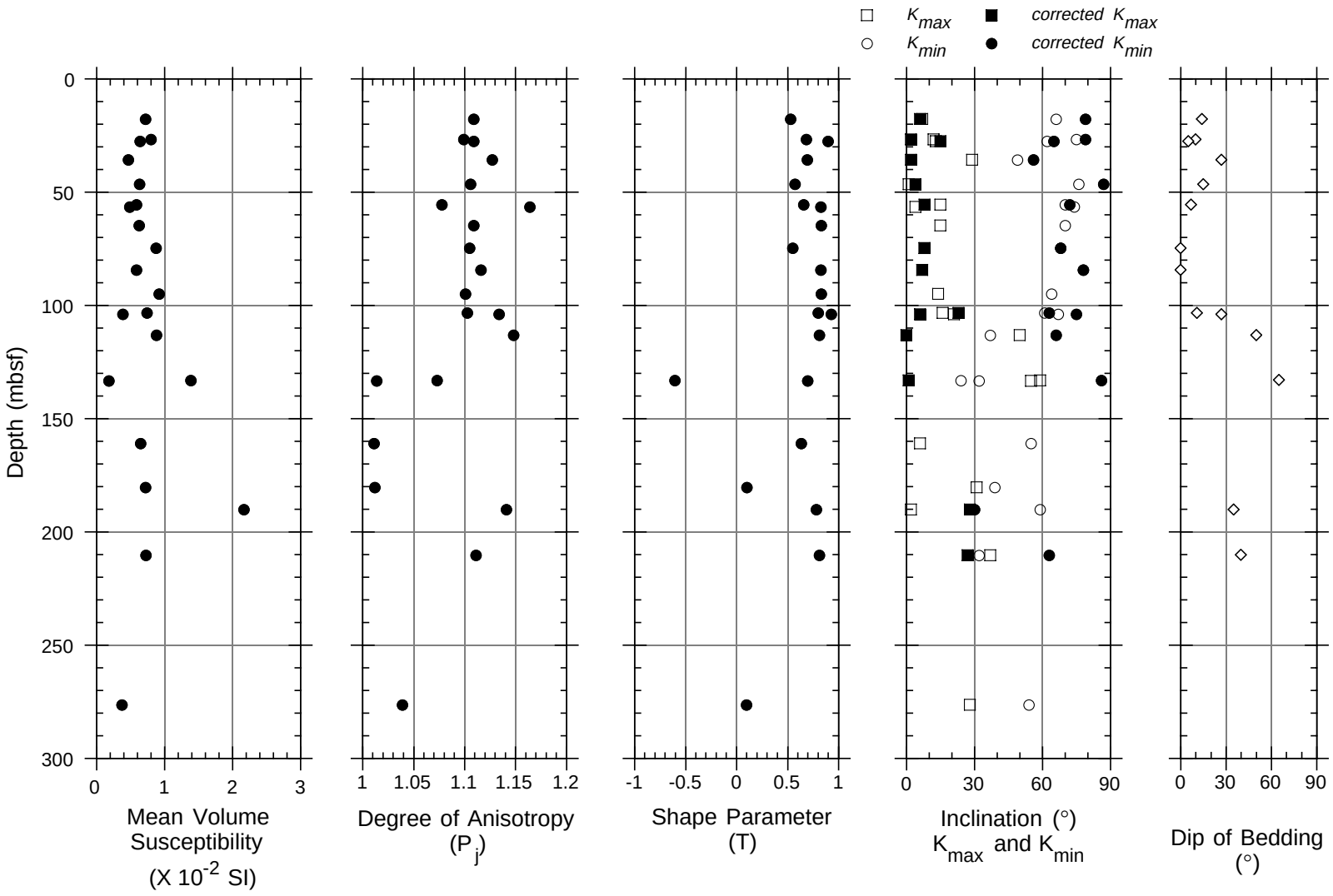

Figure F42. Demagnetization behavior of discrete samples from working halves of core sections, Site 1114. Vector plots: horizontal component = filled circles, vertical component = open circles. Stereonet plots: lower hemisphere = filled circles, upper hemisphere = open circles. **A.** Sample 180-1114A-12R-1, 77–79 cm. **B.** Sample 180-1114A-23R-CC, 7–9 cm. **C.** Sample 180-1114A-3R-2, 52–54 cm. **D.** Sample 180-1114A-13R-1, 49–51 cm. NRM = natural remanent magnetization; Div. = division; Jo = NRM intensity.

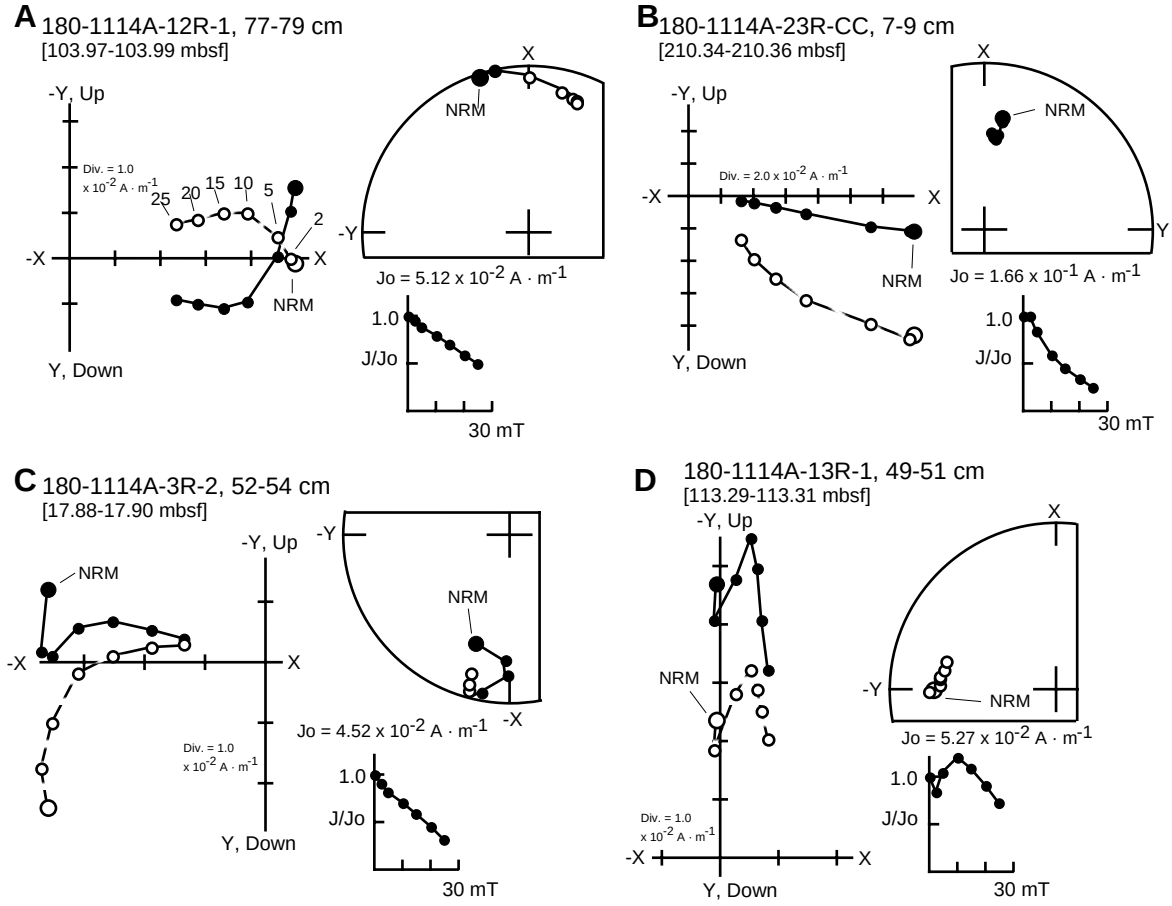

Figure F43. Downhole plots of declination, inclination, and intensity. Data from long cores of Hole 1114A after AF demagnetization at 25 mT shown as filled circles; data from discrete samples after AF demagnetization at 25 mT shown as open squares.

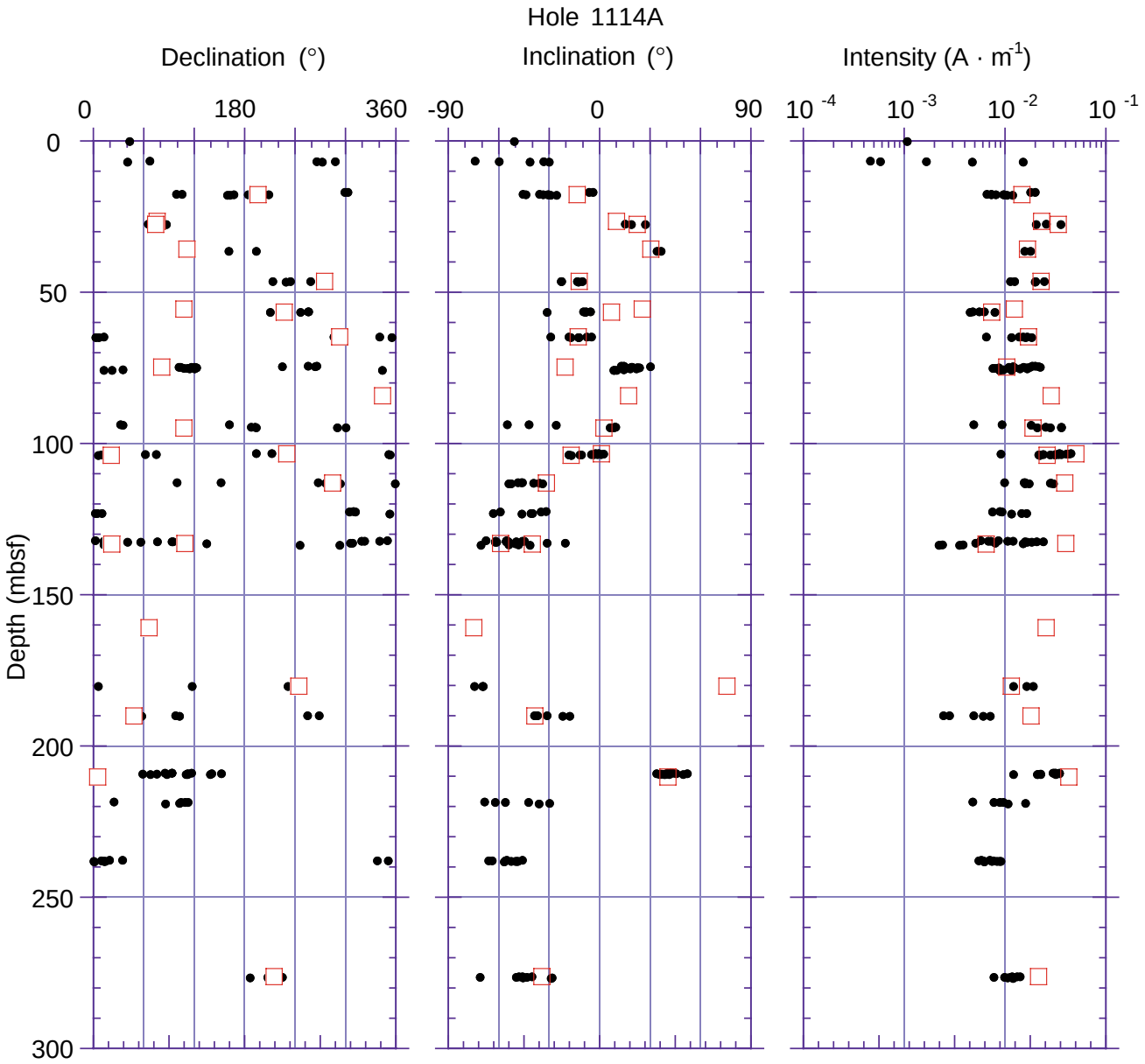

Figure F44. $CaCO_3$, organic carbon, and C/N ratio profiles, Site 1114.

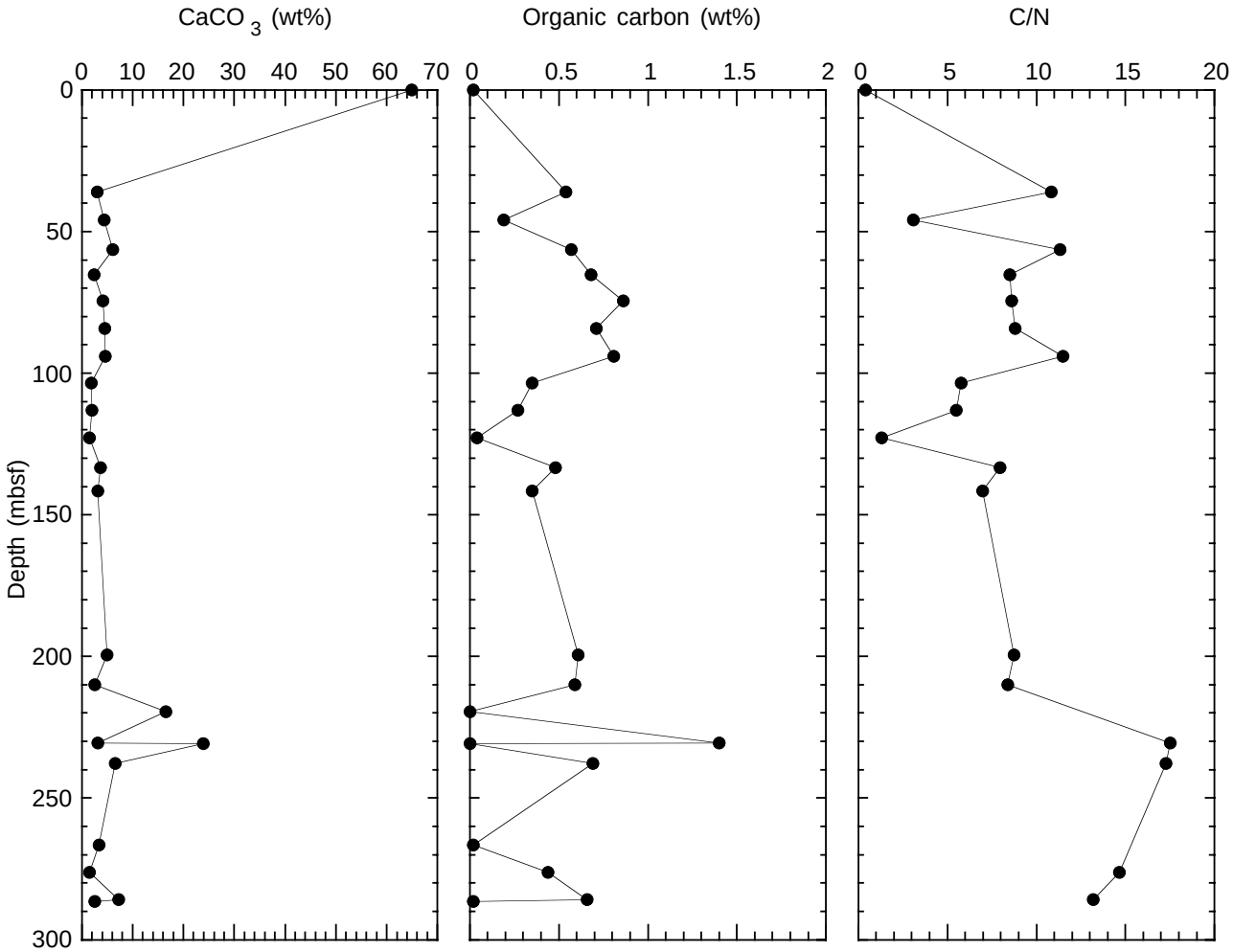

Figure F45. Site 1114 bulk density derived from GRAPE and index properties measurements.

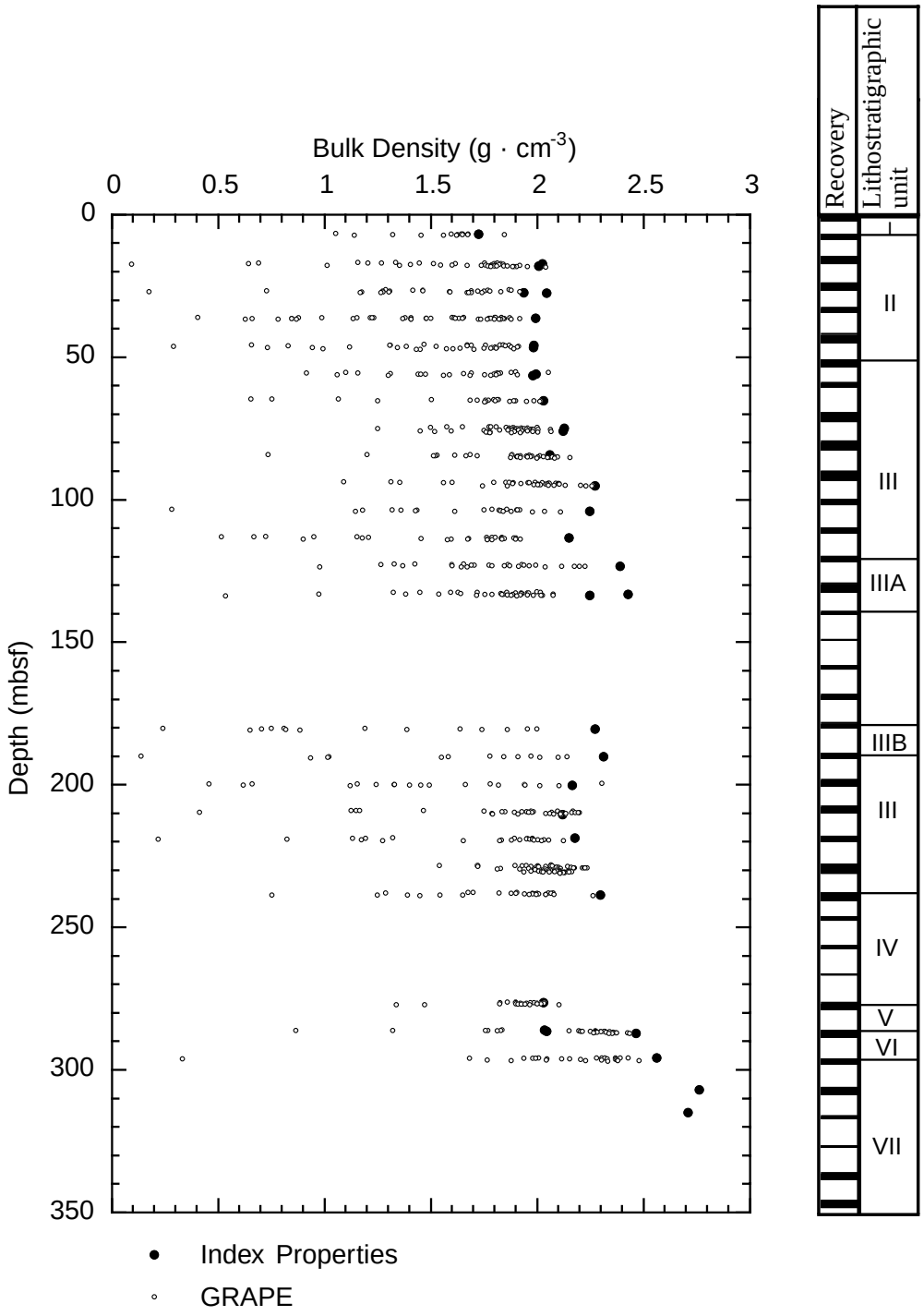

Figure F46. Site 1114 profiles of (**A**) discrete bulk density, (**B**) grain density, and (**C**) porosity.

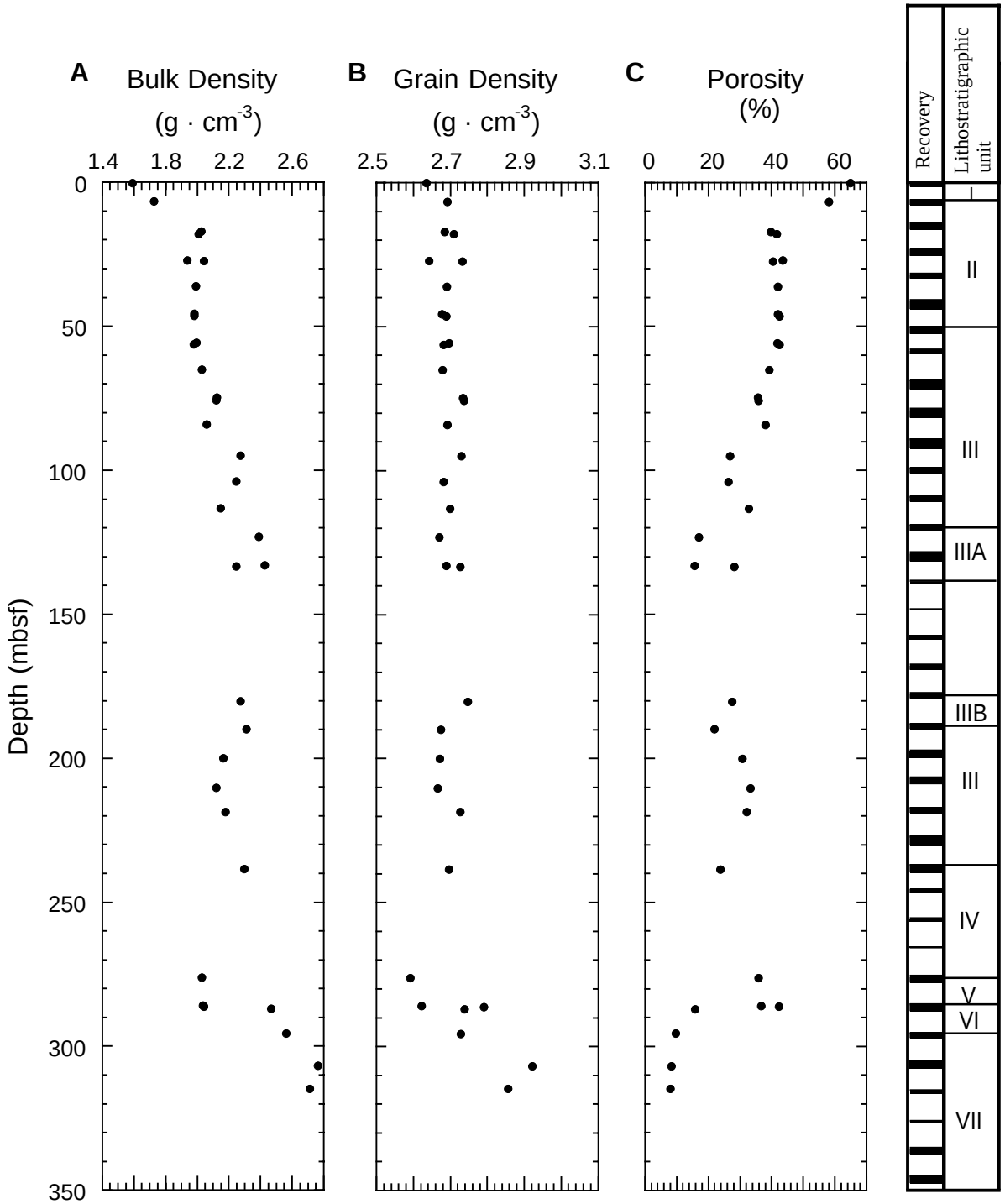

Figure F47. Regression least-squares exponential curves of porosity for (A) all data from Site 1114, (B) data below 17 mbsf, and (C) index properties porosities superposed onto the logging data.

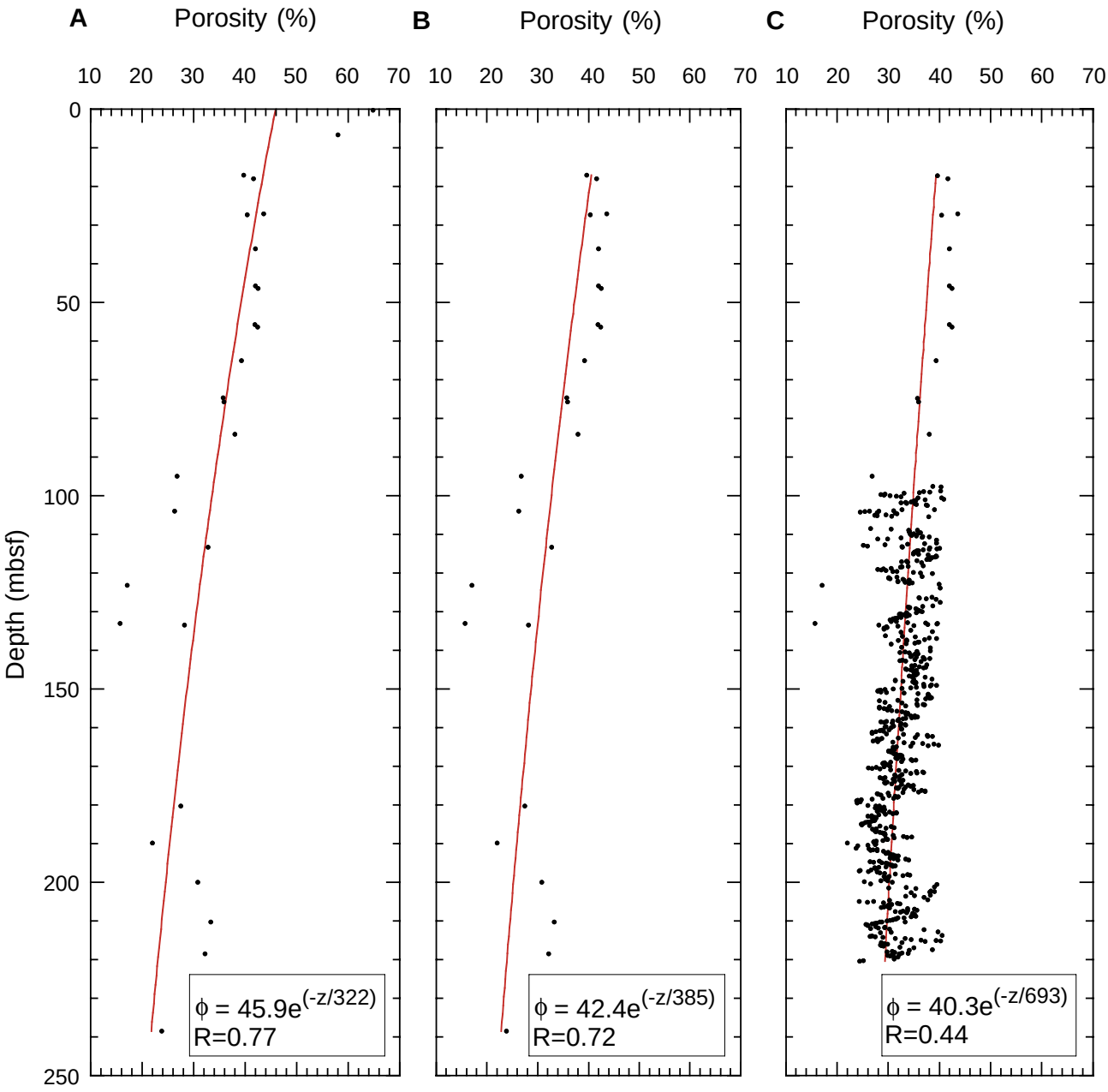

Figure F48. Site 1114 *P*-wave transverse (x, y) and longitudinal (z) velocities.

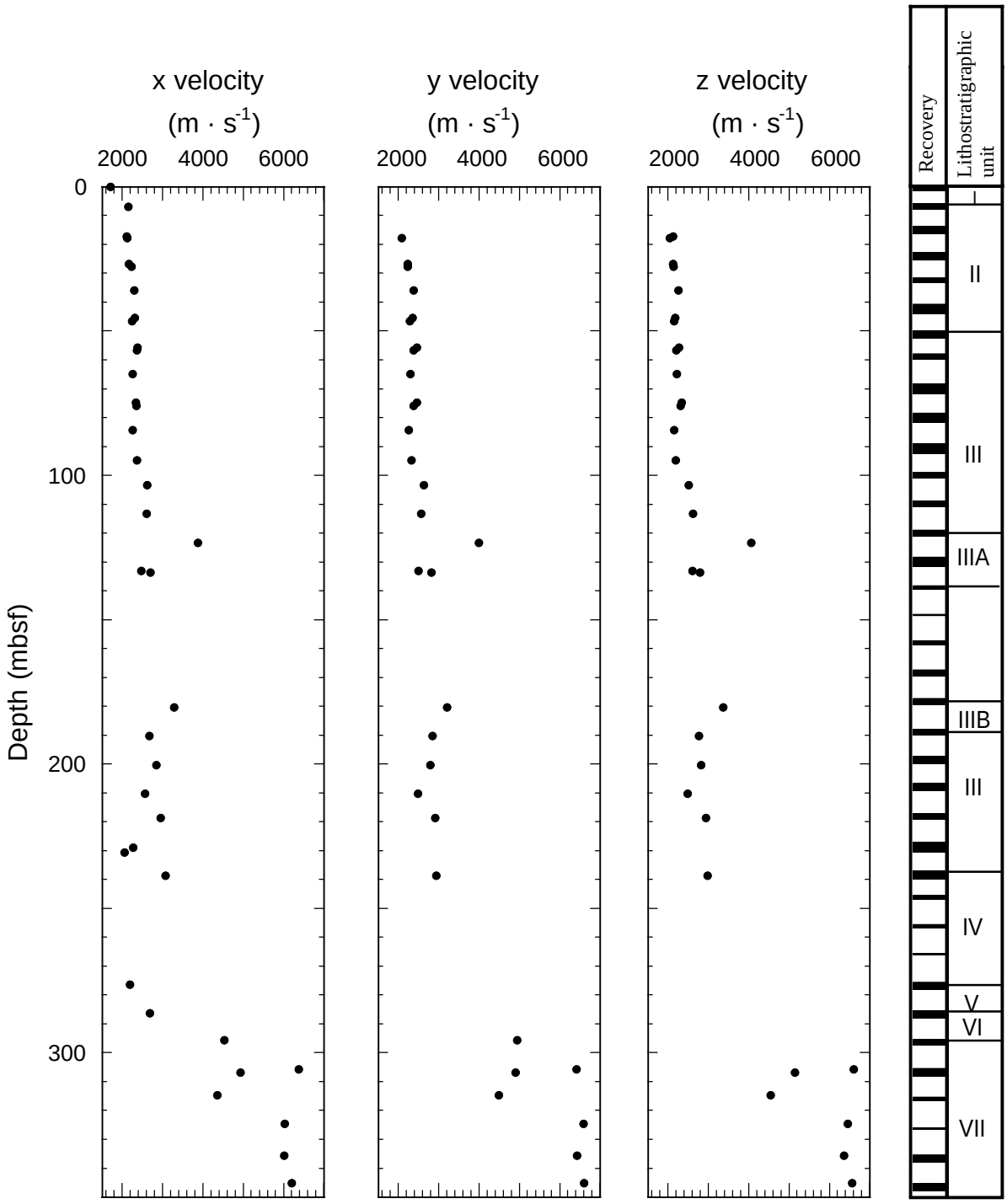

Figure F49. A. Longitudinal velocity vs. average transverse velocity. **B.** *P*-wave anisotropy with depth (see "Physical Properties," p. 28, in the "Explanatory Notes" chapter for method used). A positive anisotropy indicates that the transverse is greater than the longitudinal velocity.

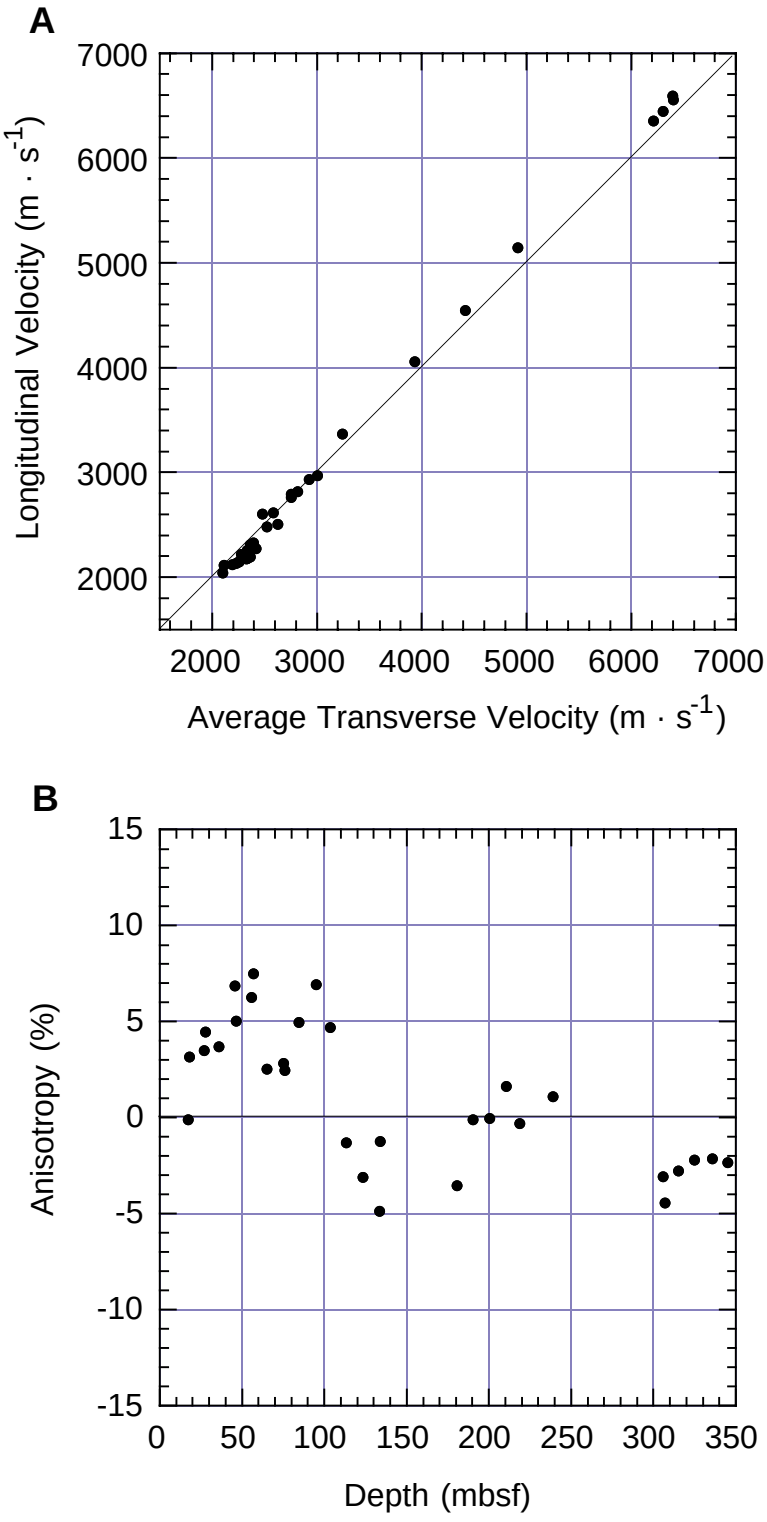

Figure F50. Site 1114 thermal conductivity measurements.

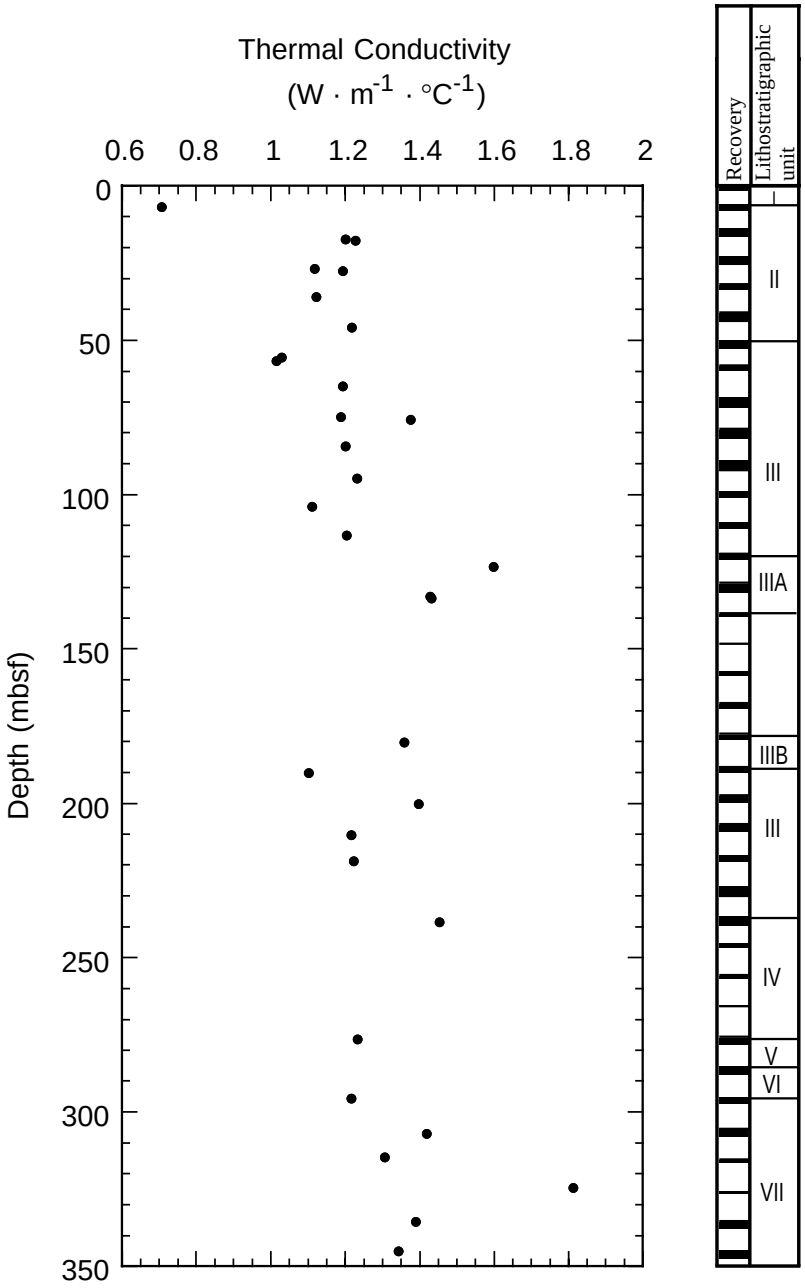

Figure F51. Site 1114 (**A**) magnetic susceptibility and (**B**) NGR data.

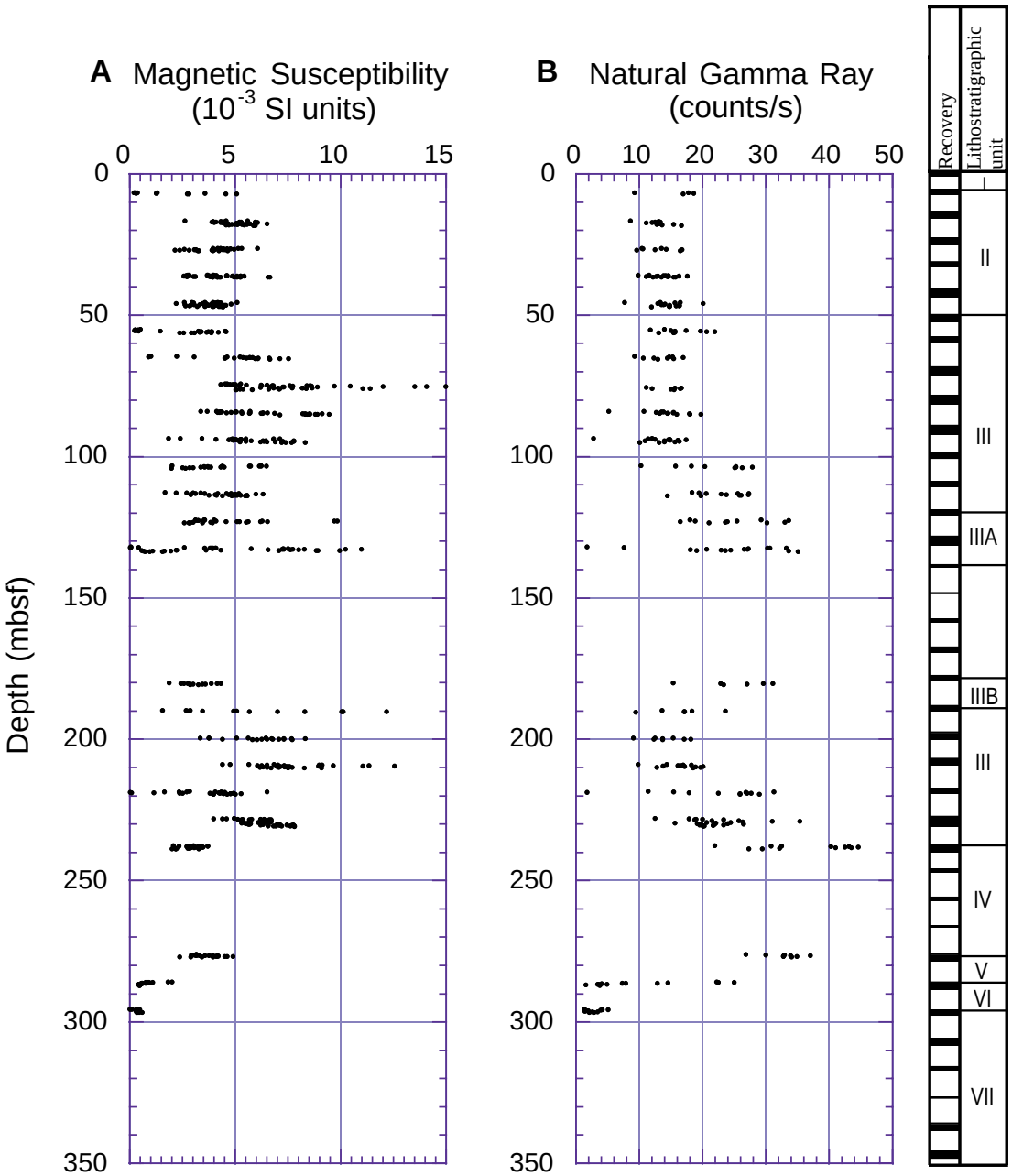

Figure F52. Comparison of Site 1114 (**A**) bulk density and (**B**) velocity data from physical properties measurements and downhole logging. The washout zones recognized down the borehole are shaded.

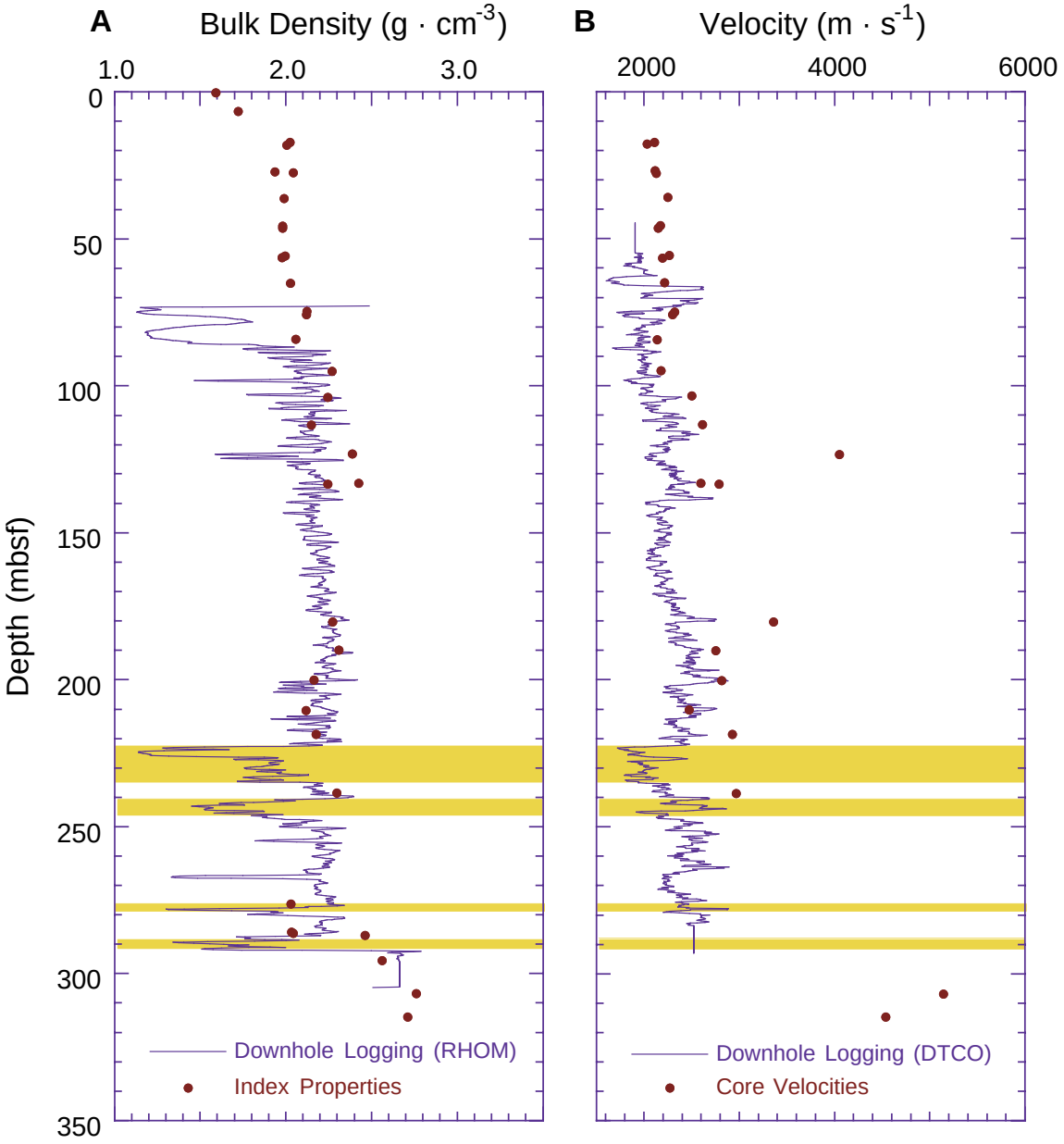

Figure F53. Hole 1114A composite log from 0 to 300 mbsf. **A.** Left to right: (1) core number and recovery intervals; (2) caliper measurement from the triple combo run; (3) total gamma-ray counts (HSGR) and total gamma-ray counts minus uranium (HCGR); (4) thorium and uranium content; (5) potassium content; (6) resistivity from the DIT tool, consisting of deep induction (IDPH), medium induction (IMPH), and shallow spherically focused current (SFLU); and (7) log units. Composite log from 0 to 150 mbsf. To compare other logs at equivalent depth, see Figure **F53B,** p. 101. (Continued on next three pages.)

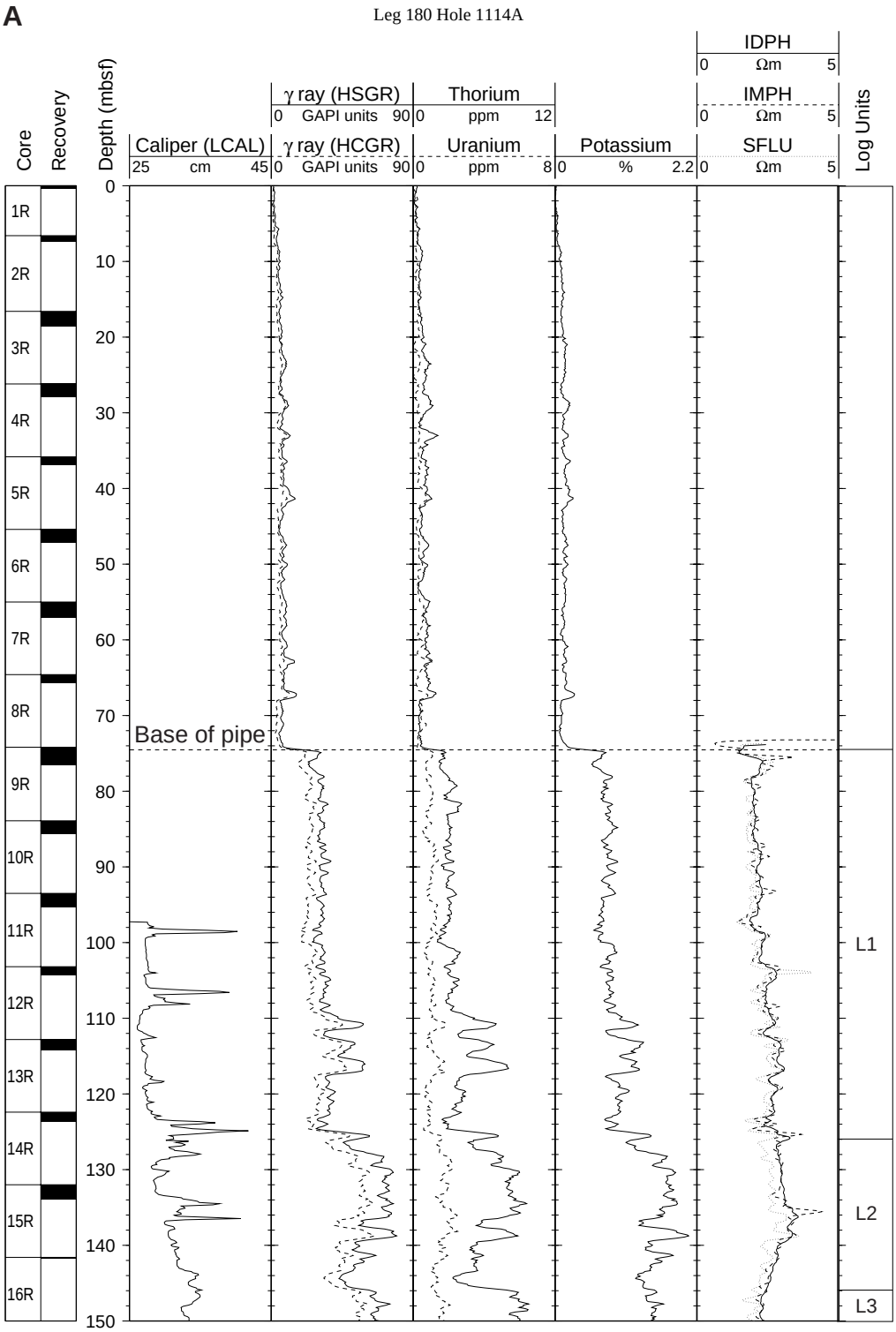

Figure F53 (continued). Composite log from 150 to 300 mbsf. To compare other logs at equivalent depth, see Figure **F53B**, p. 102.

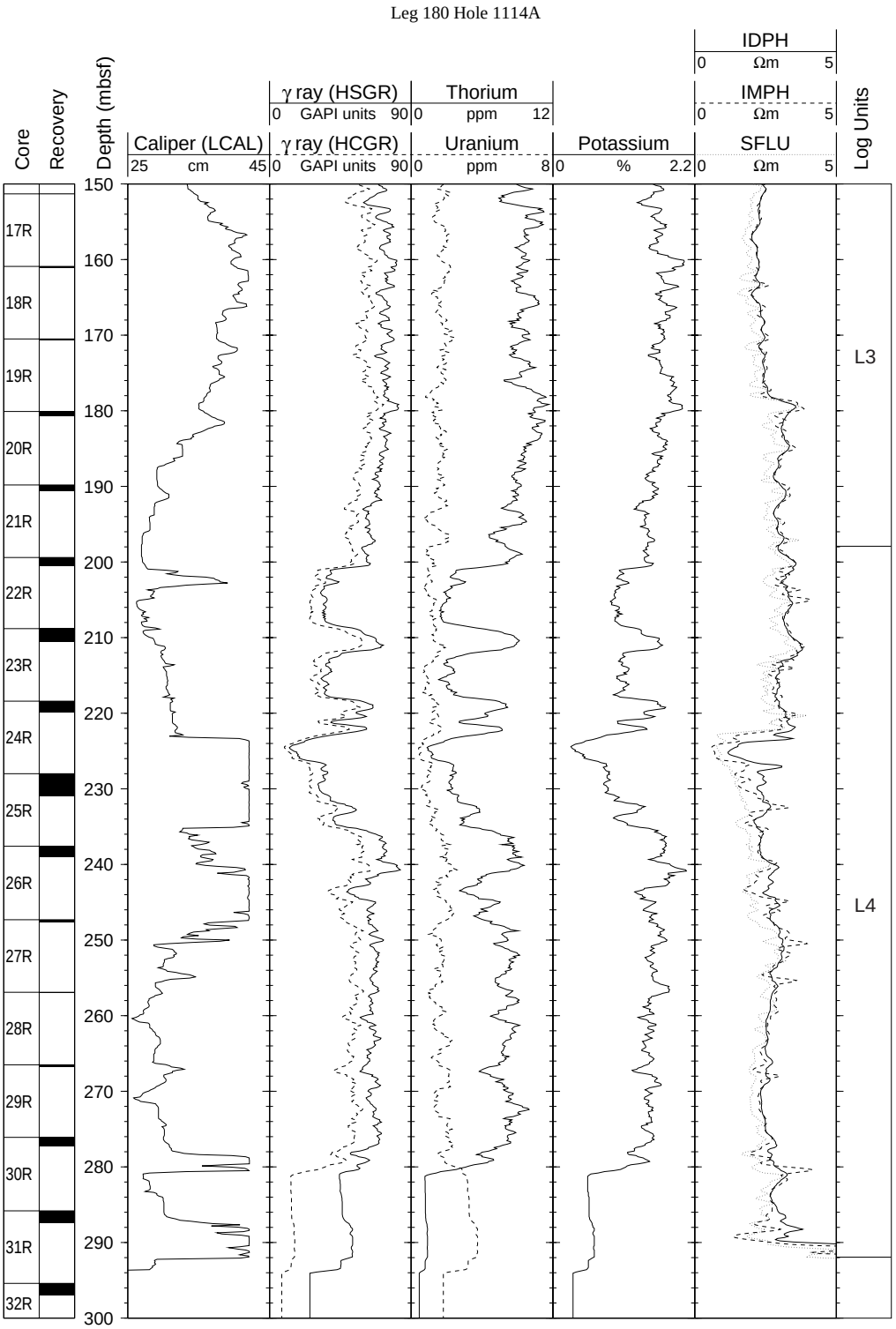

Figure F53 (continued). B. Left to right: (1) core number and recovery intervals; (2) bulk density from log (RHOM) and from physical properties measurements on cores; (3) photoelectric effect (PEFL); (4) neutron porosity (APLC), density porosity (DPHI), and porosity from physical properties measurements on cores; (5) neutron capture rate (SIGF); (6) sonic velocity from log (DTCO) and from physical properties measurements on cores; and (7) log units. Composite log from 0 to 150 mbsf. To compare other logs at equivalent depth, see Figure **F53A,** p. 99.

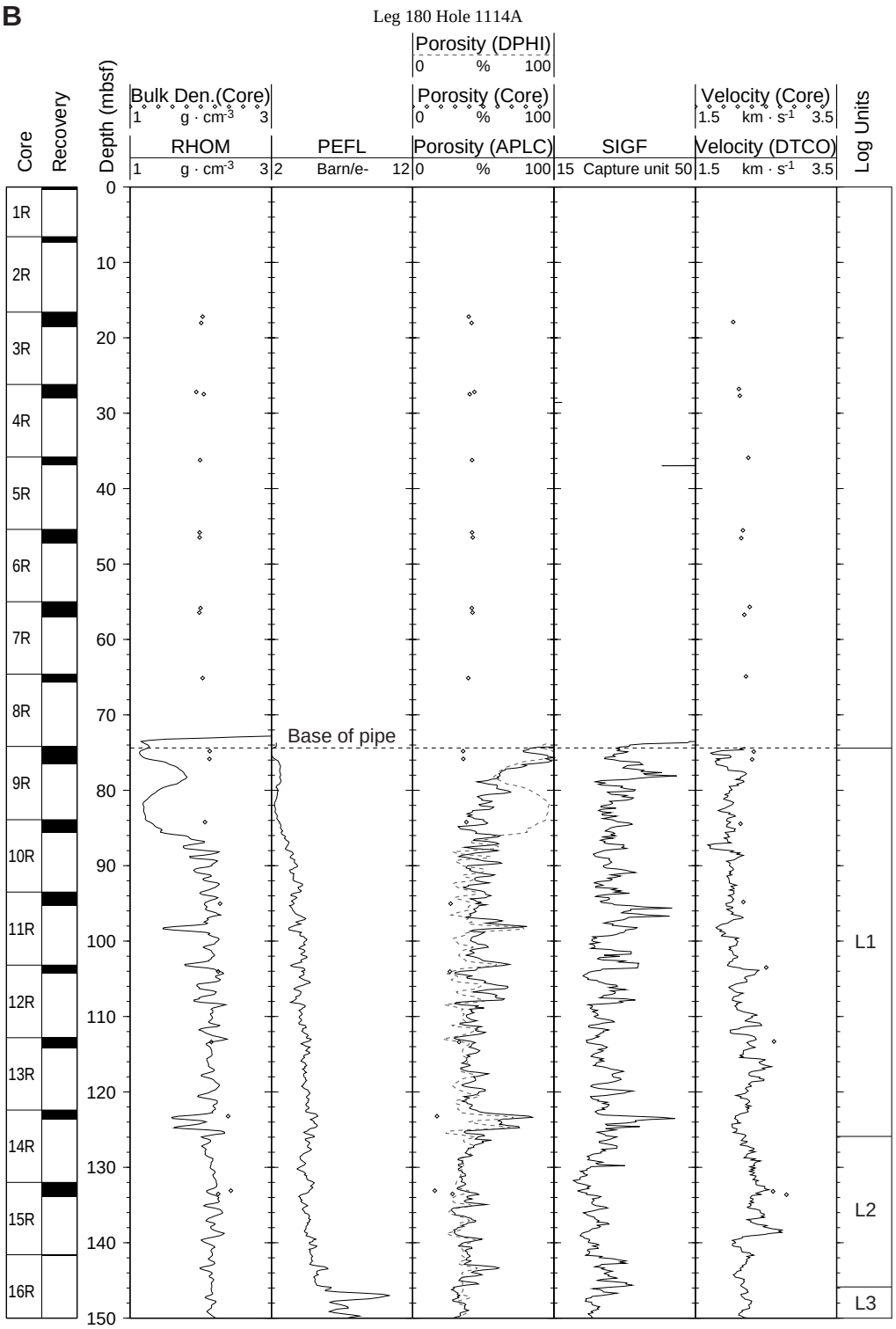

Figure F53 (continued). Composite log from 150 to 300 mbsf. To compare other logs at equivalent depth, see Figure F53A, p. 100.

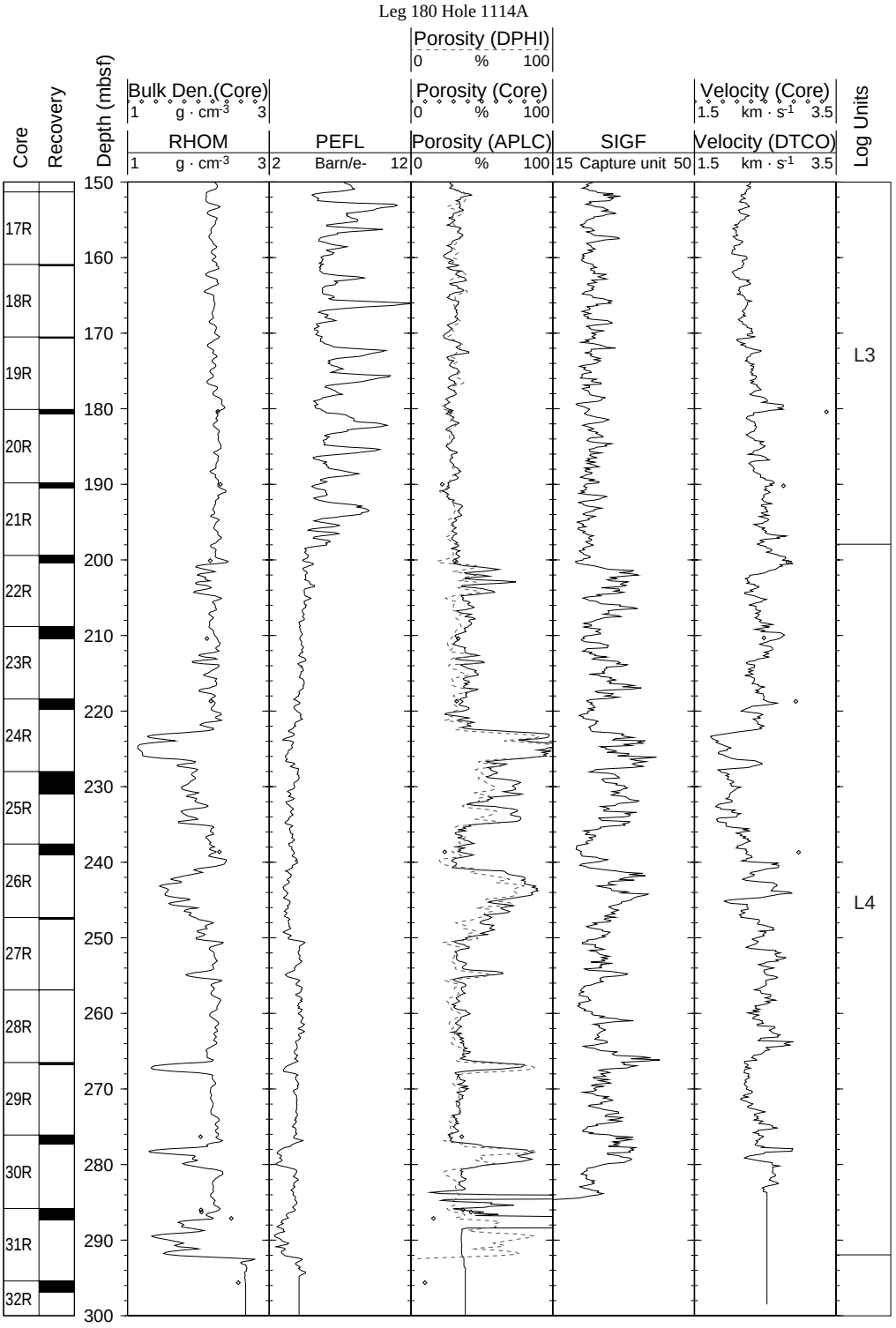

Figure F54. Hole 1114A depth-shifted total gamma ray (HSGR) from triple combo at the mudline.

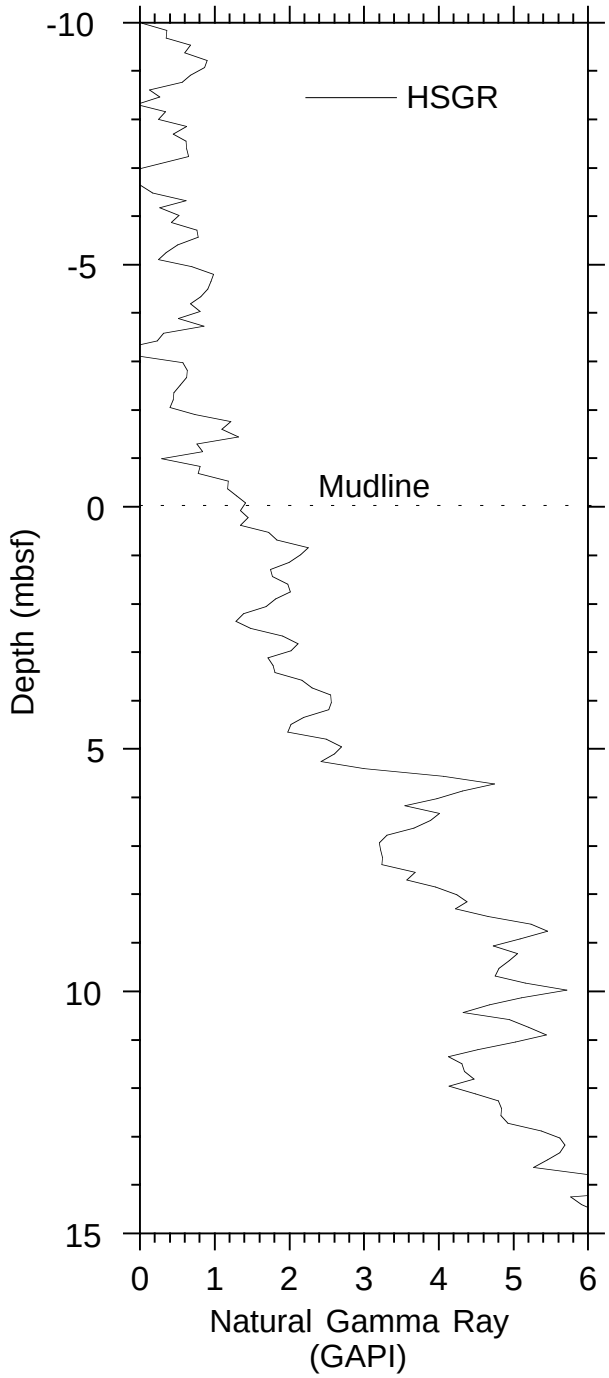

Figure F55. Hole 1114A depth-shifted total gamma ray from triple combo (HSGR) and from FMS-sonic string first and second run (SGR1 and SGR2, respectively) for intervals (**A**)110–120 mbsf and (**B**) 215–224 mbsf.

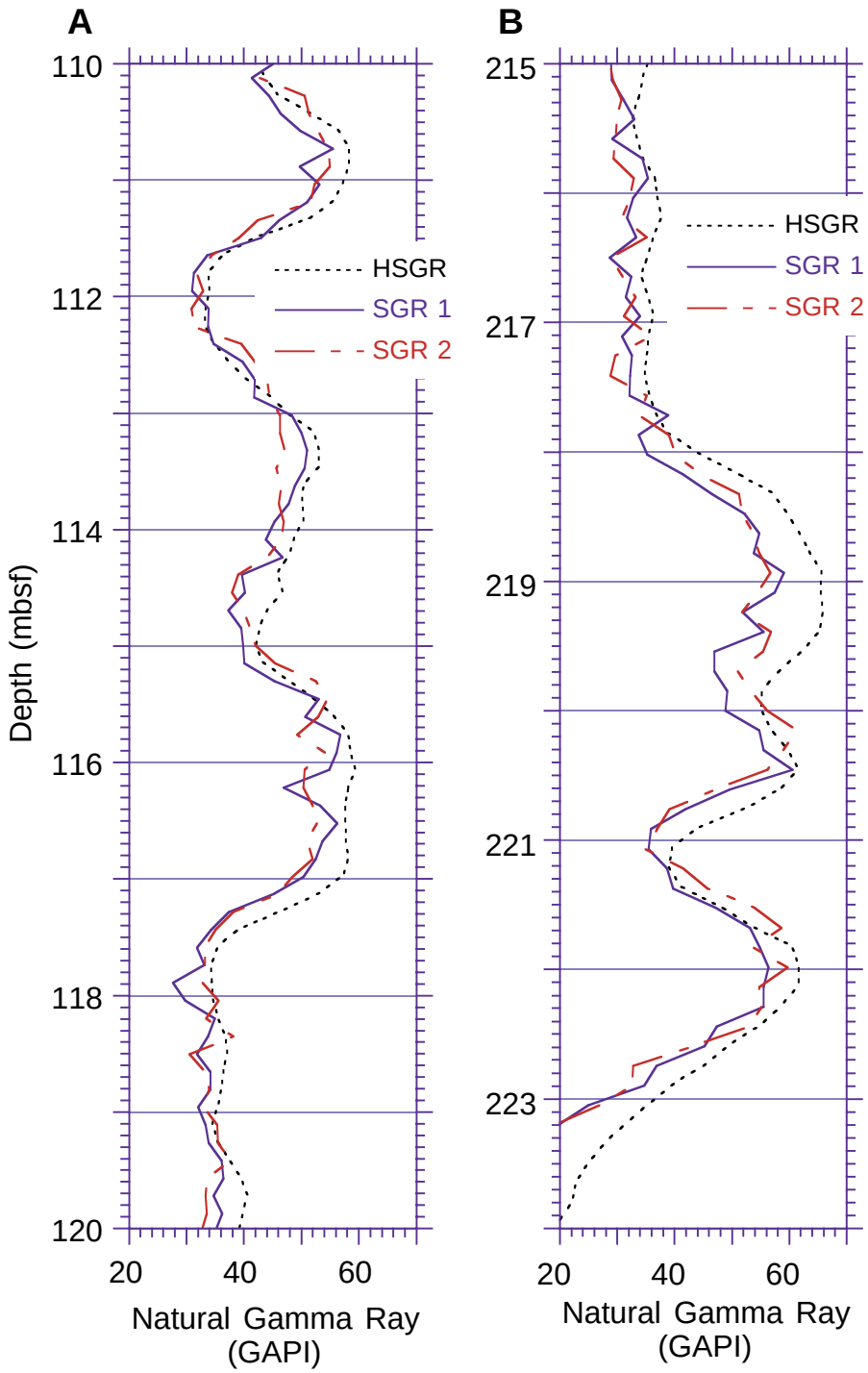

Figure F56. Hole 1114A log units and correlations. Left to right: core recovery, natural gamma ray, density (DPHI) and neutron porosity (APLC), units defined by the logging response, lithostratigraphic units (defined in **"Lithostratigraphy,"** p. 3), and intervals of pervasive scaly fabric (see **"Structural Geology,"** p. 20). Areas of maximum caliper extent during the triple combo run are shaded.

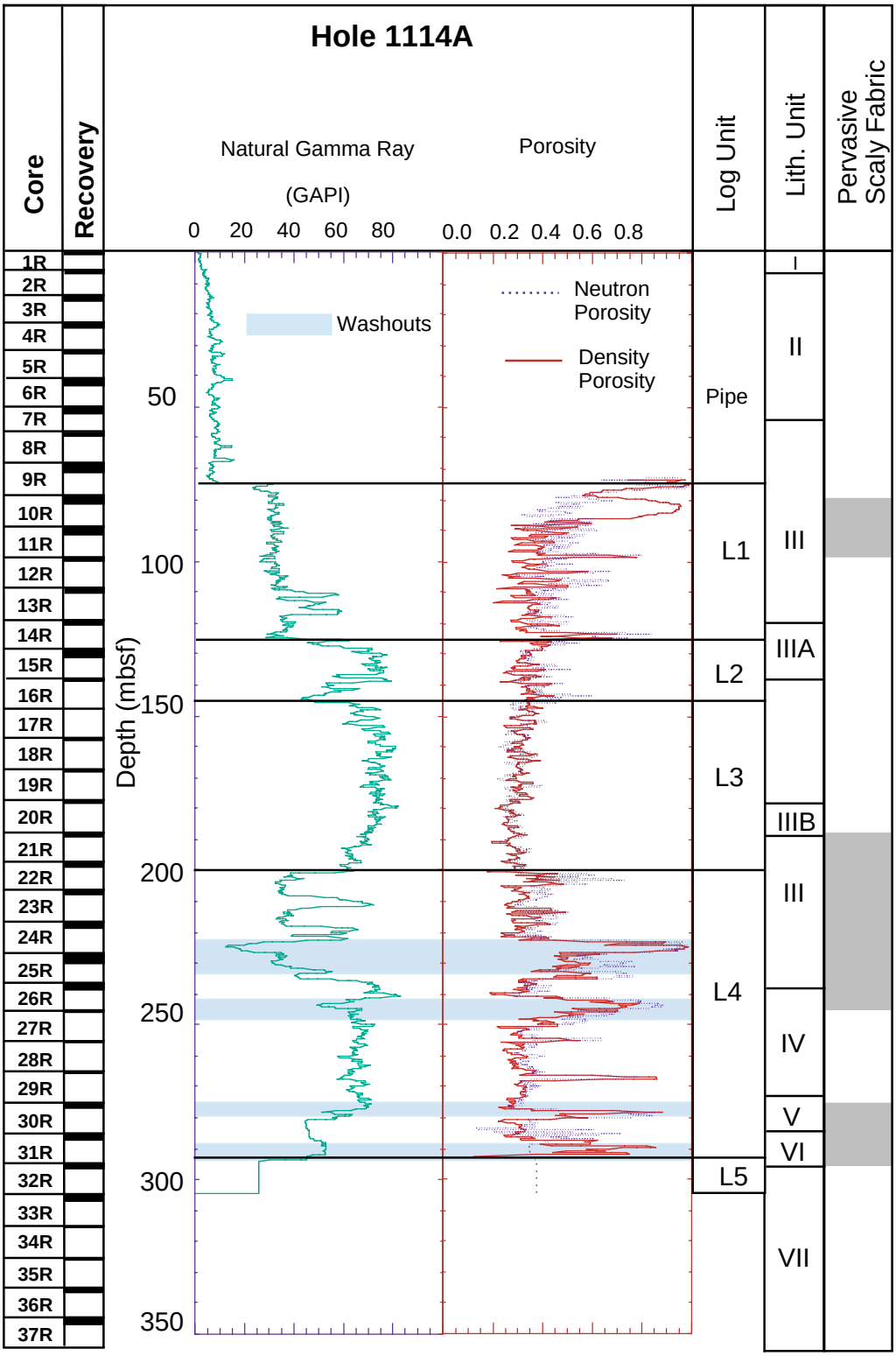

Figure F57. Hole 1114A geometry from FMS inclinometry data. **A.** Hole deviation. **B.** Hole azimuth.

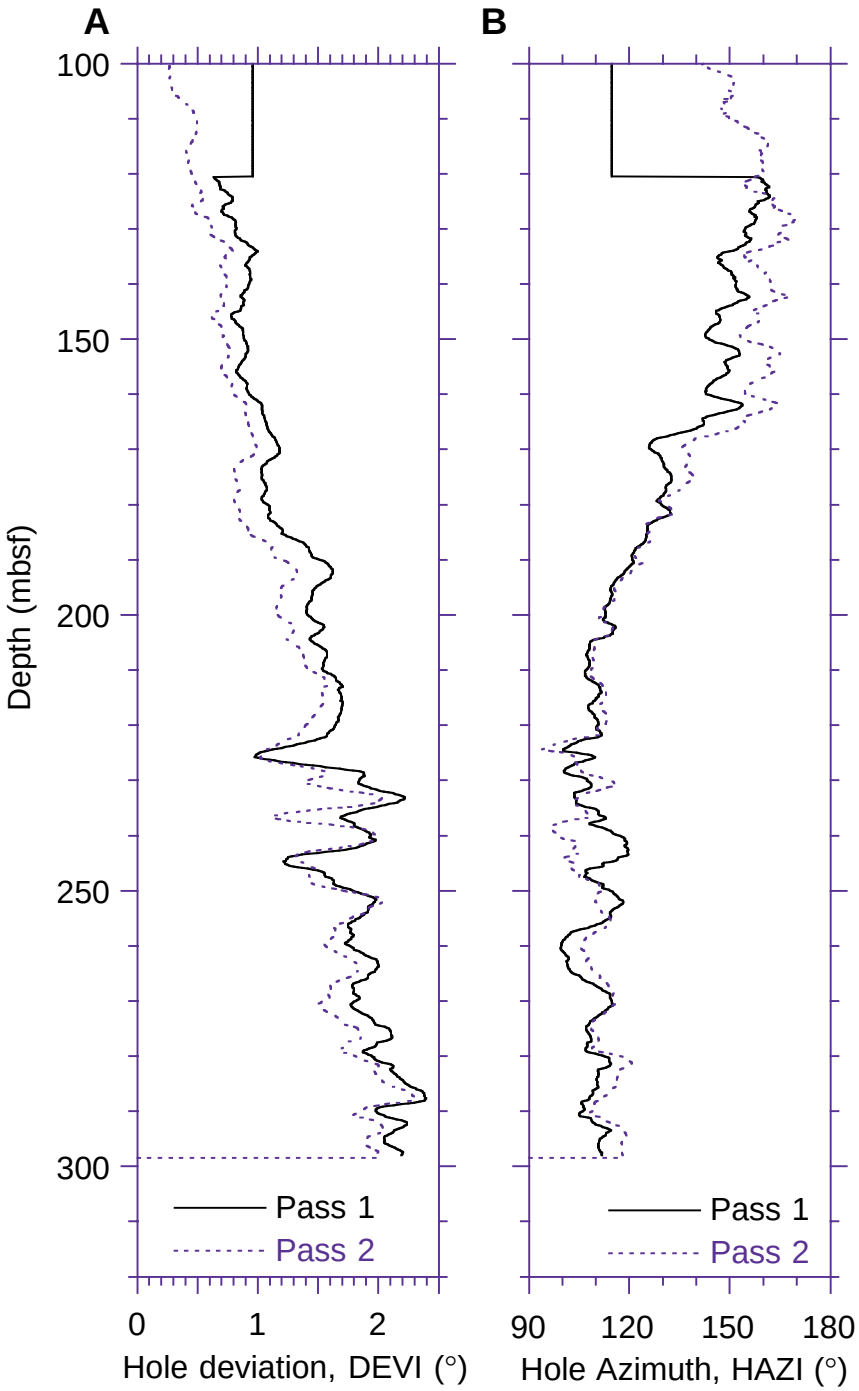

Figure F58. FMS Pad 1 azimuth with respect to geographic north in Hole 1114A.

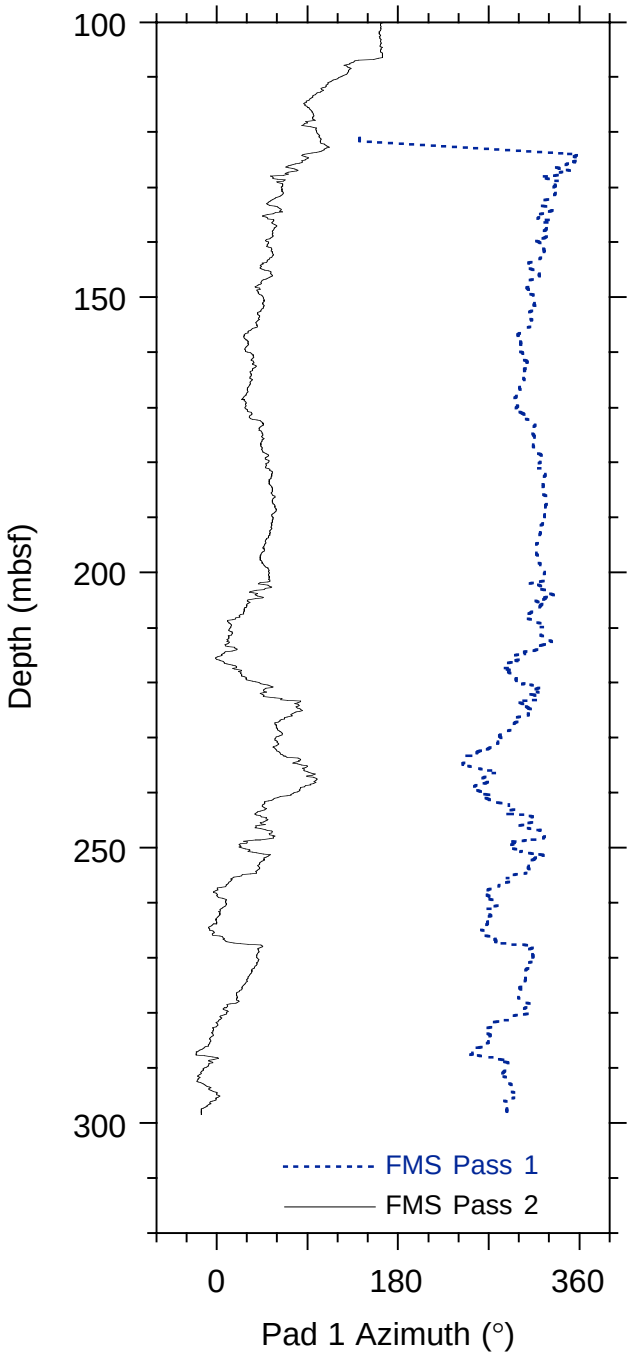

Figure F59. Hole 1114A FMS caliper data from Pad 1 (C1) and Pad 2 (C2) for (**A**) Pass 1 and (**B**) Pass 2.

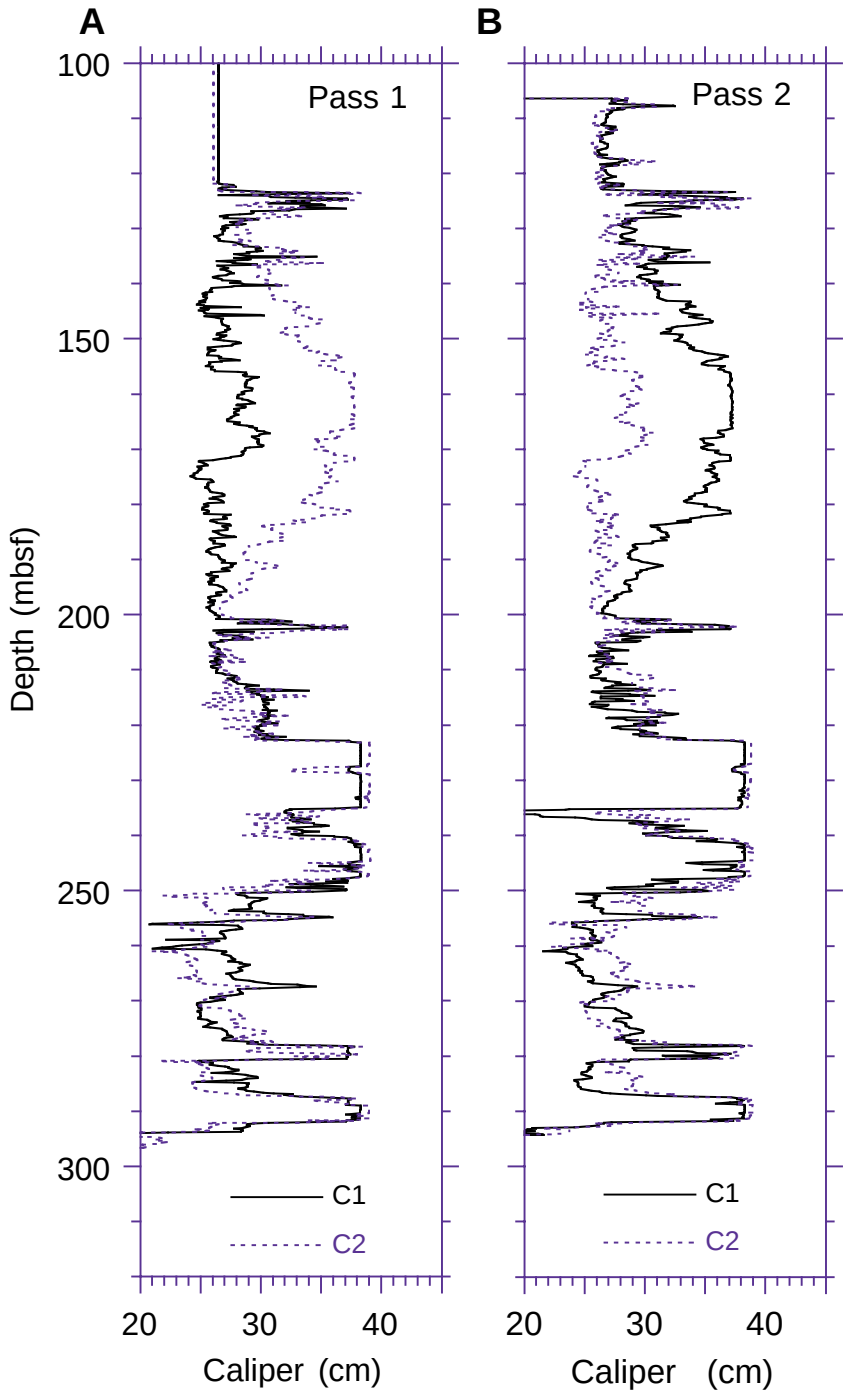

Figure F60. Hole 1114A magnetic field from FMS magnetometer. **A.** Magnetic intensity. **B.** Magnetic inclination.

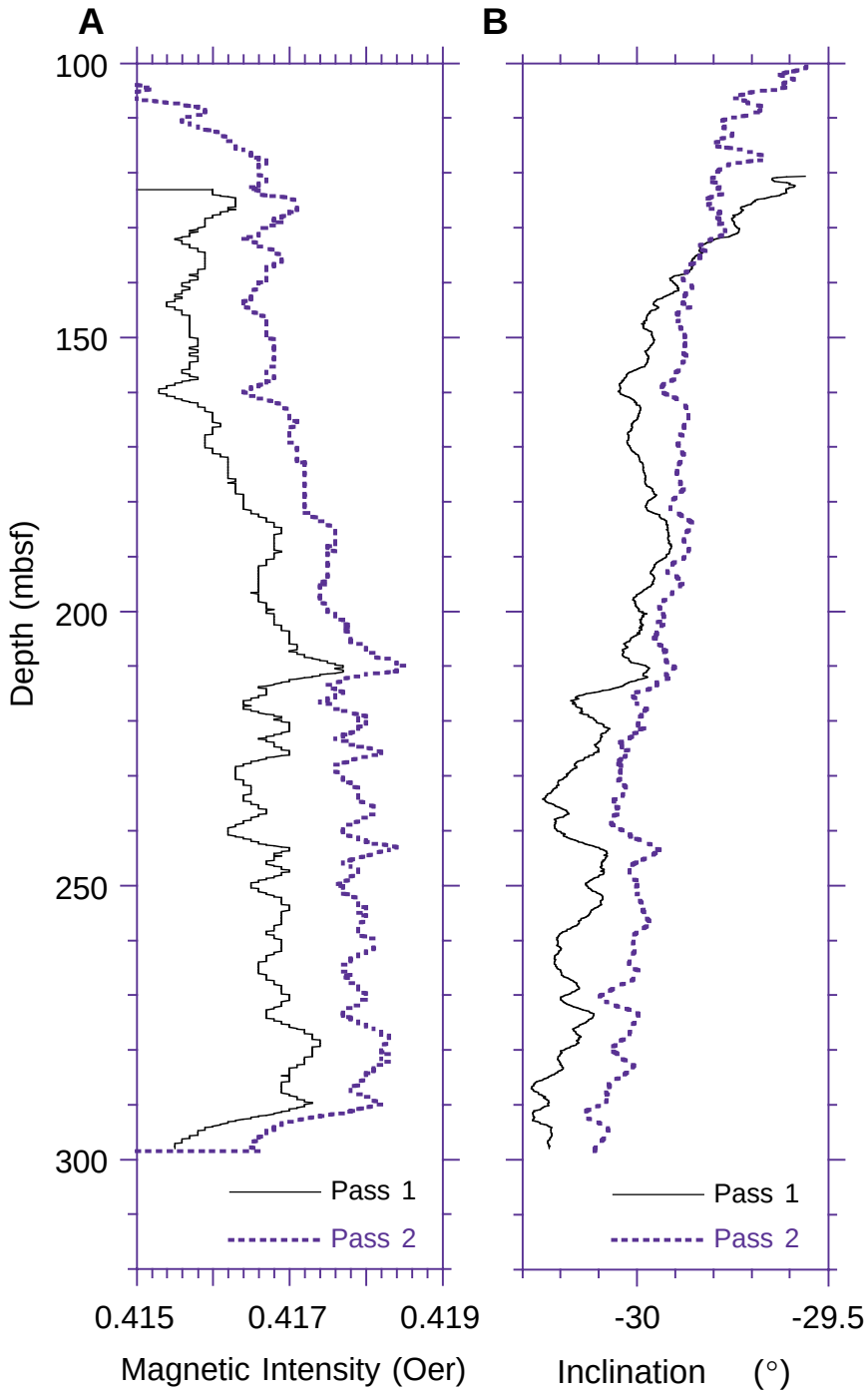

Figure F61. Wulff stereographic projection (upper hemisphere) of 46 beds (green/gray) and 35 fractures (blue/black) interpreted from the FMS images of Hole 1114A reveals one major bed dip population and two major and two minor fracture dip populations. Mean dips and dip directions for beds (mean dip 40°, mean dip direction 296°) and fractures (mean dip 62°, mean dip direction 248°) are indicated by the square symbols.

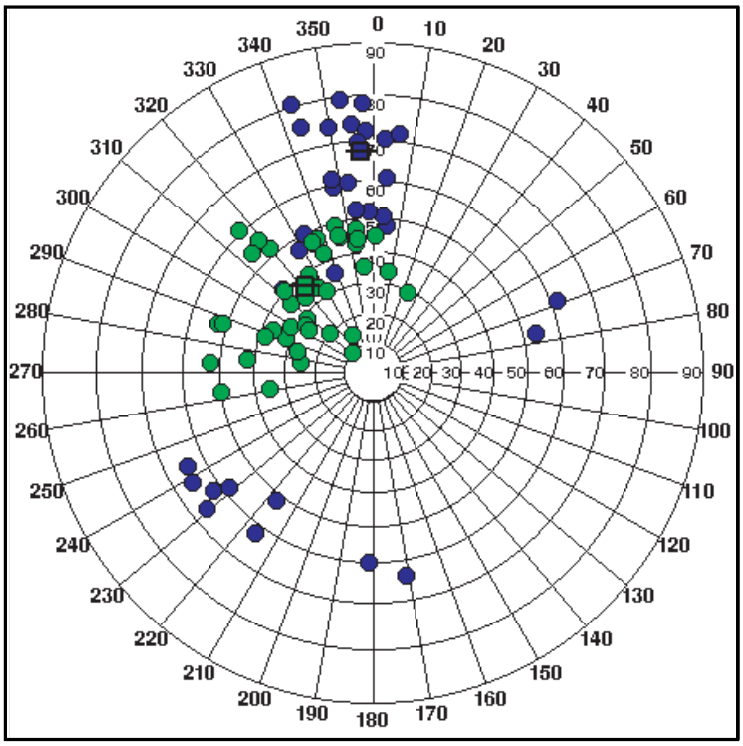

Figure F62. Hole 1114A bed and fracture orientation. **A, B.** Histograms of bed and fracture dip directions. **C, D.** Rose diagrams of bed and fracture strikes. Beds dominantly strike northeast, whereas fractures dominantly strike just north of east. Directions are relative to geographic north.

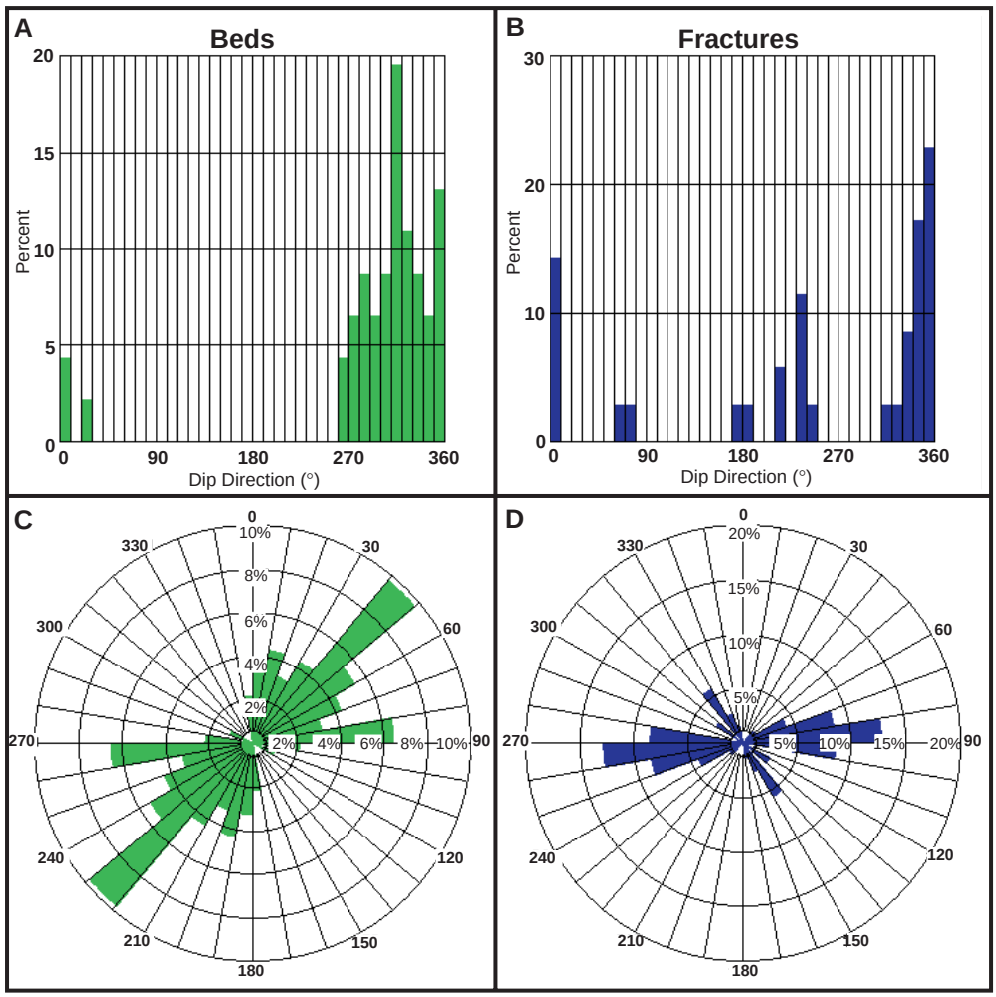

Figure F63. Hole 1114A variation of bed and fracture orientation with depth: (**A**) bed and (**B**) fracture dips and dip directions with depth. The region between 165 and 215 mbsf shows a distinct trend of increasing dip and northward verging dip direction with depth.

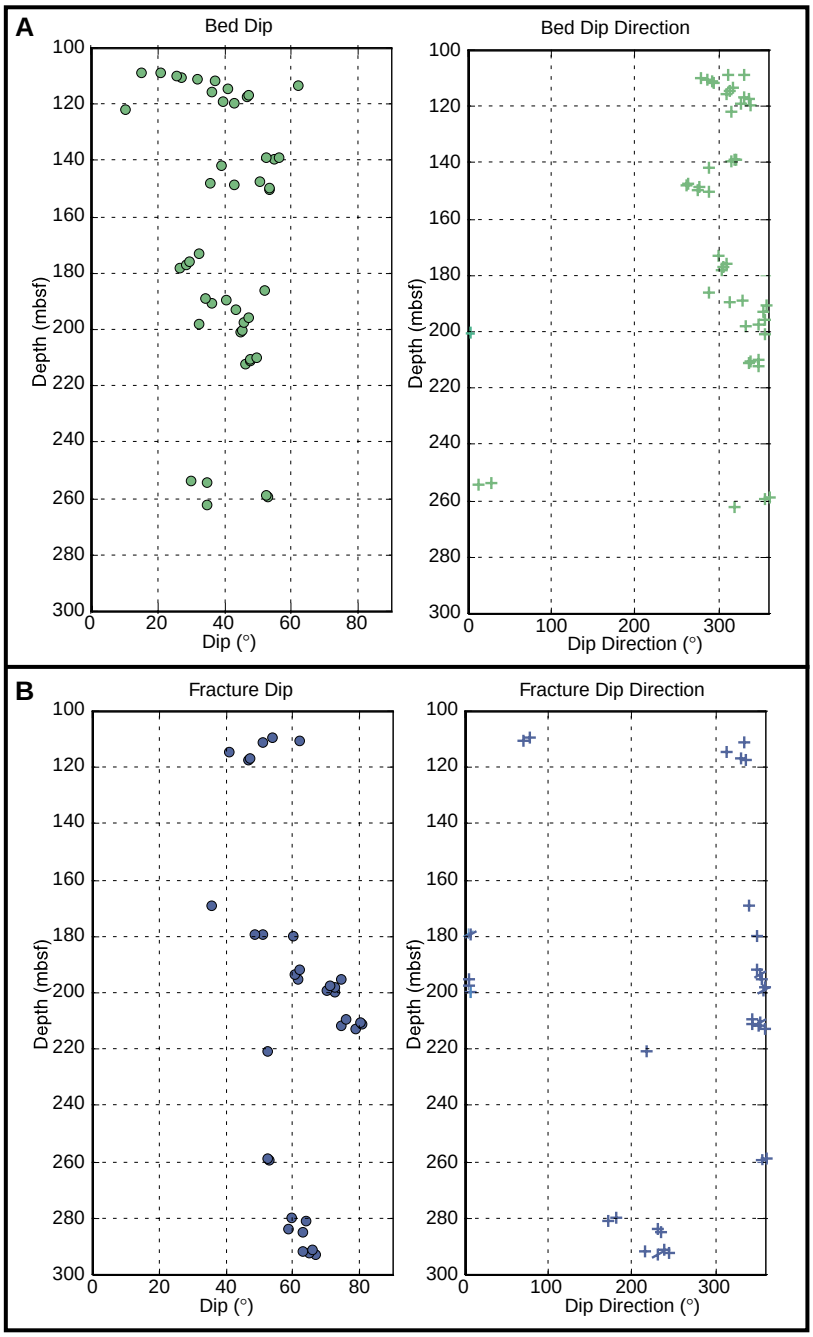

Figure F64. Hole 1114A statically normalized FMS image and tadpole plot from log Unit L1. Northwest-dipping beds steepen from ~15° to 36°. Crosscutting fractures dip northeast and north-northwest between 50° and 60°. Vertical scale = 1:20.

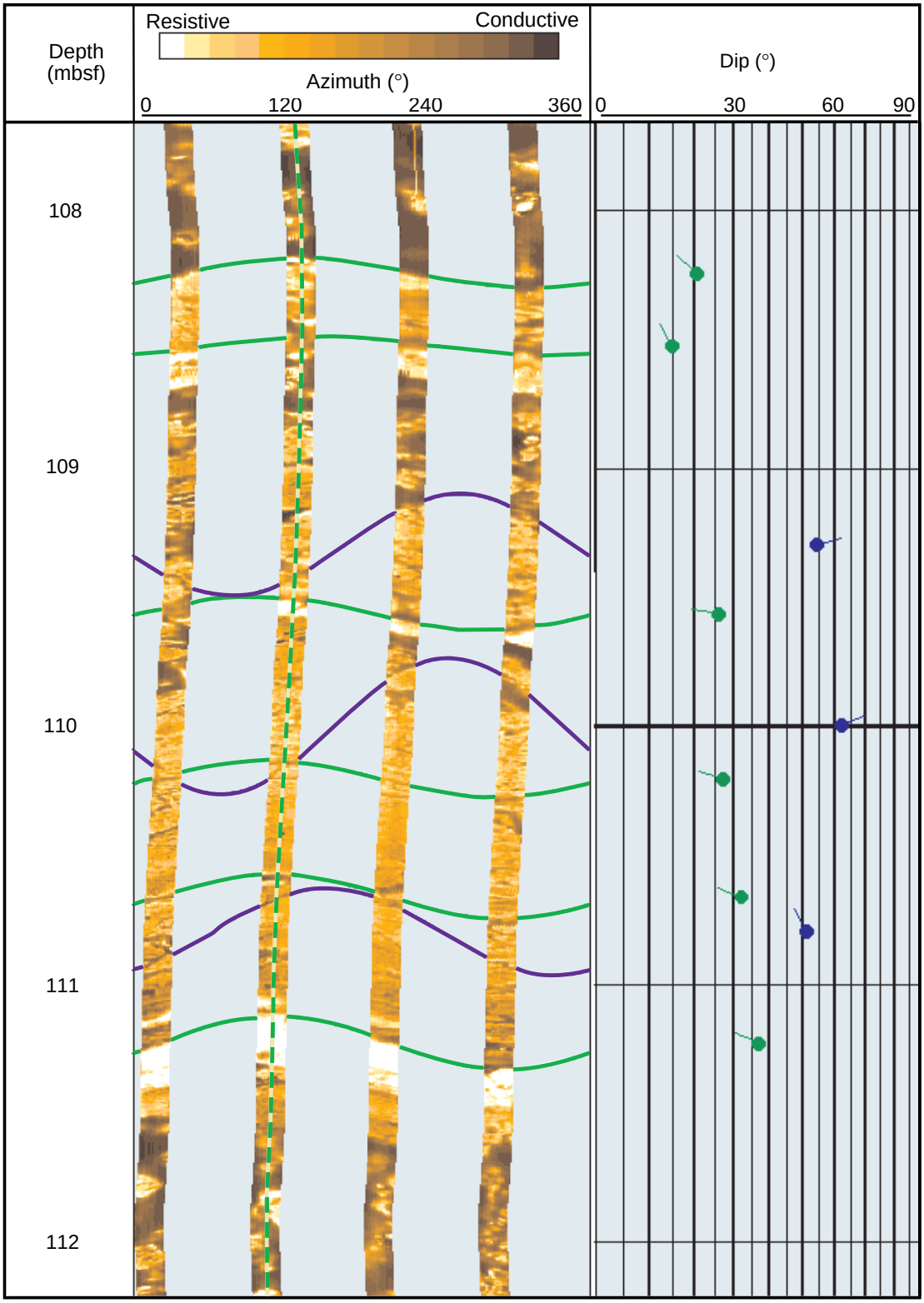

Figure F65. Hole 1114A statically normalized FMS image and tadpole plot from the upper portion of log Unit L3. Beds consistently dip westward from 35° to 50°. Fractures, if present, are poorly defined. Vertical scale = 1:20.

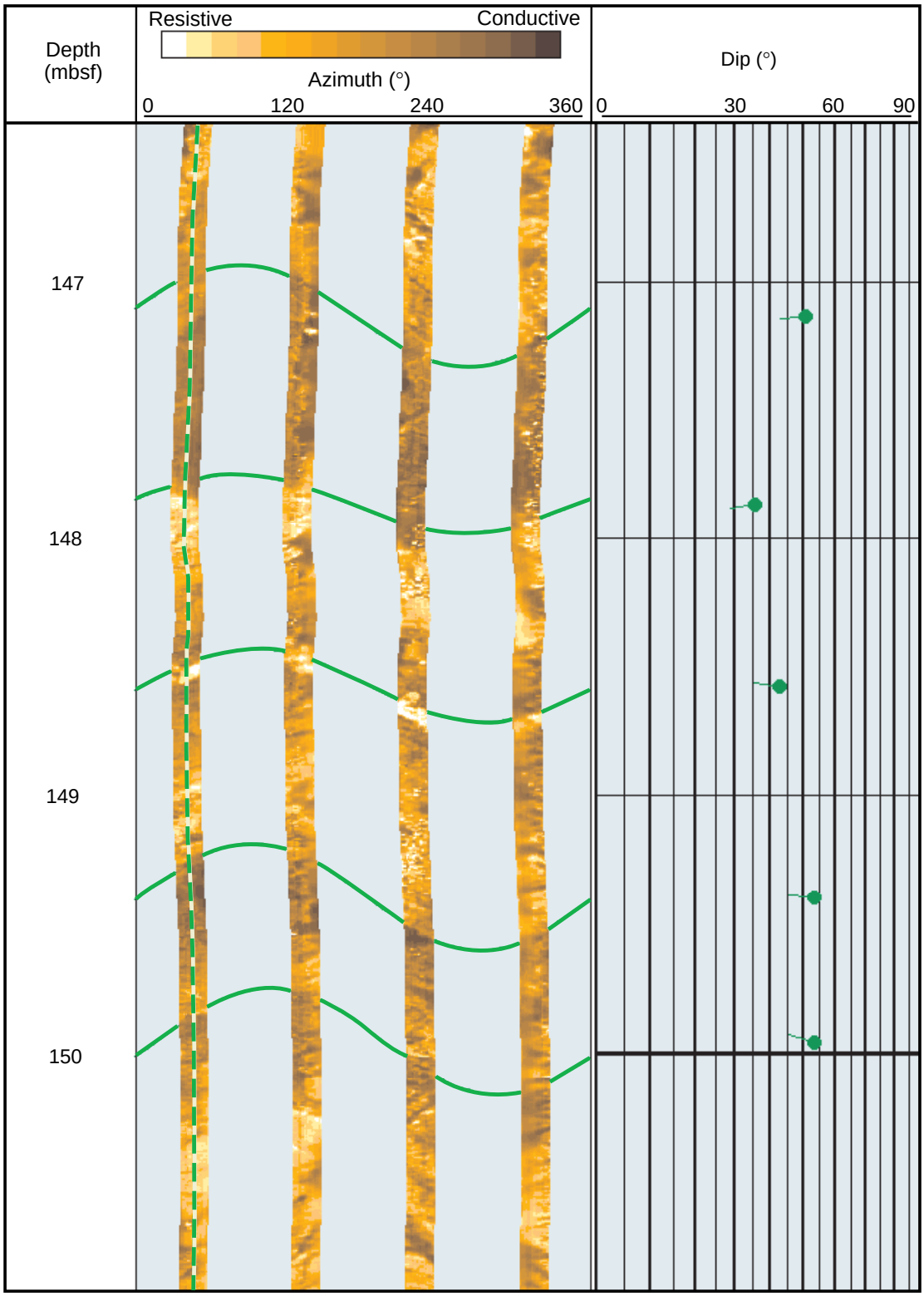

Figure F66. Hole 1114A statically normalized FMS image and tadpole plot from the lower portion of log Unit L3. The dipping beds and fractures shown lie near the top of the zone between 165 and 215 mbsf within which both bed and fracture dips steepen with depth. Vertical scale = 1:20.

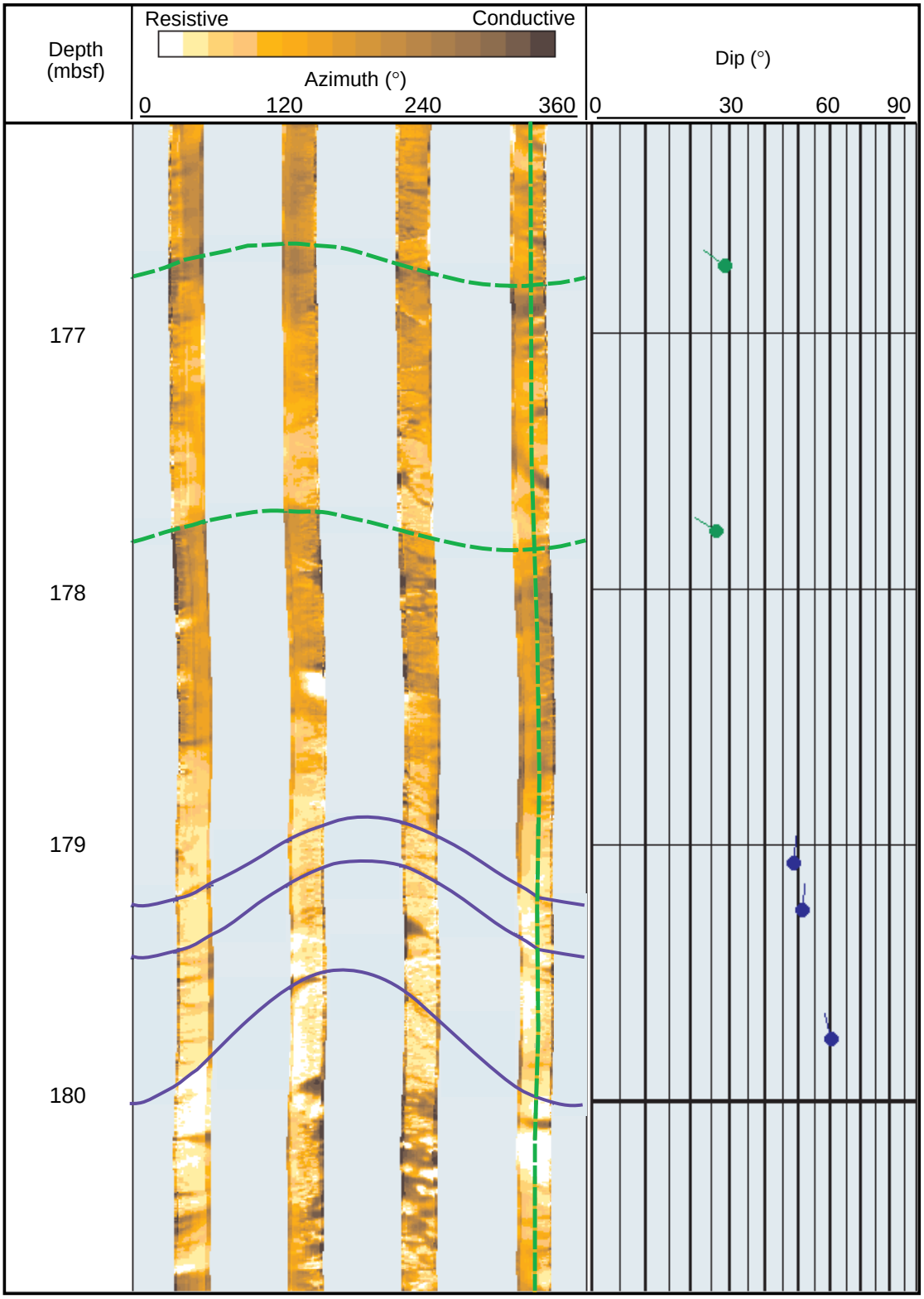

Figure F67. Hole 1114A dynamically normalized FMS image and tadpole plot from log Unit L4 showing steep (75°–80°) dipping fractures that crosscut more shallowly dipping (45°–50°) beds, both of which display a north-northwestward dip direction. Vertical scale = 1:20.

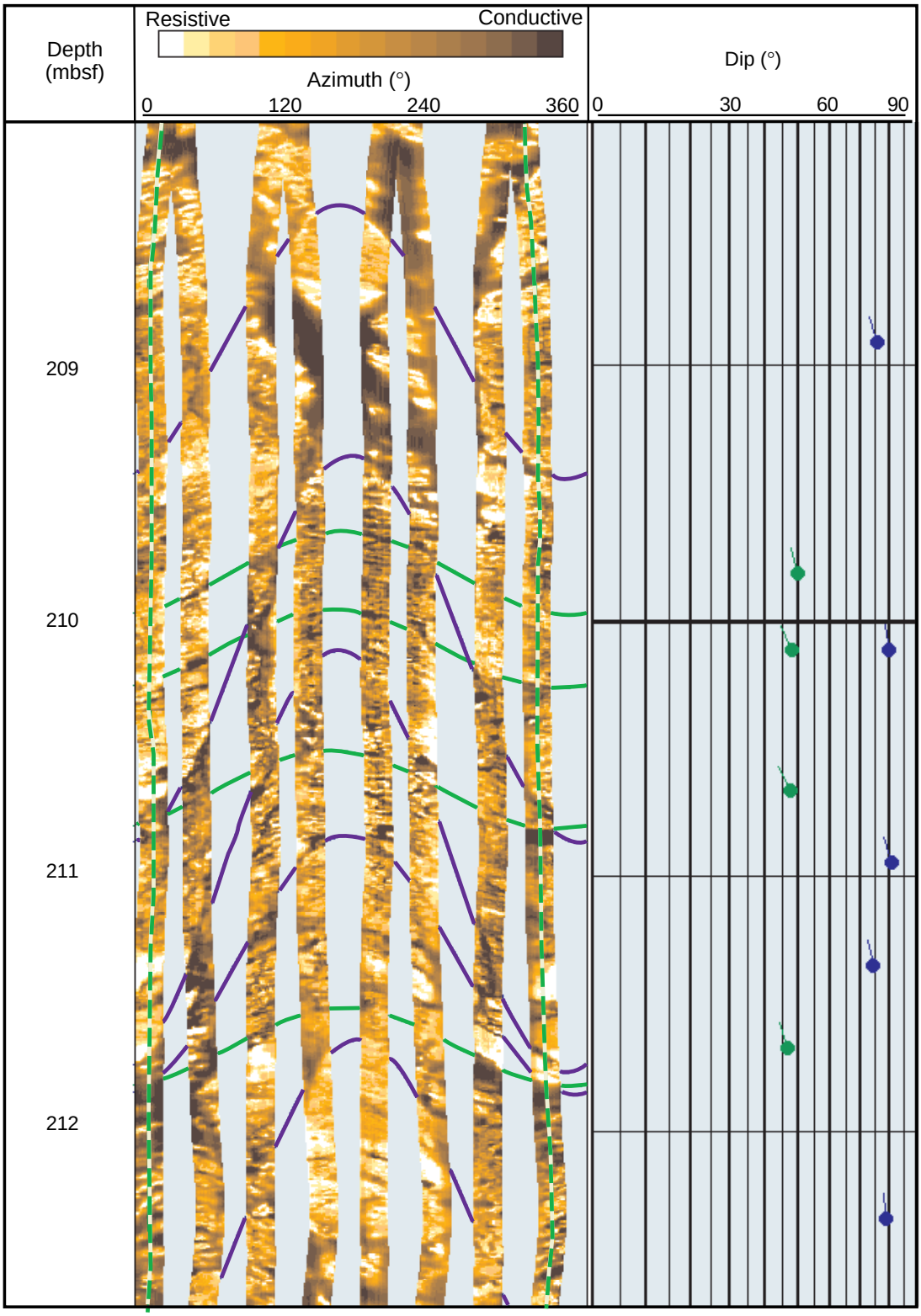

Figure F68. Hole 1114A dynamically normalized FMS image and tadpole plot from log Unit L5. Fracture-bound beds dip 65° to the southwest. Dark, conductive zones on either side of the resistive bed at 291 mbsf are washed out zones. Vertical scale = 1:20.

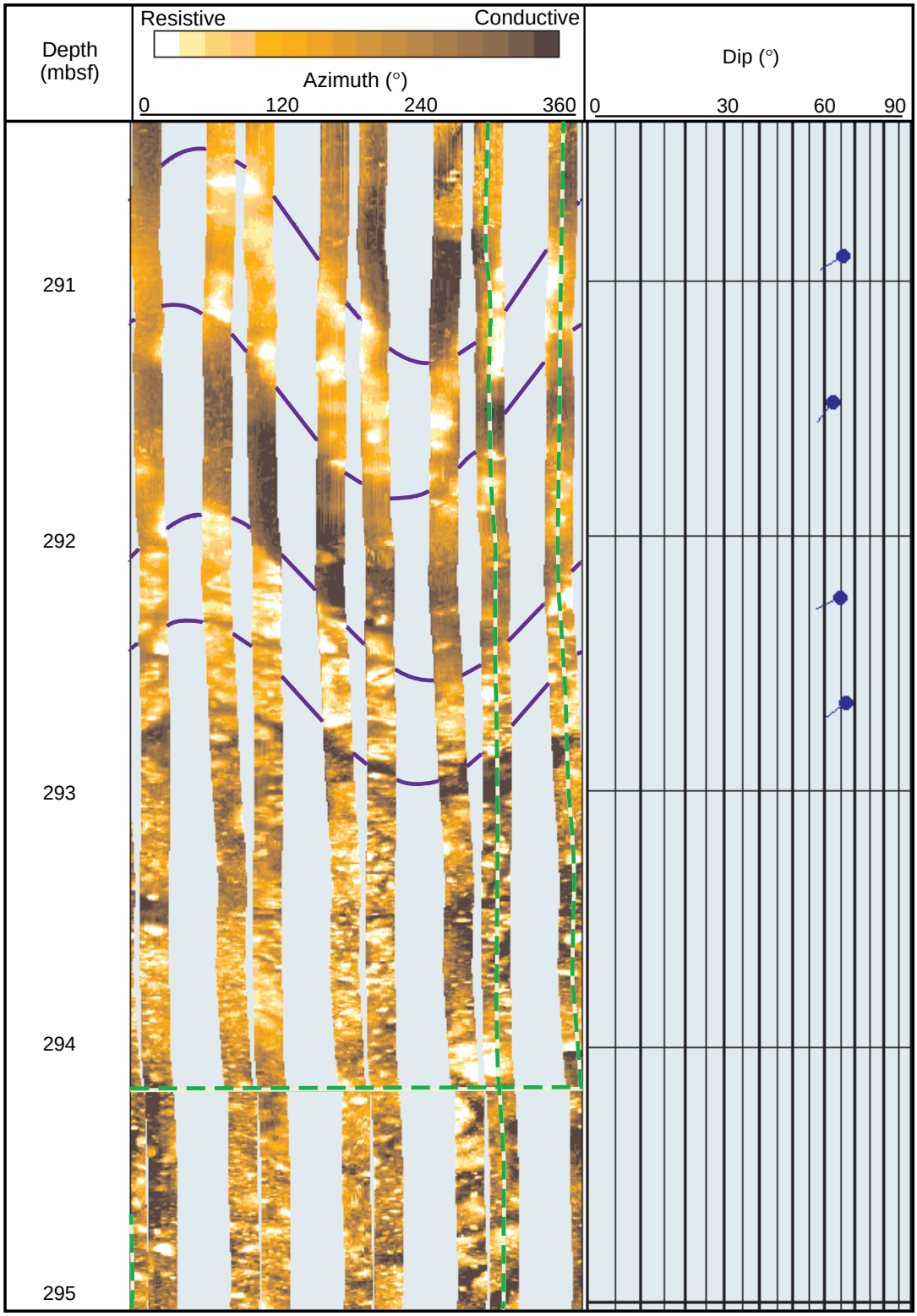

Figure F69. All temperature data from the TLT in and above Hole 1114A. T_{fast} and T_{slow} refer to the fast and slow thermistors, respectively. Arrows mark upward and downward passes of the tool.

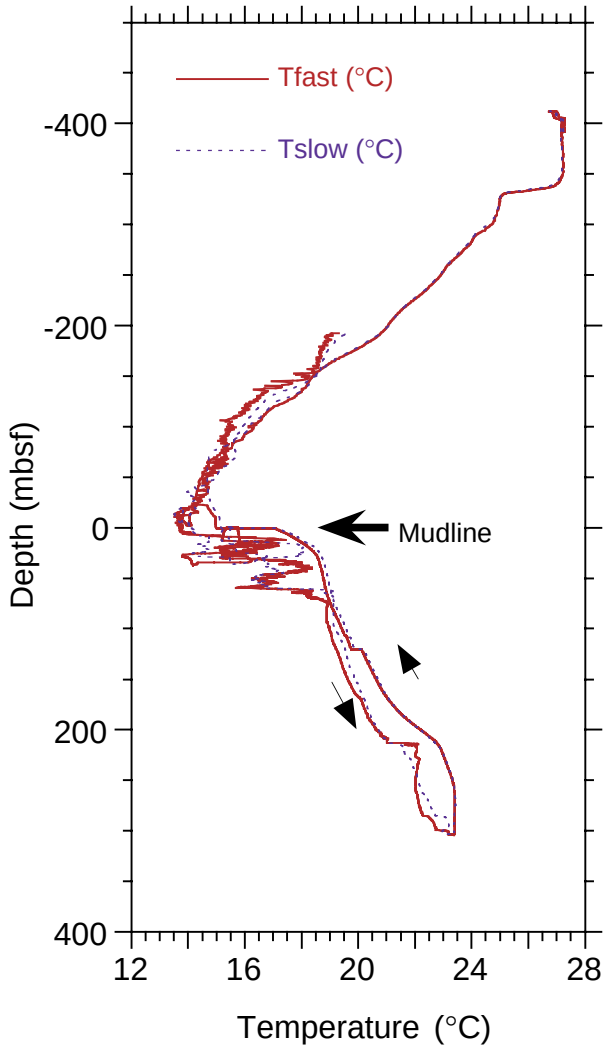

Figure F70. Hole 1114A temperature (TLT) data. T_{fast} and T_{slow} refer to the fast and slow thermistors, respectively. Arrows mark upward and downward passes of the tool.

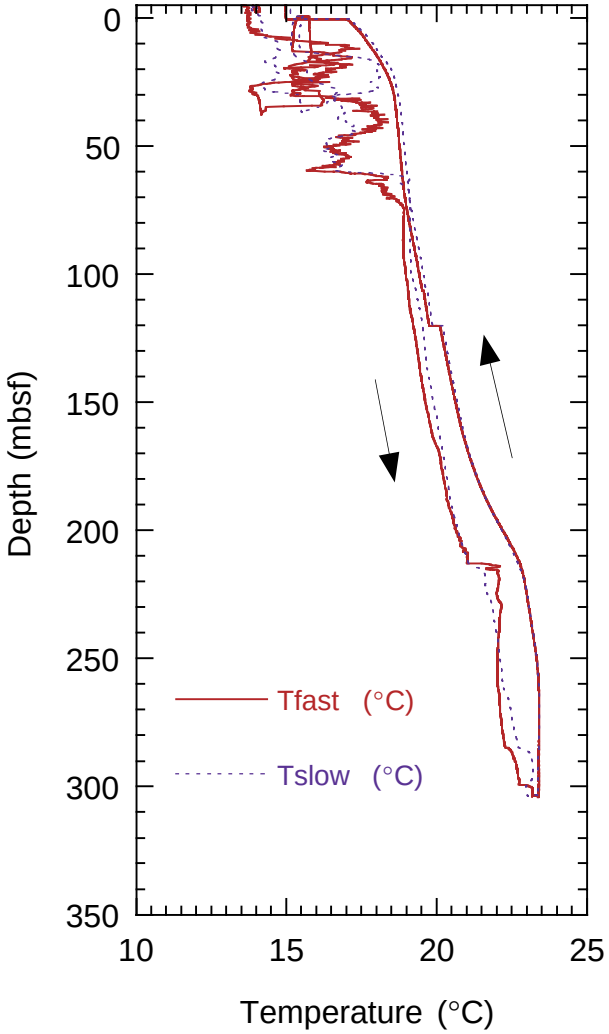

Table T1. Site 1114 coring summary.

Hole 1114A

Latitude: 9°47.613′S
Longitude: 151°34.504′E
Seafloor (drill-pipe measurement from rig floor, mbrf): 418.0
Distance between rig floor and sea level (m): 11.5
Water depth (drill-pipe measurement from sea level, m): 406.5
Total depth (from rig floor, mbrf): 770.80
Penetration (mbsf): 352.80
Total number of cores: 37
Total length of cored section (m): 352.80
Total core recovered (m): 43.78
Core recovery (%): 12

Core	Date (July 1998)	Time (UTC +10 hr)	Depth (mbsf)	Length cored (m)	Length recovered (m)	Recovery (%)
180-1114A-						
1R	13	0155	0.0-6.6	6.6	0.38	5.8
2R	13	0310	6.6-16.6	10.0	0.80	8.0
3R	13	0435	16.6-26.2	9.6	1.97	20.5
4R	13	0600	26.2-35.8	9.6	1.74	18.1
5R	13	0700	35.8-45.4	9.6	1.12	11.7
6R	13	0815	45.4-55.0	9.6	1.79	18.6
7R	13	0925	55.0-64.6	9.6	2.10	21.9
8R	13	1130	64.6-74.2	9.6	1.13	11.8
9R	13	1345	74.2-83.9	9.7	2.33	24.0
10R	13	1545	83.9-93.5	9.6	1.68	17.5
11R	13	1800	93.5-103.2	9.7	1.81	18.7
12R	13	2030	103.2-112.8	9.6	1.14	11.9
13R	13	2215	112.8-122.4	9.6	1.42	14.8
14R	13	2330	122.4-132.0	9.6	1.29	13.4
15R	14	0035	132.0-141.6	9.6	1.87	19.5
16R	14	0130	141.6-151.3	9.7	0.16	1.6
17R	14	0210	151.3-160.9	9.6	0.00	0.0
18R	14	0300	160.9-170.5	9.6	0.22	2.3
19R	14	0350	170.5-180.1	9.6	0.18	1.9
20R	14	0435	180.1-189.8	9.7	0.60	6.2
21R	14	0555	189.8-199.4	9.6	0.76	7.9
22R	14	0735	199.4-208.8	9.4	1.06	11.3
23R	14	0925	208.8-218.4	9.6	1.78	18.5
24R	14	1115	218.4-228.0	9.6	1.44	15.0
25R	14	1245	228.0-237.6	9.6	3.04	31.7
26R	14	1410	237.6-247.3	9.7	1.42	14.6
27R	14	1520	247.3-256.9	9.6	0.30	3.1
28R	14	1615	256.9-266.5	9.6	0.08	0.8
29R	14	1725	266.5-276.1	9.6	0.35	3.6
30R	14	1855	276.1-285.8	9.7	1.22	12.6
31R	14	2135	285.8-295.4	9.6	1.55	16.1
32R	15	0030	295.4-305.1	9.7	1.56	16.1
33R	15	0235	305.1-314.7	9.6	1.68	17.5
34R	15	0430	314.7-324.3	9.6	0.15	1.6
35R	15	0655	324.3-333.9	9.6	0.51	5.3
36R	15	0850	333.9-343.5	9.6	1.37	14.3
37R	15	1215	343.5-352.8	9.3	1.78	19.1
Totals:				352.8	43.78	12.4

Note: UTC = Universal Time Coordinated.

Table T2. Site 1114 coring summary by section. (Continued on next three pages.)

Core	Date (July 1998)	Time (UTC +10 hr)	Core depth (mbsf) Top	Core depth (mbsf) Bottom	Length (m) Cored	Length (m) Recovered	Recovery (%)	Section	Length (m) Liner	Length (m) Curated	Section depth (mbsf) Top	Section depth (mbsf) Bottom	Catwalk samples	Comment
180-1114A														
1R	13	0155	0.0	6.6	6.6	0.38	5.8							
								CC	0.38	0.38	0.00	0.38	PAL, HS	Trace to paleontology lab
									0.38	0.38				
2R	13	0310	6.6	16.6	10.0	0.80	8.0							
								1	0.58	0.58	6.60	7.18	HS	
								CC	0.22	0.22	7.18	7.40	PAL	
									0.80	0.80				
3R	13	0435	16.6	26.2	9.6	1.97	20.5							
								1	0.76	0.76	16.60	17.36	IW, WEL	
								2	0.95	0.95	17.36	18.31	HS	
								CC	0.26	0.26	18.31	18.57	PAL	
									1.97	1.97				
4R	13	0600	26.2	35.8	9.6	1.74	18.1							
								1	1.20	1.20	26.20	27.40	HS	
								2	0.40	0.40	27.40	27.80		
								CC	0.14	0.14	27.80	27.94	PAL	
									1.74	1.74				
5R	13	0700	35.8	45.4	9.6	1.12	11.7							
								1	0.94	0.94	35.80	36.74	HS	
								CC	0.18	0.18	36.74	36.92	PAL	
									1.12	1.12				
6R	13	0815	45.4	55.0	9.6	1.79	18.6							
								1	0.57	0.57	45.40	45.97	HS, IW	
								2	1.09	1.09	45.97	47.06	WEL	
								CC	0.13	0.13	47.06	47.19	PAL	
									1.79	1.79				
7R	13	0925	55.0	64.6	9.6	2.10	21.9							
								1	0.24	0.24	55.00	55.24	HS, WRSCR	
								2	1.03	1.03	55.24	56.27		
								3	0.60	0.60	56.27	56.87		
								CC	0.23	0.23	56.87	57.10	PAL	
									2.10	2.10				
8R	13	1130	64.6	74.2	9.6	1.13	11.8							
								1	0.90	0.90	64.60	65.50	HS	
								CC	0.23	0.23	65.50	65.73	PAL	
									1.13	1.13				
9R	13	1345	74.2	83.9	9.7	2.33	24.0							
								1	1.42	1.42	74.20	75.62	IW, HS	
								2	0.76	0.76	75.62	76.38		
								CC	0.15	0.15	76.38	76.53	PAL	
									2.33	2.33				
10R	13	1545	83.9	93.5	9.6	1.68	17.5							
								1	1.41	1.41	83.90	85.31	HS	
								CC	0.27	0.27	85.31	85.58	PAL	
									1.68	1.68				

Table T2 (continued).

Core	Date (July 1998)	Time (UTC +10 hr)	Core depth (mbsf) Top	Core depth (mbsf) Bottom	Length (m) Cored	Length (m) Recovered	Recovery (%)	Section	Length (m) Liner	Length (m) Curated	Section depth (mbsf) Top	Section depth (mbsf) Bottom	Catwalk samples	Comment
11R	13	1800	93.5	103.2	9.7	1.81	18.7							
								1	1.00	1.00	93.50	94.50		
								2	0.57	0.57	94.50	95.07	HS	
								CC	0.24	0.24	95.07	95.31	PAL	
									1.81	1.81				
12R	13	2030	103.2	112.8	9.6	1.14	11.9							
								1	0.96	0.96	103.20	104.16	HS	
								CC	0.18	0.18	104.16	104.34	PAL	
									1.14	1.14				
13R	13	2215	112.8	122.4	9.6	1.42	14.8							
								1	1.20	1.20	112.80	114.00	HS	
								CC	0.22	0.22	114.00	114.22	PAL	
									1.42	1.42				
14R	13	2330	122.4	132.0	9.6	1.29	13.4							
								1	1.12	1.12	122.40	123.52	PAL, HS	
								CC	0.17	0.17	123.52	123.69		
									1.29	1.29				
15R	14	0035	132.0	141.6	9.6	1.87	19.5							
								1	1.33	1.33	132.00	133.33	WRSCR, HS	
								2	0.37	0.37	133.33	133.70		
								CC	0.17	0.17	133.70	133.87	PAL	
									1.87	1.87				
16R	14	0130	141.6	151.3	9.7	0.16	1.6							
								CC	0.16	0.16	141.60	141.76	PAL	Trace to paleontology lab
									0.16	0.16				
17R	14	0210	151.3	160.9	9.6	0.00	0.0							No recovery
								1	0.00	0.00				
									0.00	0.00				
18R	14	0300	160.9	170.5	9.6	0.22	2.3							
								CC	0.22	0.22	160.90	161.12	PAL	Trace to paleontology lab
									0.22	0.22				
19R	14	0350	170.5	180.1	9.6	0.18	1.9							
								CC	0.18	0.18	170.50	170.68	PAL	Trace to paleontology lab
									0.18	0.18				
20R	14	0435	180.1	189.8	9.7	0.60	6.2							
								1	0.60	0.60	180.10	180.70	PAL	Trace to paleontology lab
									0.60	0.60				
21R	14	0555	189.8	199.4	9.6	0.76	7.9							
								1	0.58	0.58	189.80	190.38	HS	
								CC	0.18	0.18	190.38	190.56	PAL	Trace to paleontology lab
									0.76	0.76				
22R	14	0735	199.4	208.8	9.4	1.06	11.3							
								1	0.81	0.81	199.40	200.21	HS	
								CC	0.25	0.25	200.21	200.46	PAL	Trace to paleontology lab
									1.06	1.06				
23R	14	0925	208.8	218.4	9.6	1.78	18.5							
								1	1.11	1.11	208.80	209.91	HS, IW	

Table T2 (continued).

Core	Date (July 1998)	Time (UTC +10 hr)	Core depth (mbsf) Top	Core depth (mbsf) Bottom	Length (m) Cored	Length (m) Recovered	Recovery (%)	Section	Length (m) Liner	Length (m) Curated	Section depth (mbsf) Top	Section depth (mbsf) Bottom	Catwalk samples	Comment
								2	0.36	0.36	209.91	210.27		
								CC	0.31	0.31	210.27	210.58	PAL	
									1.78	1.78				
24R	14	1115	218.4	228.0	9.6	1.44	15.0							
								1	0.39	0.39	218.40	218.79		
								2	0.81	0.81	218.79	219.60	HS, WRSCR	
								CC	0.24	0.24	219.60	219.84	PAL	
									1.44	1.44				
25R	14	1245	228.0	237.6	9.6	3.04	31.7							
								1	0.76	0.76	228.00	228.76	HS, IW	
								2	0.74	0.74	228.76	229.50		
								3	1.42	1.42	229.50	230.92		
								CC	0.12	0.12	230.92	231.04	PAL	
									3.04	3.04				
26R	14	1410	237.6	247.3	9.7	1.42	14.6							
								1	1.21	1.21	237.60	238.81	HS	
								CC	0.21	0.21	238.81	239.02	PAL	
									1.42	1.42				
27R	14	1520	247.3	256.9	9.6	0.30	3.1							
								CC	0.30	0.30	247.30	247.60	PAL, HS	
									0.30	0.30				
28R	14	1615	256.9	266.5	9.6	0.08	0.8							
								CC	0.08	0.08	256.90	256.98		
									0.08	0.08				
29R	14	1725	266.5	276.1	9.6	0.35	3.6							
								CC	0.35	0.35	266.50	266.85	PAL, HS	
									0.35	0.35				
30R	14	1955	276.1	285.8	9.7	1.22	12.6							
								1	0.96	0.96	276.10	277.06	HS	
								CC	0.26	0.26	277.06	277.32	PAL	
									1.22	1.22				
31R	14	2135	285.8	295.4	9.6	1.55	16.1							
								1	1.33	1.33	285.80	287.13	HS	
								CC	0.22	0.22	287.13	287.35	PAL	
									1.55	1.55				
32R	15	0030	295.4	305.1	9.7	1.56	16.1							
								1	1.32	1.50	295.40	296.90	WRSCR, HS	
								2	0.00	0.42	296.90	297.32		
								CC	0.24	0.00			PAL	Trace to paleontology lab
									1.56	1.92				
33R	15	0235	305.1	314.7	9.6	1.68	17.5							
								1	0.18	1.37	305.10	306.47		
								2	1.50	0.98	306.47	307.45		
									1.68	2.35				
34R	15	0430	314.7	324.3	9.6	0.15	1.6							
								1	0.15	0.17	314.70	314.87		
									0.15	0.17				

Table T2 (continued).

Core	Date (July 1998)	Time (UTC +10 hr)	Core depth (mbsf) Top	Core depth (mbsf) Bottom	Length (m) Cored	Length (m) Recovered	Recovery (%)	Section	Length (m) Liner	Length (m) Curated	Section depth (mbsf) Top	Section depth (mbsf) Bottom	Catwalk samples	Comment
35R	15	0655	324.3	333.9	9.6	0.51	5.3							
								1	0.51	0.63	324.30	324.93		
									0.51	0.63				
36R	15	0850	333.9	343.5	9.6	1.37	14.3							
								1	1.37	1.50	333.90	335.40		
								2	0.00	0.60	335.40	336.00		
									1.37	2.10				
37R	15	1215	343.5	352.8	9.3	1.78	19.1							
								1	1.17	1.17	343.50	344.67		
								2	0.44	0.57	344.67	345.24		
								CC	0.17	0.35	345.24	345.59		
									1.78	2.09				
				Totals:	352.8	43.78	12.4							

Note: PAL = paleontology; HS = headspace; IW = interstitial water; WEL = Wellsbury microbiology; WRSCR = whole round Screaton.

Table T3. Composition of fine-grained sediments analyzed by X-ray diffraction, Hole 1114A.

Core, section, interval (cm)	Depth (mbsf)	Description	XRD identification: major (minor) minerals
180-1114A-			
1R-CC, 13-14	0.13	Foraminifer-bearing nannofossil ooze	Calcite (plagioclase)
5R-1, 17-18	35.97	Silty claystone	Plagioclase, quartz (pyroxene, chlorite, amphibole, illite)
6R-2, 4-4.5	46.01	Claystone	Plagioclase (quartz, pyroxene, illite)
7R-3, 21-22	56.48	Claystone	Quartz, plagioclase (calcite, pyroxene, chlorite, smectite?, illite, amphibole)
8R-1, 48-49	65.08	Siltstone	Plagioclase, quartz (pyroxene, chlorite, amphibole, smectite?)
9R-1, 25-26	74.45	Claystone	Quartz, plagioclase (chlorite, calcite, smectite?)
10R-1, 41-44	84.31	Silty sandstone	Quartz, plagioclase (calcite, chlorite, smectite?, amphibole)
11R-1, 56-57	94.06	Claystone	Quartz, plagioclase, calcite (chlorite, smectite?, amphibole)
12R-1, 33-35	103.53	Siltstone	Plagioclase, quartz (pyroxene, calcite, chlorite, smectite?, illite, talc?, amphibole)
13R-1, 38-39	113.18	Silty clay	Plagioclase (chlorite, smectite?)
14R-1, 46-48	122.86	Fine sandstone	Plagioclase, quartz (calcite, pyroxene, amphibole, chlorite, smectite?)
15R-2, 5-6	133.38	Sandstone	Quartz, plagioclase (calcite, chlorite)
16R-CC, 5-5.5	141.65	Clayey siltstone	Plagioclase, quartz (calcite, chlorite, smectite?)
22R-1, 14-15	199.54	Claystone	Plagioclase, quartz, calcite (chlorite, smectite?)
23R-2, 4-5	209.95	Claystone	Plagioclase, quartz (calcite, chlorite, smectite?)
24R-2, 67-68	219.46	Coarse-grained sandstone	Plagioclase, calcite (quartz, illite)
25R-3, 126-127	230.76	Fine-grained sandstone	Plagioclase, quartz (calcite, chlorite, smectite?)
26R-1, 19-20	237.79	Claystone	Quartz, plagioclase, calcite (pyrite, marcasite?, chlorite, smectite?, illite, amphibole)
29R-CC, 17-18	266.67	Very coarse sandstone	Plagioclase (quartz, pyroxene, amphibole)
30R-1, 17-18	276.27	Sandstone	Plagioclase, quartz (chlorite, smectite?, pyroxene)
31R-1, 9-10	285.89	Clay	Plagioclase, quartz (smectite?, chlorite, pyroxene)
31R-1, 75-76	286.55	Breccia with silty matrix	Plagioclase, calcite, kaolinite, smectite? (quartz)

Note: See "Lithostratigraphy," p. 3, for explanation.

Table T4. Major element compositions of dolerite and metadolerite recovered, Sites 1108, 1109, 1111, and 1114.

Core, section, interval (cm)	Sample	SiO_2	Average	TiO_2	Average	Al_2O_3	Average	Fe_2O_3	Average	MnO	Average	MgO	Average
180-1111A-													
16R-CC, 8-15	1a	47.56		1.96		16.62		13.45		0.20		6.68	
	1b	47.32	47.44	1.94	1.95	16.55	16.59	13.50	13.47	0.20	0.20	6.64	6.66
180-1108B-													
47R-CC, 1-3	2a	51.45		1.41		13.73		13.64		0.20		7.66	
	2b	51.51	51.48	1.41	1.41	13.75	13.74	13.57	13.61	0.20	0.20	7.69	7.67
180-1114A-													
36R-2, 40-42	3a	51.21		1.53		14.46		13.96		0.20		7.61	
	3b	50.45	50.85	1.49	1.51	14.32	14.39	13.71	13.65	0.19	0.19	7.57	7.59
36R-1, 70-72	4a	53.20		1.41		14.32		13.53		0.22		7.28	
	4b	52.88	53.04	1.41	1.41	14.20	14.26	13.52	13.53	0.22	0.22	7.23	7.25
180-1109D	5		51.24		1.37		14.91		12.27		0.19		6.86

Sample	CaO	Average	Na_2O	Average	K_2O	Average	P_2O_5	Average	Total	Average	LOI	Average	FeO*/ MgO	Rock type
1a	12.69		1.32		0.57		0.18		101.24		4.10			Foliated, epidote-rich schist
1b	12.60	12.65	1.27	1.29	0.57	0.57	0.18	0.18	100.76	101.00	4.10	4.10	1.82	
2a	10.56		2.58		0.15		0.09		101.47		3.43			Pebble in sediments
2b	10.57	10.56	2.49	2.53	0.16	0.15	0.09	0.09	101.43	101.50	3.43	3.43	1.60	
3a	11.21		1.85		0.39		0.13		102.46		2.53			Non-foliated metadolerite
3b	11.03	11.12	1.90	1.87	0.39	0.39	0.12	0.13	101.16	102.90	2.53	2.53	1.62	
4a	8.85		2.61		0.99		0.11		102.53		2.47			Foliated metadolerite pebble
4b	8.77	8.81	2.66	2.63	0.98	0.99	0.11	0.11	101.98	102.30	2.47	2.47	1.68	
5		12.45		1.71		0.11		0.11		101.20		1.79	1.61	Dolerite

Notes: Analyses are arranged in descending order of loss on ignition (LOI). FeO* = total Fe as FeO. Major element values are in weight percent. a and b = duplicate analyses of the same sample. 5 = average analysis of dolerite in Hole 1109D.

Table T5. Trace element composition of dolerites and metadolerites, Sites 1108, 1109, 1111, and 1114.

Core, section, interval (cm)	Sample	Nb	Zr	Y	Sr	Rb	Zn
180-1111A-							
16R-CC, 8-15	1	9	90	23	243	10	99
180-1108B-							
47R-CC, 1-3	2	4	60	19	157	2	87
180-1114A-							
36R-2, 40-42	3	6	73	24	145	7	100
36R-1, 70-72	4	6	66	23	76	15	96
180-1109D	5	4	71	22	137	2	83

Core, section, interval (cm)	Sample	Cu	Ni	Cr	V	Ce	Ba
180-1111A-							
16R-CC, 8-15	1	145	122	350	337	12	50
180-1108B-							
47R-CC, 1-3	2	170	108	271	331	7	9
180-1114A-							
36R-2, 40-42	3	166	96	191	352	10	24
36R-1, 70-72	4	154	95	182	340	6	86
180-1109D	5	140	94	363	302	10	7

Notes: Trace element values are in parts per million. 5 = average analysis of dolerite in Hole 1109D.

Table T6. Cumulative thickness of deformed clay-rich material (scaly fabrics) vs. total thickness of clay, for each section.

Core, section	Clay (cm)	Cumulative thickness (cm)		Type*	Scaly fabric (%)
		Undeformed	Scaly fabric		
180-1114A-					
8R-1	55	35	20	2	37
9R-1	46	34	12	1, 2	26
10R-1	69	34	35	3	50
11R-1	80	45	35	3	56
11R-2	45	25	20	3	44
12R-2	20	20	0		0
13R-1	15	0	15	1	100
21R-1	15	0	15	3	100
22R-1	30	0	30	1, 2	100
23R-1	30	0	30	1, 2	100
23R-2	20	0	20	1, 2	100
23R-CC	30	20	10	1, 2	33
24R-2	15	0	15	1	100
25R-1	65	0	65	3	100
25R-2	75	0	75	3	100
25R-3	140	0	140	3	100
26R-1	22	12	10	2	45
30R-1	50	0	50	3	100

Note: * 1 = incipient, 2 = intermediate, 3 = pervasive; for discussion on types of scaly fabrics see **"Domain III,"** p. 21.

Table T7. Range chart showing the distribution of selected calcareous nannofossil species, Hole 1114A.

Core, section, interval (cm)	Depth (mbsf)	Abundance	Preservation	*Calcidiscus leptoporus*	*Calcidiscus macintyrei*	*Coccolithus pelagicus*	*Dictyococcites productus*	*Discoaster brouweri*	*Discoaster pentaradiatus*	*Emiliania huxleyi*	*Gephyrocapsa caribbeanica*	*Gephyrocapsa oceanica*	*Gephyrocapsa omega*	*Helicosphaera carteri*	*Helicosphaera sellii*	*Pseudoemiliania lacunosa*	*Reticulofenestra minutula*	*Scapholithus fossilis*	*Scyphosphaera apsteinii*	*Scyphosphaera procera*	*Syracosphaera histrica*	*Thoracosphaera heimii*	*Thoracosphaera saxea*	*Umbilicosphaera sibogae*
180-1114A-																								
1R-CC, 37-38	0.37	A	G	F		R				R		F	C	F	r	r	C	R			R	R		R
2R-1, 30-32	6.90	C	G	F		R		r				F		F	R	F								
2R-1, 35-37	6.95	F	M	R	R									R	R	R								
2R-CC, 18-22	7.36	F	M	R		R					R			R		R	F				R		R	
3R-1, 22-24	16.82	F	M	R										F		R								
3R-2, 47-49	17.83	F	M	R	R	R			r					F		F								
3R-CC, 23-26	18.54	T	P													R	R							
4R-1, 95-97	27.15	F	M	R										F		R								
4R-CC, 11-14	27.91	T	P	R										R			R							
5R-1, 52-53	36.32	F	M	R										F		R								
5R-CC, 16-18	36.90	R	P	R	R	R					R			R		R	R						R	
6R-2, 96-97	46.93	F	P	R		R								R		R								
6R-CC, 10-13	47.16	F	P	R		R					R			R	R	R	F							
7R-2, 95-97	56.19	F	P	R										R		R								
7R-CC, 19-23	57.06	T	P	R										R			R							
8R-1, 29-30	64.89	T	P																					
8R-CC, 20-23	65.70	R	P			R								R										
9R-1, 42-43	74.62	R	P	R										R										
9R-CC, 12-15	76.50	R	M											R		R								
10R-1, 51-53	84.41	R	P											R										
10R-CC, 25-27	85.56	F	P	R		R		r						R										
11R-1, 75-77	94.25	R	P	R	R	R								R										
11R-CC, 13-15	95.20	R	P	R																				
12R-1, 57-60	103.77	R	P					r																
12R-CC, 6-8	104.22	F	M	R		R		R	r					F	R	R								
13R-1, 55-57	113.35			R										R		R								
13R-CC, 19-22	114.19	F	P	F	R	R								F		R								
14R-1, 0-2	122.40	F	M	R		R		R						F		R								
14R-1, 58-60	122.98	R	P	R										R										
15R-1, 60-62	132.60	R	P																					
15R-1, 86-88	132.86	T	P																					
15R-2, 9-11	133.42	R	M											R										
15R-CC, 14-17	133.84	R	P	R										R		R	R							
16R-CC, 8-9	141.68	R	P	R	R	R								R	R	R	F						R	
18R-CC, 21-22	161.11	B																						
19R-CC, 17-18	170.67	F	P	R	R	F	R							R	R	R	F		R					
20R-1, 59-60	180.69	B																						
21R-CC, 17-18	190.55	R	P	R		R								R		R	R							
22R-CC, 24-25	200.45	T	P	R		R								R		R	R							
23R-CC, 28-31	210.55	T	P											R			R							
24R-CC, 22-24	219.82	B																						
25R-CC, 9-12	231.01	F	M	R		R								R	R	R								
26R-1, 21-23	237.81	F	P	R		R								R		R	F							
26R-CC, 18-21	238.99	R	P			R																		
27R-CC, 26-27	247.56	B																						
29R-CC, 12-14	266.62	B																						
29R-CC, 33-35	266.83	B																						
30R-1, 33-35	276.43	B																						
30R-CC, 23-26	277.29	R	P	R				R						R										
31R-1, 22-24	286.02	R	P	R		R		R	R											R				
31R-1, 59-62	286.39	B																						
31R-CC, 20-22	287.33	B																						
31R-CC, 20-22	287.33	B																						
32R-CC, 23-24		B																						

Notes: Abundance (number specimens per field of view): D = dominant (>100); A = abundant (10–100); C = common (1–10); F = few (1 per 10 fields of view); R = rare (<1 per 10 fields of view); T = trace (<1 per transect); B = barren; Preservation: G = good; M = moderate; P = poor. Distribution: C = common; F = few; R = rare; r = reworked.

Table T8. Range chart showing the distribution of planktonic foraminifers, Hole 1114A.

Core, section, interval (cm)	Depth (mbsf)	Abundance	Preservation	*Bolliella calida*	*Dentoglobigerina altispira*	*Globigerinella siphonifera*	*Globigerinita glutinata*	*Globigerinoides conglobatus*	*Globigerinoides extremus*	*Globigerinoides fistulosus*	*Globigerinoides quadrilobatus*	*Globigerinoides ruber*	*Globigerinoides ruber* (pink)	*Globigerinoides sacculifer*	*Globigerinoides trilobus*	*Globorotalia crassaformis*	*Globorotalia menardii*	*Globorotalia scitula*	*Globorotalia tosaensis*	*Globorotalia truncatulinoides*	*Globorotalia tumida*	*Globorotalia tumida flexuosa*	*Globorotalia ungulata*	*Neogloboquadrina acostaensis*	*Neogloboquadrina dutertrei*	*Neogloboquadrina humerosa*	*Orbulina universa*	*Pulleniatina obliquiloculata*	*Sphaeroidinella dehiscens*	*Sphaeroidinella dehiscens* s.l.	*Zeaglobigerina rubescens*
180-1114A-																															
1R-CC, 37-38	0.37	A	G	F		F		R			R	R	A	A		R	R			R	R		R		R		F	F	F		A
2R-1, 30-32	6.90	A	G							R	A	F				F	A		F	R	F				F	A	F	A	F		
2R-1, 35-37	6.95	C	M			R		R	R		F	F		R	R		F		R		R				R	F	R	R			
2R-CC, 18-22	7.36	T	P														P				P										
3R-2, 47-49	17.83	A	M					F		F	A	A			A	F	F	R		F	F					A	R	F	F		
3R-CC, 23-26	18.54	R	P					R		R	R			R			R			R	R				R	R		R	R		
4R-1, 95-97	27.15	R	P								R	R				R	R		R	R	R					R		R	R		
4R-CC, 11-14	27.91		P																												
5R-1, 52-53	36.32		P																												
5R-CC, 16-18	36.90	T	P																												
6R-CC, 10-13	47.16	R	M								R					R	R				R					F	R	R			
7R-CC, 19-23	57.06		P																												
8R-CC, 20-23	65.70	C	M						F	R	A	F		F	A	F	F			R	F					A	R	F	F	F	
9R-CC, 12-15	76.50	F	M				R		F	R	F	F			F	R	R				R					F			R		
10R-CC, 25-27	85.56	F	P				F			R	F	F			F		R									F	R			F	
11R-CC, 13-15	95.20	F	P					R	R		F	R			F						R			R		F					
12R-CC, 6-8	104.22																														
13R-CC, 19-22	114.19	F	P				R					F			F					R	R					R					
14R-1, 0-2	122.40		P																												
15R-CC, 14-17	133.84	T	P																												
16R-CC, 8-9	141.68	F	M					R			F					R	R				R					A	F	F	R		
18R-CC, 21-22	161.11	R	P													P					P								P		
19R-CC, 17-18	170.67	C	M											R		F	F		F		F							F	F		
21R-CC, 17-18	190.55		P																												
22R-CC, 24-25	200.45	F	P					R		R	R	R		R		R	R		R		R					R	R	R			
23R-CC, 28-31	210.55	R	P											F		R					R				R			R			
24R-CC, 22-24	219.82		P																												
25R-CC, 9-12	231.01	C	P			R	F			R		F		F	F	R	R	R	R		F	R				F	R	F		R	
26R-CC, 18-21	238.99	F	P					R				F		F		R	R				R			R		F	R	R	R		
27R-CC, 26-27	247.56																														
29R-CC, 12-14	266.62	C	M			R		R				F		R	R	R	R				R			R		F	R	R	F	F	
29R-CC, 33-35	266.83																														
30R-CC, 23-26	277.29	R	P									R			F		R													R	
31R-1, 22-24	286.02	A	P		F	R		R	R		F	F		R		R	R					R	F	R		F	R		R		
31R-CC, 20-22	287.33																														
32R-CC, 23-24																															

Notes: Abundance (number of specimens per field of view): A = abundant (2–9); C = common (lower range of abundant); F = few (0.5–1.0); R = rare (1–3 per tray); P = present (1 per 2–3 trays); T = trace. Preservation: G = good; M = moderate; P = poor.

Table T9. Interstitial water geochemistry, Hole 1114A.

Core, section, interval (cm)	Depth	pH	Alkalinity (mM)	Salinity	Cl (T) (mM)	Cl (IC) (mM)	SO_4 (mM)	Na (mM)	K (mM)	Mg (mM)	Ca (mM)	Ca/Mg	Li (µM)	Sr (µM)	SiO_2 (µM)
180-1114A-															
3R-1, 66-76	17.26	8.52	3.12	34.5	556	568	28.6	484	10.7	48.1	9.4	0.20	16	80	172
6R-1, 48-57	45.88	8.31	2.08	35	565	570	29.6	479	7.3	47.7	11.4	0.24	16	63	427
9R-1, 142-152	75.52	8.75	2.26	35	565	577	28.8	463	5.3	46.1	15.9	0.34	12	40	170
23R-1, 101-111	209.91			35.5	572	583	28.4	483	6.6	49.4	15.4	0.31	23	68	150
25R-1, 68-76	228.66			34	553	567	28.2	465	6.3	49.7	15.4	0.31	20	80	168

Note: Cl (T) = chloride by titration, Cl (IC) = chloride by ion chromatography.

Table T10. Composition of headspace gas in sediments, Hole 1114A.

Core, section, interval (cm)	Depth (mbsf)	C_1	C_2	C_2=
180-1114A-				
1R-CC, 30-31	0.30	5		
2R-1, 0-1	6.60	2		
3R-2, 0-1	17.36	3		
4R-1, 119-120	27.39	3		
5R-1, 0-1	35.80	3		
6R-1, 56-57	45.96	4		1
7R-1, 0-1	55.00	3		
8R-1, 89-90	65.49	3		
9R-1, 141-142	75.61	4		
10R-1, 140-141	85.30	3		
11R-2, 0-2	94.50	3		
12R-1, 95-96	104.15	2		
13R-1, 0-1	112.80	3		
14R-1, 0-1	122.40	3		
15R-1, 0-1	132.00	3		
21R-1, 57-58	190.37	4		
22R-1, 80-81	200.20	5		
23R-1, 101-102	209.81	5		
24R-2, 80-81	219.59	3		
25R-1, 75-76	228.75	4		
26R-1, 0-1	237.60	3		
27R-CC, 0-1	247.30	3		
29R-CC, 0-1	266.50	3		
30R-1, 95-96	277.05	3		
31R-1, 132-133	287.12	2		
32R-1, 131-132	296.71	2		

Notes: All concentrations are reported in parts per million by volume. Blanks indicate values below detection limit.

Table T11. Carbon, calcium carbonate, nitrogen, and sulfur contents in sediments, Hole 1114A.

Core, section, interval (cm)	Depth (mbsf)	Inorganic carbon (wt%)	$CaCO_3$ (wt%)	Organic carbon (wt%)	Total nitrogen (wt%)	C/N	Total sulfur (wt%)
180-1114A-							
1R-CC, 15-16	0.15	7.80	64.97	0.02	0.05	0	0.07
5R-1, 16-16.5	35.96	0.37	3.07	0.54	0.05	11	0.38
6R-2, 3.5-4	46.01	0.52	4.37	0.19	0.06	3	0.18
7R-3, 23-24	56.50	0.73	6.11	0.57	0.05	11	0.15
8R-1, 58-59	65.18	0.30	2.49	0.68	0.08	9	0.60
9R-1, 26-27	74.46	0.50	4.16	0.86	0.10	9	0.33
10R-1, 40-42	84.30	0.53	4.45	0.71	0.08	9	0.27
11R-1, 55-56	94.05	0.55	4.62	0.81	0.07	12	0.40
12R-1, 33-35	103.53	0.22	1.86	0.35	0.06	6	0.36
13R-1, 37-38	113.17	0.24	1.96	0.27	0.05	5	0.18
14R-1, 46-48	122.86	0.19	1.59	0.04	0.03	1	0.10
15R-2, 6-7	133.39	0.45	3.77	0.48	0.06	8	0.35
16R-CC, 5-5.5	141.65	0.37	3.10	0.35	0.05	7	0.29
22R-1, 12-13	199.52	0.60	4.98	0.61	0.07	9	0.50
23R-2, 5-6	209.96	0.30	2.52	0.59	0.07	8	0.31
24R-2, 67-68	219.46	1.99	16.57		0.02	0	
25R-3, 107-108	230.57	0.38	3.15	1.40	0.08	18	0.28
25R-3, 124-125	230.74	2.87	23.87		0.05	0	
26R-1, 14.5-15.5	237.74	0.79	6.57	0.69	0.04	17	1.64
29R-CC, 18-19	266.68	0.40	3.33	0.02			0.16
30R-1, 16-17	276.26	0.18	1.50	0.44	0.03	15	0.42
31R-1, 8-9	285.88	0.87	7.25	0.66	0.05	13	0.61
31R-1, 71-72	286.51	0.31	2.56	0.02			0.06

Note: Blanks indicate values below detection limit, except for C/N ratio, where blanks indicate an undefined value.

Table T12. Index properties measured in cores, Site 1114.

Leg	Site	Hole	Core	Type	Section	Top (cm)	Bottom (cm)	Depth (mbsf)	Water content (bulk)	Water content (dry)	Bulk density ($g \cdot cm^{-3}$)	Dry density ($g \cdot cm^{-3}$)	Grain density ($g \cdot cm^{-3}$)	Porosity (%)	Void ratio
180	1114	A	1	R	1	29	31	0.30	41.71	71.56	1.59	0.93	2.64	64.80	1.84
180	1114	A	2	R	1	9	11	6.69	34.40	52.50	1.73	1.13	2.69	58.00	1.38
180	1114	A	3	R	1	57	59	17.17	20.10	25.10	2.03	1.62	2.69	39.70	0.66
180	1114	A	3	R	2	67	69	18.03	21.20	27.00	2.01	1.58	2.71	41.60	0.71
180	1114	A	4	R	1	96	98	27.16	23.00	29.90	1.94	1.49	2.64	43.60	0.77
180	1114	A	4	R	2	5	7	27.45	20.20	25.40	2.04	1.63	2.73	40.40	0.68
180	1114	A	5	R	1	41	43	36.21	21.60	27.50	1.99	1.56	2.69	42.00	0.72
180	1114	A	6	R	1	40	42	45.80	21.70	27.70	1.98	1.55	2.68	42.00	0.72
180	1114	A	6	R	2	48	50	46.45	21.90	28.10	1.98	1.55	2.69	42.50	0.74
180	1114	A	7	R	2	58	60	55.82	21.50	27.40	2.00	1.57	2.70	41.90	0.72
180	1114	A	7	R	3	16	18	56.43	21.90	28.10	1.98	1.55	2.68	42.40	0.74
180	1114	A	8	R	1	50	52	65.10	19.80	24.70	2.03	1.63	2.68	39.30	0.65
180	1114	A	9	R	1	59	61	74.79	17.20	20.80	2.13	1.76	2.74	35.70	0.56
180	1114	A	9	R	2	20	22	75.82	17.30	20.90	2.12	1.76	2.74	35.90	0.56
180	1114	A	10	R	1	29	31	84.19	18.90	23.30	2.06	1.67	2.69	38.00	0.61
180	1114	A	11	R	2	51	53	95.01	12.10	13.80	2.27	2.00	2.73	26.80	0.37
180	1114	A	12	R	1	81	83	104.01	12.00	13.60	2.25	1.98	2.68	26.30	0.36
180	1114	A	13	R	1	55	57	113.35	15.60	18.60	2.15	1.81	2.70	32.80	0.49
180	1114	A	14	R	1	81	83	123.21	7.40	7.90	2.39	2.21	2.67	17.10	0.21
180	1114	A	15	R	1	109	111	133.09	6.60	7.10	2.43	2.27	2.69	15.70	0.19
180	1114	A	15	R	2	20	22	133.53	12.80	14.70	2.25	1.96	2.73	28.20	0.39
180	1114	A	20	R	1	24	26	180.34	12.40	14.10	2.27	1.99	2.75	27.50	0.38
180	1114	A	21	R	1	18	20	189.98	9.80	10.80	2.31	2.09	2.68	22.00	0.28
180	1114	A	22	R	1	69	71	200.09	14.60	17.00	2.17	1.85	2.67	30.80	0.44
180	1114	A	23	R	CC	11	13	210.38	16.10	19.20	2.12	1.78	2.67	33.30	0.50
180	1114	A	24	R	1	28	30	218.68	15.10	17.80	2.18	1.85	2.73	32.20	0.48
180	1114	A	26	R	1	100	102	238.60	10.60	11.90	2.30	2.05	2.70	23.80	0.31
180	1114	A	30	R	1	20	22	276.30	18.10	22.10	2.03	1.66	2.59	35.80	0.56
180	1114	A	31	R	1	17	19	285.97	18.50	22.70	2.04	1.66	2.62	36.70	0.58
180	1114	A	31	R	1	47	49	286.27	21.20	26.90	2.04	1.61	2.79	42.30	0.73
180	1114	A	31	R	1	130	132	287.10	6.60	7.10	2.47	2.30	2.74	15.90	0.19
180	1114	A	32	R	1	20	22	295.60	3.90	4.10	2.56	2.46	2.73	9.80	0.11
180	1114	A	33	R	2	39	41	306.86	3.10	3.20	2.76	2.68	2.92	8.40	0.09
180	1114	A	34	R	1	13	15	314.83	3.00	3.10	2.71	2.63	2.86	8.00	0.09

Note: This table is also available in ASCII format in the **TABLES** directory.

Table T13. Longitudinal (z) and transverse (x and y) velocities for cores, Site 1114.

Leg	Site	Hole	Core	Type	Section	Top (cm)	Bottom (cm)	Depth (mbsf)	x-velocity ($m \cdot s^{-1}$)	y-velocity ($m \cdot s^{-1}$)	z-velocity ($m \cdot s^{-1}$)
180	1114	A	1	R	CC	11.2	11.2	0.11	1703.58		
180	1114	A	2	R	1	43	43	7.03	2138.38		
180	1114	A	3	R	1	61	61	17.21	2109.78		2111.96
180	1114	A	3	R	2	52	52	17.88	2119.87	2081.75	2035.85
180	1114	A	4	R	1	57	57	26.77	2160.83	2219.73	2115.58
180	1114	A	4	R	2	28	28	27.68	2227.11	2223.65	2128.76
180	1114	A	5	R	1	9	9	35.89	2294.06	2371.30	2248.54
180	1114	A	6	R	1	12	12	45.52	2309.79	2345.23	2173.69
180	1114	A	6	R	2	57	57	46.54	2235.23	2283.65	2148.89
180	1114	A	7	R	2	43	43	55.67	2377.07	2453.01	2269.24
180	1114	A	7	R	3	42	42	56.69	2352.38	2376.02	2193.50
180	1114	A	8	R	1	30	30	64.90	2255.08	2292.85	2217.52
180	1114	A	9	R	1	65	65	74.85	2334.22	2449.48	2325.76
180	1114	A	9	R	2	27	27	75.89	2350.57	2369.62	2303.26
180	1114	A	10	R	1	51	51	84.41	2252.20	2247.90	2141.11
180	1114	A	11	R	2	31	31	94.81	2358.57	2314.28	2180.03
180	1114	A	12	R	1	28	28	103.48	2616.07	2633.30	2504.49
180	1114	A	13	R	1	50	50	113.30	2602.60	2555.75	2613.78
180	1114	A	14	R	1	94	94	123.34	3869.62	3988.96	4054.78
180	1114	A	15	R	1	117	117	133.17	2460.71	2489.25	2599.11
180	1114	A	15	R	2	29	29	133.62	2695.68	2817.67	2791.50
180	1114	A	20	R	1	28	28	180.38	3285.62	3203.60	3361.85
180	1114	A	21	R	1	37	37	190.17	2667.38	2837.76	2755.77
180	1114	A	22	R	CC	5	5	200.26	2847.79	2781.47	2816.20
180	1114	A	23	R	CC	4	4	210.31	2560.05	2477.41	2478.37
180	1114	A	24	R	1	29	29	218.69	2940.09	2903.23	2930.65
180	1114	A	25	R	2	26.9	26.9	229.03	2268.03		
180	1114	A	25	R	3	118.8	118.8	230.69	2050.76		
180	1114	A	26	R	1	107	107	238.67	3069.87	2934.66	2969.90
180	1114	A	30	R	1	34.6	34.6	276.45	2187.00		
180	1114	A	31	R	1	53	53	286.33	2680.29		
180	1114	A	32	R	1	25	25	295.65	4531.18	4942.31	
180	1114	A	33	R	1	70.5	70.5	305.81	6370.52	6411.98	6591.69
180	1114	A	33	R	2	43.5	43.5	306.91	4930.60	4905.48	5142.09
180	1114	A	34	R	1	13	13	314.83	4346.44	4484.23	4539.98
180	1114	A	35	R	1	30	30	324.60	6025.27	6577.22	6443.63
180	1114	A	36	R	2	23	23	335.63	5999.53	6425.57	6347.54
180	1114	A	37	R	2	45	45	345.12	6200.83	6596.64	6551.51

Note: This table is also available in ASCII format in the **TABLES** directory.

Table T14. Thermal conductivity values in cores, Site 1114. (Continued on next two pages. See table note.)

Leg	Site	Hole	Core	Type	Section	Top interval (cm)	Bottom interval (cm)	Top depth (mbsf)	Bottom depth (mbsf)	Middle depth (mbsf)	Thermal conductivity ($W \cdot m^{-1} \cdot °C^{-1}$)	Thermal conductivity average ($W \cdot m^{-1} \cdot °C^{-1}$)
180	1114	A	2	R	1	30.0	30.0	6.90	6.90	6.90	0.71	
180	1114	A	2	R	1	30.0	30.0	6.90	6.90	6.90	0.70	
180	1114	A	2	R	1	30.0	30.0	6.90	6.90	6.90	0.71	0.71
180	1114	A	3	R	1	60.0	62.0	17.20	17.22	17.21	1.30	
180	1114	A	3	R	1	60.0	62.0	17.20	17.22	17.21	1.15	
180	1114	A	3	R	1	60.0	62.0	17.20	17.22	17.21	1.15	
180	1114	A	3	R	1	60.0	62.0	17.20	17.22	17.21	1.22	1.20
180	1114	A	3	R	2	33.0	34.0	17.69	17.70	17.70	1.24	
180	1114	A	3	R	2	33.0	34.0	17.69	17.70	17.70	1.23	
180	1114	A	3	R	2	33.0	34.0	17.69	17.70	17.70	1.22	
180	1114	A	3	R	2	33.0	34.0	17.69	17.70	17.70	1.22	1.23
180	1114	A	4	R	1	58.0	60.0	26.78	26.80	26.79	0.75	
180	1114	A	4	R	1	58.0	60.0	26.78	26.80	26.79	1.25	
180	1114	A	4	R	1	58.0	60.0	26.78	26.80	26.79	1.22	
180	1114	A	4	R	1	58.0	60.0	26.78	26.80	26.79	1.25	1.12
180	1114	A	4	R	2	29.0	31.0	27.69	27.71	27.70	1.18	
180	1114	A	4	R	2	29.0	31.0	27.69	27.71	27.70	1.19	
180	1114	A	4	R	2	29.0	31.0	27.69	27.71	27.70	1.19	
180	1114	A	4	R	2	29.0	31.0	27.69	27.71	27.70	1.20	
180	1114	A	4	R	2	29.0	31.0	27.69	27.71	27.70	1.21	1.19
180	1114	A	5	R	1	7.0	8.0	35.87	35.88	35.88	1.07	
180	1114	A	5	R	1	7.0	8.0	35.87	35.88	35.88	1.14	
180	1114	A	5	R	1	7.0	8.0	35.87	35.88	35.88	1.14	
180	1114	A	5	R	1	7.0	8.0	35.87	35.88	35.88	1.14	1.12
180	1114	A	6	R	1	43.0	44.0	45.83	45.84	45.84	1.20	
180	1114	A	6	R	1	43.0	44.0	45.83	45.84	45.84	1.21	
180	1114	A	6	R	1	43.0	44.0	45.83	45.84	45.84	1.24	
180	1114	A	6	R	1	43.0	44.0	45.83	45.84	45.84	1.22	1.22
180	1114	A	7	R	2	42.0	43.0	55.66	55.67	55.67	1.04	
180	1114	A	7	R	2	42.0	43.0	55.66	55.67	55.67	1.06	
180	1114	A	7	R	2	42.0	43.0	55.66	55.67	55.67	0.98	
180	1114	A	7	R	2	42.0	43.0	55.66	55.67	55.67	1.05	1.03
180	1114	A	7	R	3	43.0	44.0	56.70	56.71	56.71	0.97	
180	1114	A	7	R	3	43.0	44.0	56.70	56.71	56.71	1.03	
180	1114	A	7	R	3	43.0	44.0	56.70	56.71	56.71	1.03	
180	1114	A	7	R	3	43.0	44.0	56.70	56.71	56.71	1.02	1.02
180	1114	A	8	R	1	34.0	35.0	64.94	64.95	64.95	1.07	
180	1114	A	8	R	1	34.0	35.0	64.94	64.95	64.95	1.23	
180	1114	A	8	R	1	34.0	35.0	64.94	64.95	64.95	1.22	
180	1114	A	8	R	1	34.0	35.0	64.94	64.95	64.95	1.26	1.19
180	1114	A	9	R	1	63.0	64.0	74.83	74.84	74.84	1.24	
180	1114	A	9	R	1	63.0	64.0	74.83	74.84	74.84	1.15	
180	1114	A	9	R	1	63.0	64.0	74.83	74.84	74.84	1.18	
180	1114	A	9	R	1	63.0	64.0	74.83	74.84	74.84	1.19	1.19
180	1114	A	9	R	2	8.0	9.0	75.70	75.71	75.71	1.36	
180	1114	A	9	R	2	8.0	9.0	75.70	75.71	75.71	1.40	

Table T14 (continued).

Leg	Site	Hole	Core	Type	Section	Top interval (cm)	Bottom interval (cm)	Top depth (mbsf)	Bottom depth (mbsf)	Middle depth (mbsf)	Thermal conductivity ($W \cdot m^{-1} \cdot °C^{-1}$)	Thermal conductivity average ($W \cdot m^{-1} \cdot °C^{-1}$)
180	1114	A	9	R	2	8.0	9.0	75.70	75.71	75.71	1.36	
180	1114	A	9	R	2	8.0	9.0	75.70	75.71	75.71	1.39	1.38
180	1114	A	10	R	1	43.0	44.0	84.33	84.34	84.34	1.19	
180	1114	A	10	R	1	43.0	44.0	84.33	84.34	84.34	1.19	
180	1114	A	10	R	1	43.0	44.0	84.33	84.34	84.34	1.21	
180	1114	A	10	R	1	43.0	44.0	84.33	84.34	84.34	1.21	1.20
180	1114	A	11	R	2	32.0	33.0	94.82	94.83	94.83	1.12	
180	1114	A	11	R	2	32.0	33.0	94.82	94.83	94.83	1.21	
180	1114	A	11	R	2	32.0	33.0	94.82	94.83	94.83	1.29	
180	1114	A	11	R	2	32.0	33.0	94.82	94.83	94.83	1.31	1.23
180	1114	A	12	R	1	75.0	76.0	103.95	103.96	103.96	1.06	
180	1114	A	12	R	1	75.0	76.0	103.95	103.96	103.96	1.13	
180	1114	A	12	R	1	75.0	76.0	103.95	103.96	103.96	1.13	
180	1114	A	12	R	1	75.0	76.0	103.95	103.96	103.96	1.13	1.11
180	1114	A	13	R	1	51.0	52.0	113.31	113.32	113.32	1.16	
180	1114	A	13	R	1	51.0	52.0	113.31	113.32	113.32	1.22	
180	1114	A	13	R	1	51.0	52.0	113.31	113.32	113.32	1.18	
180	1114	A	13	R	1	51.0	52.0	113.31	113.32	113.32	1.25	1.20
180	1114	A	14	R	1	92.0	93.0	123.32	123.33	123.33	1.56	
180	1114	A	14	R	1	92.0	93.0	123.32	123.33	123.33	1.62	
180	1114	A	14	R	1	92.0	93.0	123.32	123.33	123.33	1.70	
180	1114	A	14	R	1	92.0	93.0	123.32	123.33	123.33	1.51	1.60
180	1114	A	15	R	1	114.0	116.0	133.14	133.16	133.15	1.35	
180	1114	A	15	R	1	114.0	116.0	133.14	133.16	133.15	1.41	
180	1114	A	15	R	1	114.0	116.0	133.14	133.16	133.15	1.48	
180	1114	A	15	R	1	114.0	116.0	133.14	133.16	133.15	1.47	1.43
180	1114	A	15	R	2	27.0	28.0	133.60	133.61	133.61	1.34	
180	1114	A	15	R	2	27.0	28.0	133.60	133.61	133.61	1.45	
180	1114	A	15	R	2	27.0	28.0	133.60	133.61	133.61	1.47	
180	1114	A	15	R	2	27.0	28.0	133.60	133.61	133.61	1.47	1.43
180	1114	A	20	R	1	31.0	33.0	180.41	180.43	180.42	1.27	
180	1114	A	20	R	1	31.0	33.0	180.41	180.43	180.42	1.38	
180	1114	A	20	R	1	31.0	33.0	180.41	180.43	180.42	1.41	
180	1114	A	20	R	1	31.0	33.0	180.41	180.43	180.42	1.37	1.36
180	1114	A	21	R	1	34.0	36.0	190.14	190.16	190.15	1.09	
180	1114	A	21	R	1	34.0	36.0	190.14	190.16	190.15	1.10	
180	1114	A	21	R	1	34.0	36.0	190.14	190.16	190.15	1.11	
180	1114	A	21	R	1	34.0	36.0	190.14	190.16	190.15	1.12	1.10
180	1114	A	22	R	CC	5.0	6.0	200.26	200.27	200.27	1.34	
180	1114	A	22	R	CC	5.0	6.0	200.26	200.27	200.27	1.40	
180	1114	A	22	R	CC	5.0	6.0	200.26	200.27	200.27	1.44	
180	1114	A	22	R	CC	5.0	6.0	200.26	200.27	200.27	1.41	1.40
180	1114	A	23	R	CC	6.0	7.0	210.33	210.34	210.34	1.22	
180	1114	A	23	R	CC	6.0	7.0	210.33	210.34	210.34	1.22	
180	1114	A	23	R	CC	6.0	7.0	210.33	210.34	210.34	1.22	
180	1114	A	23	R	CC	6.0	7.0	210.33	210.34	210.34	1.20	1.22
180	1114	A	24	R	1	35.0	36.0	218.75	218.76	218.76	1.18	
180	1114	A	24	R	1	35.0	36.0	218.75	218.76	218.76	1.28	
180	1114	A	24	R	1	35.0	36.0	218.75	218.76	218.76	1.22	
180	1114	A	24	R	1	35.0	36.0	218.75	218.76	218.76	1.22	1.22

Table T14 (continued).

Leg	Site	Hole	Core	Type	Section	Top interval (cm)	Bottom interval (cm)	Top depth (mbsf)	Bottom depth (mbsf)	Middle depth (mbsf)	Thermal conductivity ($W \cdot m^{-1} \cdot °C^{-1}$)	Thermal conductivity average ($W \cdot m^{-1} \cdot °C^{-1}$)
180	1114	A	26	R	1	106.0	107.0	238.66	238.67	238.67	1.41	
180	1114	A	26	R	1	106.0	107.0	238.66	238.67	238.67	1.42	
180	1114	A	26	R	1	106.0	107.0	238.66	238.67	238.67	1.55	
180	1114	A	26	R	1	106.0	107.0	238.66	238.67	238.67	1.44	1.45
180	1114	A	30	R	1	31.0	33.0	276.41	276.43	276.42	1.20	
180	1114	A	30	R	1	31.0	33.0	276.41	276.43	276.42	1.25	
180	1114	A	30	R	1	31.0	33.0	276.41	276.43	276.42	1.24	
180	1114	A	30	R	1	31.0	33.0	276.41	276.43	276.42	1.23	1.23
180	1114	A	32	R	1	23.0	24.0	295.63	295.64	295.64	1.18	
180	1114	A	32	R	1	23.0	24.0	295.63	295.64	295.64	1.27	
180	1114	A	32	R	1	23.0	24.0	295.63	295.64	295.64	1.20	
180	1114	A	32	R	1	23.0	24.0	295.63	295.64	295.64	1.21	1.22
180	1114	A	33	R	2	46.0	47.0	307.07	307.08	307.08	1.46	
180	1114	A	33	R	2	46.0	47.0	307.07	307.08	307.08	1.56	
180	1114	A	33	R	2	46.0	47.0	307.07	307.08	307.08	1.28	
180	1114	A	33	R	2	46.0	47.0	307.07	307.08	307.08	1.37	1.42
180	1114	A	34	R	1	9.0	10.0	314.79	314.80	314.80	1.29	
180	1114	A	34	R	1	9.0	10.0	314.79	314.80	314.80	1.26	
180	1114	A	34	R	1	9.0	10.0	314.79	314.80	314.80	1.43	
180	1114	A	34	R	1	9.0	10.0	314.79	314.80	314.80	1.25	1.31
180	1114	A	35	R	1	28.0	29.0	324.58	324.59	324.59	1.75	
180	1114	A	35	R	1	28.0	29.0	324.58	324.59	324.59	1.87	
180	1114	A	35	R	1	28.0	29.0	324.58	324.59	324.59	1.83	
180	1114	A	35	R	1	28.0	29.0	324.58	324.59	324.59	1.81	1.81
180	1114	A	36	R	2	21.0	22.0	335.61	335.62	335.62	1.47	
180	1114	A	36	R	2	21.0	22.0	335.61	335.62	335.62	1.40	
180	1114	A	36	R	2	21.0	22.0	335.61	335.62	335.62	1.33	
180	1114	A	36	R	2	21.0	22.0	335.61	335.62	335.62	1.36	1.39
180	1114	A	37	R	2	43.0	44.0	345.10	345.11	345.11	1.23	
180	1114	A	37	R	2	43.0	44.0	345.10	345.11	345.11	1.36	
180	1114	A	37	R	2	43.0	44.0	345.10	345.11	345.11	1.37	
180	1114	A	37	R	2	43.0	44.0	345.10	345.11	345.11	1.41	1.34

Note: This table is also available in ASCII format in the **TABLES** directory.

Table T15. Summary of logging operations.

Logging		Mudline depth (mbrf)		Pipe depth (mbsf)		Logged interval (mbsf)	
Run	Pass	Drill pipe	Wireline	Drill pipe	Wireline	Bottom	Top
1	Down	418.0	418.3	80	80.5	305.0	–26.6
1	Up	418.0	417.5	70	74.5	305.0	–27.4
2	Up 1	418.0	418.25	80		298.0	96.2
2	Up 2	418.0	418.25	70	74.5	298.6	39.1